FIBRE-LADEN FLOWS IN BIOLOGY AND BIOTECHNOLOGY

by

GEMMA CUPPLES

A thesis submitted to
The University of Birmingham
for the degree of
DOCTOR OF PHILOSOPHY

Supervisors: Professor David J. Smith & Dr Rosemary J. Dyson

School of Mathematics
College of Engineering and Physical Sciences
The University of Birmingham
January 2018

Abstract

Fibre-laden fluids are ubiquitous in biological and physical systems; the fibres alter the rheology of the fluid and hence the emergent behaviour of the system. This thesis investigates two physical situations associated with fibrous media.

Firstly we optimise the shear-induced alignment of suspensions of elongated particles, motivated by collaboration with Linear Diagnostics Ltd who are developing handheld devices to detect disruptions in fibre alignment due to pathogen presence in biological samples. Incorporating the effects of fibre dispersion and the mechanical anisotropy induced by the particles, we model suspensions of elongated particles undergoing steady or oscillating flow using a Fokker-Planck framework, producing recommendations for designs which optimise the signal to noise ratio.

Next, we investigate microscopic propulsion in perfectly aligned media; for example the evolving fibrous structure of cervical mucus and more generally the problem of propulsion and pumping of an active fluid with alignment. We model the swimming of spermatozoa by adapting Taylor's classical swimming sheet model using Ericksen's transversely isotropic constitutive law (a limit of the Fokker-Planck model), to account for an aligned fibrous network. We find that propulsion in fibre-laden fluids is drastically different from Newtonian fluids, supporting the requirement to investigate fibrous rheology.

Acknowledgments

I would like to thank Professor David Smith and Dr Rosemary Dyson for their advice, kind support and patience throughout my doctoral studies. I would also like to thank BBSRC and Linear Diagnostics Ltd for funding this work and supporting a research trip to the University of Adelaide and University of Auckland, which I thank Dr Edward Green and Dr Richard Clarke for the opportunity.

I would like to thank Dr Matt Hicks, Linear Diagnostics Ltd and The BioHub for access to their laboratory and for help with the initial experiments undertaken.

Special thanks go to Dr Craig Holloway, Dr Meurig Gallagher, Chloe Spalding and Ryan Davies for helpful discussions about my research, general support and making my time at the University of Birmingham a fantastic experience. Finally, I give thanks to my parents and my sister Kim for their constant support and encouragement, without them I could not have achieved this much.

CONTENTS

LIST OF PUBLICATIONS

1. G. Cupples, R. J. Dyson, and D. J. Smith. Viscous propulsion in active transversely isotropic media. *J. Fluid. Mech.*, $812, 501 - 524, 2017$.

2. C.R. Holloway, G. Cupples, D.J. Smith, J.E.F. Green, R.J. Clarke, and R.J. Dyson. Influences of transversely–isotropic rheology and translational diffusion on the stability of active suspension. Under review with *Eur Phys J E*, 2018.

Chapter 4 has been published as 1. The connection between suspension models and Ericksen's transversely-isotropic model, discussed in chapter 1 is under review as 2.

LIST OF FIGURES

LIST OF TABLES

GLOSSARY OF TERMS

Antibody A protein which can combat harmful pathogens and viruses. They are typically y-shaped and have a unique shape which recognises and binds to a specific pathogen.

Bacteriophage A virus that infects a bacterium and replicates within it.

Chromatography The process of separating components of a mixture based on their structural characteristics and binding affinity. The mixture is dissolved in a '*mobile phase*' and passed across a structure, such as a column, containing a different material (the '*stationary phase*'). The interaction of the mixture with the stationary phase causes its components to pass through the structure at varying speeds.

Flagellum Hair-like filamentous protein structures, attached to a cell surface, whose primary function is locomotion.

Linear Dichroism Spectroscopy A spectroscopic method measuring the differential absorbance by a sample of two light sources with orthogonal polarisation. One light source is polarised parallel to the preferred direction of the sample and the other is polarised perpendicular to this direction.

Pathogen A biological compound that is an infectious agent; they cause disease or illness in their host. Pathogens can be certain types of bacteria, viruses, fungi or parasites.

Spectroscopy Study of the interaction of light with all forms of matter.

CHAPTER 1

INTRODUCTION

Many biological fluids are complex and fibrous, and so their properties differ from Newtonian fluids. Moreover, their alignment may confer important functional properties in the flow direction; it is therefore important to understand how the presence and alignment of these fibres can affect the rheology. In this thesis we investigate two biological applications: an industrial problem aimed at optimising the detection of pathogens via flow-aligned bacteriophage, and an adaptation of Taylor's swimming sheet, biologically relevant to the efficiency of spermatozoa swimming through fibre-reinforced cervical mucus. Investigating fibre-reinforced viscous materials has a wide range of other industrial [37, 38] and physical applications; these include the mechanical behaviour of collagen gel, the growth of plant cell walls and bacterial suspensions [22, 31, 40].

1.1 Active fibre suspensions

Suspensions of micro-organisms exhibiting self-propulsion can be termed *active*; these suspensions display collective behaviour [41, 48, 82, 88] and, as seen more recently, superfluidity [59]. Modelling these suspensions is an area of significant interest, with connections to viscoelastic fluids [65], liquid crystals [58] and transversely-isotropic fluids [21, 22, 40]. Pedley & Kessler's [76] model for active suspensions of motile algae has been utilised and adapted for a variety of problems; the original work by Batchelor [2, 3] and Hinch & Leal

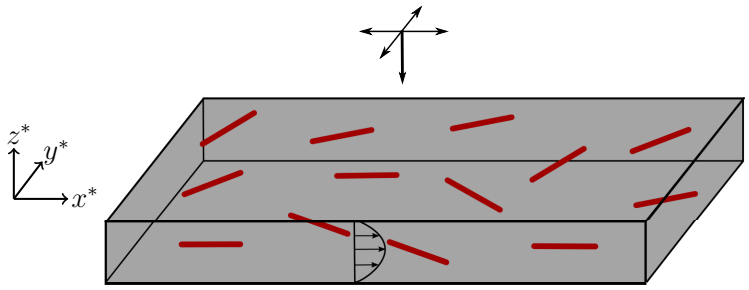

Figure 1.1: A thin rectangular channel containing a fibre-laden fluid, typical of that used by Linear Diagnostics Ltd. The light source compares light polarised parallel and perpendicular to the flow (x^*) direction and shines down through the channel, indicated by the arrows above the channel.

[35] introduced the bulk stresses associated with elongated particles in flow. Examples include, but are not limited to, a stability analysis of isotropic and aligned particle suspensions [82], the stability of suspensions under an imposed flow [25, 41], variations in the effective viscosity of a fluid [81] and suspensions of artificial particles used to transport non-motile cells [19]. Further, by linking active and transversely-isotropic fluids [39], these suspension models can be used to construct a multiphase model of extracellular matrix [21]. For detailed review see [34, 54, 83] and for a review of work relating to artificial suspensions see [75].

Externally forced flows of particle suspensions have been examined in detail; the enhancement of fluid stresses due to a suspension of particles can be calculated for an imposed simple shear [45, 55], time-dependent shear flows [36], turbulent channel flow [63, 66, 69] and constricted channels [47]. Pressure-driven channel flow, where a Newtonian flow profile is assumed and wall accumulation is investigated, has also been undertaken [25]. Taylor dispersion of bottom-heavy swimming micro-organisms is considered by [33], uniform density and bottom-heavy spherical squirmers [42] and particle collisions [97] have also been considered.

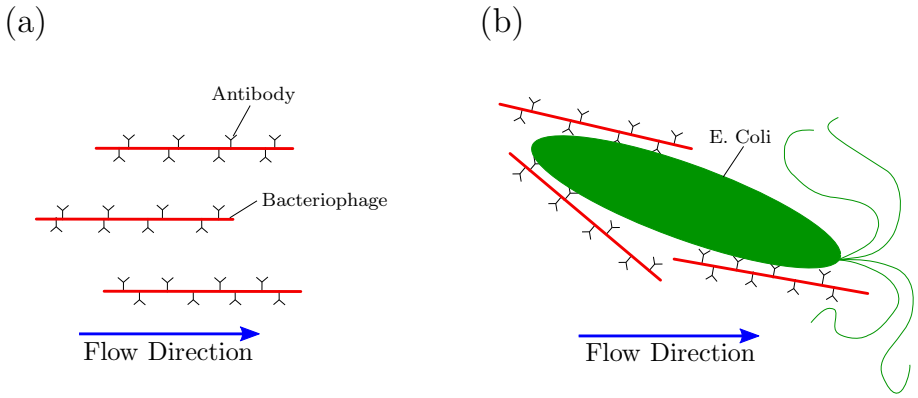

Figure 1.2: Disturbance to the alignment of a bacteriophage suspension with the presence of a pathogen. (a) The undisturbed flow-induced alignment in the flow direction. Each bacteriophage has pathogen-specific antibodies attached to their surface. (b) The disturbed alignment due to the presence of a pathogen. Multiple antibodies on multiple bacteriophage attach to binding sites on the pathogen, causing a reduction in the alignment.

1.2 Flow-induced alignment of elongated fibres

The work in chapters 2 and 3 is motivated by the aim to improve a novel technology to detect pathogens in small quantities of water or biological fluids, for example urine. The prototype device, developed by Linear Diagnostics Ltd, aims to achieve this by measuring disturbance to the flow-induced alignment of rod-shaped bacteriophage in thin rectangular channels via linear dichroism spectroscopy (figure 1.1).

We attach pathogen-specific antibodies to the surface of M13 bacteriophage and suspend the bacteriophage in the fluid sample to be tested. The suspended bacteriophage align according to the stress applied to the material (figure 1.2a); the direction and degree of alignment is inferred through a difference in absorption of light polarised parallel and orthogonal to the flow direction. Different antibodies attach to binding sites which are pathogen specific; if this pathogen of interest is present, a number of these antibodies attach to the binding sites causing clumping around the pathogen. The bacteriophage are much smaller than the pathogen (for example, *E.coli* are approximately 2 μm in length in comparison to M13 with length 800 nm, or 0.8 μm) and so as demonstrated in figure 1.2b, and the alignment is disrupted. This has been witnessed experimentally, via fluorescence

imaging (discussed in chapter 5), and by the observed drop in signal from the prototype handheld device.

Linear Diagnostics Ltd aim to exploit this disruption, resulting in a reduced linear dichroism signal, to detect pathogens in biological samples. There are multiple methods to induce alignment in flow cells; current suggestions for a pumping mechanism include a peristaltic pump, where the top face of a section of the channel is flexible and undergoes a peristaltic motion, and an oscillating pump, which forces the fluid through thin tubes and into the channel. The flow induced by the oscillating pump is assumed steady through the channel.

Linear dichroism spectroscopy is defined as the difference between absorption of light polarised parallel and perpendicular to the flow direction, or molecular orientation axis, and relies on the sample being either intrinsically oriented or oriented during experiment [7, 71]. Experimental orientation has previously been achieved via Couette flow [7], electric or magnetic fields, compressed gels or thin polymer films [72]. Linear dichroism spectroscopy can provide information on the molecular structure and composition of complex compounds such as DNA strands [7], haemoglobin [23] or the structure of the membranes in photosynthesising cells [29]; these compounds may be too large or irregular for other methods. Chapters 2 and 3 examine the shear-induced alignment from pressure driven flow through thin rectangular channels; since pathogen induced disruption to this alignment underpins this technology, the key challenge is to improve the signal to noise ratio to maximise sensitivity.

1.3 Perfectly-aligned media

Many biological fluids in which cells and organisms swim are fibre reinforced, and so it is instructive to model propulsion in such fluids. The study in chapter 4 is motivated by the fibrous nature of many biological media, for example cervical mucus encountered by spermatozoa in many internally-fertilising species, or active suspensions of elongated cells.

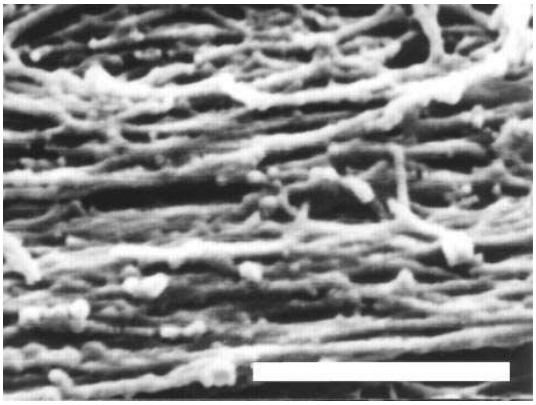

Figure 1.3: Parallel filament mesh in cervical mucus during the time of ovulation. Bar = 10 μm. Republished with permission of Oxford University Press, from 'Ultrastructure of the Human Periovulatory Cervical Mucus', F. Ceric et al, 54 (5), 2005; permission conveyed through Copyright Clearance Center, Inc.

Cervical mucus consists of a glycofilament-mucin structure, which during ovulation forms parallel networks (figure 1.3), due to hormonally-induced variations in hydration; sperm migration occurs through the spaces between this glycofilament structure and along the direction of the glycofilaments [8, 14]. To understand how these effects modify viscous propulsion, we extend Taylor's classical model of small-amplitude zero-Reynolds-number propulsion of a 'swimming sheet' via the transversely-isotropic fluid model of Ericksen, which is linear in strain rate and possesses a distinguished direction. We model the fluid as a Newtonian fluid with a suspension of elongated particles that have a uniform initial alignment; we expect the motion of the tail to disrupt the alignment of the fibres adjacent to the tail, depicted in figure 1.4; Ericksen's evolution equation [24] is used to determine the impact of a swimming sheet on the fibre orientation. This model is a simplified version of cervical mucus, neglecting other particles and potential viscoelastic behaviour of the mucus; this simplification enables a determination of the key impacts the glycofiliments have on microscopic propulsion.

In the current chapter we introduce the governing equations associated with active suspensions. The Navier-Stokes and continuity equations are first introduced, followed by the Fokker-Planck equation governing the distribution of particle orientation in section 1.4.1. Next, the extra-stress terms related to the moments of this distribution are intro-

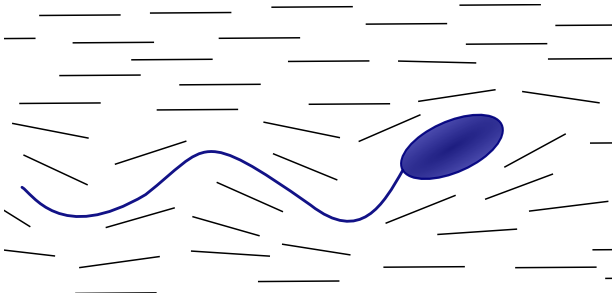

Figure 1.4: Spermatozoa swimming through an aligned fibre-reinforced fluid. Swimming occurs via a wave traversing down the tail of the cell and this waving movement may disturb the fibres adjacent to the tail.

duced in section 1.4.2 and the orientation parameter, and its relation to linear dichroism signal, is defined in section 1.4.3. Finally, the link between the particle suspension equations discussed by Pedley & Kessler [76] and the transversely-isotropic model of Ericksen [24] is established in section 1.5.

1.4 Governing equations of fibre-laden flow

In this section we define the equations governing the flow and orientation of a suspension of fibres. The fluid equations, along with extra stress terms, are introduced and coupled with a Fokker-Planck equation describing the orientation distribution in a fluid.

The dimensional Navier-Stokes and incompressibility equations are

$$\rho^* \left(\frac{\partial \boldsymbol{u}^*}{\partial t^*} + (\boldsymbol{u}^* \cdot \nabla^*)\boldsymbol{u}^* \right) = \nabla^* \cdot \boldsymbol{\sigma}^*, \tag{1.1}$$

$$\nabla^* \cdot \boldsymbol{u}^* = 0, \tag{1.2}$$

where ρ^* is density, $\boldsymbol{u}^*(\boldsymbol{x}^*, t^*)$ is the velocity vector, t^* is time, $\boldsymbol{x}^*$ represents coordinates in Cartesian space, $\boldsymbol{\sigma}^*$ is the stress tensor and ∇^* is differentiation in Cartesian space. The asterisk notation represents dimensional variables. For Newtonian fluids, the stress tensor $\boldsymbol{\sigma}^*$ is given by

$$\boldsymbol{\sigma}^* = -P^* \boldsymbol{I} + 2\mu^* \boldsymbol{e}^*, \tag{1.3}$$

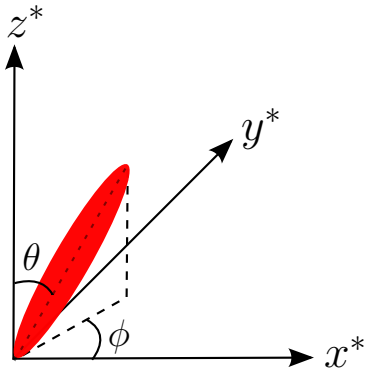

Figure 1.5: Depiction of particle orientation in term of angles, $\theta \in [0, \pi]$ and $\phi \in [0, 2\pi)$, away from the coordinate axes. The macroscopic orientation direction is defined as the x^*-direction.

where P^* is the pressure, $\boldsymbol{I}$ is the identity matrix, μ^* is the viscosity and $\boldsymbol{e}^* = (\nabla^* \boldsymbol{u}^* + \nabla^* \boldsymbol{u}^{*T})/2$ is the rate of strain tensor.

When particles are suspended in a fluid, they impact the stresses on both the fluid and themselves. These extra stresses are accounted for by altering the stress tensor associated with the fluid. To describe the evolution of particles, we introduce the probability density function $\psi(\boldsymbol{p}, \boldsymbol{x}^*, t^*)$, describing the likelihood a particle at point $\boldsymbol{x}^*$ and t^* has orientation $\boldsymbol{p}$. This probability density function is governed by the Fokker-Planck equation [39, 76, 81].

1.4.1 Particle distribution

To predict the linear dichroism signal in the channel, we must determine the efficacy of fibre orientation in flow. The Fokker-Planck equation is used to understand the evolution of fibre orientation distribution [68, 76, 80] and can also be modified to investigate collective behaviour [25, 34]. Consider a suspension of particles, dilute enough to ensure particle-particle interactions are negligible [68]. Further, assume the suspension is spatially homogeneous, then the suspension configuration can be described by the probability density function $\psi(\boldsymbol{x}^*, \boldsymbol{p}, t^*)$, satisfying the Fokker-Planck equation,

$$\frac{\partial \psi}{\partial t^*} + \nabla_{\boldsymbol{p}} \cdot (\boldsymbol{\Omega}^* \psi) = D_r^* \nabla_{\boldsymbol{p}}^2 \psi. \tag{1.4}$$

where $\nabla_{\boldsymbol{p}}$ represents differentiation in $\boldsymbol{p}$-space and D_r^* is the rotational diffusion constant. In 3D, the orientation vector $\boldsymbol{p}$ can be described in Cartesian space by

$$\boldsymbol{p} = (\sin\theta\cos\phi, \sin\theta\sin\phi, \cos\theta), \tag{1.5}$$

where $\theta \in [0, \pi]$ and $\phi \in [0, 2\pi)$ are angles away from the coordinate axes, depicted in figure 1.5. The evolution of director $\boldsymbol{p}$ is given by

$$\boldsymbol{\Omega}^* = (\boldsymbol{I} - \boldsymbol{pp}) \cdot (\alpha_0 \boldsymbol{e}^* + \boldsymbol{\omega}^*) \cdot \boldsymbol{p}, \tag{1.6}$$

where $\boldsymbol{\omega}^* = (\nabla^* \boldsymbol{u}^* - \nabla^* \boldsymbol{u}^{*T})/2$ is the vorticity tensor and $\alpha_0 = (r^2 - 1)/(r^2 + 1)$ describes how slender the body is [39]. The distribution function has two conditions, periodicity and the normalisation condition,

$$\int_s \psi d\boldsymbol{p} = 1, \tag{1.7}$$

where s is the surface of the unit sphere.

1.4.2 Extra-stress terms

Particle rotations and stresslets arise from the interaction between a fluid and a suspension of particles; the fluid transports and rotates the particles and the resulting stresses impact the fluid flow. This coupled process can be described using the Fokker-Planck equation (1.4) and via the extra stress terms associated with the particle distribution. Following Pedley & Kessler [76], the enhanced stress tensor for a suspension of particles is

$$\boldsymbol{\sigma}^* = \boldsymbol{\sigma}_I^* + \boldsymbol{\sigma}_D^* + \boldsymbol{\sigma}_P^* + \boldsymbol{\sigma}_A^*, \tag{1.8}$$

where $\boldsymbol{\sigma}_I^*$ is the Newtonian contribution (equation (1.3)), $\boldsymbol{\sigma}_D^*$ is the extra stress due to particle rotation, $\boldsymbol{\sigma}_P^*$ represents the interaction of the particles with the fluid and $\boldsymbol{\sigma}_A^*$ is the contribution from active swimming [39].

The contribution from particle rotation is

$$\boldsymbol{\sigma}_D^* = 2\mu^*\Phi D_r^*\alpha_r \int_s \left(\boldsymbol{pp} - \frac{\boldsymbol{I}}{3}\right)\psi \,\mathrm{d}\boldsymbol{p}, \tag{1.9}$$

where Φ is the volume fraction of particles, which is expected to be small in the dilute regime and α_r is a parameter determined from the aspect ratio of the suspended fibres. The stresslets arising from the interaction of suspended particles with the fluid are

$$\begin{aligned}\boldsymbol{\sigma}_P^* = 4\,\mu^*\,\Phi\Bigg[\alpha_2\,\mathbf{e}^* : \int_s \mathbf{p}\,\mathbf{p}\,\mathbf{p}\,\mathbf{p}\,\psi\,\mathrm{d}\mathbf{p} + \alpha_3\left(\boldsymbol{e}^*\cdot\int_s \boldsymbol{p}\,\boldsymbol{p}\,\psi\,\mathrm{d}\boldsymbol{p} + \int_s \boldsymbol{p}\,\boldsymbol{p}\,\psi\,\mathrm{d}\boldsymbol{p}\cdot\boldsymbol{e}^*\right)\\ + \alpha_4\,\boldsymbol{e}^* + \alpha_5\,\boldsymbol{I}\,\boldsymbol{e}^* : \int_s \boldsymbol{p}\,\boldsymbol{p}\,\psi\,\mathrm{d}\boldsymbol{p}\Bigg],\end{aligned} \tag{1.10}$$

where α_i $(i = 2\ldots5)$ are constants related to the aspect ratio of the particle. Finally, the contribution from active swimming is derived from the Oseen tensor [39] as,

$$\boldsymbol{\sigma}_A^* = \alpha_1 \int_s \left(\boldsymbol{pp} - \frac{\boldsymbol{I}}{3}\right)\psi \,\mathrm{d}\boldsymbol{p}, \tag{1.11}$$

where α_1 describes the stresslet strength; this term can be either positive or negative, describing 'puller' or 'pusher' behaviour respectively [81]. Each parameter (α_i, $i = 2,\ldots,5$, α_r) can be represented in terms of ellipsoidal integrals [44] as

$$\begin{aligned}\alpha_2 = \frac{1}{I_1}\left(1 + \frac{L_1}{L_2} - 2\frac{I_1}{I_2}\right), \quad \alpha_3 = -\frac{1}{I_1}\left(1 - \frac{I_1}{I_2}\right), \quad \alpha_4 = \frac{1}{I_1},\\ \alpha_5 = \frac{1}{3I_1}\left(1 - \frac{L_1}{L_2}\right), \quad \alpha_r = \frac{6(r^4-1)}{2r^2I_2 + (r^2+1)^2L_2}.\end{aligned} \tag{1.12}$$

The integrals I_1, I_2, L_1 and L_2 are given in terms of the aspect ratio r by

$$I_1 = \int_0^\infty \frac{2r}{(r^2+\lambda)^{1/2}(1+\lambda)^3}\,\mathrm{d}\lambda = \frac{r^2(2r^2-5+3\gamma)}{2(r^2-1)^2}, \tag{1.13}$$

$$I_2 = \int_0^\infty \frac{r(r^2+1)}{(r^2+\lambda)^{3/2}(1+\lambda)^2}\,\mathrm{d}\lambda = \frac{(r^2+1)(r^2+2-3r^2\gamma)}{2(r^2-1)^2}, \tag{1.14}$$

$$L_1 = \int_0^\infty \frac{r\lambda}{(r^2+\lambda)^{3/2}(1+\lambda)^3}\,\mathrm{d}\lambda = \frac{r^2\left[2r^2+1-\gamma(4r^2-1)\right]}{4(r^2-2)^2}, \tag{1.15}$$

$$L_2 = \int_0^\infty \frac{r\lambda}{(r^2+\lambda)^{3/2}(1+\lambda)^2}\,\mathrm{d}\lambda = I_1 - 2L_1, \tag{1.16}$$

where

$$\gamma = \frac{\cosh^{-1} r}{r(r^2-1)^{1/2}}.$$

1.4.3 Orientation parameter

Linear dichroism spectroscopy relies on a sample being oriented; to calculate the predicted signal, an orientation parameter is introduced to describe the degree of order in the system. This spectroscopic method measures the difference in absorbance of light parallel and perpendicular to a flow direction or a fixed orientation axis [71],

$$LD = A_\parallel - A_\perp, \tag{1.17}$$

where $A_\parallel$ and $A_\perp$ are the absorbance parallel and perpendicular to the flow direction respectively. The absorbance of a sample depends upon the degree to which it is oriented in each direction and so, assuming x^* is the molecular orientation axis and the light source is perpendicular to the $x^* - y^*$ plane, the orientation distribution of fibres whose orientation is given by (1.5) is

$$S = \langle p_{x^*}^2 \rangle - \langle p_{y^*}^2 \rangle, \tag{1.18}$$

where $\langle\cdot\rangle$ denotes an orientation distribution average,

$$\langle\cdot\rangle = \int_s \cdot\, \psi\, \mathrm{d}\boldsymbol{p}. \tag{1.19}$$

For a 3D suspension this is equivalent to

$$S = \langle \sin^2\theta \cos^2\phi \rangle - \langle \sin^2\theta \sin^2\phi \rangle. \tag{1.20}$$

Note that this varies from the definition in [68], who define the degree of orientation of a system as

$$S = \frac{1}{2}\left(3\int_s \cos^2\theta_S \, \psi \, \mathrm{d}\boldsymbol{p} - 1\right), \tag{1.21}$$

where

$$\theta_S = \arccos(|\sin\theta\cos\phi|).$$

This description of the degree of orientation relates to uniaxial samples such as planar membranes in which $\psi = \psi(\theta_s, t^*)$ [29, 71], rather than fibrous fluids which have a biaxial orientation distribution $\psi = \psi(\theta, \phi, t^*)$. While this formulation is correct, the use of equation (1.21) in [68], and for predicting alignment in thin channel flow, is therefore inappropriate.

A specific case of the model described here is when the suspended fibres have a preferred direction; in this case we can link the model of Pedley & Kessler with Ericksen's transversely-isotropic model [39].

1.5 Connections with perfectly-aligned media

Certain biological fluids have a preferred orientation, this fluid can be modelled via the transversely-isotropic model; a specific case of the active suspension model where the fluid has a single preferred direction [39]. One example is fibrous cervical mucus; the glycofilament-mucin structure forms parallel networks due to hormonally induced changes in the hydration of the mucus. Other applications of perfectly aligned media include the mechanical behaviour of collagen gel, the growth of plant cell walls, suspensions of biomolecules and a multiphase model of extracellular matrix [21, 22, 31, 40].

With this simplification we may derive Ericksen's transversely isotropic fluid model

[24]. Consider a distribution function $\Psi(\boldsymbol{x}^*, \boldsymbol{p}, t^*)$ satisfying the Smoluchowski equation [82],

$$\frac{\partial \Psi}{\partial t} + \boldsymbol{\nabla}_{\boldsymbol{x}} \cdot (\boldsymbol{X}\Psi) + \boldsymbol{\nabla}_{\boldsymbol{p}} \cdot (\boldsymbol{\Omega}\Psi) = D_r \nabla_p^2 \Psi + D \nabla_x^2 \Psi, \tag{1.22}$$

where $\boldsymbol{\Omega}$ is equation (1.6), $\boldsymbol{X} = V_s \boldsymbol{p} + \boldsymbol{u}$ for swimming velocity V_s, D is spatial diffusion and $\boldsymbol{\nabla}_x$ is differentiation in Cartesian space.

Consider a uniformly distributed, perfectly aligned fluid where particle diffusion is neglected ($D_r = D = 0$) and the swimming velocity of the particles is zero ($V_s = 0$) [39]. The probability density function can be written as

$$\Psi = \delta(\boldsymbol{p} - \boldsymbol{a}), \tag{1.23}$$

where $\boldsymbol{a} = \langle \boldsymbol{p} \rangle$ is the local particle director; all particles have the same uniform alignment described by $\boldsymbol{a}$ [39, 82]. It is no longer necessary to consider a distribution of orientation, but we instead derive equations governing the evolution of the average particle direction. To do this, multiply the conservation equation (1.22) by $\boldsymbol{p}$, then integrate over $\boldsymbol{p}$ to obtain

$$\int_s \boldsymbol{p} \frac{\partial \Psi}{\partial t} \, \mathrm{d}\boldsymbol{p} + \int_s \boldsymbol{p} \boldsymbol{\nabla}_{\boldsymbol{x}} \cdot (\boldsymbol{u}\Psi) \, \mathrm{d}\boldsymbol{p} + \int_s \boldsymbol{p} \boldsymbol{\nabla}_{\boldsymbol{p}} \cdot (\boldsymbol{\Omega}\Psi) \, \mathrm{d}\boldsymbol{p} = 0. \tag{1.24}$$

Using integration by parts, the third term can be written as

$$\begin{aligned} \int_s \boldsymbol{p} \boldsymbol{\nabla}_{\boldsymbol{p}} \cdot (\boldsymbol{\Omega}\Psi) \, \mathrm{d}\boldsymbol{p} &= \left[\boldsymbol{p} \cdot \boldsymbol{\Omega}\Psi \right]_s - \int_s \boldsymbol{\Omega}\Psi \, \mathrm{d}\boldsymbol{p} \\ &= - \int_s \boldsymbol{\Omega}\Psi \, \mathrm{d}\boldsymbol{p} \\ &= -\alpha_0 (\boldsymbol{e} \cdot \langle \boldsymbol{p} \rangle - \boldsymbol{e} : \langle \boldsymbol{ppp} \rangle) - \boldsymbol{\omega} \cdot \langle \boldsymbol{p} \rangle. \end{aligned} \tag{1.25}$$

Since Ψ is the delta function, $\langle \boldsymbol{ppp} \rangle = \langle \boldsymbol{p} \rangle \langle \boldsymbol{p} \rangle \langle \boldsymbol{p} \rangle = \boldsymbol{aaa}$ and so (1.24) becomes

$$\int_s \boldsymbol{p} \frac{\partial \Psi}{\partial t} \, \mathrm{d}\boldsymbol{p} + \int_s \boldsymbol{p} \boldsymbol{\nabla}_{\boldsymbol{x}} \cdot (\boldsymbol{u}\Psi) \, \mathrm{d}\boldsymbol{p} - \boldsymbol{\omega} \cdot \boldsymbol{a} = \alpha_0 (\boldsymbol{e} \cdot \boldsymbol{a} - \boldsymbol{e} : \boldsymbol{aaa}). \tag{1.26}$$

To deal with the remaining two terms, rewrite both as

$$\boldsymbol{p}\,\frac{\partial \Psi}{\partial t} = \frac{\partial}{\partial t}\left(\boldsymbol{p}\Psi\right) - \Psi\,\frac{\partial \boldsymbol{p}}{\partial t}\,, \tag{1.27}$$

$$\begin{aligned}\boldsymbol{p}\boldsymbol{\nabla}_x \cdot (\boldsymbol{u}\Psi) &= \boldsymbol{p}\Psi\boldsymbol{\nabla}_x \cdot \boldsymbol{u} + \boldsymbol{p}\,\boldsymbol{u}\cdot\boldsymbol{\nabla}_x\Psi \\ &= \boldsymbol{p}\,\boldsymbol{u}\cdot\boldsymbol{\nabla}_x\Psi = (\boldsymbol{u}\cdot\nabla_x)(\boldsymbol{p}\Psi) - \Psi(\boldsymbol{u}\cdot\boldsymbol{\nabla}_x)\boldsymbol{p},\end{aligned} \tag{1.28}$$

hence (1.26) becomes

$$\frac{\partial \boldsymbol{a}}{\partial t} - \int_s \Psi\,\frac{\partial \boldsymbol{p}}{\partial t}\,\mathrm{d}\boldsymbol{p} + (\boldsymbol{u}\cdot\boldsymbol{\nabla}_x)\boldsymbol{a} - \int_s \Psi(\boldsymbol{u}\cdot\boldsymbol{\nabla}_{\boldsymbol{x}})\boldsymbol{p}\,\mathrm{d}\boldsymbol{p} - \boldsymbol{\omega}\cdot\boldsymbol{a} = \alpha_0(\boldsymbol{e}\cdot\boldsymbol{a} - \boldsymbol{e}:\boldsymbol{aaa}). \tag{1.29}$$

Since $\boldsymbol{p}$ is a coordinate, it has no time or spatial dependence, hence the remaining integrals are zero and we obtain the kinematic condition of Ericksen [24],

$$\frac{\partial \boldsymbol{a}}{\partial t} + (\boldsymbol{u}\cdot\boldsymbol{\nabla}_x)\boldsymbol{a} - \boldsymbol{\omega}\cdot\boldsymbol{a} = \alpha_0(\boldsymbol{e}\cdot\boldsymbol{a} - \boldsymbol{e}:\boldsymbol{aaa}). \tag{1.30}$$

The governing equations are identical to (1.1) and (1.2); however, upon setting the rotational diffusion constant to zero ($D_r^* = 0$), the stress tensor is given by

$$\boldsymbol{\sigma}^* = -p^*\boldsymbol{I} + 2\bar{\mu}^*\boldsymbol{e}^* + \mu_1^*\boldsymbol{aa} + \mu_2^*\boldsymbol{aaaa}:\boldsymbol{e}^* + 2\mu_3^*(\boldsymbol{aa}\cdot\boldsymbol{e}^* + \boldsymbol{e}^*\cdot\boldsymbol{aa}) \tag{1.31}$$

where

$$\bar{\mu}^* = \mu^*(1 + 2\Phi\alpha_4), \quad \mu_1^* = n_d^*\alpha_1, \quad \mu_2^* = 4\mu^*\Phi\alpha_2, \quad \mu_3^* = 2\mu^*\Phi\alpha_3, \tag{1.32}$$

and where the pressure has been modified as

$$p^* = P^* + \frac{n_d^*\alpha_1}{3} - 4\mu^*\Phi\alpha_5\boldsymbol{aa}:\boldsymbol{e}^*. \tag{1.33}$$

The parameters can be interpreted as viscosity-like terms: setting $\mu_1^* = \mu_2^* = \mu_3^* = 0$, the stress tensor for an incompressible Newtonian fluid remains, with 'matrix viscosity'

μ^* [40]. The term with μ_1^* has no dependence on velocity, suggesting that μ_1^* relates to a tension in the fibre direction [22]. This term can also be related to the stresslet-type active behaviour of fibres in a perfectly aligned active fluid [39] and so this quantity is referred to as the *active parameter*. For a simple fluid with 2D deformations in the plane of fibres, the viscosity associated with extensional flow parallel to the fibre direction is $\mu_{\parallel}^* = \mu^* + (\mu_2^* + 4\mu_3^*)/2$, the viscosity associated with the flow orthogonal to the fibre direction is $\mu_{\perp}^* = \mu^*$ and the viscosity of shear flow in the fibre direction is $\mu_s^* = \mu^* + \mu_3^*$ [22]. Since μ_2^* only has an impact on extensional viscosity parallel to the fibre direction, $\mu_{\parallel}^*$, it is termed the *anisotropic extensional viscosity*. The parameter μ_3^* distinguishes $\mu_{\perp}^*$ from μ_s^* and so is labelled the *anisotropic shear viscosity*; this parameter represents the difference between shear viscosities parallel and perpendicular to the fibre direction [22, 31, 40].

Thus, we can link models of suspensions of elongated particles to the transversely-isotropic model for a perfectly aligned fluid. Ericksen's model will form the basis for the study of chapter 4.

1.6 Summary

In this chapter, the coupled flow and distribution equations describing flows of particle suspensions are introduced, along with the degree of orientation of a fibre-laden fluid. This consists of the Navier-Stokes equations (1.1), along with the Newtonian stress tensor (1.3) and extra stress terms (1.9)-(1.11), the continuity equation (1.2) and the Fokker-Planck equation (1.4). The degree of orientation S (equation (1.20)) is found by calculating the difference between the proportion of particles oriented parallel and perpendicular to the molecular orientation axis, as an average over orientation space. Finally, section 1.5 discussed the link between active and transversely-isotropic fluids, highlighting a specific case of Pedley & Kessler's [76] active suspension model where the particles are perfectly aligned.

This model, along with appropriate boundary conditions, is used to examine a simple 2D channel and a rectangular channel bounded by two walls in chapter 2. Both 2D and 3D distribution equations are coupled to a flow problem; the 3D distribution produces a lower degree of orientation due to the particles rotating out of the plane, highlighting the need to consider the full 3D model. The particle suspension consists of passive bacteriophage and so we neglect active terms defined in (1.11) (*i.e.* $\alpha_1 = 0$). In chapter 3 this is extended to a 3D rectangular channel, in line with the flow set-up used by Linear Diagnostics Ltd. In both chapters, the bacteriophage used have a large aspect ratio, and so α_0 will be close or equal to one for our analysis. The fluid velocity, degree of orientation and linear dichroism signal are calculated while varying parameters such as inlet pressure gradient, number density of particles, oscillating frequency and the dimensions of the channel. We find that increasing the pressure gradient increases the orientation and hence the signal, while increasing the oscillating frequency has the opposite effect. Increasing the channel depth is seen to increase the orientation of the system, however this result is reversed for rapid oscillations; the results for oscillating flow are in general smaller than those for steady flow, leading to a discussion into the feasibility and effectiveness of this system.

Finally, chapter 4 investigates a conceptual model of propulsion at low Reynolds numbers in complex fluids. This is a departure from previous work, however remains within the theme of fibre-laden fluids for medical applications. Here we consider a fluid with a preferred alignment and hence utilise the transversely-isotropic model, described in section 1.5 and [39]. The energetic costs of swimming are significantly altered by all rheological parameters and the initial fibre angle. A passive fluid produces an enhanced mean rate of working and has no impact on the mean swimming velocity, whereas an active fluid dramatically changes the mean rate of working, swimming velocity, streamlines and flow field; fibres aligned with the swimming direction increase the energetic demands of the sheet. The constant fibre stress may also result in a reversal of the mean swimming velocity and a negative mean rate of working, if sufficiently large relative to the other rheological parameters.

CHAPTER 2

PREDICTING ORIENTATION AND LINEAR DICHROISM SIGNAL OF BACTERIOPHAGE SUSPENSIONS: A SIMPLIFIED CHANNEL APPROXIMATION

This chapter investigates a simplified version of the industrial problem of interest; the flow-induced alignment of bacteriophage in thin rectangular channels. This work is in collaboration with Linear Diagnostics Ltd, who aim to increase the signal to noise ratio produced by samples, aligned by flow through thin channels, in a handheld device. We consider a fluid bound by two walls and investigate the alignment and signal in steady and oscillatory flows.

2.1 Introduction

We consider the shear-induced alignment of suspensions of elongated fibres in thin channels; the alignment induced by the flow is integral to detecting a linear dichroism signal, useful for determining the components and structure of complex fluids. Previous work in this area includes suspensions of dumbbells in a two-dimensional start-up plane Poiseuille flow using a mixed finite-difference/spectral method [60]. A spectral method has also been utilised to investigate short particle suspensions in recirculating flows [13]. The coupled flow dynamics and orientation distribution are solved for a suspension of elongated fibres

in a parallel plate channel using an iterative approach, a method also used in the work by Chiba et al. [12]. This work considers extra stress terms consisting of a fourth order orientation tensor only; we include all extra stress terms for fibres without self-motility described by Pedley & Kessler [76], and detailed in section 1.4 of chapter 1. Further, pressure-driven channel flow, assuming a Newtonian flow profile and incorporating wall accumulation [25, 33] and a 2D flow calculation in constricted channels [47] have been considered.

To develop our understanding of alignment and linear dichroism signal, a suspension of elongated particles in thin rectangular channels is considered. An important mathematical approach we will use in our calculations is lubrication theory, reducing the flow equations to consider the important hydrodynamic effects. We calculate the flow profile, orientation parameter and expected linear dichroism signal. The Fokker-Planck equation is solved numerically using either a Fourier transform or spherical harmonics. Spherical harmonics are the angular solution to the Laplace equation in spherical coordinates; they can be used to simplify complex partial differential equations and have previously been used to model flows of suspensions of dumbbells in 3D FENE fluids [10], with a prescribed shear rate influencing convective terms. Spherical harmonics have also been used to solve the Fokker-Planck equation for a simple shear flow [68, 87]; this method is adapted in our work to account for channel flow.

We begin by summarising the governing equations used for this model in section 2.2. Next we consider a 2D channel and solve the corresponding flow equations coupled with a 2D Fokker-Planck equation. Semi-analytic expressions are calculated for steady flow in section 2.3.1 and coupled via an iterative method. For the oscillatory problem in section 2.3.2, a perturbation expansion in the volume fraction of fibres decouples the equations and allows for an analytical calculation of the velocity profile. Next, the Fokker-Planck equation is extended to consider 3D rotations; steady and oscillatory problems are again considered in sections 2.4.1 and 2.4.2 respectively. Here the Fokker-Planck equation is solved using spherical harmonics and the fluid equations are solved numerically for

oscillating flow. In all cases, the velocity profile, degree of orientation and predicted linear dichroism signal are calculated and the results are compared in section 2.5.

2.2 Summary of equations governing fibrous fluids

A summary of the equations discussed in chapter 1 are given here. The dimensional Navier-Stokes and incompressibility equations are

$$\rho^* \left(\frac{\partial \boldsymbol{u}^*}{\partial t^*} + (\boldsymbol{u}^* \cdot \nabla^*)\boldsymbol{u}^* \right) = \nabla^* \cdot \boldsymbol{\sigma}^*, \tag{2.1}$$

$$\nabla^* \cdot \boldsymbol{u}^* = 0, \tag{2.2}$$

where ρ^* is density, $\boldsymbol{u}^*(\boldsymbol{x}^*, t^*)$ is the velocity vector for spatial coordinate $\boldsymbol{x}^*$ and time t^*, $\boldsymbol{\sigma}^*$ is the stress tensor and ∇^* is differentiation in Cartesian space. The asterisk notation represents dimensional variables.

To determine the bulk stresses in the fluid due to the particles, we define a probability density function $\psi(\theta, \phi, \boldsymbol{x}^*, t^*)$ satisfying the Fokker-Planck equation [68],

$$\frac{\partial \psi}{\partial t^*} + \nabla_{\boldsymbol{p}} \cdot (\boldsymbol{\Omega}^* \psi) = D_r^* \nabla_{\boldsymbol{p}}^2 \psi, \tag{2.3}$$

where $\boldsymbol{p}$ is the unit orientation vector, $\nabla_{\boldsymbol{p}}$ represents differentiation in $\boldsymbol{p}$-space and D_r^* is the rotational diffusion constant. The evolution of director $\boldsymbol{p}$ is given by

$$\boldsymbol{\Omega}^* = (\boldsymbol{I} - \boldsymbol{pp}) \cdot (\alpha_0 \boldsymbol{e}^* + \boldsymbol{\omega}^*) \cdot \boldsymbol{p}, \tag{2.4}$$

where $\boldsymbol{e}^* = (\nabla^* \boldsymbol{u}^* + \nabla^* \boldsymbol{u}^{*T})/2$ is the rate of strain tensor, $\boldsymbol{\omega}^* = (\nabla^* \boldsymbol{u}^* - \nabla^* \boldsymbol{u}^{*T})/2$ is the vorticity tensor and $\alpha_0 = (r^2 - 1)/(r^2 + 1)$ describes how slender the body is [39]. The distribution function has two conditions, periodicity and the normalisation condition,

$$\int_s \psi d\boldsymbol{p} = 1, \tag{2.5}$$

where s is the unit surface of a sphere.

Following Pedley & Kessler [76], the enhanced stress tensor for a suspension of active particles is

$$\boldsymbol{\sigma}^* = \boldsymbol{\sigma}^*_I + \boldsymbol{\sigma}^*_D + \boldsymbol{\sigma}^*_P, \tag{2.6}$$

where the Newtonian contribution is

$$\boldsymbol{\sigma}^*_I = -P^* \boldsymbol{I} + 2\mu^* \boldsymbol{e}^*, \tag{2.7}$$

for pressure P^*, identity matrix $\boldsymbol{I}$ and viscosity μ^*. Here, $\boldsymbol{\sigma}^*_D$ is the extra stress due to particle rotation and $\boldsymbol{\sigma}^*_P$ represents the interaction of the particles with the fluid, given by

$$\boldsymbol{\sigma}^*_D = 2\mu^* \Phi D^*_r \alpha_r \int_s \left(\boldsymbol{pp} - \frac{\boldsymbol{I}}{3} \right) \psi \, \mathrm{d}\boldsymbol{p}, \tag{2.8}$$

$$\begin{aligned} \boldsymbol{\sigma}^*_P = 4\,\mu^*\,\Phi \Bigg[\alpha_2\, \boldsymbol{e}^* : \int_s \boldsymbol{p}\,\boldsymbol{p}\,\boldsymbol{p}\,\boldsymbol{p}\,\psi \, \mathrm{d}\mathbf{p} + \alpha_3 \left(\boldsymbol{e}^* \cdot \int_s \boldsymbol{p}\,\boldsymbol{p}\,\psi \, \mathrm{d}\boldsymbol{p} + \int_s \boldsymbol{p}\,\boldsymbol{p}\,\psi \, \mathrm{d}\boldsymbol{p} \cdot \boldsymbol{e}^* \right) \\ + \alpha_4\, \boldsymbol{e}^* \int_s \psi \, \mathrm{d}\boldsymbol{p} + \alpha_5\, \boldsymbol{I}\, \boldsymbol{e}^* : \int_s \boldsymbol{p}\,\boldsymbol{p}\,\psi \, \mathrm{d}\boldsymbol{p} \Bigg], \end{aligned} \tag{2.9}$$

where Φ is the volume fraction and α_i ($i = 2 \ldots 5$, r) are constants related to the aspect ratio of the particle. A term accounting for the self-motile behaviour of a suspension can also be defined (equation (1.11) in chapter 1), however in the present study the elongated fibres are taken to be passive M13 bacteriophage and so this term is neglected. Each parameter (α_i, $i = 2, \ldots, 5$, α_r) can be represented in terms of ellipsoidal integrals [2, 44], which are detailed in equations (1.12)-(1.16) in chapter 1.

Finally, the degree of orientation of a system can be described by an orientation parameter, S, defined as the difference in orientation parallel and perpendicular to a molecular orientation axis (here the x^*–axis),

$$S = \langle p^2_{x^*} \rangle - \langle p^2_{y^*} \rangle, \tag{2.10}$$

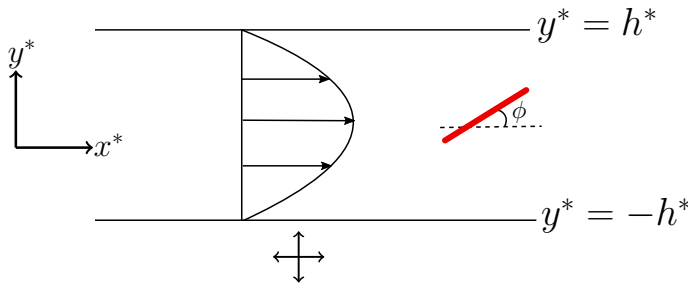

Figure 2.1: The flow channel, where a parabolic flow profile is expected, containing a fibre-laden fluid. The light polarisations are parallel and perpendicular to the flow direction, highlighted by the arrows below the channel. The fibres rotate in plane and their orientation is described by polar coordinates with angle $\phi \in [0, 2\pi)$.

which will be defined for 2D and 3D orientation distribution functions in the relevant sections.

2.3 Solving the Fokker-Planck equation in 2D

Due to the mathematical complexity, we initially consider both steady and oscillating flow through a 2D thin rectangular channel, bounded by walls at $y^* = -h^*$ and $y^* = h^*$ and with length scale L^*, using a lubrication approximation (figure 2.1). It is assumed the particles remain in plane, *i.e.* we consider 2D rotations in the Fokker-Planck equation. In each case we solve the Navier-Stokes and incompressibility equations (2.1), (2.2) and the Fokker-Planck equation (2.3), to determine the degree of orientation of the suspension, and approximate the linear dichroism signal. The orientation parameters (2.10) and (1.21) are compared for steady flow.

2.3.1 Steady channel flow

We assume the flow through the channel is forced by a constant pressure gradient and hence consider a fully developed flow profile. The light source used for linear dichroism spectroscopy compares light polarised parallel and perpendicular to the flow direction, as shown by the arrows in figure 2.1, along with the expected parabola. The boundary

conditions are given by no-slip conditions at the walls,

$$u^*(x^*, -h^*) = u^*(x^*, h^*) = 0, \tag{2.11}$$

$$v^*(x^*, -h^*) = v^*(x^*, h^*) = 0. \tag{2.12}$$

Since the width of the channel is much smaller than its length scale, $\delta = h^*/L^* \ll 1$, a lubrication theory approximation for thin channels can be used to simplify the equations of motion. The Fokker-Planck equation is first solved for a Newtonian flow profile which is then used to recalculate the velocity, and the iteration is repeated until convergence is obtained.

Non-dimensionalisation

The system is scaled against the inlet pressure gradient G^* as follows,

$$u^* = \frac{G^* h^{*2}}{\mu^*} u, \quad v^* = \frac{\delta G^* h^{*2}}{\mu^*} v, \quad x^* = \frac{h^*}{\delta} x, \quad y^* = h^* y, \quad P^* = \frac{G^* h^*}{\delta} P. \tag{2.13}$$

Substituting (2.13) into both components of the Navier-Stokes equations (2.1), retaining leading terms (since $\delta \ll 1$), we have

$$\begin{aligned} \frac{\partial P}{\partial x} = \frac{\mathrm{d}}{\mathrm{d}y} \Bigg\{ & \frac{2\Phi\alpha_r}{P_G} \int_0^{2\pi} \cos\phi \sin\phi \, \psi \, \mathrm{d}\phi \\ & + \left(1 + 4\Phi \left[\alpha_2 \int_0^{2\pi} \cos^2\phi \sin^2\phi \, \psi \, \mathrm{d}\phi + \frac{\alpha_3 + \alpha_4}{2} \int_0^{2\pi} \psi \, \mathrm{d}\phi \right] \right) \frac{\mathrm{d}u}{\mathrm{d}y} \Bigg\}, \end{aligned} \tag{2.14}$$

$$\frac{\partial P}{\partial y} = 0, \tag{2.15}$$

where $P_G = G^* h^* / D_r^* \mu^*$ is the Peclet number associated with pressure driven flow. The orientation vector reduces to

$$\boldsymbol{p} = (\cos\phi, \sin\phi), \tag{2.16}$$

where ϕ is the angle of the fibres with the x^*–axis and is shown in figure 2.1. Finally, the incompressibility condition, (2.2), is unchanged. From (2.15), $P = P(x)$ (*i.e.* $\partial P^*/\partial x^* = -G^*$) and since we have scaled against the constant pressure gradient, (2.14) becomes

$$-1 = \frac{\mathrm{d}}{\mathrm{d}y}\left\{\frac{2\Phi\alpha_r}{P_G}\int_0^{2\pi}\cos\phi\sin\phi\,\psi\,\mathrm{d}\phi + \left(1+4\Phi\left[\alpha_2\int_0^{2\pi}\cos^2\phi\sin^2\phi\,\psi\,\mathrm{d}\phi + \frac{\alpha_3+\alpha_4}{2}\int_0^{2\pi}\psi\,\mathrm{d}\phi\right]\right)\frac{\mathrm{d}u}{\mathrm{d}y}\right\}, \tag{2.17}$$

with corresponding dimensionless boundary conditions

$$u(-1) = u(1) = 0. \tag{2.18}$$

To derive an appropriate form of the Fokker-Planck equation we scale $\mathbf{\Omega}^* = G^* h^* \mathbf{\Omega}/\mu^*$, where

$$\mathbf{\Omega} = (-\sin\phi, \cos\phi)\overline{p}, \quad \overline{p} = \frac{1}{2}(\alpha_0\cos 2\phi - 1)\,\frac{\mathrm{d}u}{\mathrm{d}y}\,. \tag{2.19}$$

The full dimensionless model is

$$-1 = \frac{\mathrm{d}}{\mathrm{d}y}\left\{\frac{2\Phi\alpha_r}{P_G}\int_0^{2\pi}\cos\phi\sin\phi\,\psi\,\mathrm{d}\phi + \left(1+4\Phi\left[\alpha_2\int_0^{2\pi}\cos^2\phi\sin^2\phi\,\psi\,\mathrm{d}\phi + \frac{\alpha_3+\alpha_4}{2}\int_0^{2\pi}\psi\,\mathrm{d}\phi\right]\right)\frac{\mathrm{d}u}{\mathrm{d}y}\right\}, \tag{2.20}$$

$$P_G\nabla_p\cdot(\mathbf{\Omega}\psi) = \nabla_p^2\psi, \tag{2.21}$$

where $\mathbf{\Omega}$ is given by (2.19) and the boundary conditions are

$$u(-1) = u(1) = 0, \tag{2.22}$$

$$\int_0^{2\pi}\psi\,\mathrm{d}\phi = 1, \quad \psi(0,y) = \psi(2\pi,y). \tag{2.23}$$

Finally, the orientation parameter (2.10) in 2D becomes

$$S = 2\int_0^{2\pi} \cos^2\phi\,\psi\,\mathrm{d}\phi - 1, \tag{2.24}$$

Solving the Fokker-Planck equation

For a known velocity u, the probability distribution function $\psi(\phi, y)$ can be calculated semi-analytically. Expressing equation (2.21) in spherical polar coordinates we have

$$\frac{P_G}{2}\frac{\mathrm{d}u}{\mathrm{d}y}\frac{\partial}{\partial\phi}\left[\left(-1+\alpha_0(1-2\sin^2\phi)\right)\psi\right] = \frac{\partial^2\psi}{\partial\phi^2}\,, \tag{2.25}$$

this is rewritten as

$$\frac{\partial}{\partial\phi}\left[\frac{\partial\psi}{\partial\phi} + \frac{P_G}{2}\frac{\mathrm{d}u}{\mathrm{d}y}\,(1-\alpha_0\cos 2\phi)\psi\right] = 0. \tag{2.26}$$

After integrating equation (2.26) once,

$$\frac{\partial\psi}{\partial\phi} + \frac{P_G}{2}\frac{\mathrm{d}u}{\mathrm{d}y}\,(1-\alpha_0\cos 2\phi)\psi = c_0, \tag{2.27}$$

for constant c_0. Then by defining an integrating factor

$$I(\phi, y) = \exp\left[\frac{P_G}{2}\frac{\mathrm{d}u}{\mathrm{d}y}\int(1-\alpha_0\cos 2\phi)\,\mathrm{d}\phi\right] = \exp\left[\frac{P_G}{2}\frac{\mathrm{d}u}{\mathrm{d}y}\left(\phi - \frac{\alpha_0}{2}\sin 2\phi\right)\right], \tag{2.28}$$

the expression for the distribution function, ψ, can be written as

$$\psi(\phi, y) = \frac{c_1\left(c_2\int I(\phi, y)\,\mathrm{d}\phi + 1\right)}{I(\phi, y)}, \tag{2.29}$$

for constants c_1 and c_2 calculated from the periodicity and normalisation conditions as

$$c_2 = \frac{I(2\pi, y) - 1}{\int_0^{2\pi} I(\phi, y)\,\mathrm{d}\phi}, \tag{2.30}$$

$$c_1 = \frac{1}{\int_0^{2\pi} A(\phi, y)\,\mathrm{d}\phi}, \tag{2.31}$$

where

$$A(\phi, y) = \frac{c_2 \int I(\phi, y)\, \mathrm{d}\phi + 1}{I(\phi, y)}. \tag{2.32}$$

Once the probability density function is known, the extra stress terms (2.8) and (2.9) can be calculated.

Solving the fluid flow equations with extra stress terms

For a known probability density function $\psi(\phi, y)$, the extra stress components (equations (2.8) and (2.9)) can be calculated and are hence known functions of y. Integration of (2.20) gives

$$\begin{aligned} -y + d_1 = \frac{2\Phi\alpha_r}{P_G} \int_0^{2\pi} \cos\phi \sin\phi\, \psi\, \mathrm{d}\phi \\ + \left(1 + 4\Phi \left[\alpha_2 \int_0^{2\pi} \cos^2\phi \sin^2\phi\, \psi\, \mathrm{d}\theta + \frac{\alpha_3 + \alpha_4}{2} \int_0^{2\pi} \psi\, \mathrm{d}\phi\right]\right) \frac{\mathrm{d}u}{\mathrm{d}y}, \end{aligned} \tag{2.33}$$

for a constant d_1. Integrating (2.33),

$$u = \int_{-1}^{y} \frac{d_1 - \overline{y} - \hat{\alpha}_r(\overline{y})}{A(\overline{y})}\, \mathrm{d}\overline{y} + d_2, \tag{2.34}$$

for constant d_2 and where

$$A(y) = \left(1 + 4\Phi \left[\alpha_2 \int_0^{2\pi} \cos^2\phi \sin^2\phi\, \psi\, \mathrm{d}\phi + \frac{\alpha_3 + \alpha_4}{2}\right]\right), \tag{2.35}$$

$$\hat{\alpha}_r(y) = \frac{2\Phi\alpha_r}{P_G} \int_0^{2\pi} \cos\phi \sin\phi\, \psi\, \mathrm{d}\phi. \tag{2.36}$$

The no-slip conditions, (2.22) give $d_2 = 0$ and

$$d_1 = \frac{\int_{-1}^{1} \frac{y}{A(y)}\, \mathrm{d}y + \int_{-1}^{1} \frac{\hat{\alpha}_r(y)}{A(y)}\, \mathrm{d}y}{\int_{-1}^{1} \frac{1}{A(y)}\, \mathrm{d}y}. \tag{2.37}$$

After the velocity for particle suspensions has been calculated, it can be substituted

back into the expression for ψ, (2.29), and the above process is repeated.

Summary

The solution to the coupled problem given by equations (2.20) and (2.21) along with boundary and normalisation conditions (2.22) and (2.23) can be found iteratively, beginning with the Newtonian flow and calculating the extra stress terms, detailed here:

- Take the Newtonian velocity profile, $u^{(0)}(y)$ and evaluate the probability density function $\psi^{(0)}(\phi, y)$.
- The extra stress terms, and hence the updated velocity $u^{(1)}(y)$, can be calculated from $\psi^{(0)}(\phi, y)$.
- This velocity can then be used to calculate the updated probability density function $\psi^{(1)}(\phi, y)$.
- Repeat the above steps where for a given iteration step we have,

$$\psi^{(n)}(\phi, y) = f(\phi, y, u^{(n)}), \quad u^{(n+1)}(y) = g(y, \psi^{(n)}),$$

  where f and g are functions given by equations (2.29) and (2.34) respectively.
- The iteration terminates when

$$||u^{(n+1)} - u^{(n)}|| < \tau,$$

  for some tolerance τ.

We require an absolute tolerance of $\tau = 10^{-8}$ in our numerical calculation.

Due to the no-slip conditions, the flow profile will be up-down symmetric; the bottom half of the profile ($-1 < y < 0$) will mirror the top half ($0 < y < 1$). Hence the problem is solved only for the bottom half of the channel. In this section, numerical error due

to the integrating factor, (2.28), being very small is avoided, since the Peclet number is positive in this region. The solution can then be mapped onto the top half of the channel. The ϕ-integrals are computed numerically using the trapezium rule and the y-integrals are computed using the mid-point method.

Results

Dimensionless scalings are calculated from data provided by Linear Diagnostics Ltd. to aid in plotting results. The depth of the channel is $2h^* = 6 \times 10^{-4}$ m. The volume fraction can be written as $\Phi = V_c^* n_d^*$, where $V_c^* = 4\pi a^* {b^*}^2/3$ is the volume of one particle and n_d^* is the particle number density. The bacteriophage in suspension have principal axis $a^* = 800$ nm and minor axes $b^* = c^* = 6$ nm, and hence volume $V_c^* \approx 1.21 \times 10^{-21}$ m^3. To calculate the number density of phage, we use the formula $n_d^* = C^* N_A / M^*$, with phage concentration $C^* = 0.02$ g/litre and molecular mass $M^* \approx 1.64 \times 10^7$ g/mol. The resulting number density is $n_d^* \approx 7.33 \times 10^{17}$ phage/m^3, which provides a volume fraction $\Phi \approx 1.11 \times 10^{-5}$.

To determine how dilute the suspension is, the definition of a semi-dilute suspension is verified; a semi-dilute suspension satisfies $n_d^* {a^*}^3 \gg 1$ and $n_d^* {a^*}^2 b^* \ll 1$. When $n_d^* {a^*}^3 \gg 1$, a particle may interact with any other fibre in suspension at any point in time [86]. Using the values $n_d^* \approx 7.33 \times 10^{17}$ phage/m^3 and $a^* = 800$ nm, $n_d^* {a^*}^3 = 0.3753 < 1$ and so we are not in the semi-dilute regime.

Next, the Peclet number $P_G = G^* h^* / D_r^* \mu^*$ is calculated. Following [68], the dimensional diffusion coefficient D_r^* is

$$D_r^* = \frac{k_B^* T^*}{8\pi \mu^* a^* {b^*}^3 F_r}, \tag{2.38}$$

Table 2.1: List of parameters used, their units and their values. Parameters a^*, b^*, T^*, μ^*, K_B^* and D_r^* are kept the same, all others are subject to change

Parameter	Description	Units	Value
a^*	Particle length	m	8×10^{-7}
b^*	Particle width	m	6×10^{-9}
T^*	Temperature (water)	K	295
μ^*	Viscosity (water)	Pa s	9.5×10^{-4}
K_B^*	Boltzmann constant	Kg m^2/K s^2	1.38×10^{-23}
D_r^*	Diffusion coefficient	s^{-1}	40.65
h^*	Channel half-depth	m	3×10^{-4}
n_d^*	Number density	phage/m^3	7.33×10^{17}
G^*	Pressure gradient	Pa/m	4.4×10^3
Φ	Volume fraction	-	1.11×10^{-5}
P_G	Peclet number	-	34.17

where k_B^* is the Boltzmann constant, T^* is temperature and

$$F_r = \frac{4(r^4-1)}{3r^2\left[\frac{2(2r^2-1)}{r^{3/4}F_t} - 2\right]}, \tag{2.39}$$

$$F_t = \frac{\sqrt{r^2-1}}{r^{1/3}\ln(r+\sqrt{r^2-1})}. \tag{2.40}$$

See also [11, 76, 81]. Assuming the bacteriophage are suspended in water, we use the known viscosity at 22°C ($\approx$ 295K), $\mu^* = 9.5 \times 10^{-4}$ Pa s. Hence the diffusion coefficient is $D_r^* \approx 40.65$ s^{-1}. Using the fixed pressure gradient $G^* \approx 4.4 \times 10^3$ Pa/m, provided by Linear Diagnostics Ltd, the dimensionless Peclet number is $P_G \approx 34.17$; advection slightly dominates diffusion.

To calculate the linear dichroism signal, the orientation is integrated over the channel depth, dependent on the number of phage in the sample,

$$LD = \frac{\epsilon^* m_w^* n_d^*}{N_A^*} \int_{-h^*}^{h^*} S \, \mathrm{d}y^*, \tag{2.41}$$

where N_A^* is the Avagadro constant ($\approx 6 \times 10^{23}$ phage/mol), m_w^* is the molecular weight and ϵ^* is the extinction coefficient (m^2/mol), which is a measure of the absorption of light through the sample. We use an extinction coefficient of 0.38 m^2/g at 269 nm [1, 30, 70] and the molecular weight of bacteriophage (provided by Linear Diagnostics) $m_w^* \approx 2 \times 10^7$ g/mol.

Spatial averages are used at times to simplify presentation of results, using the formula

$$\bar{\cdot} = \frac{1}{2}\int_{-1}^{1} \cdot \, \mathrm{d}y. \tag{2.42}$$

Figure 2.2 shows the results for the flow profile, orientation parameter and probability density function for the specific pressure gradient $G^* \approx 4.4 \times 10^3$ Pa/m. The dashed line in figure 2.2a represents the Newtonian solution and the red line depicts the flow profile with extra stress terms included. For this volume fraction of phage ($\Phi = 1.11 \times 10^{-5}$), the reduction in the velocity profile from the Newtonian case is small. We see, as expected, that the bacteriophage prefer to orient with an angle slightly off $\phi = 0$, in line with the flow direction (figure 2.2c). Comparison can be made between the orientation parameter described in McLachlan et al. [68] (equation (1.21)) and equation (1.20); these results can be seen in figure 2.2b, where the dashed line represents equation (1.20). The expression proposed by [68] initially ranges from 0.25 to 0.65 and our orientation parameter ranges from 0 at the centre of the channel to 0.6 at the walls. Due to zero shear at the centre of the channel, no alignment is predicted, hence it can be seen that the orientation parameter for uniaxial systems does not adequately capture the behaviour of these pressure-driven flows. Finally, the linear dichroism signal is 8.9×10^{-5}.

Figure 2.3 compares the flow profile and orientation parameter for a range of inlet pressure gradients. As the pressure gradient increases, the velocity through the channel increases (figure 2.3a), as expected. Mirroring the results seen in figure 2.2a, the decrease in velocity due to the fibres is small and predominantly in the centre of the channel. The orientation parameter also increases with the flow rate (figure 2.3b), however this only

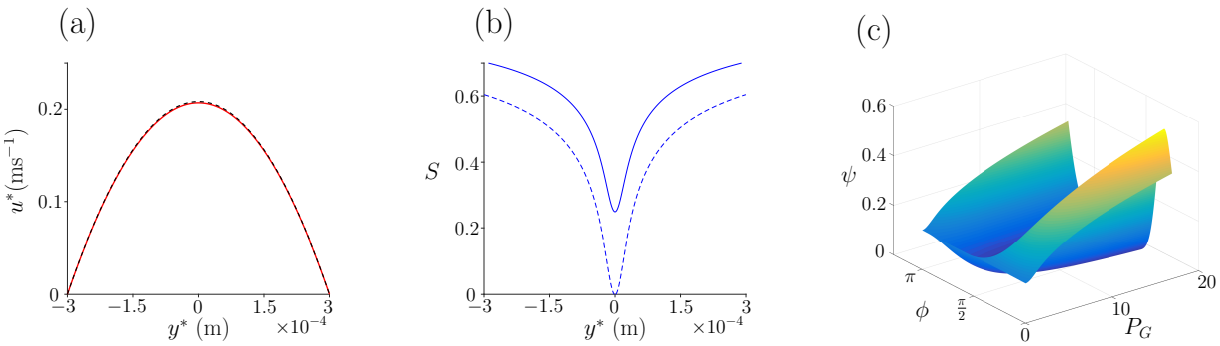

Figure 2.2: Steady flow results for a fixed pressure gradient. (a) Velocity profile comparing the Newtonian solution (dashed black line) to the solution incorporating the suspended fibres (red line). (b) Orientation parameter S varying across the channel; a comparison between the uniaxial equation suggested by McLachlan [68] (solid line) and the biaxial equation (2.24) (dashed line). (c) Probability density function ψ for a range of Peclet numbers and for ϕ between 0 and π. Note we do not consider ϕ from π to 2π as the results are π-periodic.

occurs away from the centre of the channel. The linear dichroism signal increases with the pressure gradient, from 6.3×10^{-5} to 1.1×10^{-4}.

Finally, the impact of varying channel width and particle number density is considered. Figure 2.4 depicts how the spatially averaged orientation parameter and linear dichroism signal vary with channel dimension and number density. Increasing the channel width increases the orientation parameter (figure 2.4a) and the number density has little impact. Similarly, increasing the channel width increases the signal, however the number density now has a much larger impact; increasing the linear dichroism signal with increasing value (figure 2.4b).

2.3.2 Oscillating flow

To reduce the volume of sample needed, an oscillating system has been proposed; theoretically the fluid is contained within a channel of much smaller volume, where it can be oscillated back and forth in front of light sensors. To explore the potential to generate a signal in this system, consider a pressure gradient which oscillates in time. Since the suspension is assumed to be dilute, the volume fraction is small and so we consider a perturbation in terms of this parameter.

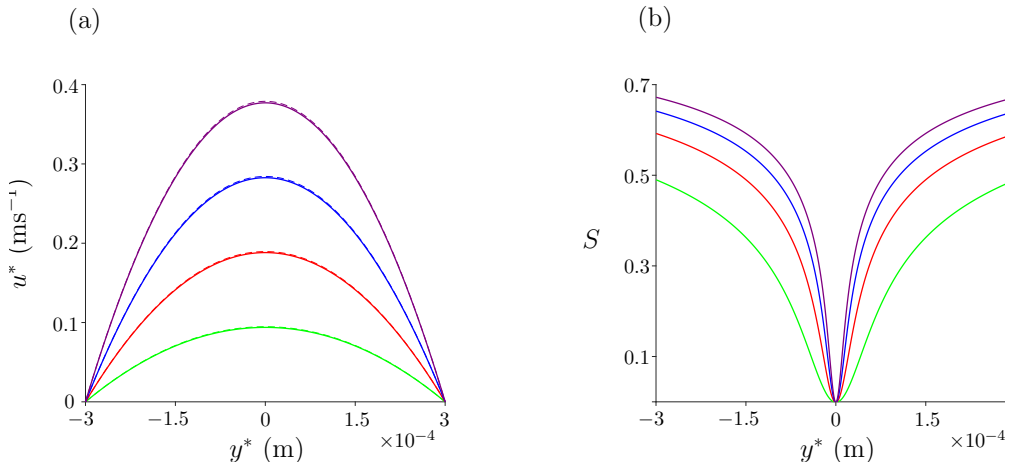

Figure 2.3: Steady flow results for a range of imposed pressure gradients. (a) Velocity for a bacteriophage suspension (solid line) compared with the Newtonian solution (dashed line) and (b) orientation parameter. For all figures, pressure gradient values $G^* = 2 \times 10^3$ Pa/m (green line), $G^* = 4 \times 10^3$ Pa/m (red line), $G^* = 6 \times 10^3$ Pa/m (blue line) and $G^* = 8 \times 10^3$ Pa/m (purple line) were used for comparison. Here $h^* = 3 \times 10^{-4}$ m and $n_d^* = 7.33 \times 10^{17}$ phage/m^3.

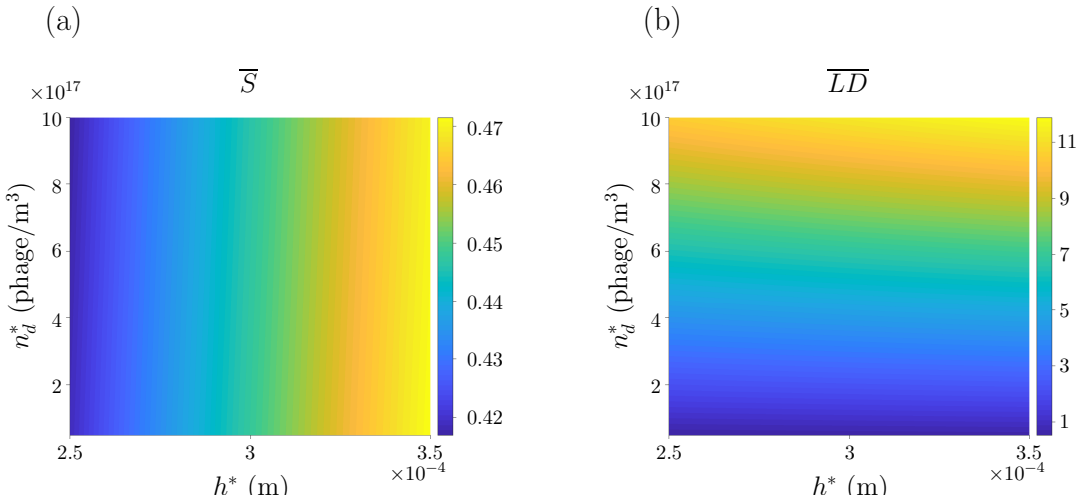

Figure 2.4: Steady flow results for a range of channel width and number density. (a) $\overline{S}$ and (b) $\overline{LD}$. The pressure gradient is $G^* \approx 4.4 \times 10^3$ Pa/m.

Recall the dimensional Navier-Stokes, continuity and Fokker-Planck equations given by equations (2.1), with stress terms (2.7), (2.8) and (2.9), (2.2) and (2.3), with (2.4), respectively. The equations are non-dimensionalised the same way as in equation (2.13), along with scaling the time as

$$t^* = \frac{t}{\omega^*}, \tag{2.43}$$

for oscillating frequency ω^*.

Perturbation Expansion

We introduce a perturbation from the Newtonian case, u_N by expanding about the small volume fraction Φ (see section 2.3.1),

$$u \approx u_N(y,t) + \Phi\, u_1(x,y,t), \tag{2.44}$$

$$v \approx \quad +\Phi\, v_1(x,y,t), \tag{2.45}$$

$$P \approx P_N(x,t) + \Phi\, P_1(x,y,t), \tag{2.46}$$

$$\psi \approx \psi_N(x,t) + \Phi\, \psi_1(x,y,t). \tag{2.47}$$

Substituting (2.44)-(2.47) into the dimensionless Navier-Stokes, continuity and Fokker-Planck equations, we have at leading order

$$\alpha^2 \frac{\partial u_N}{\partial t} = -\frac{\partial P_N}{\partial x} + \frac{\partial^2 u_N}{\partial y^2}\,, \tag{2.48}$$

$$\frac{\partial \psi_N}{\partial t} = \frac{1}{2P_G}\frac{\partial U_N}{\partial y}\frac{\partial}{\partial \phi}\left((1-\alpha_0\cos 2\theta)\psi_N\right) + \frac{1}{Pe}\frac{\partial^2 \psi_N}{\partial \phi^2}\,, \tag{2.49}$$

where $\alpha^2 = \omega^* {h^*}^2 \rho^*/\mu^*$ is the Womersley parameter and $Pe = \omega^*/D_r^*$ is the Peclet number related to oscillating flow. The boundary conditions are

$$u_N(-1,t) = u_N(1,t) = 0, \tag{2.50}$$

$$\int_0^{2\pi} \psi_N \,\mathrm{d}\theta = 1, \quad \psi_N(0,y,t) = \psi_N(2\pi,y,t). \tag{2.51}$$

The two equations are decoupled and equation (2.48) is the Newtonian equation for unidirectional unsteady flow, which is first solved analytically.

Calculating the velocity profile

Following [74], assume an oscillating pressure gradient and velocity profile, *i.e.*

$$\frac{\partial P_N}{\partial x} = e^{it}, \quad u_N = \bar{u}(y)e^{it}. \tag{2.52}$$

Substituting expressions (2.52) into equation (2.48) reduces the problem to an ordinary differential equation in $\bar{u}$,

$$i\alpha^2\bar{u} = -1 + \frac{\mathrm{d}^2\bar{u}}{\mathrm{d}y^2}\,, \tag{2.53}$$

$$\frac{\mathrm{d}\bar{u}}{\mathrm{d}y}(0) = 0, \quad \bar{u}(1) = 0. \tag{2.54}$$

We make the substitution

$$\bar{u} = \hat{u} + \frac{i}{\alpha^2}, \tag{2.55}$$

to remove the pressure gradient from equation (2.53), hence obtaining

$$i\alpha^2\hat{u} = \frac{\mathrm{d}^2\hat{u}}{\mathrm{d}y^2}\,, \tag{2.56}$$

$$\hat{u}(-1) = \hat{u}(1) = -\frac{i}{\alpha^2}. \tag{2.57}$$

Equation (2.56) has the general solution

$$\hat{u} = A\cosh(\sqrt{i\alpha^2}\,y) + B\sinh(\sqrt{i\alpha^2}\,y). \tag{2.58}$$

From the boundary conditions (2.57), $B = 0$ and $\hat{u}$ can be written as

$$\hat{u} = \frac{1}{i\alpha^2}\frac{\cosh(\sqrt{i\alpha^2}\,y)}{\cosh(\sqrt{i\alpha^2})}. \tag{2.59}$$

Remembering that $\bar{u} = \hat{u} + i/\alpha^2$ and $u_N = \bar{u}e^{it}$, the leading order velocity is

$$u_N = \frac{e^{it}}{i\alpha^2}\left(\frac{\cosh(\sqrt{i\alpha^2}\,y)}{\cosh(\sqrt{i\alpha^2})} - 1\right). \tag{2.60}$$

Fokker-Planck equation

Now the velocity has been obtained, the Fokker-Planck equation (2.49) can be solved. Substituting (2.60) into the leading order Fokker-Planck equation we have

$$\frac{\partial \psi_N}{\partial t} = \Re\left[\frac{P_G \sinh(\sqrt{i\alpha^2}\,y)e^{it}}{2Pe\sqrt{i\alpha^2}\cosh(\sqrt{i\alpha^2})}\right]\frac{\partial}{\partial \phi}\left((1-\alpha_0\cos 2\phi)\psi_N\right) + \frac{1}{Pe}\frac{\partial^2 \psi_N}{\partial \phi^2}, \tag{2.61}$$

where $\Re[\cdot]$ represents the real part. To solve this non-linear, second order partial differential equation we use a Fourier transform to obtain an initial value problem which is then solved via the built in Matlab functions '*ode15s*' and '*fft*'.

Introduce the truncated Fourier transform

$$\psi_N(\phi, t) = \sum_{k=-M}^{M} \Psi_k(t) e^{ik\phi}, \tag{2.62}$$

$$\Psi_k(t) = \frac{1}{2\pi}\int_0^{2\pi} \psi_N(\phi, t) e^{-ik\phi}\,\mathrm{d}\phi. \tag{2.63}$$

Next, substitute (2.62) into (2.61), utilising the exponential notation of sine and cosine, then consider modes of e^{ikx} to obtain a system of ordinary differential equations

$$\dot{\Psi}_k = ik\,D\left[\Psi_k - \frac{\alpha_0}{2}(\Psi_{k-2} + \Psi_{k+2})\right] - \frac{k^2}{Pe}\Psi_k, \tag{2.64}$$

where $-L \le k \le L$, $\dot{\Psi}_k = \mathrm{d}\Psi_k/\,\mathrm{d}t$, and

$$D = \Re\left[\frac{P_G \sinh(\sqrt{i\alpha^2}\,y)e^{it}}{2Pe\sqrt{i\alpha^2}\cosh(\sqrt{i\alpha^2})}\right]. \tag{2.65}$$

From the periodicity condition and the properties of Fourier transforms, the system of

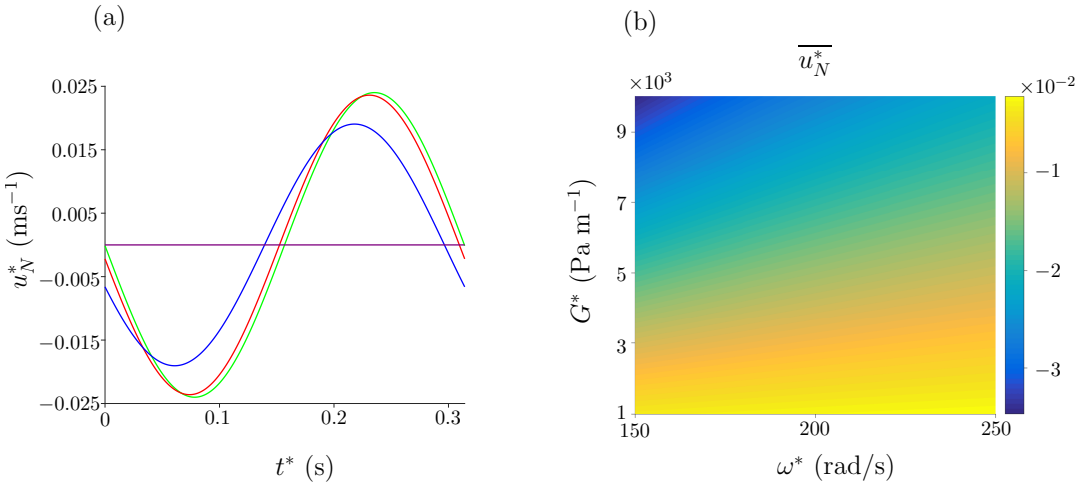

Figure 2.5: Velocity profile for oscillating flow. (a) Velocity profile changing with time over one time period where $\omega^* = 200$ rad/s. Four different y^* values are plotted: $y^* = 0$ m (green line), $y^* = 1 \times 10^{-4}$ m (red line), $y^* = 2 \times 10^{-4}$ m (blue line) and $y^* = 3 \times 10^{-4}$ m (purple line). (b) Time and spatially averaged velocity profile for a range of inlet flow rates and oscillating frequencies.

equations are re-derived for $1 \leq j \leq 2L+1$, by shifting the first L entries along by $2L+1$.

Assuming the fibres are initially uniformly distributed, *i.e.* $\psi_N(\phi, y, 0) = 1/2\pi$, and taking the fast Fourier transform (*'fft'*) of this condition in Matlab, the ordinary differential equation solver '*ode15s*' is used to solve the system $\dot{\Psi}_j$ (equation (2.64)). Once this solution has been found, the inverse fast Fourier transform (*'ifft'*) can be applied to obtain the required solution $\psi(\phi, y, t)$. For reference, an in-depth description of how we exploited the '*fft*'/'*ifft*' functions in Matlab, including reassigning indices, has been detailed for the less complex advection-diffusion equation, with constant coefficients, in Appendix A.

Results

Comparisons can be made between steady and oscillating flow by spatially averaged results; this definition is given in (2.42). Currently, the prototype handheld device provides a mean reading and so we calculate the time-average orientation parameter ($\overline{S}_{av}$) in line with this method; if absorption measurements can be taken quickly enough, the peak orientation in the channel will be recorded and so we compare time average with the peak over one

time period ($\overline{S}_{peak}$). For oscillating flow, the Womersley number $\alpha^2 = \rho^* h^{*2} \omega^* / \mu^* \approx 18.95$, taking the density of water as $\rho^* = 1 \times 10^3$ Kg/m^3 and $\omega^* = 200$ rad/s.

Figure 2.5a depicts how the velocity changes with time over one time period. At the wall, the velocity is zero, due to the no-slip condition, and the absolute value of the velocity increases moving away from the walls to the centre of the channel. Note that only positive values of y^* are shown, since the flow is symmetric, and that the velocity changes sign close to midway through the time period. Figure 2.5b depicts how the time and spatially averaged velocity profile changes with oscillating frequency ω^* and inlet pressure gradient G^*. The absolute value of the velocity increases for larger pressure gradients and smaller oscillating frequencies.

Time and spatial averages of the orientation parameter (figure 2.6a) and linear dichroism signal (figure 2.6b) have been considered for varying imposed pressure gradient and oscillating frequency. As the pressure gradient increases, both the orientation parameter and linear dichroism signal increase. Decreasing the oscillating frequency has a similar impact on both results. The results for a time averaged signal, in figure 2.6, can be compared with the peak orientation parameter or linear dichroism signal over an oscillation (figure 2.7). In both sub-plots, the trends of the results are identical, however $\overline{S}_{peak}$ is larger than $\overline{S}_{av}$ in general; the same is seen for the linear dichroism signal.

Finally, figure 2.8 compares the averaged orientation parameter and linear dichroism signal for a range of channel width and number density, for two different values of ω^*. For small values of ω^*, the orientation parameter (figure 2.8a) and linear dichroism signal (figure 2.8b) are similar to the steady problem (figure 2.4), though their values are reduced. As before, increasing the width of the channel increases the orientation parameter, and the number density impacts the linear dichroism signal only. In contrast, when $\omega^* = 200$ rad/s (figures 2.8c and d), the relationship between h^* and $\overline{S}_{av}$ switches; increasing the channel width decreases the degree of orientation in the system. The linear dichroism signal is affected significantly more by the number density than the orientation parameter, showing an increase with increasing number density regardless of the choice of ω^*. As with changes

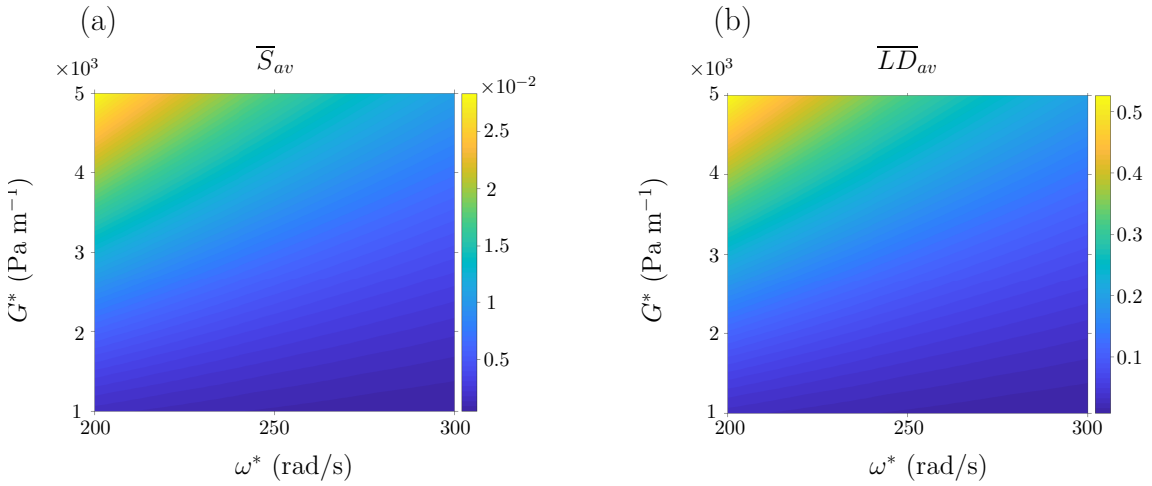

Figure 2.6: Depiction of $\overline{S}_{av}$ and $\overline{LD}_{av}$, for oscillating flow, as the imposed pressure gradient and oscillating frequency vary. (a) Orientation parameter and (b) linear dichroism signal. The channel width is $h^* = 3 \times 10^{-4}$ m and the number density is $n_d^* = 7.33 \times 10^{17}$ phage/m^3.

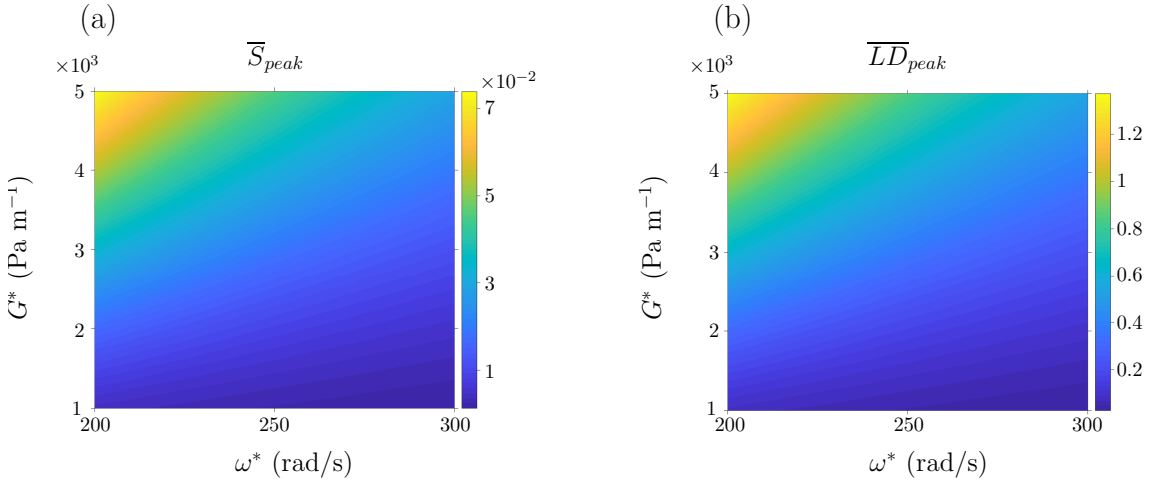

Figure 2.7: Depiction of $\overline{S}_{peak}$ and $\overline{LD}_{peak}$, for oscillating flow, as the imposed pressure gradient and oscillating frequency vary. (a) Orientation parameter and (b) linear dichroism signal. The channel width is $h^* = 3 \times 10^{-4}$ m and the number density is $n_d^* = 7.33 \times 10^{17}$ phage/m^3.

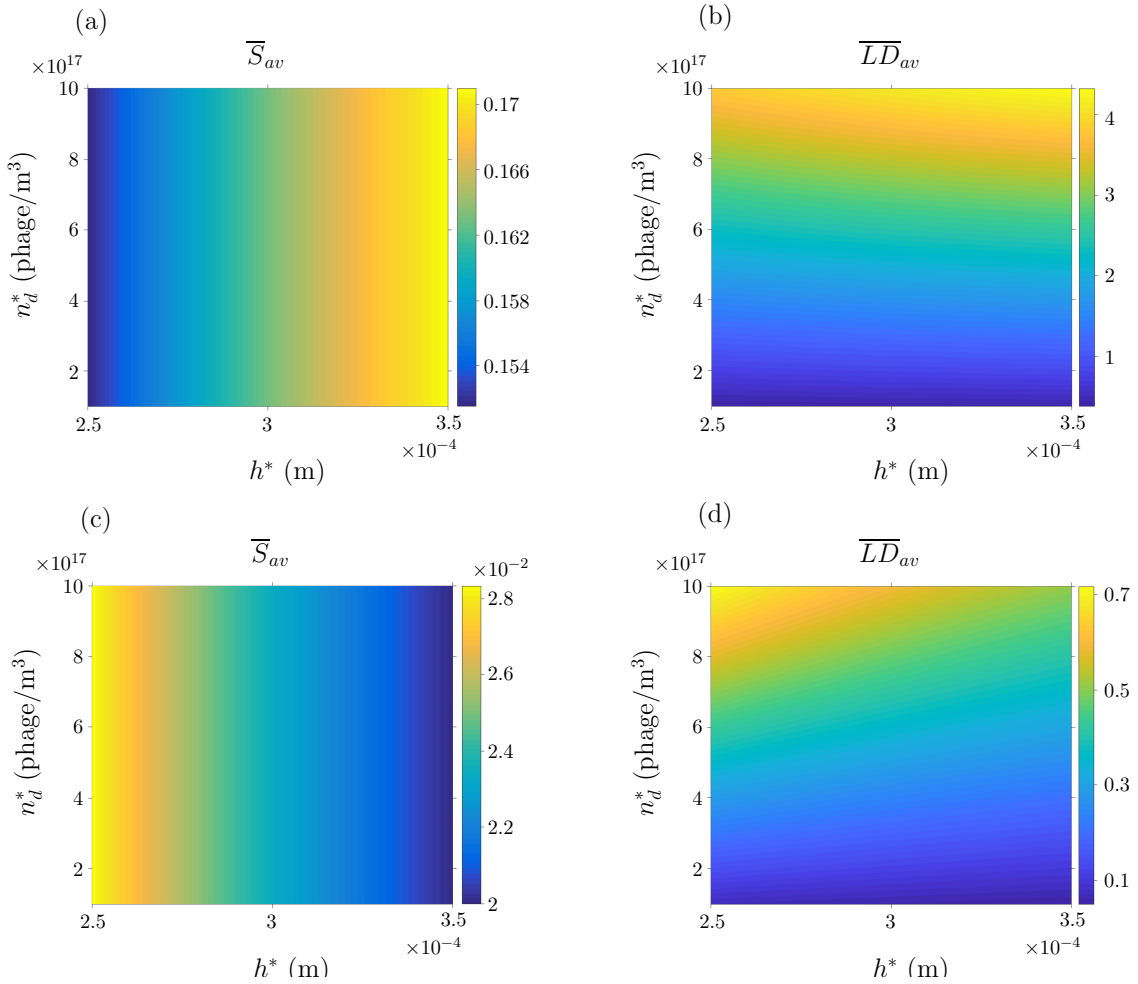

Figure 2.8: Oscillating flow results for a range of channel width and particle number density. (a) And (c) $\overline{S}_{av}$ and (b) and (d) $\overline{LD}_{av}$. The pressure gradient is $G^* = 4.4 \times 10^3$ Pa/m throughout and the oscillating frequency is $\omega^* = 10$ rad/s in (a) and (b) and $\omega^* = 200$ rad/s in (c) and (d).

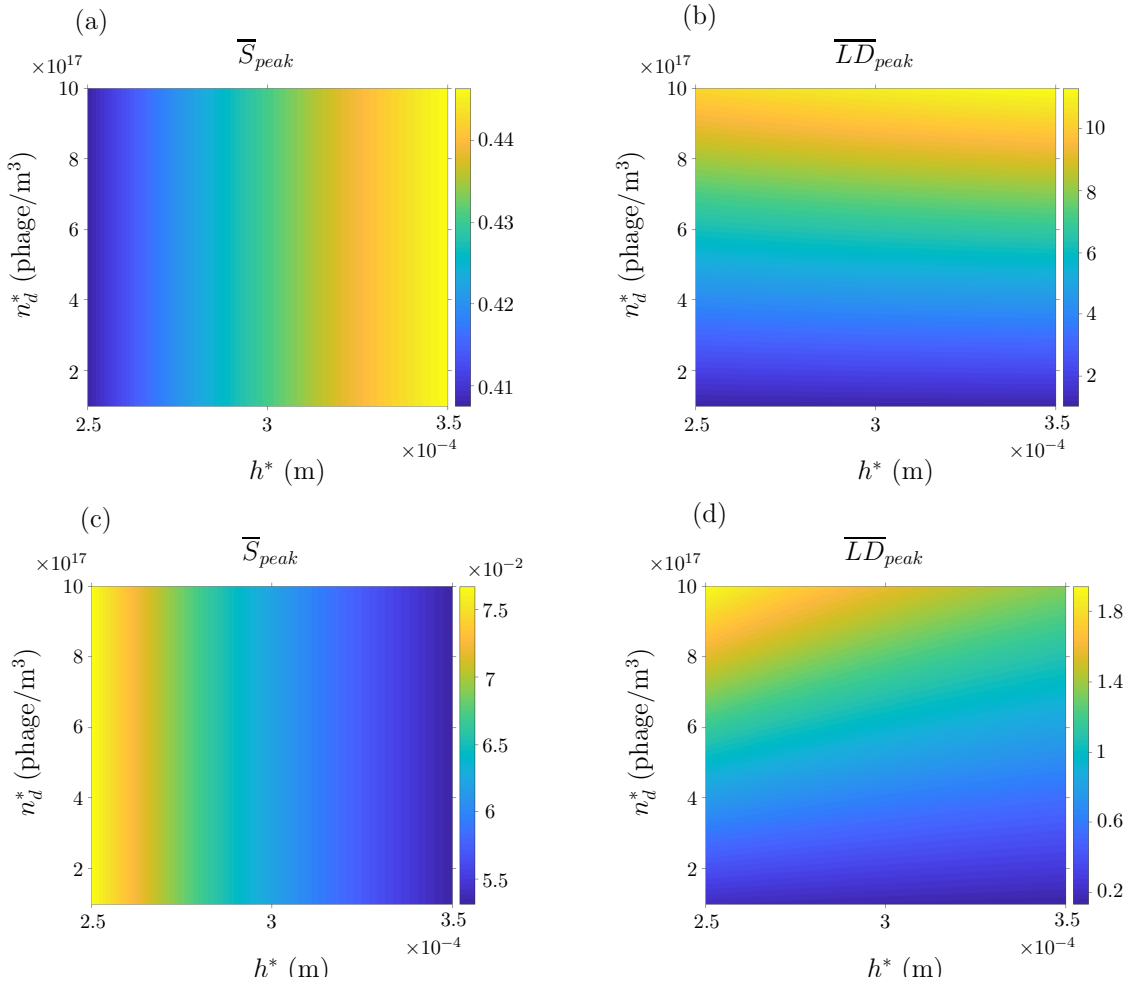

Figure 2.9: Oscillating flow results for a range of channel width and particle number density. (a) And (c) $\overline{S}_{peak}$ and (b) and (d) $\overline{LD}_{peak}$. The pressure gradient is $G^* = 4.4 \times 10^3$ Pa/m throughout and the oscillating frequency is $\omega^* = 10$ rad/s in (a) and (b) and $\omega^* = 200$ rad/s in (c) and (d).

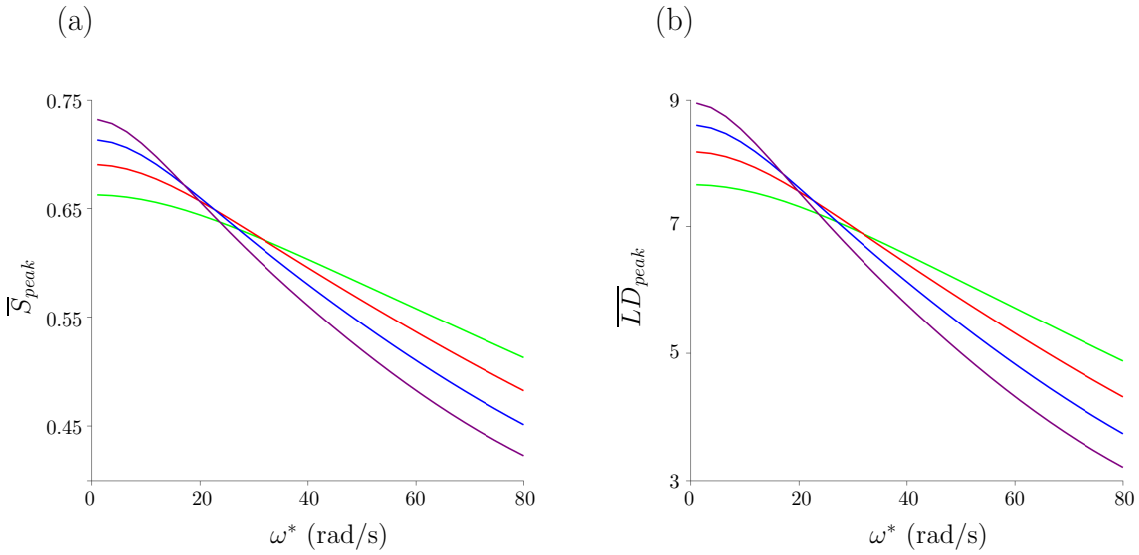

Figure 2.10: (a) $\overline{S}_{peak}$ and (b) $\overline{LD}_{peak}$ changing with ω^* for a range of channel widths. For both figures the following channel widths are plotted: $h^* = 2.5 \times 10^{-4}$ m (green line), $h^* = 3 \times 10^{-4}$ m (red line), $h^* = 3.5 \times 10^{-4}$ m (blue line), $h^* = 4 \times 10^{-4}$ m (purple line)

in oscillating frequency and pressure gradient, we compare the peak values ($\overline{\cdot}_{peak}$) over an oscillation with the average; the corresponding results in general are larger in figure 2.9 than figure 2.8.

To investigate at which oscillating frequencies this change occurs, $\overline{S}_{peak}$ and $\overline{LD}_{peak}$ are calculated, for multiple channel depth values, as the oscillating frequency increases (figure 2.10). Figure 2.10a shows $\overline{S}_{peak}$ for multiple channel depths and increasing oscillating frequency; by $\omega^* \approx 32$ rad/s, increasing h^* decreases the orientation parameter. The same can be seen for the linear dichroism signal in figure 2.10b. The values obtained for the orientation parameter and linear dichroism signal in the oscillating flow case are much smaller than those in the steady case, with the decrease in the orientation parameter being much more rapid in the oscillatory case.

Summary

The 2D coupled flow and distribution problem has been solved for flow in thin rectangular channels. Results for the flow profile and degree of orientation S have been calculated and can be summarised as follows:

- Increasing the pressure gradient G^* increases the orientation parameter $\overline{S}_{av}$ in both steady and oscillatory flows.

- The number density n_d^* has only a small impact to decrease $\overline{S}_{av}$ in steady flow via the velocity; the overall effect of increasing number density is to increase signal.

- Increasing the channel height h^* increases $\overline{S}_{av}$ and $\overline{LD}_{av}$ for steady flow and slow oscillations. For oscillating frequencies greater than $\omega^* \approx 30$ rad/s, this relationship reverses.

- The velocity and alignment for steady flow are in general larger than for oscillating flow for a given G^*, n_d^* and h^*.

- For the peak values $\overline{S}_{peak}$ and $\overline{LD}_{peak}$, the trends were in general the same as $\overline{S}_{av}$ and $\overline{LD}_{av}$, however the peak values are larger.

This simplified 2D channel provides an introduction to suspensions of elongated particles in channel flow. There are restrictions in the range of parameter space that can be explored, due to the integrating factor (2.28), and the predicted linear dichroism signal does not capture particles rotating out of the plane. Hence, to explore 3D rotations and more accurately predict the maximum attainable orientation, we consider a simple 3D channel, and incorporate the 3D Fokker-Planck equation.

2.4 Solving the Fokker-Planck equation in 3D

Next, consider the flow of a bacteriophage suspension in a 3D channel, bounded by walls at $z^* = -h^*$ and $z^* = h^*$, with length scale L^* (figure 2.11). The light source used for linear dichroism spectroscopy propagates between the channel walls and compares light polarised parallel and perpendicular to the flow direction, as shown by the arrows in figure 2.11. In contrast to section 2.3, to more accurately describe the orientation distribution in the channel, the 3D rotation effects of the Fokker-Planck equation are instead coupled

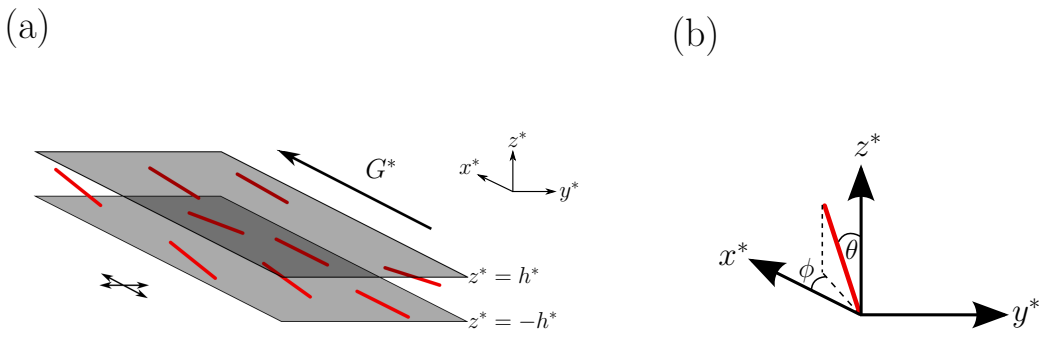

Figure 2.11: A fibrous fluid bound between two walls. The fibres are aligned according to an imposed pressure gradient. (a) Flow channel where G^* is the pressure gradient and x^* is the flow direction. The light polarisation directions are parallel and perpendicular to the flow direction and it is assumed the light source shines down onto the x^*–y^* plane. (b) The orientation of bacteriophage can be given as angles $\theta \in [0, \pi]$ and $\phi \in [0, 2\pi)$ away from the coordinate axes.

to the flow equations for the system, similar to those described in section 2.3; we again solve steady and oscillatory flow problems.

2.4.1 Steady channel flow

The boundary conditions are given by the no-slip conditions

$$\begin{aligned} u^*(x^*, y^*, -h^*) &= u^*(x^*, y^*, h^*) = 0, \\ v^*(x^*, y^*, -h^*) &= v^*(x^*, y^*, h^*) = 0, \\ w^*(x^*, y^*, -h^*) &= w^*(x^*, y^*, h^*) = 0. \end{aligned} \tag{2.66}$$

We now assume the walls are infinite in the x^*– and y^*– directions and scale our variables in a similar manner to (2.13),

$$\begin{gathered} u^* = \frac{G^* h^{*2}}{\mu^*} u, \quad v^* = \frac{\delta G^* h^{*2}}{\mu^*} v, \quad w^* = \frac{\delta G^* h^{*2}}{\mu^*} w, \quad P^* = \frac{G^* h^*}{\delta} P, \\ x^* = \frac{h^*}{\delta} x, \quad y^* = \frac{h^*}{\delta} y, \quad z^* = h^* z. \end{gathered} \tag{2.67}$$

By neglecting $\mathcal{O}(\delta)$ terms or smaller, the dimensionless Navier-Stokes equations are,

$$\frac{\partial P}{\partial x} = \frac{\mathrm{d}}{\mathrm{d}z}\left\{\frac{2\Phi\alpha_r}{P_G}\int_s p_1 p_3\,\psi\,\mathrm{d}\boldsymbol{p} + \left(1 + 4\Phi\left[\alpha_2\int_s p_1^2 p_3^2\,\psi\,\mathrm{d}\boldsymbol{p} + \frac{\alpha_3}{2}\int_s (p_1^2+p_3^2)\psi\,\mathrm{d}\boldsymbol{p} + \frac{\alpha_4}{2}\right]\right)\frac{\mathrm{d}u}{\mathrm{d}z}\right\}, \tag{2.68}$$

$$\frac{\partial P}{\partial y} = \frac{\mathrm{d}}{\mathrm{d}z}\left\{\frac{2\Phi\alpha_r}{P_G}\int_s p_2 p_3\,\psi\,\mathrm{d}\boldsymbol{p} + 4\Phi\left[\alpha_2\int_s p_1 p_2 p_3^2\,\psi\,\mathrm{d}\boldsymbol{p} + \frac{\alpha_3}{2}\int_s p_1 p_2\,\psi\,\mathrm{d}\boldsymbol{p}\right]\frac{\mathrm{d}u}{\mathrm{d}z}\right\}, \tag{2.69}$$

$$\frac{\partial P}{\partial z} = 0. \tag{2.70}$$

Due to the walls being infinite in y, we expect the orientation distribution about ϕ to be symmetric, *i.e.* $\phi \in [0,\pi]$ is equivalent to $\phi \in [-\pi, 0]$; this would also mean $\psi(\theta,\phi) = \psi(\theta,-\phi)$ is an even function. Considering the integrals in equation (2.69),

$$\int_s p_2 p_3\,\psi\,\mathrm{d}\boldsymbol{p} = \int_{-\pi}^{\pi}\int_0^{\pi} \sin^2\theta\cos\theta\sin\phi\,\psi\,\mathrm{d}\theta\,\mathrm{d}\phi, \tag{2.71}$$

$$\int_s p_1 p_2 p_3^2\,\psi\,\mathrm{d}\boldsymbol{p} = \frac{1}{2}\int_{-\pi}^{\pi}\int_0^{\pi} \sin^3\theta\cos^2\theta\sin 2\phi\,\psi\,\mathrm{d}\theta\,\mathrm{d}\phi, \tag{2.72}$$

$$\int_s p_1 p_2\,\psi\,\mathrm{d}\boldsymbol{p} = \frac{1}{2}\int_{-\pi}^{\pi}\int_0^{\pi} \sin^3\theta\sin 2\phi\,\psi\,\mathrm{d}\theta\,\mathrm{d}\phi. \tag{2.73}$$

Each integral contains an odd function of ϕ and so will integrate to zero, hence equation (2.69) can be rewritten as $\partial P/\partial y = 0$ and so $P = P(x)$ and equations (2.68)-(2.70) reduce to

$$-1 = \frac{\mathrm{d}}{\mathrm{d}z}\left\{\frac{2\Phi\alpha_r}{P_G}\int_{-\pi}^{\pi}\int_0^{\pi} \sin^2\theta\cos\theta\cos\phi\,\psi\,\mathrm{d}\theta\,\mathrm{d}\phi + \left(1 + 4\Phi\left[\alpha_2\int_{-\pi}^{\pi}\int_0^{\pi} \sin^3\theta\cos^2\theta\cos^2\phi\,\psi\,\mathrm{d}\theta\,\mathrm{d}\phi + \frac{\alpha_3}{2}\int_{-\pi}^{\pi}\int_0^{\pi} (\sin^2\theta\cos^2\phi + \cos^2\theta)\psi\sin\theta\,\mathrm{d}\theta\,\mathrm{d}\phi + \frac{\alpha_4}{2}\right]\right)\frac{\mathrm{d}u}{\mathrm{d}z}\right\}, \tag{2.74}$$

where the pressure gradient has been scaled to minus one. This equation is solved and re-dimensionalised before being used in the Fokker-Planck equation.

Solving the Fokker-Planck equation

To investigate 3D orientation of bacteriophage, first express the unit orientation vector $\boldsymbol{p}$ as

$$\boldsymbol{p} = (\sin\theta\cos\phi, \sin\theta\sin\phi, \cos\theta), \tag{2.75}$$

for $\theta \in [0, \pi]$ and $\phi \in [0, 2\pi)$. The particles in the flow are small enough that each particle at a point in space will experience an approximately linear flow, and hence a constant shear rate $\dot{\gamma}^*$. Following [5, 87], assuming $\alpha_0 = 1$ and analysing the steady state, the Fokker-Planck equation reduces to

$$\frac{1}{6}\Lambda(\psi) = P_\lambda \Omega(\psi), \tag{2.76}$$

where $P_\lambda = \dot{\gamma}^*/6D_r^*$ is the Peclet number and

$$\Lambda(\psi) = \frac{1}{\sin\theta}\frac{\partial}{\partial\theta}\left(\sin\theta\frac{\partial\psi}{\partial\theta}\right) + \frac{1}{\sin^2\theta}\frac{\partial^2\psi}{\partial\phi^2}, \tag{2.77}$$

$$\Omega(\psi) = \frac{\sin\phi\cos\phi}{\sin\theta}\frac{\partial}{\partial\theta}\left(\sin^2\theta\cos\theta\,\psi\right) - \frac{\partial}{\partial\phi}\left(\sin^2\phi\,\psi\right). \tag{2.78}$$

The Fokker-Planck equation (2.76) is solved using Spherical Harmonics [5, 68, 87]. We discretise the spatial part of the orientation distribution using spherical harmonics, the angular solution to Laplace's equation on a sphere, which take the form

$$\psi(\theta,\phi) = \sum_{n=0}^{N}\sum_{m=0}^{n}\left(A^m_{0\,n}P^m_n(\cos\theta)\cos(m\phi) + A^m_{1\,n}P^m_n(\cos\theta)\sin(m\phi)\right), \tag{2.79}$$

where P^m_n are the associated Legendre polynomials. This is substituted into equation

(2.76), where Γ and Ω are given by

$$\Lambda(P_n^m(\cos\theta)\cos(m\phi)) = -n(n+1)P_n^m(\cos\theta)\cos(m\phi), \tag{2.80}$$

$$\Lambda(P_n^m(\cos\theta)\sin(m\phi)) = -n(n+1)P_n^m(\cos\theta)\sin(m\phi), \tag{2.81}$$

$$\Omega(P_n^m(\cos\theta)\cos(m\phi)) = -\sum_{p=m-2}^{m+2}\sum_{q=n-2}^{n+2} a_{n,q}^{m,p} P_n^m(\cos\theta)\sin(m\phi), \quad m \geq 0, \tag{2.82}$$

$$\Omega(P_n^m(\cos\theta)\sin(m\phi)) = \sum_{p=m-2}^{m+2}\sum_{q=n-2}^{n+2} a_{n,q}^{m,p} P_n^m(\cos\theta)\cos(m\phi), \quad m > 0. \tag{2.83}$$

The first two results stem from the definition of a spherical harmonic. The other two are a linear combination of spherical harmonics, where there are seven non-zero constants $a_{n,q}^{m,p}$, reproduced from [5, 87] as follows

$$a_{n,n-2}^{m,m-2} = \frac{(n-2)(n+m)!(1-\delta_{m0})}{4(2n+1)(2n-1)(n+m-4)!}, \tag{2.84}$$

$$a_{n,n}^{m,m-2} = \frac{3(n-m+2)!(n+m)!(1-\delta_{m0})}{4(2n+3)(2n-1)(n+m-2)!(n-m)!}, \tag{2.85}$$

$$a_{n,n+2}^{m,m-2} = -\frac{(n+3)(n-m+4)!(1-\delta_{m0})}{4(2n+1)(2n+3)(n-m)!}, \tag{2.86}$$

$$a_{n,n}^{m,m} = -\frac{m}{2}, \tag{2.87}$$

$$a_{n,n-2}^{m,m+2} = -\frac{(n-2)(1+\delta_{m0})}{4(2n+1)(2n-1)}, \tag{2.88}$$

$$a_{n,n}^{m,m+2} = -\frac{3(1+\delta_{m0})}{4(2n+3)(2n-1)}, \tag{2.89}$$

$$a_{n,n+2}^{m,m+2} = \frac{(n+3)(1+\delta_{m0})}{4(2n+1)(2n+3)}. \tag{2.90}$$

Substituting (2.80)-(2.83) into (2.76), equating coefficients of sine and cosine terms, we derive a system of equations for $A_{0\,n}^m$ and $A_{1\,n}^m$

$$\frac{q(q+1)}{6}A_{0\,q}^p = -P_\lambda \sum_{n=0}^{N}\sum_{m=0}^{n} a_{n,q}^{m,p} A_{1\,n}^m, \tag{2.91}$$

$$\frac{q(q+1)}{6}A_{1\,q}^p = P_\lambda \sum_{n=0}^{N}\sum_{m=0}^{n} a_{n,q}^{m,p} A_{0\,n}^m, \tag{2.92}$$

for integer N, $q = 0, 2, \ldots, N$ and $p = 0, 2, \ldots, n$. Here, $A^0_{0\,0} = 1/4\pi$ to satisfy the normalisation condition, and we have $A^0_{1\,n} = 0$ for all n. Due to particle symmetry, if n or m are odd then $A^m_{0\,n} = A^m_{1\,n} = 0$.

Equations (2.91) and (2.92) are solved numerically by setting up a matrix of equations $\boldsymbol{A}\boldsymbol{x} = \boldsymbol{b}$ for operator matrix $\boldsymbol{A}$ and right hand side vector $\boldsymbol{b}$. The vector $\boldsymbol{b}$ is a vector of zeros with one entry, $b_1 = 1/4\pi$, to satisfy the normalisation condition. The vector $\boldsymbol{x}$ has length $N/2(N/2+3)+2$, where the first $N/4(N/2+3)+1$ entries are the $A^p_{0\,q}$ terms and the second $N/4(N/2+3)+1$ are $A^p_{1\,q}$ terms,

$$\boldsymbol{x} = (A^0_{0\,0},\, A^0_{0\,2},\, A^2_{0\,2},\, \ldots,\, A^N_{0\,N},\, A^0_{1\,0},\, A^0_{1\,2},\, \ldots,\, A^N_{1\,N})^T. \tag{2.93}$$

The operator matrix has dimensions $(N/2(N/2+3)+2) \times (N/2(N/2+3)+2)$. To select appropriate matrix entries, define $q = 2j$ and $p = 2i$ such that for $j = 1, 2, \ldots, N/2$ and $i = 1, 2, \ldots, j$, the $A^p_{0\,q}$ and $A^p_{1\,q}$ entries are given by $\boldsymbol{x}(j(j+1)/2 + i + 1)$ and $\boldsymbol{x}(N/4(N/2+3) + 1 + j(j+1)/2 + i + 1)$ respectively.

The operator matrix can be divided into four sections

$$\boldsymbol{A} = \left(\begin{array}{c|c} \boldsymbol{B} & \boldsymbol{C} \\ \hline \boldsymbol{D} & \tilde{\boldsymbol{B}} \end{array}\right). \tag{2.94}$$

The top left and bottom right sections of the matrix, given by matrices $\boldsymbol{B}$ and $\tilde{\boldsymbol{B}}$, are formed from the first terms in equations (2.91) and (2.92) respectively. Here, $\boldsymbol{B}$ and $\tilde{\boldsymbol{B}}$ are diagonal matrices with entries $-j(2j+1)/3$, with the $m = 0$ entries set to zero in $\tilde{\boldsymbol{B}}$. The top right and bottom left sections, matrices $\boldsymbol{C}$ and $\boldsymbol{D} = -\boldsymbol{C}$ contain entries for the summation term in equations (2.91) and (2.92) respectively. Both matrices are given by the non-zero $a^{m,p}_{n,q}$ entries which can be set up in a matrix $\boldsymbol{M}$. To do this, introduce two new indices $n = 2l$ and $m = 2k$, where $l = 1, 2, \ldots, N/2$ and $k = 1, 2, \ldots, l$. The non-zero entries for the coefficients can be calculated and stored in a $(N/4(N/2+3) +$

1) $\times$ $(N/4(N/2+3)+1)$ matrix $\boldsymbol{M}$,

$$\boldsymbol{M} = \begin{pmatrix} a_{0,0}^{0,0} & a_{2,0}^{0,0} & a_{2,0}^{2,0} & \dots & \dots & a_{N,0}^{N,0} \\ a_{0,2}^{0,0} & a_{2,2}^{0,0} & a_{2,2}^{2,0} & \dots & \dots & a_{N,2}^{N,0} \\ \vdots & \ddots & \ddots & \ddots & \ddots & \vdots \\ \vdots & \ddots & \ddots & \ddots & \ddots & \vdots \\ a_{0,N}^{0,N} & a_{2,N}^{0,N} & a_{2,N}^{2,N} & \dots & \dots & a_{N,N}^{N,N} \end{pmatrix}, \tag{2.95}$$

which when multiplied by the Peclet number gives the two required matrices $\boldsymbol{C} = -P_\lambda \boldsymbol{M}$ and $\boldsymbol{D} = P_\lambda \boldsymbol{M}$. Again the corresponding $A_{1\,n}^0$ entries are set to zero.

The system of equations is solved using backslash in Matlab, resulting in a vector of $A_{i,n}^m$ values which can be used to construct ψ from equation (2.79).

Incorporating extra stress terms

The Newtonian problem is taken to initialise the iteration. Then, once the probability density function is known, the velocity can be solved semi-analytically. This calculation is identical to the calculation in section 2.3, with resulting velocity

$$u = \int_{-1}^{z} \frac{d_1 - \overline{z} - \hat{\alpha}_r(\overline{z})}{A(\overline{z})}\,\mathrm{d}\overline{z}, \tag{2.96}$$

where

$$\begin{aligned} A(z) = 1 + 4\Phi \Bigg[& \alpha_2 \int_{-\pi}^{\pi}\int_{0}^{\pi} \sin^3\theta \cos^2\theta \cos^2\phi\, \psi \,\mathrm{d}\theta\,\mathrm{d}\phi \\ & + \frac{\alpha_3}{2}\int_{-\pi}^{\pi}\int_{0}^{\pi} (\sin^2\theta\cos^2\phi + \cos^2\theta)\psi \sin\theta\,\mathrm{d}\theta\,\mathrm{d}\phi + \frac{\alpha_4}{2}\Bigg], \end{aligned} \tag{2.97}$$

$$\hat{\alpha}_r(z) = \frac{2\Phi\alpha_r}{P_G}\int_{-\pi}^{\pi}\int_{0}^{\pi} \sin^2\theta\cos\theta\cos\phi\,\psi\,\mathrm{d}\theta\,\mathrm{d}\phi, \tag{2.98}$$

$$d_1 = \frac{\int_{-1}^{1}\frac{z}{A(z)}\,\mathrm{d}z + \int_{-1}^{1}\frac{\hat{\alpha}_r(z)}{A(z)}\,\mathrm{d}z}{\int_{-1}^{1}\frac{1}{A(z)}\,\mathrm{d}z}. \tag{2.99}$$

The θ– and ϕ– integrals are computed numerically using the left-hand rule and the z-integrals are computed using the mid-point method. The solution is calculated iteratively, as described in section 2.3.1.

Numerical Convergence

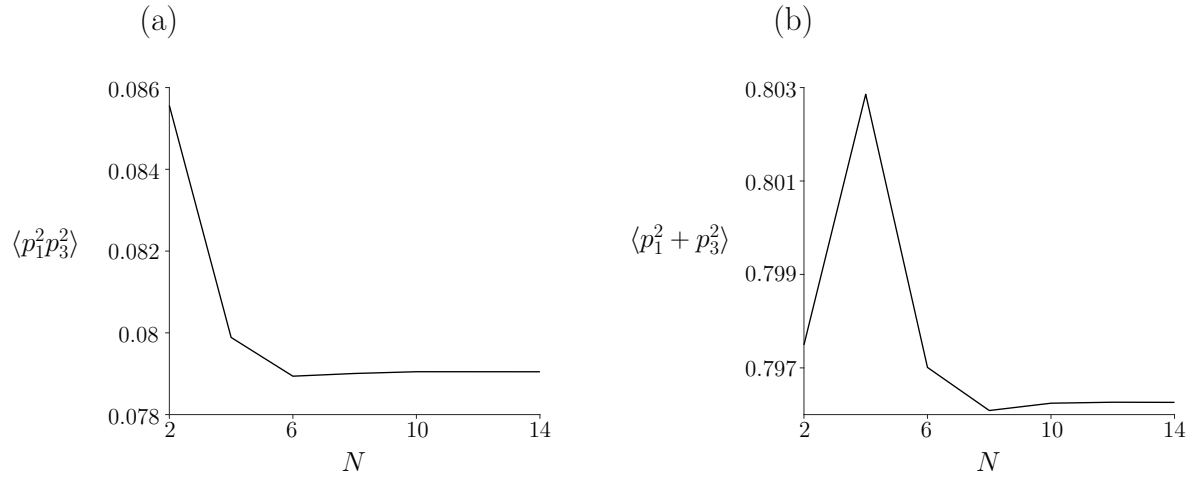

Figure 2.12: Numerical convergence of the moments of ψ for an increasing number of modes N. (a) $\langle p_1^2 p_3\rangle$ and (b) $\langle p_1^2 + p_3^2\rangle$. Convergence is obtained for $N = 10$.

To optimise the efficiency of the above processes, the convergence of the spherical harmonic solution and the finite difference approximation are investigated. To examine the accuracy of the spherical harmonics solution, consider how the moments of ψ change for increasing modes N. Figure 2.12 depicts the moments associated with the extra stress

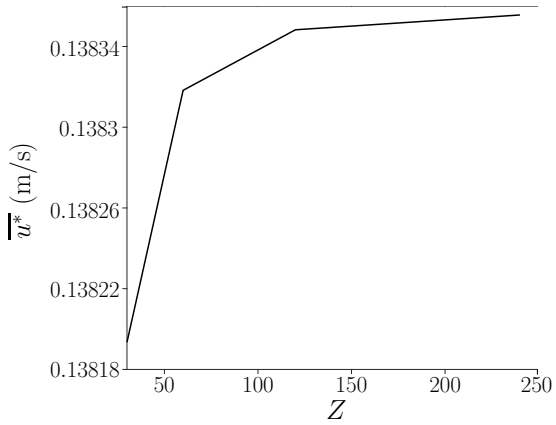

Figure 2.13: Convergence of the time and spatially averaged Newtonian velocity $\overline{u^*}$ for increasing steps in z^*. The number of gridpoints for convergence to 0.01% of the value of $\overline{u^*}$ is $Z = 150$.

terms,

$$\begin{aligned}\langle p_1^2 + p_3^2 \rangle(z) &= \int_{-\pi}^{\pi}\int_{0}^{\pi} p_1^2 + p_3^2 \, \psi \sin\theta \, \mathrm{d}\theta \, \mathrm{d}\phi \\ &= \int_{-\pi}^{\pi}\int_{0}^{\pi} (\sin^2\theta\cos^2\phi + \cos^2\theta) \, \psi \sin\theta \, \mathrm{d}\theta \, \mathrm{d}\phi,\end{aligned} \tag{2.100}$$

$$\langle p_1^2 p_3^2 \rangle(z) = \int_{-\pi}^{\pi}\int_{0}^{\pi} p_1^2 p_3^2 \, \psi \sin\theta \, \mathrm{d}\theta \, \mathrm{d}\phi = \int_{-\pi}^{\pi}\int_{0}^{\pi} \sin^3\theta\cos^2\theta\cos^2\phi \, \psi \, \mathrm{d}\theta \, \mathrm{d}\phi. \tag{2.101}$$

Both $\langle p_1^2 + p_3^2 \rangle$ and $\langle p_1^2 p_3^2 \rangle$ are averaged over the channel, and their change with increasing N is shown in figures 2.12a and 2.12b respectively. Once $N = 10$ the value of these moments do not change, hence this is our choice for all numerical calculations.

Similarly, we investigate the convergence of the finite difference approximation. We solve the Newtonian flow equations and average the velocity; figure 2.13 depicts how the average changes when increasing the number of steps Z. The difference between the average calculated at $Z = 150$ and $Z = 200$ is 0.01% of the value itself, hence we take $Z = 150$ in our calculations.

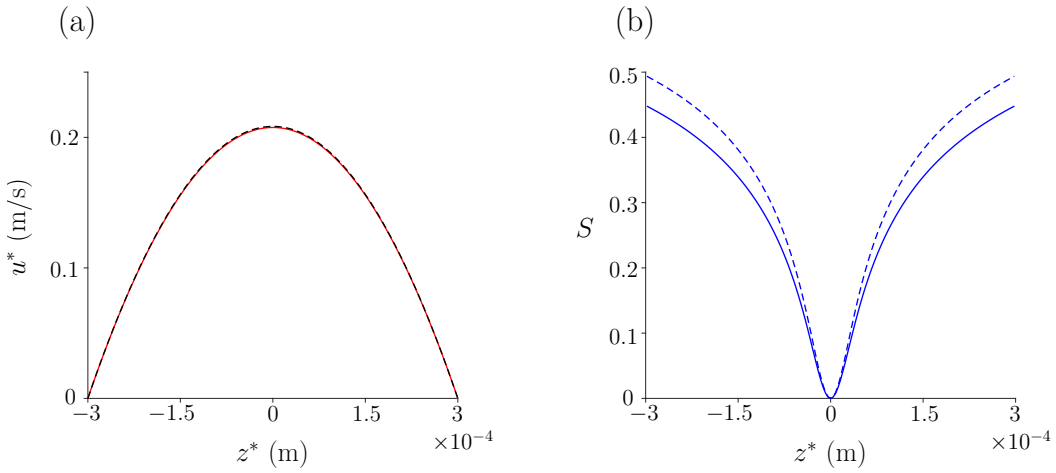

Figure 2.14: Results for the flow profile of a suspension of bacteriophage in a channel with two walls in 3D orientation space. (a) Velocity profile (red) in comparison with the Newtonian velocity profile (dashed line), (b) orientation parameter S changing across the channel, where equation (1.20) (dashed line) is compared with equation (1.21). The parameters used are given in table 2.1: $G^* = 4.4 \times 10^3$ Pa/m, $h^* = 3 \times 10^{-4}$ m, and $n_d^* = 7.33 \times 10^{17}$ phage/m^3.

Results

The parameter values used initially are the same as those in table 2.1. First we see how the velocity and orientation parameter change in z^* (figure 2.14). The reduction in velocity due to the phage, depicted by the red line in figure 2.14a, is almost unseen. Figure 2.14b shows the orientation parameter S larger close to the walls and dropping to zero in the centre of the channel for both the dashed and solid lines. However, we can see that the version of the orientation parameter used in [68] does not predict as large a degree of orientation; both the 2D and 3D versions of this equation differ from (1.20).

Next we consider how the number density and inlet pressure gradient influence the velocity and orientation parameter (figure 2.15). The larger number density at each pressure gradient is shown by the black dashed line; increasing the number density of phage has no noticeable impact on the fluid velocity or orientation parameter. Increasing the pressure gradient increases the velocity profile and hence the orientation parameter away from the centre of the channel.

The orientation parameter and linear dichroism signal are calculated for a range of

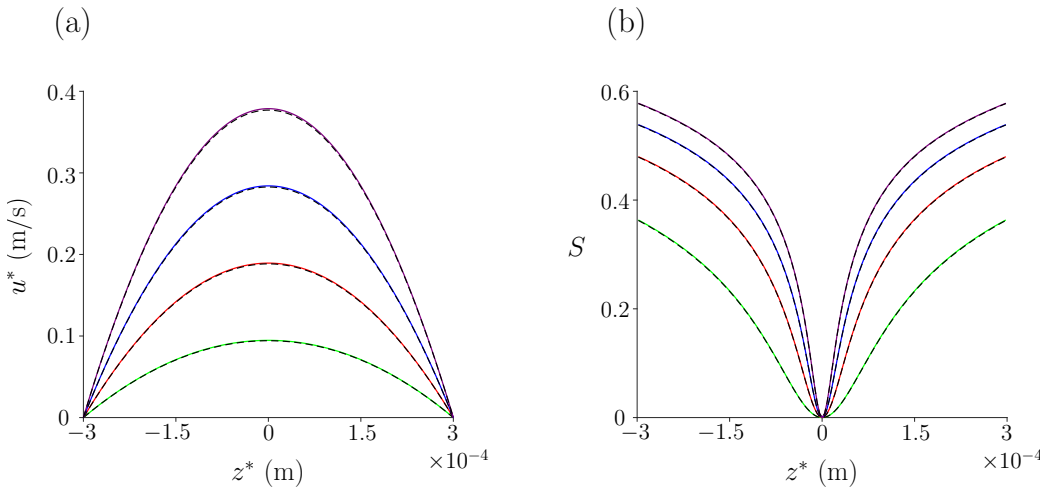

Figure 2.15: Velocity and orientation parameter for varying pressure gradient and particle number density. (a) Velocity profile, and (b) orientation parameter. For all results, the following pressure gradients are used: $G^* = 2 \times 10^3$ Pa/m (green line), $G^* = 4 \times 10^3$ Pa/m (red line), $G^* = 6 \times 10^3$ Pa/m (blue line), $G^* = 8 \times 10^3$ Pa/m (purple line). The coloured lines represent $n_d^* = 1 \times 10^{17}$ phage/m^3 and the black dashed line next to each result signifies the same pressure gradient for $n_d^* = 1 \times 10^{18}$ phage/m^3. The channel depth remains as $h^* = 3 \times 10^{-4}$ m.

number density and channel width in figure 2.16 where the orientation parameter is averaged over the channel width. The orientation parameter increases with the channel width, while the number density, as expected, has little impact (figure 2.16a). The linear dichroism signal however behaves differently (figure 2.16b); here the number density is having a more drastic effect, while increasing with the channel width as before.

Finally, we investigate the ability for the model to predict a maximum orientation parameter by varying the channel depth and pressure gradient (figure 2.17), the two parameters which have the largest impact. As seen in other results, the orientation parameter increases as both the channel depth and pressure gradient increase; however in figure 2.17 we see that $\overline{S}$ tends towards $\overline{S} \approx 0.74$ for a channel depth greater than $h^* \approx 4 \times 10^{-3}$ m and pressure gradient greater than $G^* \approx 5 \times 10^4$ Pa/m.

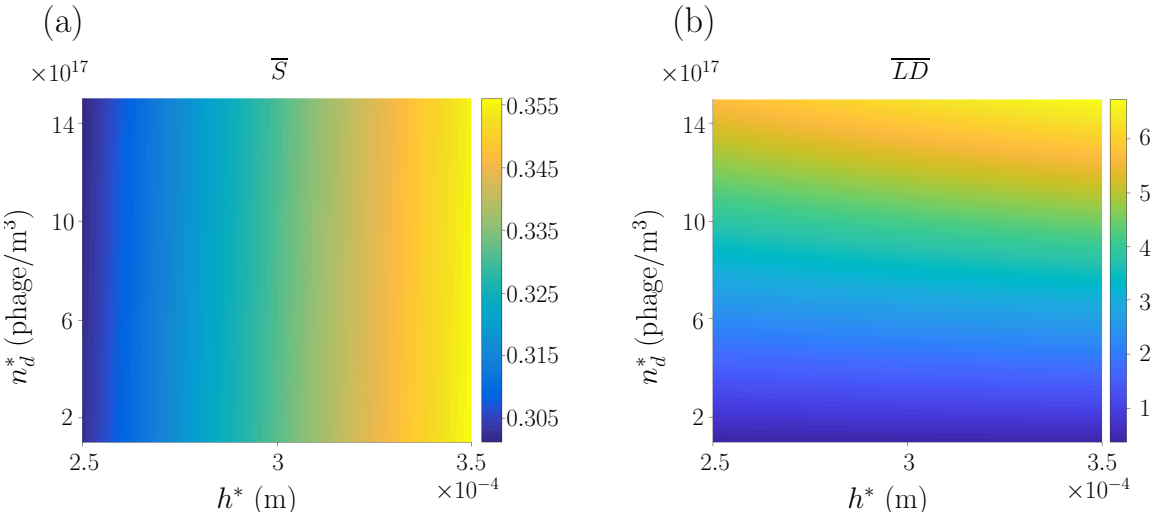

Figure 2.16: Orientation parameter and linear dichroism signal for a range of number density and channel depth. (a) $\overline{S}$ and (b) $\overline{LD}$. The pressure gradient is $G^* = 4.4 \times 10^3$ Pa/m throughout.

2.4.2 Oscillating pressure gradient

Next we reconsider the theoretical oscillatory system, coupled this time with the 3D Fokker-Planck equation. The equations governing the problem remain as (2.1), (2.2) and (2.3), however the pressure gradient now takes an exponential form

$$\frac{\partial P^*}{\partial x^*} = G^* \exp(i\omega^* t^*). \tag{2.102}$$

The other variables are non-dimensionalised as in equations (2.67); the continuity equation (2.2) is unchanged and the Navier-Stokes equations (2.1) reduce to

$$\begin{aligned} \alpha^2 \frac{\partial u}{\partial t} = -\exp(it) + \frac{\mathrm{d}}{\mathrm{d}z}\Bigg\{ & \frac{2\Phi\alpha_r}{P_G}\int_{-\pi}^{\pi}\int_{0}^{\pi} \sin^2\theta\cos\theta\cos\phi\,\psi\,\mathrm{d}\theta\,\mathrm{d}\phi \\ & + \Bigg(1 + 4\Phi\Bigg[\alpha_2\int_{-\pi}^{\pi}\int_{0}^{\pi} \sin^3\theta\cos^2\theta\cos^2\phi\,\psi\,\mathrm{d}\theta\,\mathrm{d}\phi \\ & + \frac{\alpha_3}{2}\int_{-\pi}^{\pi}\int_{0}^{\pi} (\sin^2\theta\cos^2\phi + \cos^2\theta)\psi\sin\theta\,\mathrm{d}\theta\,\mathrm{d}\phi + \frac{\alpha_4}{2}\Bigg]\Bigg)\frac{\mathrm{d}u}{\mathrm{d}z}\Bigg\}. \end{aligned} \tag{2.103}$$

As in the steady case, we iterate between the equation for ψ and u^* to obtain a solution.

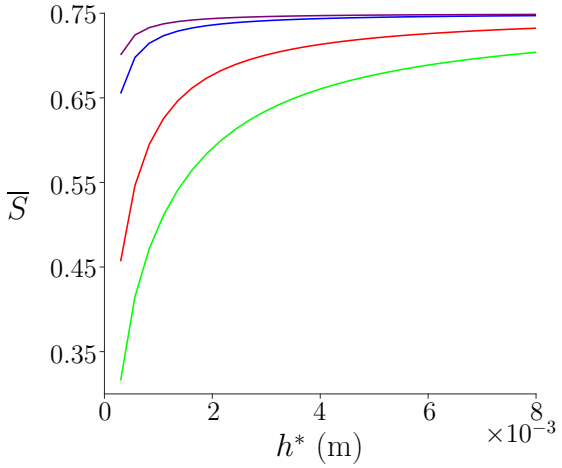

Figure 2.17: The limit of the degree of orientation as the channel depth h^* and pressure gradient G^* increase. Each line represents a different pressure gradient: $G^* = 4{\times}10^3$ Pa/m (green line), $G^* = 1 \times 10^4$ Pa/m (red line), $G^* = 5 \times 10^4$ Pa/m (blue line) and $G^* = 1 \times 10^5$ Pa/m (purple line).

Solving the Fokker-Planck equation

Again following [5, 87], assuming $\alpha_0 = 1$ and including time derivatives, the Fokker-Planck equation is

$$\frac{\partial \psi}{\partial \tau} = \frac{1}{6}\Lambda(\psi) - P_\lambda(t)\Omega(\psi), \tag{2.104}$$

where $t^* = \tau/(6D_r^*)$, $P_\lambda(t) = \dot{\gamma}^*/6D_r^*$ is the Peclet number and $\Lambda(\psi)$ and $\Omega(\psi)$ are given by (2.77) and (2.78) respectively. The numerical solution in [68] is adapted to account for a time dependent Peclet number P_λ, then solved for each point in z^*. The method is detailed below.

The Fokker-Planck equation (2.104) is discretised using Spherical Harmonics [5, 68, 87]; assume the solution takes the form

$$\psi(\theta, \phi, t) = \sum_{n=0}^{N} \sum_{m=0}^{n} \left(A_{0\,n}^m(t) P_n^m(\cos\theta)\cos(m\phi) + A_{1\,n}^m(t) P_n^m(\cos\theta)\sin(m\phi) \right). \tag{2.105}$$

This is substituted into equation (2.104), where Γ and Ω are given by (2.80)-(2.83).

Substituting (2.80)-(2.83) into (2.104), equating coefficients of sine and cosine terms,

we derive a system of odes for $A^m_{0\,n}$ and $A^m_{1\,n}$

$$\frac{\mathrm{d}A^p_{0\,q}}{\mathrm{d}t} = -\frac{q(q+1)}{6}A^p_{0\,q} - P_\lambda(t)\sum_{n=0}^{N}\sum_{m=0}^{n} a^{m,p}_{n,q}A^m_{1\,n}, \tag{2.106}$$

$$\frac{\mathrm{d}A^p_{1\,q}}{\mathrm{d}t} = -\frac{q(q+1)}{6}A^p_{1\,q} + P_\lambda(t)\sum_{n=0}^{N}\sum_{m=0}^{n} a^{m,p}_{n,q}A^m_{0\,n}, \tag{2.107}$$

for integer N, $q = 0, 2, \ldots, N$ and $p = 0, 2, \ldots, n$. Here, $A^0_{0\,0}(t) = 1/4\pi$ to satisfy the normalisation condition.

The ordinary differential equations (2.106) and (2.107) are solved numerically using '*ode45*' in Matlab, by constructing an operator matrix identical to (2.94). The solution can then be reconstructed using the spherical harmonic substitution (2.105). Once the velocity is known, the new Peclet number can be calculated by calculating the shear rate $\dot{\gamma} = \partial u^*/\partial z^*$, which can be used to calculate $\psi(\theta, \phi, t^*; z^*)$ and its moments.

Incorporating extra stress terms

The Newtonian flow is first calculated and the Fokker-Planck equation is solved. From here, the moments of $\psi(\theta, \phi, t^*, z^*)$ are calculated and the updated flow equations can be solved numerically using a finite difference scheme.

Firstly we seek a solution to the Newtonian equation,

$$\alpha^2 \frac{\partial u}{\partial t} = e^{it} + \frac{\partial^2 u}{\partial z^2}\,, \tag{2.108}$$

$$u(-1, t) = u(1, t) = 0, \qquad u(z, 0) = 0. \tag{2.109}$$

Discretising, using an implicit finite difference scheme, we have

$$\alpha^2 \frac{u_i^{n+1} - u_i^n}{\Delta t} = e^{i\left(t^n + \frac{\pi}{2}\right)} + \frac{u_{i+1}^{n+1} - 2u_i^{n+1} + u_{i-1}^{n+1}}{\Delta z^2}, \tag{2.110}$$

where $i = 1, 2, \ldots, Z$, $n = 1, 2, \ldots, T$ represent the steps in z and t respectively and t has

been shifted by $\pi/2$ to account for the initial condition. Rearranging,

$$\left(1+\frac{2\Delta t}{\alpha^2\Delta z^2}\right)u_i^{n+1}-\frac{\Delta t}{\alpha^2\Delta z^2}(u_{i+1}^{n+1}+u_{i-1}^{n+1})=\frac{\Delta t}{\alpha^2}e^{i\left(t^n+\frac{\pi}{2}\right)}+u_i^n, \tag{2.111}$$

the left hand side matrix of coefficients and right hand side vector, $\boldsymbol{Au}=\boldsymbol{b}$, can be constructed and solved at each time step to update the velocity. The left hand side matrix is the tri-diagonal $Z\times Z$ matrix

$$\boldsymbol{A}=\begin{pmatrix} 1 & 0 & 0 & \dots & \dots & \dots & 0 \\ C_w & C_0 & C_e & 0 & \dots & \dots & 0 \\ 0 & C_w & C_0 & C_e & 0 & \dots & 0 \\ \vdots & \ddots & \ddots & \ddots & \ddots & \ddots & \vdots \\ \vdots & & \ddots & \ddots & \ddots & \ddots & 0 \\ 0 & \dots & \dots & 0 & C_w & C_0 & C_e \\ 0 & \dots & \dots & \dots & 0 & 0 & 1 \end{pmatrix}, \tag{2.112}$$

where $C_w=C_e=-r_z/\Delta z$ and $C_0=1+2r_z/\Delta z$, for $r_z=\Delta t/(\alpha^2\Delta z)$ and the first and last rows enforce the boundary conditions. The right hand side vector entries are $b_i^n=u_i^n+e^{i\left(t^n+\frac{\pi}{2}\right)}\Delta t/\alpha^2$, where $b_1^n=b_Z^n=0$ are set to satisfy the boundary conditions. The matrix equation is solved at each time step using backslash in Matlab where the fluid is assumed to be initially at rest.

For the suspension model, a similar approach is taken. Due to the extra complexity, an upwind discretisation is needed to adequately account for single derivatives. Equation

(2.34) becomes,

$$\alpha^2 \frac{u_i^{n+1} - u_i^n}{\Delta t} = e^{i\left(t^n + \frac{\pi}{2}\right)} + \hat{\alpha}_i^{n+1} + A_i^{n+1} \frac{u_{i+1}^{n+1} - 2u_i^{n+1} + u_{i-1}^{n+1}}{\Delta z^2} + \begin{cases} dA_i^{n+1} \frac{u_i^{n+1} - u_{i-1}^{n+1}}{\Delta z} & \text{when} \quad dA_i^{n+1} \geq 0 \\ \\ dA_i^{n+1} \frac{u_{i+1}^{n+1} - u_i^{n+1}}{\Delta z} & \text{when} \quad dA_i^{n+1} < 0 \end{cases}, \tag{2.113}$$

where

$$A(z,t) = 1 + 4\Phi \left[\alpha_2 \int_{-\pi}^{\pi} \int_0^{\pi} \sin^3\theta \cos^2\theta \cos^2\phi \, \psi \, \mathrm{d}\theta \, \mathrm{d}\phi + \frac{\alpha_3}{2} \int_{-\pi}^{\pi} \int_0^{\pi} (\sin^2\theta \cos^2\phi + \cos^2\theta) \psi \sin\theta \, \mathrm{d}\theta \, \mathrm{d}\phi + \frac{\alpha_4}{2} \right], \tag{2.114}$$

$$\hat{\alpha}(z,t) = \frac{2\Phi\alpha_r}{P_G} \int_{-\pi}^{\pi} \int_0^{\pi} \sin^2\theta \cos\theta \cos\phi \, \psi \, \mathrm{d}\theta \, \mathrm{d}\phi, \tag{2.115}$$

and $dA = \partial A / \partial z$ are known functions of z and t. The left hand side matrix is the tri-diagonal matrix (2.112), but the entries now vary depending on the sign of dA. When $dA_i^n \geq 0$,

$$C_w(i,n) = -r_z \left(\frac{A_i^n}{\Delta z} - dA_i^n \right), \tag{2.116}$$

$$C_0(i,n) = 1 + r_z \left(\frac{2A_i^n}{\Delta z} - dA_i^n \right), \tag{2.117}$$

$$C_e(i,n) = -\frac{r_z}{\Delta z} A_i^n, \tag{2.118}$$

and when $dA_i^n < 0$

$$C_w(i,n) = -\frac{r_z}{\Delta z} A_i^n, \tag{2.119}$$

$$C_0(i,n) = 1 + r_z \left(\frac{2A_i^n}{\Delta z} + dA_i^n \right), \tag{2.120}$$

$$C_e(i,n) = -r_z \left(\frac{A_i^n}{\Delta z} + dA_i^n \right). \tag{2.121}$$

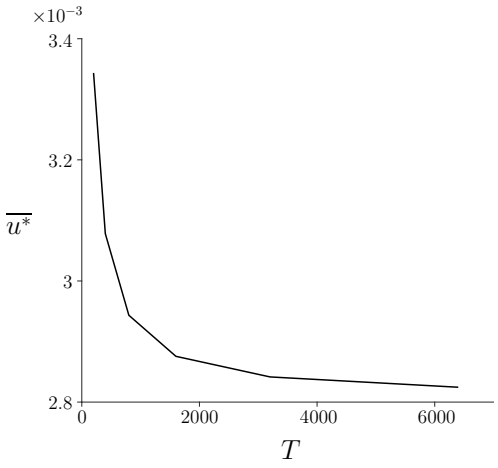

Figure 2.18: Convergence of the finite difference method with increasing time steps T. The number of steps for z has been set as $Z = 150$. Convergence to 0.01% of the value of $\overline{u^*}$ was achieved for $T = 3200$.

These values are stored in a $Z \times T$ matrix and, at each point in time, the associated vectors are chosen from $\boldsymbol{C_w}$, $\boldsymbol{C_0}$ and $\boldsymbol{C_e}$ to form the entries of the tri-diagonal matrix. The right hand side vector is now given by $b_i^n = u_i^n + e^{i\left(t^n + \frac{\pi}{2}\right)} \Delta t/\alpha^2 + \hat{\alpha}_i^n \Delta t/\alpha^2$, with equivalent boundary conditions. The solution method for the Newtonian problem is repeated here.

Numerical convergence

We consider the convergence of the numerical methods to optimise the computational efficiency and accuracy. The convergence of the spherical harmonic scheme is unchanged from the steady case, *i.e.* $N = 10$, and the step size for z^* is kept as $Z = 150$. Figure 2.18 shows how the time and spatially averaged velocity changes with increasing time step and shows convergence to within 0.01% at $T = 3200$.

Results

We use the parameter values defined in table 2.1 and $\alpha^2 \approx 18.95$ for $\omega^* = 200$ rad/s. Results for velocity, orientation parameter and linear dichroism signal are explored for a range of particle number density, inlet pressure gradient, oscillating frequency and channel depth. Again, spatial and temporal averages, averaging over one half of a time period,

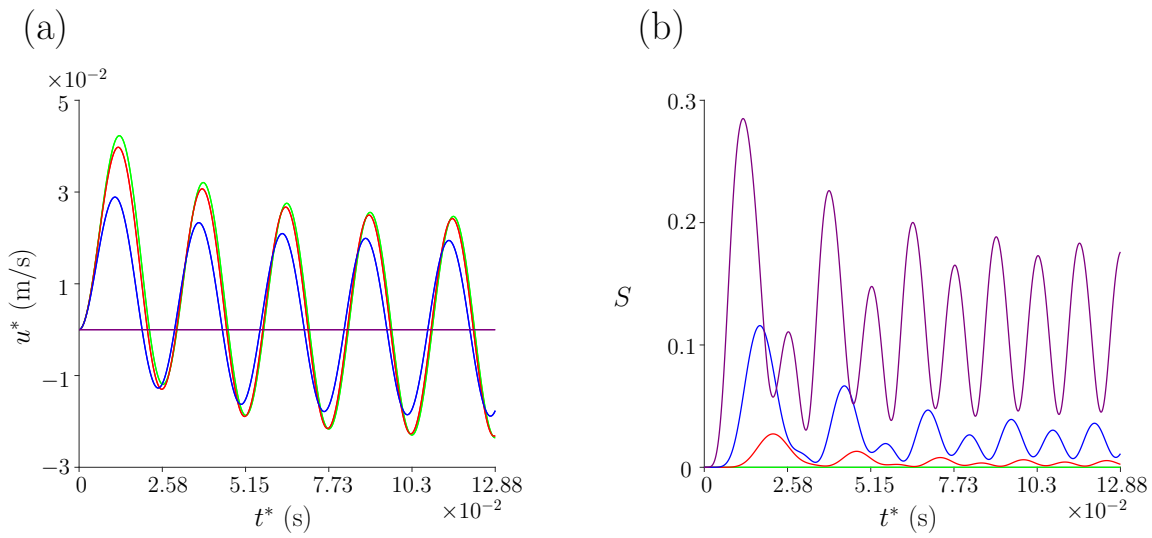

Figure 2.19: Velocity and orientation parameter over five oscillations. (a) Velocity profile and (b) orientation parameter. Four different z^* values are presented: $z^* = 0$ m (green line), $z^* = 1 \times 10^{-4}$ m (red line), $z^* = 2 \times 10^{-3}$ m (blue line) and $z^* = 3 \times 10^{-3}$ m (purple line).

and the peak values over a time period are considered. The results for $\overline{S}_{peak}$ and $\overline{LD}_{peak}$ have been presented in appendix A.1.

First, figure 2.19 depicts the results for velocity and orientation parameter, calculated using the values provided by Linear Diagnostics Ltd. Since the system starts from rest, five oscillations are plotted to understand how these profiles develop. The velocity profile is shown in figure 2.19a, for a range of z^* values. Close to the walls the velocity is zero, and increases sharply towards the centre of the channel. We see that as the oscillations develop the velocity moves to oscillate about $u^* = 0$. Figure 2.19b depicts the orientation parameter, varying with time over five oscillations, for a range of z^* values in the top half of the channel. It appears to take the form of two Fourier modes, and as we move closer to the channel walls the shear rate, and hence the orientation parameter, increases. To check when the results become pseudo-steady, i.e. the results no longer vary between oscillations, the orientation parameter and velocity, averaged over space, were compared in successive time periods. We find the difference between the seventh and eighth oscillations to be small enough that convergence has been achieved. Continuing from this, all time

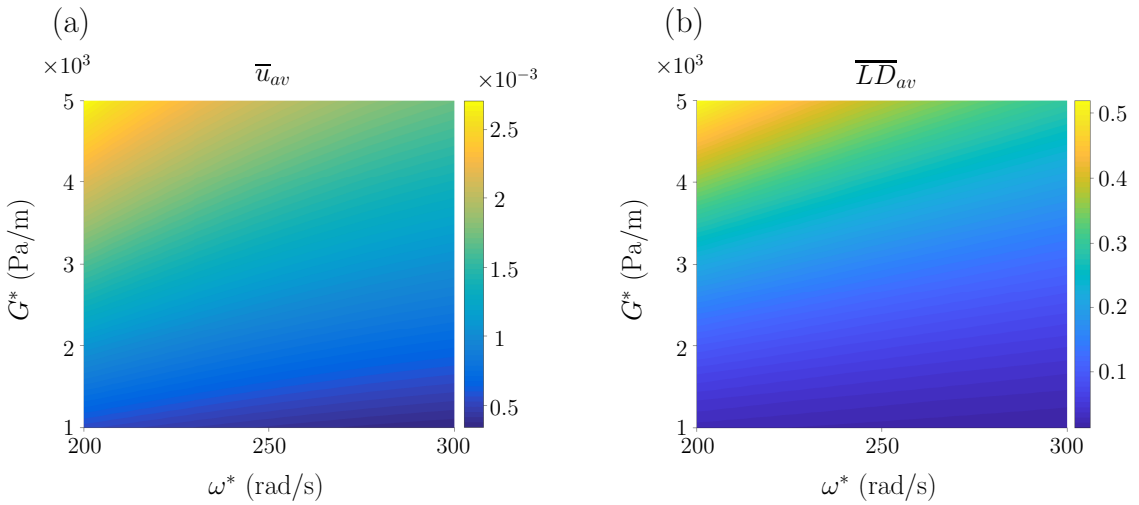

Figure 2.20: Velocity, averaged over space and time, and linear dichroism signal, averaged over time, for a range of inlet pressure gradient and oscillating frequency. (a) $\overline{u^*}_{av}$ and (b) $\overline{LD}_{av}$. The channel depth and number density remain the same, $h^* = 3 \times 10^{-4}$ m and $n_d^* = 7.33 \times 10^{17}$ phage/m^3 respectively.

averages are taken in the eighth oscillation to describe the long-time behaviour of the results.

Next, the velocity profile and expected linear dichroism signal are compared for a range of pressure gradient and oscillating frequency (figure 2.20). As the oscillating frequency increases, the absolute value of the velocity decreases (figure 2.20a), in turn decreasing the linear dichroism signal (figure 2.20b). In contrast, increasing the pressure gradient increases both the velocity and signal at approximately the same rate. The peak linear dichroism signal over an oscillation has been plotted for a range of oscillating frequency and pressure gradient (figure A.1) and, as seen in section 2.3.2, the peak values are larger in general than the corresponding averages.

Based on the results in section 2.3, we investigate how the relationship between $\overline{S}_{av}$ and channel depth changes as oscillating effects begin to dominate the flow (figure 2.21). Firstly, $\overline{S}_{av}$ is plotted as the channel depth increases for a number of oscillating frequencies (figure 2.21a). We find that as the oscillating frequency increases, the dependence reverses; for small ω^*, the orientation increases as the channel depth increases, whereas when $\omega^* > 30$ rad/s the relationship swaps and h^* also has a diminished impact. This is highlighted by figure 2.21b, where $\overline{S}_{av}$ is plotted against ω^* for a range of h^* values.

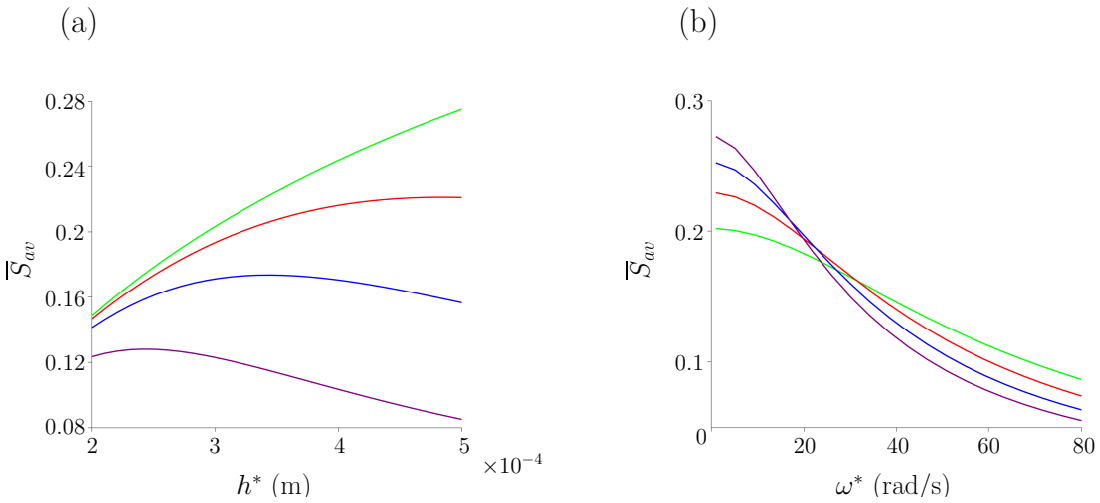

Figure 2.21: $\overline{S}_{av}$ changing with channel depth and oscillating frequency. (a) $\overline{S}_{av}$ changing with channel width for multiple oscillating frequencies: $\omega^* = 1$ rad/s (green line), $\omega^* = 10$ rad/s (red line), $\omega^* = 20$ rad/s (blue line) and $\omega^* = 40$ rad/s (purple line). (b) $\overline{S}_{av}$ changing with oscillating frequency for multiple h^* values: $h^* = 2.5 \times 10^{-4}$ m (green line), $h^* = 3 \times 10^{-4}$ m (red line), $h^* = 3.5 \times 10^{-4}$ m (blue line), $h^* = 4 \times 10^{-4}$ m (purple line). The pressure gradient is $G^* = 4.4 \times 10^3$ Pa/m and the number density is $n_d^* = 7.33 \times 10^{17}$ phage/m^3 throughout.

Finally we investigate how the orientation parameter and expected linear dichroism signal change with number density and channel depth (figure 2.22), for small and large oscillating frequencies. When ω^* is small (figure 2.22a and b) increasing the channel depth increases the orientation parameter, with the number density forcing a small decrease; increasing number density has a much larger impact to increase the signal. However, when $\omega^* = 200$ rad/s (figure 2.22c and d), the relationship switches so that increasing the channel width decreases both the orientation parameter and linear dichroism signal, agreeing with the results in the previous section (figure 2.16). For comparison, the same results plotted with the peak orientation parameter and linear dichroism signal ($\overline{S}_{peak}$ and $\overline{LD}_{peak}$ respectively) in figure A.3; these results are larger in comparison to the equivalent plot in figure 2.22.

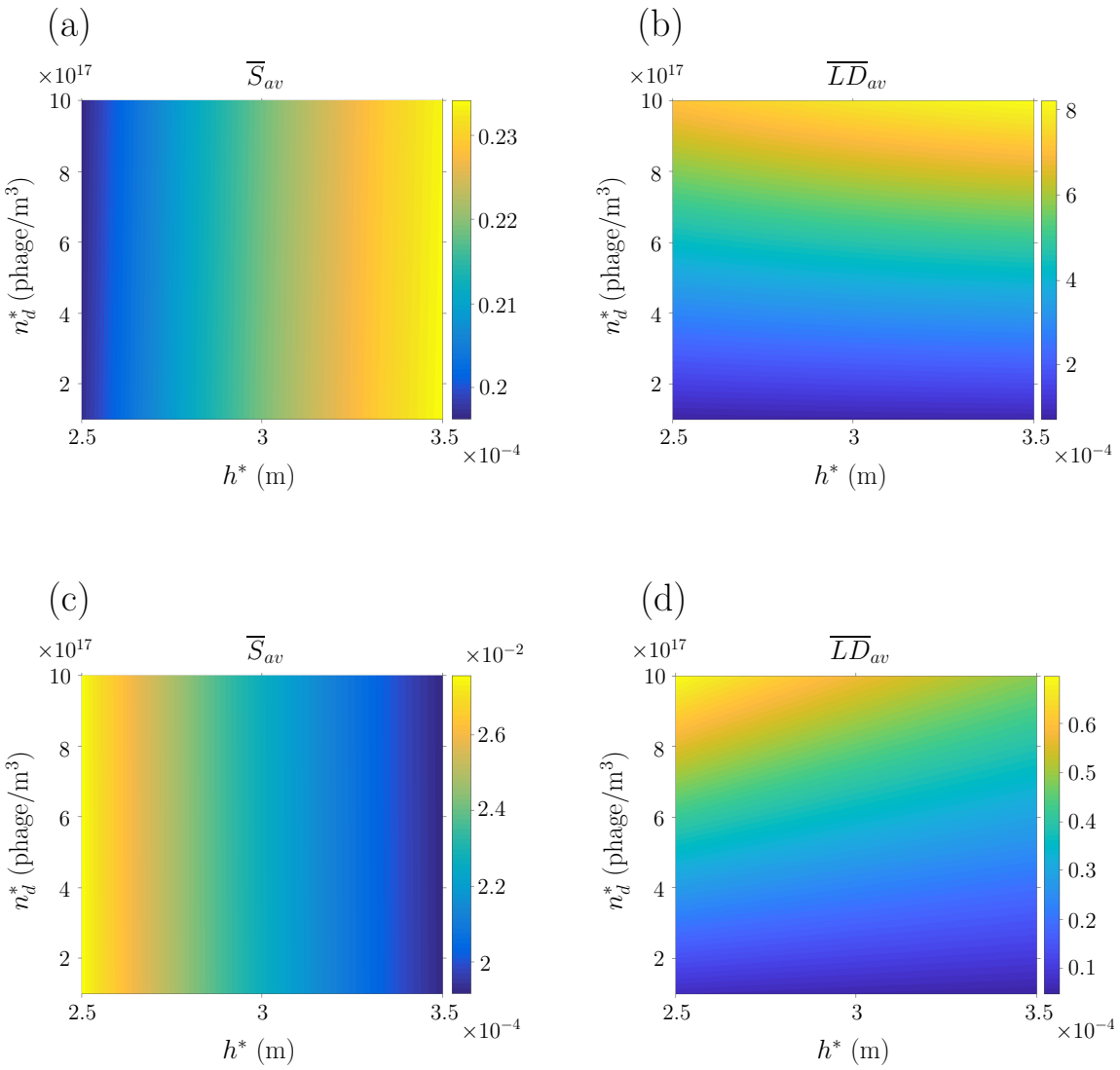

Figure 2.22: Orientation parameter and linear dichroism signal for a range of particle number density and channel depth. (a) and (c) $\overline{S}_{av}$ and (b) and (d) $\overline{LD}_{av}$. The pressure gradient is $G^* = 4.4 \times 10^3$ Pa/m and the oscillating frequency is $\omega^* = 10$ rad/s for (a) and (b) and $\omega^* = 200$ rad/s for (c) and (d).

2.5 Discussion

A suspension of bacteriophage in a thin rectangular channel has been modelled by coupling the flow equations to an equation describing the distribution of bacteriophage orientation. The bacteriophage were initially able to rotate in 2D, where lubrication theory, a perturbation expansion and numerical methods have been used to approximate the flow. Steady and oscillatory flows have been considered, introducing a perturbation expansion in the particle volume fraction for oscillatory flow. This was then extended so the bacteriophage had a full range of rotation described by the 3D Fokker-Planck equation; spherical harmonics were utilised to obtain a solution for the distribution of fibre orientation. The steady flow profile was solved semi-analytically and the oscillating flow used a fully numerical finite difference approach. The velocity, orientation parameter and linear dichroism signal are compared for a range of pressure gradient, oscillating frequency, channel depth and number density. Results have been plotted in dimensional quantities where possible.

The steady flow profile shows only a small deviation from the Newtonian case. When the velocity reaches its maximum at the centre of the channel, the shear rate is zero, and so we have zero alignment. This also increases, along with the shear rate, close to the channel walls, as seen throughout the results. The bacteriophage prefer to align in the flow direction due to the induced shear rate, represented by the peak in the probability density function value close to $\phi = 0$. Increasing the particle number density slightly decreases the velocity, due to an enhanced apparent viscosity, and finally, increasing the pressure gradient increases the velocity as expected, since the force on the fluid is greater.

The orientation parameter mainly displays comparable results; however no changes result from varying the number density. Particle-particle interactions are neglected in this study and so changing the number of particles should not change their alignment more than a slight reduction in the shear rate. An increase in the pressure gradient increases the Peclet number $P_\lambda = \dot{\gamma}^*/D_r^*$, and so flow effects dominate diffusive effects to increase the degree of orientation. Increasing the depth of the channel increases the shear rate produced (the shear rate $\dot{\gamma}^* = \partial u^*/\partial z^*$ scales as $G^* h^*/\mu^*$) which in turn increases

the orientation parameter. To maintain the pressure gradient in a larger channel, the flow rate must increase, leading to a larger shear rate and alignment.

The impact of number density on linear dichroism signal is more striking than the other parameters; increasing the number density decisively increases the signal. Having a greater number of particles in a sample means that a larger number will be aligned, even though the proportion which aligns is unchanged; this increases the absorption of light and the signal produced. The signal exhibits the same characteristics as the orientation parameter when the channel depth and pressure gradient are varied.

For the oscillatory case, increasing the oscillating frequency decreases the magnitude of all results. The oscillating frequency describes how quickly the flow direction changes, increasing this means the fibres are forced to change direction quicker and hence do not achieve as large a velocity or alignment. Since the variation from the Newtonian flow is small for varying number density, this reinforced the approach of a perturbation expansion in the volume fraction. However, when incorporating 3D rotation, this expansion was not used. Here, the flow takes a while to settle into a pseudo-steady state; the initial oscillation causes unrest in the system which takes time to dampen. When the oscillations are slow, all results in the steady case are mirrored by the oscillating flow results. However, when the oscillations become more rapid, the relationship between orientation parameter and channel depth reverses, a result mirrored by the linear dichroism signal. The inertial effects are dominating the orientation when ω^* is large. For slow oscillations ($\omega^* \approx 10$ rad/s), the spatially averaged orientation parameter does not differ much from that produced in steady flow ($\overline{S}_{av} \approx 0.1 - 0.2$ for oscillating and $S \approx 0.3$ for steady). The oscillating system may be practical if the oscillations are slow; the orientation rapidly decreases as the oscillations increase, reducing the signal comparative to steady flow.

To further predict the feasibility of the oscillating system, the time-averaged orientation parameter and linear dichroism signal were compared with the peak over an oscillation. In general the peak values were larger than the time-averaged values, an unsurprising result given the oscillating nature of the flow. If the light absorption can be measured at

quick enough speeds, it would be possible to detect the maximum signal, resulting in a larger signal than would be acquired by averaging over multiple time steps.

In general, the results presented from the 2D Fokker-Planck equation agreed with those for the 3D equation, though the magnitude of the results was reduced for 3D rotations. This agreement is mirrored by the comparison between 2D and 3D FENE models for suspensions of dumbbells [10]. For 3D tumbling, a lower degree of alignment is seen in general as the fibres may be rotating out of the plane in which the signal is taken; since this is not taken into account in the 2D model, it is beneficial to consider the full Fokker-Planck equation, even with the simplification of $\alpha_0 = 1$ ($\alpha_0 \approx 0.9999$ for M13 bacteriophage). The 3D model predicts a maximum degree of orientation of $\overline{S} \approx 0.74$, corresponding to a channel depth around $h^* \approx 4 \times 10^{-3}$ m and pressure gradient around $G^* \approx 5 \times 10^4$ Pa/m; increasing the values above this would have no benefit to the system. Further, as h^* becomes larger, the possibility of light scattering and hence signal noise increases. We have shown that the orientation parameter used in [68] does not capture all features of the orientation of the system, as it would for flat membranes where the distribution is dependent on fibre movements in one plane only.

We predict that an increase in the pressure gradient will increase the signal produced in general. Further, we believe a deeper channel may result in a stronger signal for steady flow; an increased number of phage are between the light source and the detector, allowing for more absorption. We also predict that increasing the number density of the phage would increase the apparent viscosity of the fluid-phage composite, in turn reducing the velocity, with the impact on the signal to be determined. Finally, increasing the oscillating frequency is creating more disturbances in the channel and hence would reduce the overall signal produced. This work provides a platform to consider flow through a thin 3D channel, enabling a more accurate prediction of the flow profile and degree of orientation. The flow channel of interest is a thin rectangular channel, the width and depth of the channel are comparable and so all their contributions should be included. The solutions obtained could also be used to predict orientation speeds of bacteriophage

at different inlet pressure gradients or an investigation into the collective behaviour of these fibres in flow. Experimentally verifying the maximum degree of alignment would be of interest, along with comparing alignment in different flow set-ups with our predictions. A peristaltic pumping mechanism may be of interest to recirculate the sample, as an alternative to an oscillating pump. Finally, a consideration for light scattering must be made; a higher proportion of phage may increase the noise and hence decrease the signal.

2.6 Summary

The key findings in this chapter are summarised here:

- Oscillating flow achieves weaker but still useful alignment for slow oscillations, increasing the oscillating frequency further reduces the alignment.
- For steady flow, the model predicts a maximum achievable degree of orientation $\overline{S} \approx 0.74$.
- Increasing the channel width and pressure gradient increases the orientation in steady flow and for slow oscillations.
- Oscillating flow will optimise differently, the orientation has a non-monotonic response to h^*, depending on the size of ω^*.
- The peak orientation parameter and linear dichrosim signal over one oscillation is larger in general than the time averaged version; rapid signal detection may provide a larger signal as opposed to averaging multiple measurements.
- Incorporating 3D rotations slightly decreased the degree of orientation due to particles rotating out of plane, however the results in general displayed the same behaviour.

In the following chapter, a full 3D channel is coupled with the 3D Fokker-Planck equation.

CHAPTER 3

PREDICTING ORIENTATION AND LINEAR DICHROISM SIGNAL OF SUSPENSIONS: FLOW IN 3D RECTANGULAR CHANNELS

This chapter extends the work in chapter 2 to solve the coupled problem for a full 3D channel. The 3D flow equations are coupled with a 3D Fokker-Planck equation to predict alignment and signal in thin rectangular channels. As before, this is relevant to the industrial problem associated with Linear Diagnostics Ltd.

3.1 Introduction

The shear-induced orientation of a suspension of passive bacteriophage is considered for thin 3D rectangular channels in this chapter. Linear Diagnostics Ltd aim to optimise the signal to noise ratio produced by the alignment of bacteriophage suspensions in these thin rectangular channels. Currently, the fluid is recirculated either by a pump or via the peristaltic motion of a section of the channel. In comparison with chapter 2, where flow through a thin channel bound by two walls is modelled, we investigate flows of suspensions in thin rectangular channels where only the flow direction is assumed infinite. Previous work into 3D suspensions has included modelling pulp fibres in 3D turbulent flow [17] and 3D FENE models of dumbbell suspensions [10]; these works consider an imposed flow and calculate the impact on the particles. Here we iteratively couple the fluid and

particle equations which has been done for 2D suspensions in [12] and where all stress terms associated with particle suspensions are included in chapter 2.

The 3D flow channel in this chapter introduces a degree of mathematical complexity; the problem is now dealt with numerically, using either a finite difference approximation or an alternating direction implicit (ADI) method for time-dependent flows. The enhancement to the stress tensor, described by Pedley & Kessler [76], is again used here and the Fokker-Planck equation is used to determine the degree of orientation in the system. We use spherical harmonics to solve the Fokker-Planck equation, following the method of [68, 87], and couple the flow and orientation distribution equations iteratively for both steady and oscillatory flows. This study is the first to solve the coupled flow and distribution equations for a suspension of elongated particles in 3D channel flow.

The chapter is organised as follows: the Navier-Stokes and Fokker-Planck equations, along with all related equations, are summarised in section 3.2. The steady problem is discussed in section 3.3; the numerical solution for 3D Newtonian flow and for a fibre suspension are presented and results are displayed for a range of parameter values. The theoretical oscillatory problem is then presented in section 3.4, where an ADI method is utilised to solve the flow problem. Finally, results are discussed and compared with chapter 2 in section 3.5.

3.2 Summary of equations governing fibrous fluids

A summary of the equations discussed in chapter 1 are given here. The dimensional Navier-Stokes and incompressibility equations are

$$\rho^* \left(\frac{\partial \boldsymbol{u}^*}{\partial t^*} + (\boldsymbol{u}^* \cdot \nabla^*)\boldsymbol{u}^* \right) = \nabla^* \cdot \boldsymbol{\sigma}^*, \tag{3.1}$$

$$\nabla^* \cdot \boldsymbol{u}^* = 0, \tag{3.2}$$

where ρ^* is density, $\boldsymbol{u}^*(\boldsymbol{x}^*, t^*)$ is the velocity vector for spatial coordinate $\boldsymbol{x}^*$ and time t^*, $\boldsymbol{\sigma}^*$ is the stress tensor and ∇^* is differentiation in Cartesian space. The asterisk notation represents dimensional variables.

To determine the bulk stresses in the fluid due to the particles, we define a probability density function $\psi(\theta, \phi, \boldsymbol{x}^*, t^*)$ satisfying the Fokker-Planck equation [68],

$$\frac{\partial \psi}{\partial t^*} + \nabla_{\boldsymbol{p}} \cdot (\boldsymbol{\Omega}^* \psi) = D_r^* \nabla_{\boldsymbol{p}}^2 \psi, \tag{3.3}$$

where $\boldsymbol{p}$ is the unit orientation vector, $\nabla_{\boldsymbol{p}}$ represents differentiation in $\boldsymbol{p}$-space and D_r^* is the rotational diffusion constant. The evolution of director $\boldsymbol{p}$ is given by

$$\boldsymbol{\Omega}^* = (\boldsymbol{I} - \boldsymbol{pp}) \cdot (\alpha_0 \boldsymbol{e}^* + \boldsymbol{\omega}^*) \cdot \boldsymbol{p}, \tag{3.4}$$

where $\boldsymbol{e}^* = (\nabla^* \boldsymbol{u}^* + \nabla^* \boldsymbol{u}^{*T})/2$ is the rate of strain tensor, $\boldsymbol{\omega}^* = (\nabla^* \boldsymbol{u}^* - \nabla^* \boldsymbol{u}^{*T})/2$ is the vorticity tensor and $\alpha_0 = (r^2 - 1)/(r^2 + 1)$ describes how slender the body is [39]. The distribution function has two conditions, periodicity and the normalisation condition,

$$\int_s \psi d\boldsymbol{p} = 1, \tag{3.5}$$

where s is the unit surface of a sphere.

Following Pedley & Kessler [76], the enhanced stress tensor for a suspension of particles is

$$\boldsymbol{\sigma}^* = \boldsymbol{\sigma}_I^* + \boldsymbol{\sigma}_D^* + \boldsymbol{\sigma}_P^*, \tag{3.6}$$

where the Newtonian contribution is

$$\boldsymbol{\sigma}_I^* = -P^* \boldsymbol{I} + 2\mu^* \boldsymbol{e}^*, \tag{3.7}$$

for pressure P^*, identity matrix $\boldsymbol{I}$ and viscosity μ^*. Here, $\boldsymbol{\sigma}_D^*$ is the extra stress due to particle rotation and $\boldsymbol{\sigma}_P^*$ represents the interaction of the particles with the fluid, given

by

$$\boldsymbol{\sigma}_D^* = 2\mu^*\Phi D_r^*\alpha_r \int_s \left(\boldsymbol{pp} - \frac{\boldsymbol{I}}{3}\right)\psi \,\mathrm{d}\boldsymbol{p}, \tag{3.8}$$

$$\begin{aligned}\boldsymbol{\sigma}_P^* = 4\,\mu^*\,\Phi\Bigg[\alpha_2\,\boldsymbol{e}^* : \int_s \boldsymbol{p}\,\boldsymbol{p}\,\boldsymbol{p}\,\boldsymbol{p}\,\psi\,\mathrm{d}\mathbf{p} + \alpha_3\left(\boldsymbol{e}^*\cdot\int_s \boldsymbol{p}\,\boldsymbol{p}\,\psi\,\mathrm{d}\boldsymbol{p} + \int_s \boldsymbol{p}\,\boldsymbol{p}\,\psi\,\mathrm{d}\boldsymbol{p}\cdot\boldsymbol{e}^*\right)\\ + \alpha_4\,\boldsymbol{e}^*\int_s \psi\,\mathrm{d}\boldsymbol{p} + \alpha_5\,\boldsymbol{I}\,\boldsymbol{e}^* : \int_s \boldsymbol{p}\,\boldsymbol{p}\,\psi\,\mathrm{d}\boldsymbol{p}\Bigg],\end{aligned} \tag{3.9}$$

where Φ is the volume fraction and α_i ($i = 2\ldots5,\ r$) are constants related to the aspect ratio of the particle. A term accounting for the self-motile behaviour of a suspension can also be defined (equation (1.11) in chapter 1), however in the present study the elongated fibres are taken to be passive M13 bacteriophage and so this term is neglected. Each parameter ($\alpha_i,\ i = 2,\ldots,5,\ \alpha_r$) can be represented in terms of ellipsoidal integrals [2, 44], which are detailed in equations (1.12)-(1.16) in chapter 1.

Finally, the degree of orientation of a system can be described by an orientation parameter, S, calculated as

$$\begin{aligned}S &= \langle p_{x^*}^2\rangle - \langle p_{y^*}^2\rangle,\\ &= \langle \sin^2\theta\cos^2\phi\rangle - \langle \sin^2\theta\sin^2\phi\rangle.\end{aligned} \tag{3.10}$$

It is assumed that x^* is the macroscopic orientation axis, or flow direction, and the linear dichroism light source is directed down through the channel; thus the polarisation is parallel and perpendicular to the x^*–direction and lies in the x^*–y^* plane (figure 3.1a). A distribution of the fibre orientation is expected and their orientation can be described by orientation angles away from the coordinate axis, shown in figure 3.1b.

3.3 Steady flow

Consider a 3D rectangular channel of width $2W^*$, depth $2h^*$ and length scale L^*, where $h^*,\ W^* \ll L^*$. The axis origin is at the centre of the channel and it is assumed that the

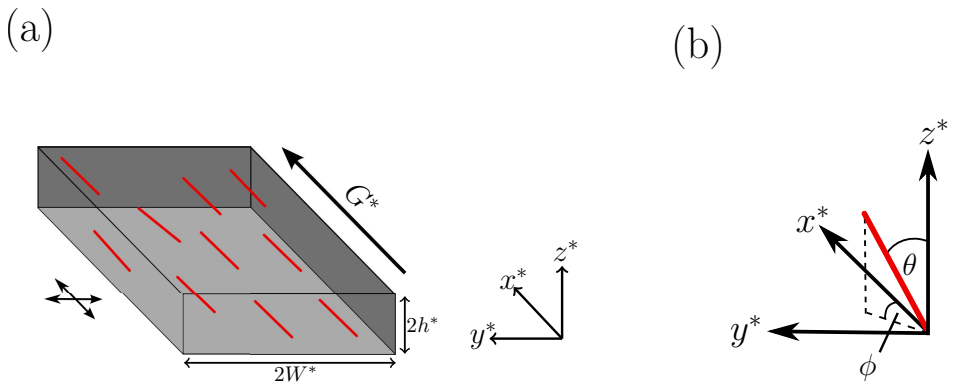

Figure 3.1: Schematic of the flow of a fibre-laden fluid, with a distribution of orientation, in a thin rectangular channel. (a) Rectangular channel of width $2W^*$ and depth $2h^*$ and the x^*–axis is the molecular orientation axis. The linear dichroism signal compares absorption of light parallel and perpendicular to the flow direction, highlighted by the arrows to the left of the channel. (b) The orientation angles $\theta \in [0, \pi]$ and $\phi \in [0, 2\pi)$ away from the coordinate axis describe the orientation of the fibres.

flow direction induced by a constant pressure gradient, or molecular orientation axis, is the x^*-direction (figure 3.1a). The boundary conditions are given by no slip at the walls,

$$\begin{aligned} u^*(x^*, -W^*, z^*) = u^*(x^*, W^*, z^*) = 0, \qquad & u^*(x^*, y^*, -h^*) = u^*(x^*, y^*, h^*) = 0, \\ v^*(x^*, -W^*, z^*) = v^*(x^*, W^*, z^*) = 0, \qquad & v^*(x^*, y^*, -h^*) = v^*(x^*, y^*, h^*) = 0, \\ w^*(x^*, -W^*, z^*) = w^*(x^*, W^*, z^*) = 0, \qquad & w^*(x^*, y^*, -h^*) = w^*(x^*, y^*, h^*) = 0. \end{aligned} \tag{3.11}$$

Since the width and depth of the channel are comparable and much smaller than the length scale, we use a lubrication approximation, by introducing the dimensionless parameter $\delta = h^*/L^* \ll 1$ to allow in depth analysis of the significant hydrodynamic interactions.

The problem is solved using an iterative approach, initially taking the Newtonian flow profile and using this to calculate the orientation distribution. After this, the moments of ψ can be calculated and used to solve the Navier-Stokes equations with extra stress terms; the above process is repeated until convergence is achieved. We begin by discussing the solution to the Fokker-Planck equation.

3.3.1 Calculating the orientation distribution function

With a known velocity, initially the Newtonian solution, the orientation distribution of the bacteriophage can be calculated by considering each point in the cross-section of the channel; the particles in the flow are small enough that each particle at a point in space will experience an approximately linear flow, and hence a constant shear rate $\dot{\gamma}^*$. This method follows exactly from Chapter 2 and is summarised here.

To investigate 3D orientation of bacteriophage, first express the unit orientation vector $\boldsymbol{p}$ as

$$\boldsymbol{p} = (\sin\theta\cos\phi, \sin\theta\sin\phi, \cos\theta), \tag{3.12}$$

for $\theta \in [0, \pi]$ and $\phi \in [0, 2\pi)$, angles away from the coordinate axis (figure 3.1b). Following [5, 87], assuming $\alpha_0 = 1$ and investigating steady state behaviour, the Fokker-Planck equation reduces to

$$\frac{1}{6}\Lambda(\psi) = P_\lambda \Omega(\psi), \tag{3.13}$$

where $P_\lambda = \dot{\gamma}^*/6D_r^*$ is the Peclet number and

$$\Lambda(\psi) = \frac{1}{\sin\theta}\frac{\partial}{\partial\theta}\left(\sin\theta\frac{\partial\psi}{\partial\theta}\right) + \frac{1}{\sin^2\theta}\frac{\partial^2\psi}{\partial\phi^2}, \tag{3.14}$$

$$\Omega(\psi) = \frac{\sin\phi\cos\phi}{\sin\theta}\frac{\partial}{\partial\theta}\left(\sin^2\theta\cos\theta\,\psi\right) - \frac{\partial}{\partial\phi}\left(\sin^2\phi\,\psi\right). \tag{3.15}$$

The Fokker-Planck equation (3.13) is spatially discretised via Spherical Harmonics [5, 68, 87]. Assume the solution takes the form

$$\psi(\theta,\phi) = \sum_{n=0}^{N}\sum_{m=0}^{n}\left(A^m_{0\,n}P^m_n(\cos\theta)\cos(m\phi) + A^m_{1\,n}P^m_n(\cos\theta)\sin(m\phi)\right), \tag{3.16}$$

where P^m_n are the associated Legendre polynomials. By substituting (3.16) into equation

(3.13), Γ and Ω are given by

$$\Lambda(P_n^m(\cos\theta)\cos(m\phi)) = -n(n+1)P_n^m(\cos\theta)\cos(m\phi), \tag{3.17}$$

$$\Lambda(P_n^m(\cos\theta)\sin(m\phi)) = -n(n+1)P_n^m(\cos\theta)\sin(m\phi), \tag{3.18}$$

$$\Omega(P_n^m(\cos\theta)\cos(m\phi)) = -\sum_{p=m-2}^{m+2}\sum_{q=n-2}^{n+2} a_{n,q}^{m,p} P_n^m(\cos\theta)\sin(m\phi), \quad m \geq 0, \tag{3.19}$$

$$\Omega(P_n^m(\cos\theta)\sin(m\phi)) = \sum_{p=m-2}^{m+2}\sum_{q=n-2}^{n+2} a_{n,q}^{m,p} P_n^m(\cos\theta)\cos(m\phi), \quad m > 0. \tag{3.20}$$

The first two results stem from the definition of a spherical harmonic, *i.e.* the solution to the spherical part of Laplace's equation on a sphere; the other two are a linear combination of spherical harmonics where there are seven non-zero constants $a_{n,q}^{m,p}$, reproduced from [5, 87] and given in section 2.4 of chapter 2. The resulting system of equations for $A_{0\,n}^m$ and $A_{1\,n}^m$, found by equating coefficients of sine and cosine, are

$$\frac{q(q+1)}{6} A_{0\,q}^p = -P_\lambda \sum_{n=0}^{N}\sum_{m=0}^{n} a_{n,q}^{m,p} A_{1\,n}^m, \tag{3.21}$$

$$\frac{q(q+1)}{6} A_{1\,q}^p = P_\lambda \sum_{n=0}^{N}\sum_{m=0}^{n} a_{n,q}^{m,p} A_{0\,n}^m, \tag{3.22}$$

for integer N, $q = 0, 2, \ldots, N$ and $p = 0, 2, \ldots, n$. Here, $A_{0\,0}^0 = 1/4\pi$ to satisfy the normalisation condition, and we have $A_{1\,n}^0 = 0$ for all n. Due to particle symmetry, if n or m are odd then $A_{0\,n}^m = A_{1\,n}^m = 0$.

Equations (3.21) and (3.22) are solved numerically by setting up a matrix of equations and using the direct solver backslash in Matlab. This method is detailed in section 2.4 of chapter 2 and so is not repeated here.

3.3.2 Calculating the flow profile

With a known orientation distribution $\psi(\theta, \phi, y^*, z^*)$, the extra stress terms in the Navier-Stokes equations, and hence the velocity, can be calculated. To begin with, the equations

are non-dimensionalised and a lubrication approximation is used to simplify the fluid equations. The matrix equation and numerical methods are discussed for Newtonian and fibre-laden flows.

Non-dimensionalisation

We scale equations (3.1) and (3.2) against the imposed pressure gradient G^* as follows,

$$\begin{gathered} u^* = \frac{G^* h^{*2}}{\mu^*} u, \quad v^* = \frac{\delta G^* h^{*2}}{\mu^*} v, \qquad w^* = \frac{\delta G^* h^{*2}}{\mu^*} w, \\ x^* = \frac{h^*}{\delta} x, \quad y^* = h^* y, \quad z^* = h^* z, \quad P^* = \frac{G^* h^*}{\delta} P. \end{gathered} \tag{3.23}$$

Upon scaling the system, neglecting terms $\mathcal{O}(\delta)$ and smaller, the continuity equation is unchanged and the Navier-Stokes equations reduce to

$$\begin{aligned} -1 = \frac{\partial}{\partial y} \Bigg(& \left\{ 1 + 4\Phi \left[\alpha_2 \int_{\boldsymbol{s}} p_1^2 p_2^2 \psi \, \mathrm{d}\boldsymbol{p} + \frac{\alpha_3}{2} \int_{\boldsymbol{s}} (p_1^2 + p_2^2) \psi \, \mathrm{d}\boldsymbol{p} + \frac{\alpha_4}{2} \right] \right\} \frac{\partial u}{\partial y} \\ & + 4\Phi \left[\alpha_2 \int_{\boldsymbol{s}} p_1^2 p_2 p_3 \psi \, \mathrm{d}\boldsymbol{p} + \frac{\alpha_3}{2} \int_{\boldsymbol{s}} p_2 p_3 \psi \, \mathrm{d}\boldsymbol{p} \right] \frac{\partial u}{\partial z} \Bigg) \\ + \frac{\partial}{\partial z} \Bigg(& \left\{ 1 + 4\Phi \left[\alpha_2 \int_{\boldsymbol{s}} p_1^2 p_3^2 \psi \, \mathrm{d}\boldsymbol{p} + \frac{\alpha_3}{2} \int_{\boldsymbol{s}} (p_1^2 + p_3^2) \psi \, \mathrm{d}\boldsymbol{p} + \frac{\alpha_4}{2} \right] \right\} \frac{\partial u}{\partial z} \\ & + 4\Phi \left[\alpha_2 \int_{\boldsymbol{s}} p_1^2 p_2 p_3 \psi \, \mathrm{d}\boldsymbol{p} + \frac{\alpha_3}{2} \int_{\boldsymbol{s}} p_2 p_3 \psi \, \mathrm{d}\boldsymbol{p} \right] \frac{\partial u}{\partial y} \Bigg) \\ + \frac{2\Phi\alpha_r}{P_G} & \left(\frac{\partial}{\partial y} \int_{\boldsymbol{s}} p_1 p_2 \psi \, \mathrm{d}\boldsymbol{p} + \frac{\partial}{\partial z} \int_{\boldsymbol{s}} p_1 p_3 \psi \, \mathrm{d}\boldsymbol{p} \right), \end{aligned} \tag{3.24}$$

where the y– and z–components of the dimensionless Navier-Stokes equations suggest $P = P(x)$ and so the pressure gradient reduces to -1. In comparison with chapter 2, the distribution is not necessarily symmetric in y and so all moments of ψ are retained. The boundary conditions are now given by

$$u(x, -\overline{W}, z) = u(x, \overline{W}, z) = 0, \qquad u(x, y, -1) = u(x, y, 1) = 0, \tag{3.25}$$

where $\overline{W} = W^*/h^*$. This is solved numerically using a finite difference scheme.

Numerical method

To solve the fluid problem we construct a matrix equation by employing a finite difference scheme to discretise spatial derivatives. We begin by solving the problem for steady Newtonian flow,

$$-1 = \frac{\partial^2 u}{\partial y^2} + \frac{\partial^2 u}{\partial z^2}\,. \tag{3.26}$$

The equation is discretised as

$$-1 = -2\left(\frac{1}{\Delta y^2} + \frac{1}{\Delta z^2}\right) u_{i,j} + \frac{1}{\Delta y^2}\left(u_{i+1,j} + u_{i-1,j}\right) + \frac{1}{\Delta z^2}\left(u_{i,j+1} + u_{i,j-1}\right), \tag{3.27}$$

for step sizes Δy and Δz and where $i = 1, 2, \ldots, Y$ represent spatial gridpoints in y and $j = 1, 2, \ldots Z$ represent gridpoints in z.

We express equation (3.27) in a matrix system $\boldsymbol{A}\boldsymbol{u} = \boldsymbol{b}$, where $\boldsymbol{u}$ is the vector

$$\boldsymbol{u} = (u_{1,1},\, u_{1,2},\, \ldots u_{1,Z},\, u_{2,1}, \ldots\, u_{i,j},\, \ldots\, u_{Y,1},\, \ldots u_{Y,Z})^T, \tag{3.28}$$

and by constructing a sparse $YZ \times YZ$ matrix,

$$\boldsymbol{A} = \begin{pmatrix} \boldsymbol{I} & \boldsymbol{0} & \boldsymbol{0} & \cdots & \cdots & \cdots & \boldsymbol{0} \\ \boldsymbol{B} & \boldsymbol{C} & \boldsymbol{B} & \boldsymbol{0} & \cdots & \cdots & \boldsymbol{0} \\ \boldsymbol{0} & \boldsymbol{B} & \boldsymbol{C} & \boldsymbol{B} & \boldsymbol{0} & & \vdots \\ \vdots & \ddots & \ddots & \ddots & \ddots & \ddots & \vdots \\ \vdots & & \ddots & \ddots & \ddots & \ddots & \boldsymbol{0} \\ \boldsymbol{0} & \cdots & \cdots & \boldsymbol{0} & \boldsymbol{B} & \boldsymbol{C} & \boldsymbol{B} \\ \boldsymbol{0} & \cdots & \cdots & \cdots & \boldsymbol{0} & \boldsymbol{0} & \boldsymbol{I} \end{pmatrix}. \tag{3.29}$$

Here, $\boldsymbol{B}$, $\boldsymbol{C}$, $\boldsymbol{I}$ and $\boldsymbol{0}$ are $Z \times Z$ matrices arranged in the $Y \times Y$ matrix (3.29); $\boldsymbol{I}$ is the

identity matrix, $\mathbf{0}$ is a matrix of zeros,

$$\boldsymbol{B} = \begin{pmatrix} 1 & 0 & 0 & \dots & \dots & 0 \\ 0 & r_y & 0 & \dots & \dots & 0 \\ \vdots & \ddots & \ddots & \ddots & & \vdots \\ \vdots & & \ddots & \ddots & \ddots & \vdots \\ 0 & & & 0 & r_y & 0 \\ 0 & \dots & \dots & 0 & 0 & 1 \end{pmatrix}, \tag{3.30}$$

where $r_y = 1/\Delta y^2$, and

$$\boldsymbol{C} = \begin{pmatrix} 1 & 0 & 0 & \dots & \dots & 0 \\ r_z & -2r & r_z & 0 & \dots & 0 \\ 0 & r_z & -2r & r_z & \ddots & \vdots \\ \vdots & \ddots & \ddots & \ddots & \ddots & 0 \\ 0 & \dots & 0 & r_z & -2r & r_z \\ 0 & \dots & \dots & 0 & 0 & 1 \end{pmatrix}, \tag{3.31}$$

for $r_z = 1/\Delta z^2$ and $r = \left(1/\Delta y^2 + 1/\Delta z^2\right)$. The right hand side vector consists of minus one entries, where the corresponding no-slip boundary conditions are set to zero, *i.e.* entries $i = 1, Y$ and $j = 1, Z$. This system is solved using the direct solver backslash in Matlab and the resulting vector is reshaped to obtain a $Y \times Z$ matrix for the velocity u. From here, the velocity is re-dimensionalised and the shear rate can be calculated at each point in y^* and z^* as

$$\dot{\gamma}^* = \sqrt{\left(\frac{\partial u^*}{\partial y^*}\right)^2 + \left(\frac{\partial u^*}{\partial z^*}\right)^2}. \tag{3.32}$$

Once the Newtonian profile has been established, the Fokker-Planck equation can be solved via the methods discussed in chapter 2 and briefly described in section 3.3. The resulting orientation distribution $\psi(\theta, \phi, y^*, z^*)$ and its moments are then used to solve

equation (3.24). Equation (3.24) is discretised using a finite difference scheme,

$$
\begin{aligned}
-1 - F_{i,j} = &\begin{cases} G_{i,j}\frac{u_{i,j}-u_{i-1,j}}{\Delta y} & \text{for } G_{i,j}\geq 0 \\ G_{i,j}\frac{u_{i+1,j}-u_{i,j}}{\Delta y} & \text{for } G_{i,j}<0 \end{cases} + \begin{cases} H_{i,j}\frac{u_{i,j}-u_{i,j-1}}{\Delta z} & \text{for } H_{i,j}\geq 0 \\ H_{i,j}\frac{u_{i,j+1}-u_{i,j}}{\Delta z} & \text{for } H_{i,j}<0 \end{cases} \\
&+ J_{i,j}\frac{u_{i+1,j}-2u_{i,j}+u_{i-1,j}}{\Delta y^2} + K_{i,j}\frac{u_{i,j+1}-2u_{i,j}+u_{i,j-1}}{\Delta z^2} \\
&+ L_{i,j}\frac{u_{i+1,j+1}-u_{i-1,j+1}-u_{i+1,j-1}+u_{i-1,j-1}}{4\Delta y \Delta z},
\end{aligned} \tag{3.33}
$$

where the second order derivatives are discretised via second order central differences, an upwind scheme has been used to treat first order derivatives and

$$
\boldsymbol{F} = \frac{2\Phi\alpha_r}{P_G}\left(\frac{\partial}{\partial y}\int_{\boldsymbol{s}} p_1 p_2 \psi \ \mathrm{d}\boldsymbol{p} + \frac{\partial}{\partial z}\int_{\boldsymbol{s}} p_1 p_3 \psi \ \mathrm{d}\boldsymbol{p}\right), \tag{3.34}
$$

$$
\begin{aligned}
\boldsymbol{G} = &\ 4\Phi\frac{\partial}{\partial y}\left\{\alpha_2\int_{\boldsymbol{s}} p_1^2 p_2^2 \psi \ \mathrm{d}\boldsymbol{p} + \frac{\alpha_3}{2}\int_{\boldsymbol{s}}(p_1^2+p_2^2)\psi \ \mathrm{d}\boldsymbol{p}\right\} \\
&+ 4\Phi\frac{\partial}{\partial z}\left\{\alpha_2\int_{\boldsymbol{s}} p_1^2 p_2 p_3 \psi \ \mathrm{d}\boldsymbol{p} + \frac{\alpha_3}{2}\int_{\boldsymbol{s}} p_2 p_3 \psi \ \mathrm{d}\boldsymbol{p}\right\},
\end{aligned} \tag{3.35}
$$

$$
\begin{aligned}
\boldsymbol{H} = &\ 4\Phi\frac{\partial}{\partial z}\left\{\alpha_2\int_{\boldsymbol{s}} p_1^2 p_3^2 \psi \ \mathrm{d}\boldsymbol{p} + \frac{\alpha_3}{2}\int_{\boldsymbol{s}}(p_1^2+p_3^2)\psi \ \mathrm{d}\boldsymbol{p}\right\} \\
&+ 4\Phi\frac{\partial}{\partial y}\left\{\alpha_2\int_{\boldsymbol{s}} p_1^2 p_2 p_3 \psi \ \mathrm{d}\boldsymbol{p} + \frac{\alpha_3}{2}\int_{\boldsymbol{s}} p_2 p_3 \psi \ \mathrm{d}\boldsymbol{p}\right\},
\end{aligned} \tag{3.36}
$$

$$
\boldsymbol{J} = 1 + 4\Phi\left[\alpha_2\int_{\boldsymbol{s}} p_1^2 p_2^2 \psi \ \mathrm{d}\boldsymbol{p} + \frac{\alpha_3}{2}\int_{\boldsymbol{s}}(p_1^2+p_2^2)\psi \ \mathrm{d}\boldsymbol{p} + \frac{\alpha_4}{2}\right], \tag{3.37}
$$

$$
\boldsymbol{K} = 1 + 4\Phi\left[\alpha_2\int_{\boldsymbol{s}} p_1^2 p_3^2 \psi \ \mathrm{d}\boldsymbol{p} + \frac{\alpha_3}{2}\int_{\boldsymbol{s}}(p_1^2+p_3^2)\psi \ \mathrm{d}\boldsymbol{p} + \frac{\alpha_4}{2}\right], \tag{3.38}
$$

$$
\boldsymbol{L} = 8\Phi\left\{\alpha_2\int_{\boldsymbol{s}} p_1^2 p_2 p_3 \psi \ \mathrm{d}\boldsymbol{p} + \frac{\alpha_3}{2}\int_{\boldsymbol{s}} p_2 p_3 \psi \ \mathrm{d}\boldsymbol{p}\right\}. \tag{3.39}
$$

The operator matrix $\boldsymbol{A}$ takes on a similar form to (3.29),

$$\boldsymbol{A} = \begin{pmatrix} \boldsymbol{I} & \boldsymbol{0} & \boldsymbol{0} & \cdots & \cdots & \cdots & \boldsymbol{0} \\ \boldsymbol{B}_2 & \boldsymbol{C}_2 & \boldsymbol{D}_2 & \boldsymbol{0} & \cdots & \cdots & \boldsymbol{0} \\ \boldsymbol{0} & \boldsymbol{B}_3 & \boldsymbol{C}_3 & \boldsymbol{D}_3 & \boldsymbol{0} & & \vdots \\ \vdots & \ddots & \ddots & \ddots & \ddots & \ddots & \vdots \\ \vdots & & \ddots & \ddots & \ddots & \ddots & \boldsymbol{0} \\ \boldsymbol{0} & \cdots & \cdots & \boldsymbol{0} & \boldsymbol{B}_{Y-1} & \boldsymbol{C}_{Y-1} & \boldsymbol{D}_{Y-1} \\ \boldsymbol{0} & \cdots & \cdots & \cdots & \boldsymbol{0} & \boldsymbol{0} & \boldsymbol{I} \end{pmatrix}. \tag{3.40}$$

However, the matrices $\boldsymbol{B}_i$, $\boldsymbol{C}_i$ and $\boldsymbol{D}_i$ change with each step in y and take on a more complex form:

$$\boldsymbol{B}_i = \begin{pmatrix} 0 & 0 & 0 & \dots & \dots & \dots & 0 \\ E_{i,2} & C_{i,2}^{(w,0)} & -E_{i,2} & 0 & \dots & \dots & 0 \\ 0 & E_{i,3} & C_{i,3}^{(w,0)} & -E_{i,3} & 0 & & \vdots \\ \vdots & \ddots & \ddots & \ddots & \ddots & \ddots & \vdots \\ \vdots & & \ddots & \ddots & \ddots & \ddots & 0 \\ 0 & \cdots & \cdots & 0 & E_{i,Z-1} & C_{i,Z-1}^{(w,0)} & -E_{i,Z-1} \\ 0 & \cdots & \cdots & \cdots & 0 & 0 & 0 \end{pmatrix}, \tag{3.41}$$

$$\boldsymbol{C}_i = \begin{pmatrix} 1 & 0 & 0 & \dots & \dots & \dots & 0 \\ C_{i,2}^{(0,w)} & C_{i,2}^{(0,0)} & C_{i,2}^{(0,e)} & 0 & \dots & \dots & 0 \\ 0 & C_{i,3}^{(0,w)} & C_{i,3}^{(0,0)} & C_{i,3}^{(0,e)} & 0 & & \vdots \\ \vdots & \ddots & \ddots & \ddots & \ddots & \ddots & \vdots \\ \vdots & & \ddots & \ddots & \ddots & \ddots & 0 \\ 0 & \dots & \dots & 0 & C_{i,Z-1}^{(0,w)} & C_{i,Z-1}^{(0,0)} & C_{i,Z-1}^{(0,e)} \\ 0 & \cdots & \cdots & \cdots & 0 & 0 & 1 \end{pmatrix}, \tag{3.42}$$

and

$$\boldsymbol{D}_i = \begin{pmatrix} 0 & 0 & 0 & \dots & \dots & \dots & 0 \\ -E_{i,2} & C_{i,2}^{(e,0)} & E_{i,2} & 0 & \dots & \dots & 0 \\ 0 & -E_{i,3} & C_{i,3}^{(e,0)} & E_{i,3} & 0 & & \vdots \\ \vdots & \ddots & \ddots & \ddots & \ddots & \ddots & \vdots \\ \vdots & & \ddots & \ddots & \ddots & \ddots & 0 \\ 0 & \cdots & \cdots & 0 & -E_{i,Z-1} & C_{i,Z-1}^{(e,0)} & E_{i,Z-1} \\ 0 & \cdots & \cdots & \cdots & 0 & 0 & 0 \end{pmatrix}. \tag{3.43}$$

The various matrix entries are given by expressions relating to (3.34)-(3.39) and depend upon the sign of $\boldsymbol{G}$ and $\boldsymbol{H}$ at each point in space; for brevity they are detailed in appendix B.1. The right hand side vector is now given by $\boldsymbol{b} = -\boldsymbol{1} - \boldsymbol{F}$, where $\boldsymbol{F}$ is restructured in the same way as the velocity, and the matrix system is solved using backslash in Matlab.

The above process is repeated until the solution converges, the iterative process is as follows:

- Calculate the Newtonian velocity profile, $u^{(0)}(y, z)$, re-dimensionalise and evaluate the probability density function $\psi^{(0)}(\theta, \phi, y^*, z^*)$.
- The moments of $\psi^{(0)}(\theta, \phi, y^*, z^*)$, and hence the updated velocity $u^{(1)}(y, z)$, can be calculated from $\psi^{(0)}(\theta, \phi, y^*, z^*)$.
- The dimensional velocity $u^{*(1)}(y^*, z^*)$ can then be used to calculate the probability density function $\psi^{(1)}(\theta, \phi, y^*, z^*)$.
- Repeat the above steps where, for a given iteration step, we have

$$\psi^{(n)}(\theta, \phi, y^*, z^*) = f(\theta, \phi, y^*, z^*, u^{*(n)}), \quad u^{(n+1)}(y, z) = g(y, z, \psi^{(n)}),$$

  where f and g are the numerical solutions to the Fokker-Planck equation and the Navier-Stokes equations, with extra stress terms, respectively.

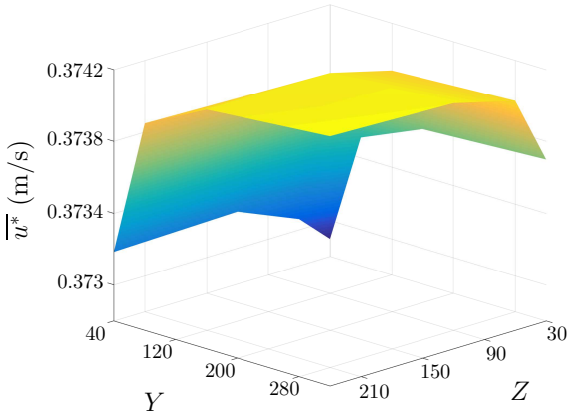

Figure 3.2: Convergence of the spatially averaged velocity $\overline{u^*}$ for an increasing number of steps in y^* and z^*. The grid points where convergence is achieved are $Y = 150$ and $Z = 120$.

- The iteration terminates when

$$||u^{(n+1)} - u^{(n)}|| < \tau$$

, for some tolerance τ.

We require an absolute tolerance of $\tau = 10^{-8}$ in our numerical calculation.

Numerical convergence

As in chapter 2, we know that $N = 10$ ensures convergence of the solution to the Fokker-Planck equation, so it remains to check the finite difference approximation for the number of steps Y and Z. Figure 3.2 shows the spatially averaged velocity $\overline{u^*}$ for increasing gridpoints Y and Z; the results agree to within 0.01% at $Y = 150$ and $Z = 120$.

3.3.3 Results

The velocity, orientation and linear dichroism signal are compared for a range of particle number density, channel dimensions and pressure gradient. Initially, the parameters pro-

Table 3.1: Summary of parameter values discussed in chapter 2. Parameters a^*, b^*, T^*, μ^*, K_B^* and D_r^* are unchanged throughout the results, all others are subject to variation.

Parameter	Description	Units	Value
a^*	Particle length	m	8×10^{-7}
b^*	Particle width	m	6×10^{-9}
T^*	Temperature (water)	K	295
μ^*	Viscosity (water)	Pa s	9.5×10^{-4}
K_B^*	Boltzmann constant	Kg m^2/K s^2	1.38×10^{-23}
D_r^*	Diffusion coefficient	s^{-1}	40.65
h^*	Channel half-depth	m	3×10^{-4}
W^*	Channel half-width	m	1×10^{-3}
n_d^*	Number density	phage/m^3	7.33×10^{17}
G^*	Pressure gradient	Pa/m	4.4×10^3
Φ	Volume fraction	-	1.11×10^{-5}
P_G	Peclet number	-	34.17

vided by Linear Diagnostics Ltd. are used; these parameters are detailed in the results section of section 2.3 and summarised in table 3.1. The notation $\bar{\cdot}$ represents the spatial average for steady flow, given by equation (2.42),

$$\bar{\cdot} = \frac{1}{4W^*h^*} \int_{-W^*}^{W^*} \int_{-h^*}^{h^*} \cdot \, \mathrm{d}y^* \, \mathrm{d}z^*, \tag{3.44}$$

and the linear dichroism signal is assumed proportional to the particle number density and obtained by integrating over the channel depth,

$$LD = \frac{\epsilon^* m_w^* n_d^*}{N_A^*} \int_{-h^*}^{h^*} S \, \mathrm{d}z^*, \tag{3.45}$$

for extinction coefficient ϵ^*, molecular weight m_w^* and Avagadro constant N_A^*.

Figure 3.3 depicts the velocity profile, orientation parameter and linear dichroism signal through the cross section of the channel where $G^* \approx 4.4{\times}10^3$ Pa/m, $h^* = 3{\times}10^{-4}$ m, $W^* = 1 \times 10^{-3}$ m and $n_d^* \approx 7.33 \times 10^{17}$ phage/m^3. The velocity increases from zero at

the channel walls to a maximum in the centre (figure 3.3a), corresponding to a minimum in the orientation parameter (figure 3.3b). The linear dichroism signal is highest near the channel walls and drops off towards the centre (figure 3.3c); there is an increase in the centre of the channel however, where a larger contribution from the orientation parameter comes from near the walls at $z^* = -h^*$ and $z^* = h^*$.

The orientation parameter is plotted against z^* for multiple points across the channel width in figure 3.4a and compared to the results for the 3D channel bound by two walls (chapter 2), and those produced from (1.21), in figure 3.4b. Towards the centre of the channel, the pink line in figure 3.4a matches the blue line in figure 3.4b, *i.e.* the simplified channel matches the behaviour in the centre of the full 3D channel. As we move away from the centre, the orientation parameter is increasing; at the wall the relationship between S and the channel depth inverts so that the alignment is at its highest at $z^* = 0$. When comparing the simplified channel to the full 3D approximation, we take the average of S across the channel width and compare it to the calculation in section 2.4.1 of chapter 2. The red line in figure 3.4b, showing the width-averaged orientation parameter calculated in the current chapter, does not reach zero at the centre of the channel; in comparison, the simplified approximation, shown by the blue line, predicts no alignment at the centre of the channel. The range of results is also smaller in the current work, with the average over the depth being $\overline{S} \approx 0.33$ as opposed to $\overline{S} \approx 0.27$ for the simplified channel. We compare the 2D and 3D orientation parameter with equation (1.21) (black dashed line); the profile calculated from (1.21) is similar to $\overline{S}$ (black dashed and red lines respectively), however equation (1.21) still predicts a lower degree of orientation across the channel.

Next we consider how the pressure gradient G^* and particle number density n_d^* impact the spatially averaged orientation parameter $\overline{S}$ and linear dichroism signal $\overline{LD}$. In figure 3.5a we see that increasing the pressure gradient increases $\overline{S}$, though the increase is not linear. The number density is only having a very small impact to decrease the orientation parameter, seen in the magnified section; when $n_d^* = 1 \times 10^{18}$ phage/m^3 the difference is more prominent than for the smaller values. However, due to the linear relationship

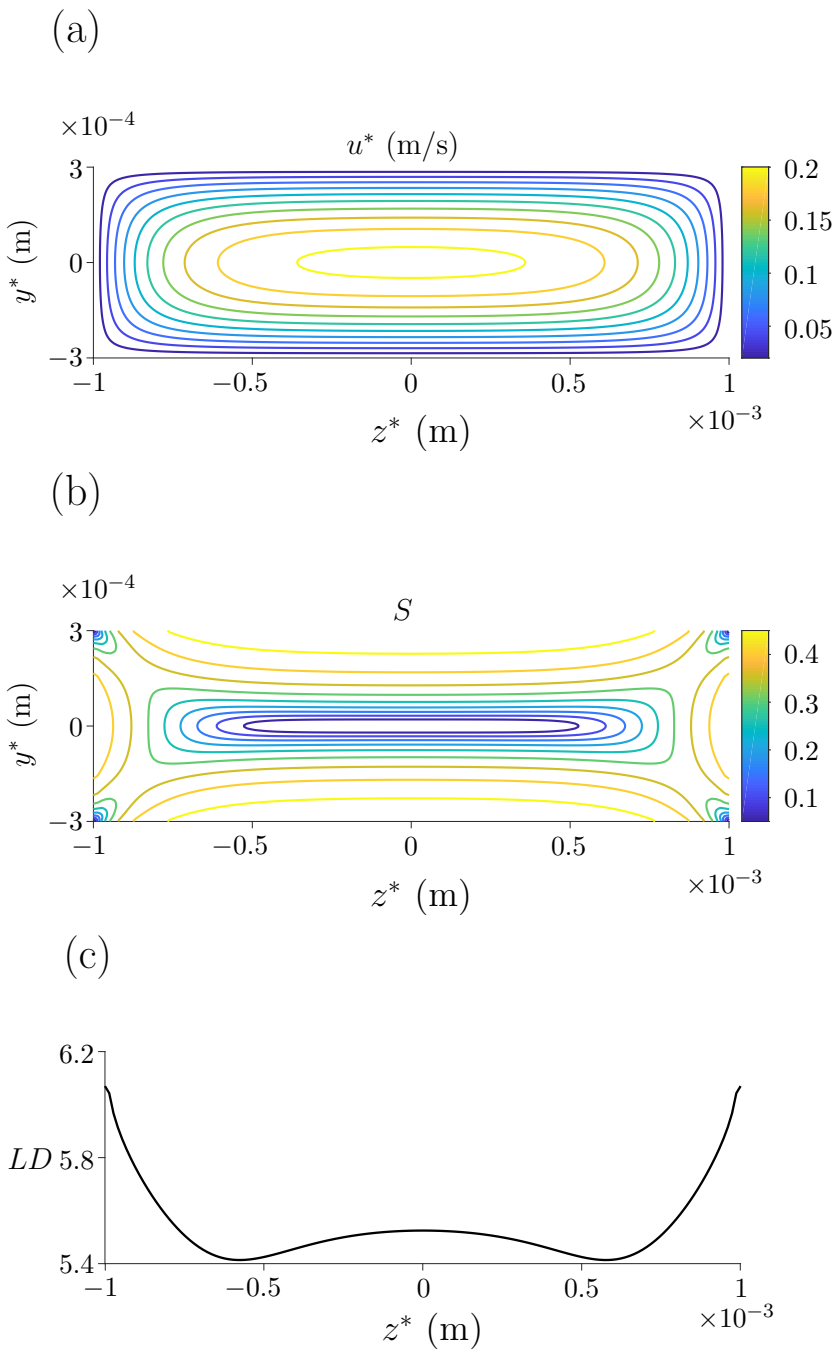

Figure 3.3: Initial results for (a) velocity profile, (b) orientation parameter and (c) linear dichroism signal. The parameters used are as in table 3.1.

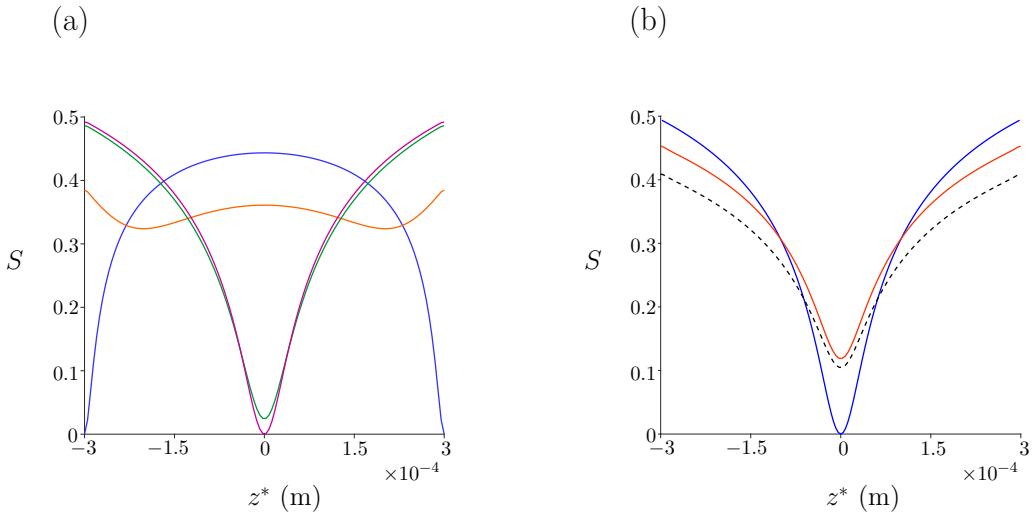

Figure 3.4: (a) The orientation parameter calculated at different points across the channel width: $y^* = 1 \times 10^{-3}$ m (blue line), $y^* = 0.9 \times 10^{-3}$ m (orange line), $y^* = 0.45 \times 10^{-3}$ m (green line) and $y^* = 0$ m (pink line). (b) A comparison between the width averaged orientation parameter calculated in the current chapter (red line), the definition used by McLachlan et. al [68] (black dashed line) and the orientation parameter calculated in section 2.4.1 of chapter 2 for a channel bound only by two walls (blue line).

between number density and linear dichroism signal, increasing the number density has a much more drastic impact (figure 3.5b).

Finally, the channel dimensions were varied and the orientation parameter was calculated. Figure 3.6a depicts $\overline{S}$ varying with channel width and depth; increasing the channel depth increases $\overline{S}$ as expected, however increasing the width appears to only impact the results when W^* is small. This has been shown in figure 3.6b, where $\overline{S}$ is compared for increasing channel width and multiple values of small W^*. When the width is small, increasing it increases the degree of orientation in the channel; as the width increases however, its impact becomes less prominent.

3.4 Oscillatory flow

Next, consider an oscillatory flow system. Theoretically, the fluid is not recirculated but contained within a smaller channel and moves back and forth in front of light sensors. This system has been proposed by Linear Diagnostics Ltd to reduce the volume of the

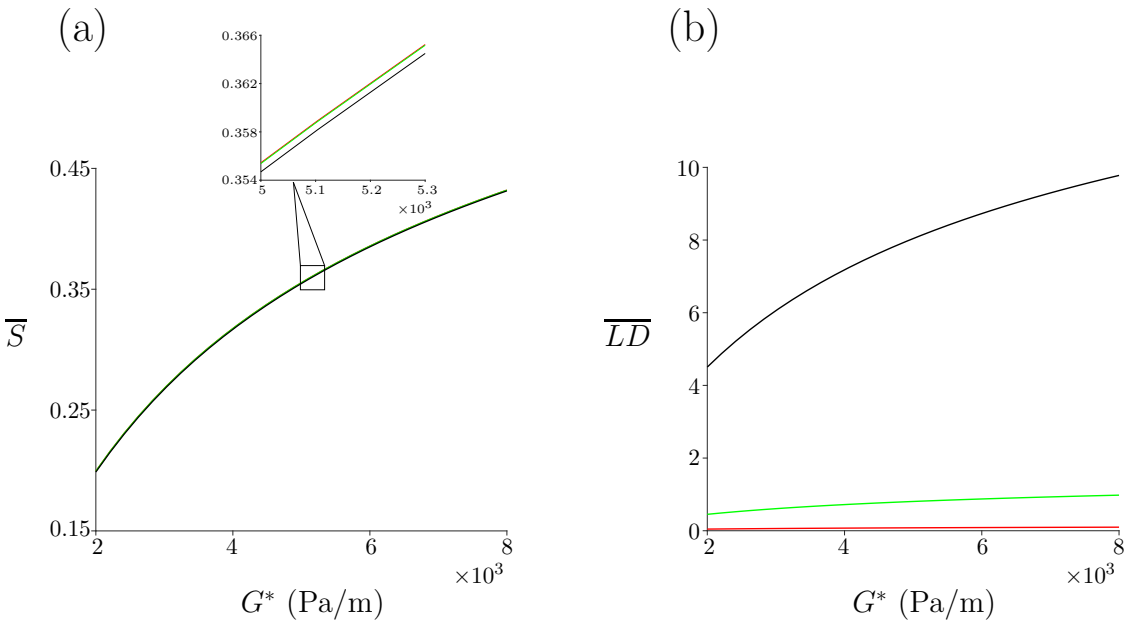

Figure 3.5: (a) $\overline{S}$ and (b) $\overline{LD}$ changing with increasing pressure gradient G^* for three different particle number densities: $n_d^* = 1\times10^{16}$ phage/m^3 (red line), $n_d^* = 1\times10^{17}$ phage/m^3 (green line) and $n_d^* = 1 \times 10^{18}$ phage/m^3 (black line).

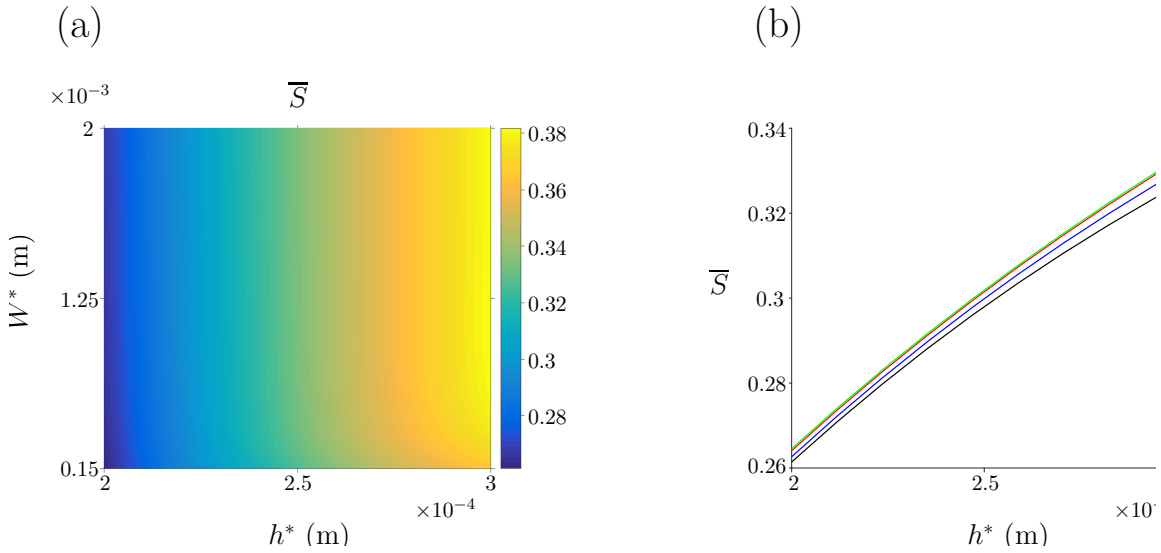

Figure 3.6: Results for varying channel dimensions. (a) $\overline{S}$ for a range of channel width and depth, (b) $\overline{S}$ changing with increasing channel depth h^* for multiple small channel width values: $W^* \approx 0.5\times10^{-3}$ m (black line), $W^* \approx 0.6\times10^{-3}$ m (blue line), $W^* \approx 0.7\times10^{-3}$ m (red line) and $W^* \approx 0.8 \times 10^{-3}$ m (green line).

sample needed and so we seek to determine the feasibility and effectiveness of producing a signal via oscillating flow. Here we redefine the pressure gradient as,

$$\frac{\partial P^*}{\partial x^*} = G^* \exp(i\omega^* t^*), \tag{3.46}$$

for oscillating frequency ω^*. The Fokker-Planck and flow equations are coupled iteratively; the velocity is re-dimensionalised before substitution into the Fokker-Planck equation.

3.4.1 Calculating orientation distribution

Following [87], the Fokker-Planck equation for constant shear rate is

$$\frac{\partial \psi}{\partial \tau} = \frac{1}{6}\Lambda(\psi) - P_\lambda(t)\Omega(\psi), \tag{3.47}$$

where $P_\lambda = \dot{\gamma}^*/6D_r^*$ is the Peclet number, $t^* = \tau/6D_r^*$ and Λ and Ω are given by (3.14) and (3.15) respectively.

We assume at each point in the channel the flow is approximately linear, and so the shear rate is constant. Hence, the Fokker-Planck equation (3.47) is solved for each point in the cross-sectional face of the channel. Discretise the orientation distribution function spatially in the basis of spherical harmonics,

$$\psi(\theta, \phi, t) = \sum_{n=0}^{N} \sum_{m=0}^{n} \left(A_{0\,n}^m(t) P_n^m(\cos\theta)\cos(m\phi) + A_{1\,n}^m(t) P_n^m(\cos\theta)\sin(m\phi) \right). \tag{3.48}$$

This is substituted into equation (3.47), where Λ and Ω are given by (3.17)-(3.20).

Substituting (3.17)-(3.20) into (3.47), equating coefficients of sine and cosine terms,

the resulting system of odes for $A^m_{0\,n}$ and $A^m_{1\,n}$ is

$$\frac{\mathrm{d}A^p_{0\,q}}{\mathrm{d}t} = -\frac{q(q+1)}{6}A^p_{0\,q} - P_\lambda(t)\sum_{n=0}^{N}\sum_{m=0}^{n} a^{m,p}_{n,q}A^m_{1\,n}, \tag{3.49}$$

$$\frac{\mathrm{d}A^p_{1\,q}}{\mathrm{d}t} = -\frac{q(q+1)}{6}A^p_{1\,q} + P_\lambda(t)\sum_{n=0}^{N}\sum_{m=0}^{n} a^{m,p}_{n,q}A^m_{0\,n}, \tag{3.50}$$

for integer N, $q = 0, 2, \ldots, N$ and $p = 0, 2, \ldots, n$. Here, $A^0_{0\,0}(t) = 1/4\pi$ to satisfy the normalisation condition, $A^0_{1\,n} = 0$ for all n and $A^m_{0\,n} = A^m_{1\,n} = 0$ for odd n, m.

The ODEs (3.49) and (3.50) are solved numerically using '*ode45*' in Matlab; the equations are first written in a matrix system, described for solving the steady Fokker-Planck equation in section 2.4 of chapter 2. The solution can then be reconstructed via (3.48) and the moments of $\psi(\theta, \phi, t^*; y^*, z^*)$ can be calculated. From here, the Navier-Stokes equations with extra stress terms can be solved numerically.

3.4.2 Calculating the flow profile

We solve the Navier-Stokes equations (3.1), along with extra stress terms (3.7)-(3.9), and the continuity equation (3.2) for oscillating pressure gradient (3.46).

The dimensional scalings used for steady flow (equation (3.23)) are used here, and the time is scaled against the oscillating frequency, $t^* = t/\omega^*$. Scaling equations (3.1) and (3.2), retaining terms larger than $\mathcal{O}(\delta)$, the continuity equation is unchanged and the

dimensionless Navier-Stokes equations become

$$\begin{aligned}\alpha^2\frac{\partial u}{\partial t} =& -\exp(it)+\frac{2\Phi\alpha_r}{P_G}\left(\frac{\partial}{\partial y}\int_{\boldsymbol{s}} p_1p_2\psi\ \mathrm{d}\boldsymbol{p}+\frac{\partial}{\partial z}\int_{\boldsymbol{s}} p_1p_3\psi\ \mathrm{d}\boldsymbol{p}\right)\\ &+\frac{\partial}{\partial y}\left(\left\{1+4\Phi\left[\alpha_2\int_{\boldsymbol{s}} p_1^2p_2^2\psi\ \mathrm{d}\boldsymbol{p}+\frac{\alpha_3}{2}\int_{\boldsymbol{s}}(p_1^2+p_2^2)\psi\ \mathrm{d}\boldsymbol{p}+\frac{\alpha_4}{2}\right]\right\}\frac{\partial u}{\partial y}\right.\\ &\qquad\left.+4\Phi\left[\alpha_2\int_{\boldsymbol{s}} p_1^2p_2p_3\psi\ \mathrm{d}\boldsymbol{p}+\frac{\alpha_3}{2}\int_{\boldsymbol{s}} p_2p_3\psi\ \mathrm{d}\boldsymbol{p}\right]\frac{\partial u}{\partial z}\right)\\ &+\frac{\partial}{\partial z}\left(\left\{1+4\Phi\left[\alpha_2\int_{\boldsymbol{s}} p_1^2p_3^2\psi\ \mathrm{d}\boldsymbol{p}+\frac{\alpha_3}{2}\int_{\boldsymbol{s}}(p_1^2+p_3^2)\psi\ \mathrm{d}\boldsymbol{p}+\frac{\alpha_4}{2}\right]\right\}\frac{\partial u}{\partial z}\right.\\ &\qquad\left.+4\Phi\left[\alpha_2\int_{\boldsymbol{s}} p_1^2p_2p_3\psi\ \mathrm{d}\boldsymbol{p}+\frac{\alpha_3}{2}\int_{\boldsymbol{s}} p_2p_3\psi\ \mathrm{d}\boldsymbol{p}\right]\frac{\partial u}{\partial y}\right).\end{aligned} \tag{3.51}$$

The no-slip conditions are

$$\begin{aligned} u(x,-\overline{W},z,t)=u(x,\overline{W},z,t)=0, \qquad & u(x,y,-1,t)=u(x,y,1,t)=0,\\ v(x,-\overline{W},z,t)=v(x,\overline{W},z,t)=0, \qquad & v(x,y,-1,t)=u(x,y,1,t)=0,\\ w(x,-\overline{W},z,t)=w(x,\overline{W},z,t)=0, \qquad & w(x,y,-1,t)=u(x,y,1,t)=0, \end{aligned} \tag{3.52}$$

where $\overline{W}=W^*/h^*$ and it is assumed the system is initially at rest, accounted for by altering the dimensionless pressure gradient to $\partial P/\partial x=\exp(i(t+\pi/2))$.

Numerical method

We solve for the velocity using an ADI method; this method splits each discretised time step in half and solves implicitly for one spatial variable in each time step [18]. Mixed derivatives are treated explicitly throughout this section. We begin with the Newtonian equation,

$$\alpha^2\frac{\partial u}{\partial t}=-e^{i\left(t+\frac{\pi}{2}\right)}+\frac{\partial^2 u}{\partial y^2}+\frac{\partial^2 u}{\partial z^2}\,. \tag{3.53}$$

Discretising the above and splitting into two half-time steps we have

$$\alpha^2 \frac{u_{i,j}^{n+1/2} - u_{i,j}^{n}}{\Delta t/2} = -e^{i\left(t^{n+1/2}+\frac{\pi}{2}\right)} + \frac{u_{i+1,j}^{n+1/2} - 2u_{i,j}^{n+1/2} + u_{i-1,j}^{n+1/2}}{\Delta y^2} + \frac{u_{i,j+1}^{n} - 2u_{i,j}^{n} + u_{i,j-1}^{n}}{\Delta z^2}, \tag{3.54}$$

$$\alpha^2 \frac{u_{i,j}^{n+1} - u_{i,j}^{n+1/2}}{\Delta t/2} = -e^{i\left(t^{n+1}+\frac{\pi}{2}\right)} + \frac{u_{i+1,j}^{n+1/2} - 2u_{i,j}^{n+1/2} + u_{i-1,j}^{n+1/2}}{\Delta y^2} + \frac{u_{i,j+1}^{n+1} - 2u_{i,j}^{n+1} + u_{i,j-1}^{n+1}}{\Delta z^2}. \tag{3.55}$$

The first half time step is implicit in y and is solved for each point in z, the second half time step uses the solution to the first equation, $u_{i,j}^{n+1/2}$, as the explicit velocity and is solved implicitly in z and explicitly in y. Rearranging each of the above we have

$$\left(1 + \frac{\Delta t}{\alpha^2 \Delta y^2}\right) u_{i,j}^{n+1/2} - \frac{\Delta t}{2\alpha^2 \Delta y^2}(u_{i+1,j}^{n+1/2} + u_{i-1,j}^{n+1/2}) = -\frac{\Delta t}{2\alpha^2} e^{i\left(t^{n+1/2}+\frac{\pi}{2}\right)} + \left(1 - \frac{\Delta t}{\alpha^2 \Delta z^2}\right) u_{i,j}^{n} + \frac{\Delta t}{2\alpha^2 \Delta z^2}(u_{i,j+1}^{n} + u_{i,j-1}^{n}), \tag{3.56}$$

$$\left(1 + \frac{\Delta t}{\alpha^2 \Delta z^2}\right) u_{i,j}^{n+1} - \frac{\Delta t}{2\alpha^2 \Delta z^2}(u_{i,j+1}^{n+1} + u_{i,j-1}^{n+1}) = -\frac{\Delta t}{2\alpha^2} e^{i\left(t^{n+1}+\frac{\pi}{2}\right)} + \left(1 - \frac{\Delta t}{\alpha^2 \Delta y^2}\right) u_{i,j}^{n+1/2} + \frac{\Delta t}{2\alpha^2 \Delta y^2}(u_{i+1,j}^{n+1/2} + u_{i-1,j}^{n+1/2}), \tag{3.57}$$

which are both solved via a matrix equation. All matrices in this method are sparse tridiagonal matrices; the operator matrix for the first time step is

$$\boldsymbol{A} = \begin{pmatrix} 1 & 0 & 0 & \dots & \dots & \dots & 0 \\ C_w & C_0 & C_e & 0 & \dots & \dots & 0 \\ 0 & C_w & C_0 & C_e & 0 & & \vdots \\ \vdots & \ddots & \ddots & \ddots & \ddots & \ddots & \vdots \\ \vdots & & \ddots & \ddots & \ddots & \ddots & 0 \\ 0 & \dots & \dots & 0 & C_w & C_0 & C_e \\ 0 & \dots & \dots & \dots & 0 & 0 & 1 \end{pmatrix}, \tag{3.58}$$

where $C_w = C_e = -\Delta t/(2\alpha^2 \Delta y^2)$ and $C_0 = 1 + \Delta t/(\alpha^2 \Delta y^2)$. For the matrix equation $\boldsymbol{Au} = \boldsymbol{b}$, the right hand side vector $\boldsymbol{b}$ is given by the right hand side of equation (3.56), where the first and last entries are zero, satisfying the boundary conditions. This is solved using the direct solver backslash in Matlab for each $j = 2, \dots, Z-1$, and the boundary conditions $u_{i,1}^{n+1/2} = u_{i,Z}^{n+1/2} = 0$ are enforced afterwards.

The second half time step follows a similar method. Since the boundary conditions for y and z are the no-slip conditions, the operator matrices are the same, however the entries for the second time step are now given by $C_w = C_e = -\Delta t/(2\alpha^2 \Delta z^2)$ and $C_0 = 1 + \Delta t/(\alpha^2 \Delta z^2)$ and the right hand side vector is given by the right hand side of equation (3.57) with equivalent boundary conditions. This is solved for each $i = 2, \dots, Y-1$ and both the above steps are completed to update the velocity at time step t^{n+1}.

Once the velocity is known, the new Peclet number can be calculated by evaluating the shear rate $\dot{\gamma}^* = \sqrt{(\partial u^*/\partial y^*)^2 + (\partial u^*/\partial z^*)^2}$, which can be used to calculate $\psi(\theta, \phi, t^*; y^*, z^*)$ and its moments as functions of y, z and t, and the velocity incorporating extra stress terms can be determined. Discretising equation (3.51) and splitting

into two half-time steps we have

$$\alpha^2\frac{u_{i,j}^{n+1/2}-u_{i,j}^{n}}{\Delta t/2}=e^{i\left(t^{n+1/2}+\frac{\pi}{2}\right)}+F_{i,j}^{n+1/2}+\begin{cases}G_{i,j}^{n+1/2}\,\frac{u_{i,j}^{n+1/2}-u_{i-1,j}^{n+1/2}}{\Delta y} & \text{for } G_{i,j}^{n+1/2}\geq 0\\ G_{i,j}^{n+1/2}\,\frac{u_{i+1,j}^{n+1/2}-u_{i,j}^{n+1/2}}{\Delta y} & \text{for } G_{i,j}^{n+1/2}<0\end{cases}$$
$$+\begin{cases}H_{i,j}^{n}\frac{u_{i,j}^{n}-u_{i,j-1}^{n}}{\Delta z} & \text{for } H_{i,j}^{n}\geq 0\\ H_{i,j}^{n}\frac{u_{i,j+1}^{n}-u_{i,j}^{n}}{\Delta z} & \text{for } H_{i,j}^{n}<0\end{cases}+K_{i,j}^{n}\frac{u_{i,j+1}^{n}-2u_{i,j}^{n}+u_{i,j-1}^{n}}{\Delta z^2} \tag{3.59}$$
$$+J_{i,j}^{n+1/2}\,\frac{u_{i+1,j}^{n+1/2}-2u_{i,j}^{n+1/2}+u_{i-1,j}^{n+1/2}}{\Delta y^2}$$
$$+L_{i,j}^{n}\frac{u_{i+1,j+1}^{n}-u_{i-1,j+1}^{n}-u_{i+1,j-1}^{n}+u_{i-1,j-1}^{n}}{4\Delta y\Delta z},$$

$$\alpha^2\frac{u_{i,j}^{n+1}-u_{i,j}^{n+1/2}}{\Delta t/2}=e^{i\left(t^{n+1/2}+\frac{\pi}{2}\right)}+F_{i,j}^{n+1}+\begin{cases}G_{i,j}^{n+1/2}\,\frac{u_{i,j}^{n+1/2}-u_{i-1,j}^{n+1/2}}{\Delta y} & \text{for } G_{i,j}^{n+1/2}\geq 0\\ G_{i,j}^{n+1/2}\,\frac{u_{i+1,j}^{n+1/2}-u_{i,j}^{n+1/2}}{\Delta y} & \text{for } G_{i,j}^{n+1/2}<0\end{cases}$$
$$+\begin{cases}H_{i,j}^{n+1}\,\frac{u_{i,j}^{n+1}-u_{i,j-1}^{n+1}}{\Delta z} & \text{for } H_{i,j}^{n+1}\geq 0\\ H_{i,j}^{n+1}\,\frac{u_{i,j+1}^{n+1}-u_{i,j}^{n+1}}{\Delta z} & \text{for } H_{i,j}^{n+1}<0\end{cases}+K_{i,j}^{n+1}\frac{u_{i,j+1}^{n+1}-2u_{i,j}^{n+1}+u_{i,j-1}^{n+1}}{\Delta z^2} \tag{3.60}$$
$$+J_{i,j}^{n+1/2}\,\frac{u_{i+1,j}^{n+1/2}-2u_{i,j}^{n+1/2}+u_{i-1,j}^{n+1/2}}{\Delta y^2}$$
$$+L_{i,j}^{n+1/2}\frac{u_{i+1,j+1}^{n+1/2}-u_{i-1,j+1}^{n+1/2}-u_{i+1,j-1}^{n+1/2}+u_{i-1,j-1}^{n+1/2}}{4\Delta y\Delta z},$$

where the coefficients $\boldsymbol{F}-\boldsymbol{L}$ are known expressions given by (3.34)-(3.39), but are now also time dependent. The operator matrices and right hand side vectors at each half-time step are now dependent on the sign of $\boldsymbol{G}$ and $\boldsymbol{H}$; all other factors of the method are unchanged. The coefficients of the operator matrices and right hand side vectors are given in appendix B.2.

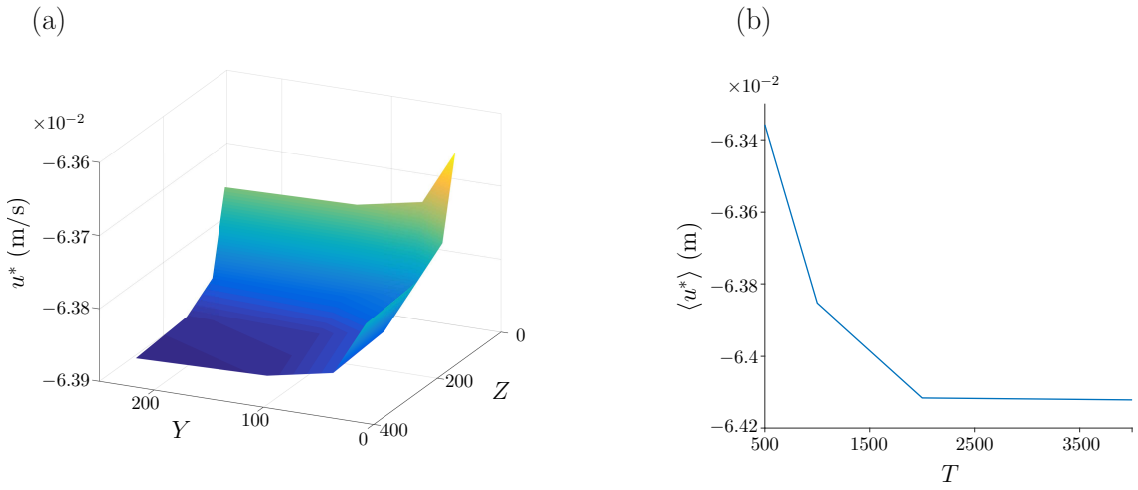

Figure 3.7: Convergence of the oscillating ADI scheme for (a) gridpoints Y and Z for $T = 1000$, where the convergence of the scheme is achieved for $Y = 150$ and $= 120$. (b) Time steps T for $Y = 120$ and $Z = 150$; convergence is achieved for $T = 2000$.

Numerical convergence

From chapter 2 and the numerical convergence study in section 3.3.2 we have that $N = 10$ for the number of modes in the spherical harmonics discretisation and $Y = 150$, $Z = 120$ in the finite difference scheme. We check the convergence of the finite difference scheme for steps Y and Z in figure 3.7a and find the convergence matches section 3.3.2 (figure 3.2). We then consider a variety of time steps T (figure 3.7b) where $Y = 150$ and $Z = 120$ were used for these calculations. The difference between values at $T = 2000$ and $T = 4000$ is $\approx 0.01\%$ and so we take $T = 2000$ in our calculations.

3.4.3 Results

A small sample of parameter space has been selected and the velocity, orientation parameter and linear dichroism signal have been calculated. The initial parameters used are detailed in chapter 2 (and summarised in table 3.1). Here we start with $\omega^* = 10$ rad/s, resulting in $\alpha^2 \approx 0.94$ for the density of water $\rho^* = 1 \times 10^3$ Kg/m^3. We consider changes in the channel width and depth, pressure gradient, particle number density and the oscillating frequency; the results are plotted in dimensional quantities where possible.

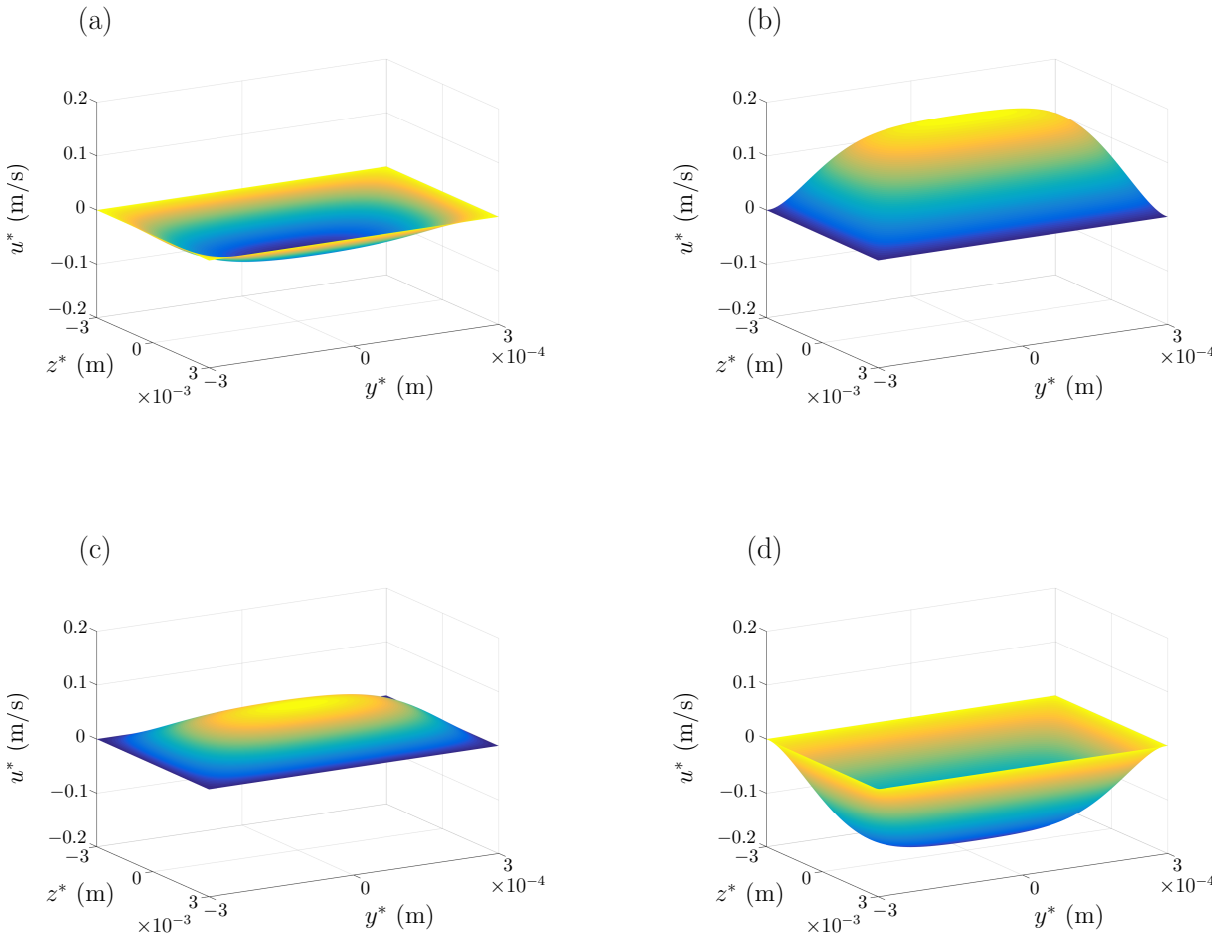

Figure 3.8: Velocity profile evolving over one time period. The length of the period is T_p and each figure shows different stages of the cycle: (a) $t = t_0$, the start of the oscillation, (b) $t = t_0 + T_p/4$, (c) $t = t_0 + T_p/2$ and (d) $t = t_0 + 3T_p/4$.

The computational walltime for this problem was large and hence a smaller range of parameter space has been considered. The numerical solution was parallelised using *'parfor'* in Matlab by splitting the solution to the Fokker-Planck equation, solved at each point in space, across five cores. For this process, the runtime varied between 33 and 69 hours, depending on the number of iterations needed for the solution to converge. To allow comparison between the channel dimensions, pressure gradient, particle number density and oscillating frequency, we calculated results for 41 different sets of parameter space and consider both a time averaged orientation parameter $\overline{S}_{av}$ and the peak orientation parameter over a time period $\overline{S}_{peak}$, where $\overline{\cdot}$ is the spatial average (equation (3.44)).

The initial results for the velocity and orientation are depicted in figures 3.8 and

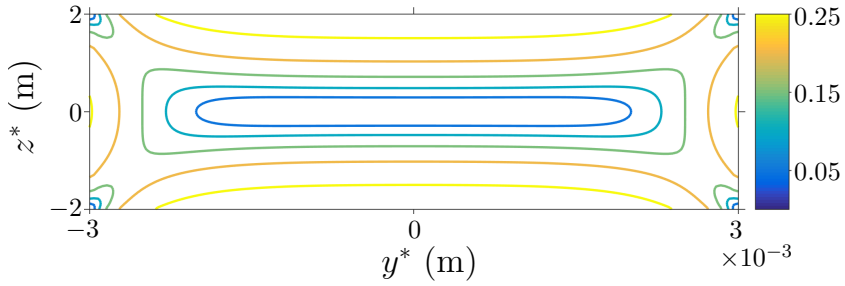

Figure 3.9: Orientation parameter S, averaged over one half of the time period, through the cross-sectional face of the rectangular channel, or the y^*–z^* plane.

3.9 respectively. Since the flow oscillates, it is instructive to examine how the velocity varies over time. Figure 3.8a shows the velocity close to the start of the period, and the following figures are displayed for each quarter of a time period. The velocity increases to a maximum a quarter of the way through a period (figure 3.8b), and reaches a minimum three quarters of the way through (figure 3.8d); during this time, the profile retraces its path, reaching zero half way through the time period (figure 3.8c). The orientation parameter has been averaged over one half of the time period, to avoid cancellation, and plotted over the cross-section of the rectangular channel in figure 3.9. The orientation parameter increases towards the channel walls, where the shear rate is highest, and drops to zero at the centre of the channel.

Next we investigate how the orientation parameter varies with channel depth, oscillating frequency and pressure gradient. Figures 3.10a, c and e show results for $\omega^* = 10$ rad/s and figures 3.10b, d and f show results for $\omega^* = 200$ rad/s; in all cases there is a reduction in the degree of orientation from the steady case as the oscillating frequency is increased. Increasing the pressure gradient increases the value of the orientation parameter in general, and reduces the area where S reaches a minimum (figures 3.10a and c); increasing the channel depth further increases the orientation parameter for small oscillations (comparatively figures 3.10c and e), however the opposite occurs when ω^* is large (figures 3.10f). Here, the orientation parameter appears to decrease slightly in the centre of the channel with increasing h^*.

Further, consider the linear dichroism signal for a range of channel width and pressure

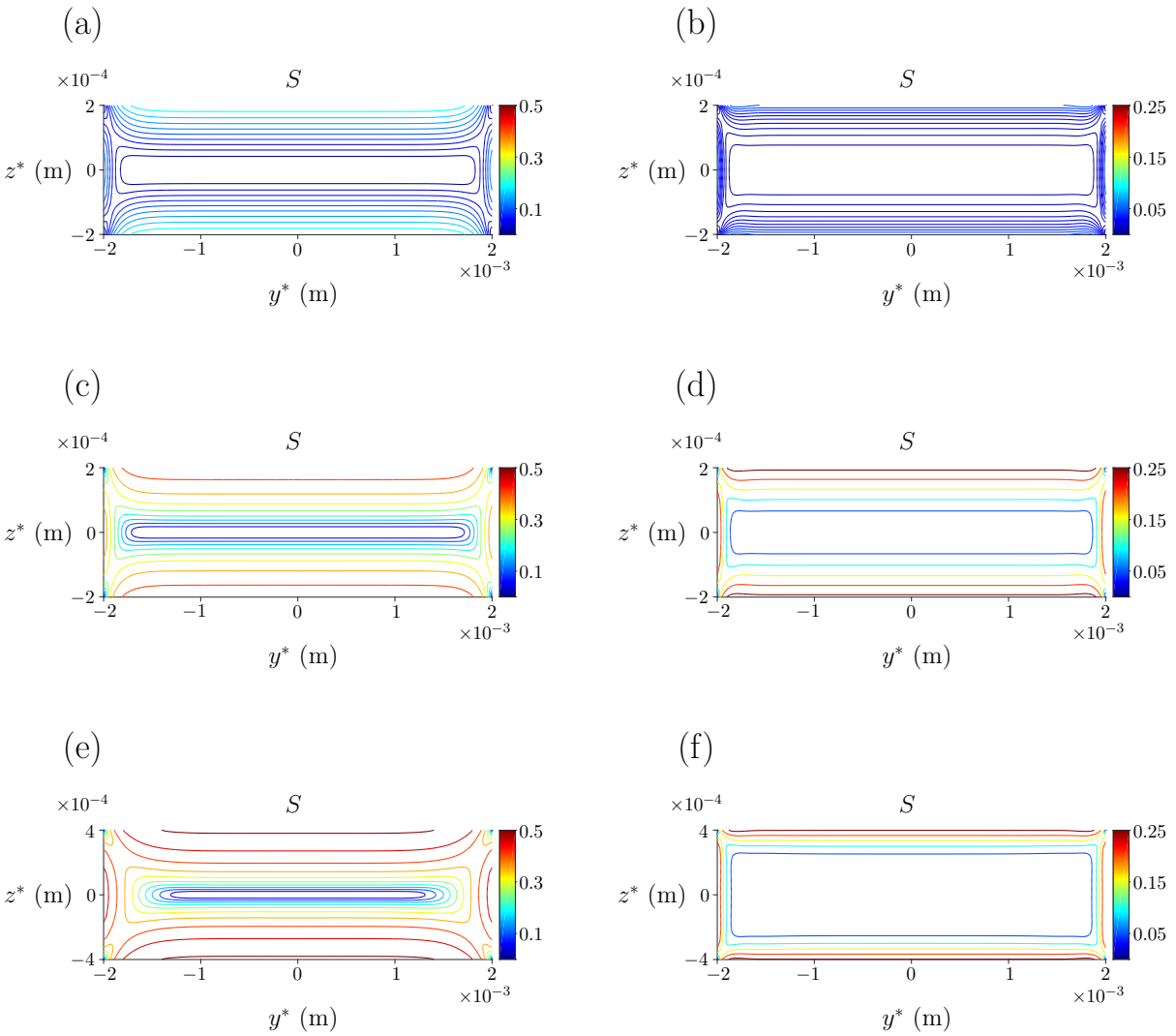

Figure 3.10: Orientation parameter S through the cross-section of the rectangular channel for a range of channel depth, oscillating frequency and pressure gradient. Throughout the results, $W^* = 2\times10^{-3}$ m and $n_d^* = 1\times10^{18}$ phage/m^3. (a) $h^* = 2\times10^{-4}$ m, $\omega^* = 10$ rad/s and $G^* = 2\times10^3$ Pa/m. (b) $h^* = 2\times10^{-4}$ m, $\omega^* = 200$ rad/s and $G^* = 8\times10^3$ Pa/m. (c) $h^* = 2\times10^{-4}$ m, $\omega^* = 10$ rad/s and $G^* = 8\times10^3$ Pa/m. (d) $h^* = 2\times10^{-4}$ m, $\omega^* = 200$ rad/s and $G^* = 8\times10^3$ Pa/m. (e) $h^* = 4\times10^{-4}$ m, $\omega^* = 10$ rad/s and $G^* = 8\times10^3$ Pa/m. (f) $h^* = 4\times10^{-4}$ m, $\omega^* = 200$ rad/s and $G^* = 8\times10^3$ Pa/m.

gradient (figure 3.11). The channel width and number density of particles are fixed as $W^* = 2 \times 10^{-3}$ m and $n_d^* = 1 \times 10^{18}$ phage/m^3 and the linear dichroism signal is averaged over half a time period. Two values of oscillating frequency are plotted, $\omega^* = 10$ rad/s (figure 3.11a) and $\omega^* = 200$ rad/s (figure 3.11b). As the pressure gradient increases, the linear dichroism signal increases, however the rate of increase is lower as the pressure gradient becomes larger. For a small oscillating frequency, the signal increases with increasing channel depth; when a large oscillating frequency is instead used, the relationship of the signal with h^* is reversed and its impact is reduced. The signal is smaller in general in figure 3.11b than in figure 3.11a due to a larger oscillating frequency. Since only a small parameter range has been investigated, the full extent of the relationship with h^* and ω^* is currently unknown.

The light source shines through the centre portion of the channel and so we average the orientation parameter over the depth and centre third of the channel, for the parameters depicted in figure 3.11, summarised in table 3.2; the average orientation parameter and the peak orientation parameter are calculated and compared. It can be seen that increasing h^* for $\omega^* = 10$ rad/s increases the orientation parameter and decreases it for $\omega^* = 200$ rad/s. Further, the alignment is reduced by increasing the oscillating frequency and is increased by increasing the pressure gradient, as seen previously. The averaged results are lower than the peak orientation; the difference is seen less as the oscillating frequency increases since the orientation parameter is smaller.

Finally we investigate how the depth averaged orientation parameter, $\overline{S}^z_{av}$ changes with particle number density (figure 3.12). We plot $\overline{S}^z_{av}$ rather than the linear dichroism signal, due to the linear relationship between the signal and the number density; the results would be less comparable as they would appear an order of magnitude apart. To enable comparison we neglect this relationship and look instead at how the total alignment, averaged over the channel depth, changes with these parameters. Increasing the oscillating frequency from $\omega^* = 10$ rad/s to $\omega^* = 200$ rad/s drastically decreases the alignment in the system, seen in all four figures in 3.12. The number density is having

Table 3.2: The orientation parameter, averaged over the depth and centre third of the channel, compared for both a time average ($\overline{S}_{av}$) and the peak value over a period ($\overline{S}_{peak}$) for the results displayed in figure 3.11. Throughout these results, $n_d^* = 1 \times 10^{18}$ phage/m^3 and $W^* = 2 \times 10^{-3}$ m.

ω^*	G^*	h^*	$\overline{S}_{av}$	$\overline{S}_{peak}$
10	2×10^3	2×10^{-4}	0.086	0.117
		4×10^{-4}	0.151	0.201
	6×10^3	2×10^{-4}	0.236	0.308
		4×10^{-4}	0.318	0.398
	8×10^3	2×10^{-4}	0.280	0.359
		4×10^{-4}	0.362	0.444
	1×10^4	2×10^{-4}	0.314	0.395
		4×10^{-4}	0.396	0.478
200	2×10^3	2×10^{-4}	0.014	0.018
		4×10^{-4}	0.007	0.009
	6×10^3	2×10^{-4}	0.079	0.100
		4×10^{-4}	0.041	0.053
	8×10^3	2×10^{-4}	0.110	0.139
		4×10^{-4}	0.059	0.074
	1×10^4	2×10^{-4}	0.138	0.172
		4×10^{-4}	0.075	0.093

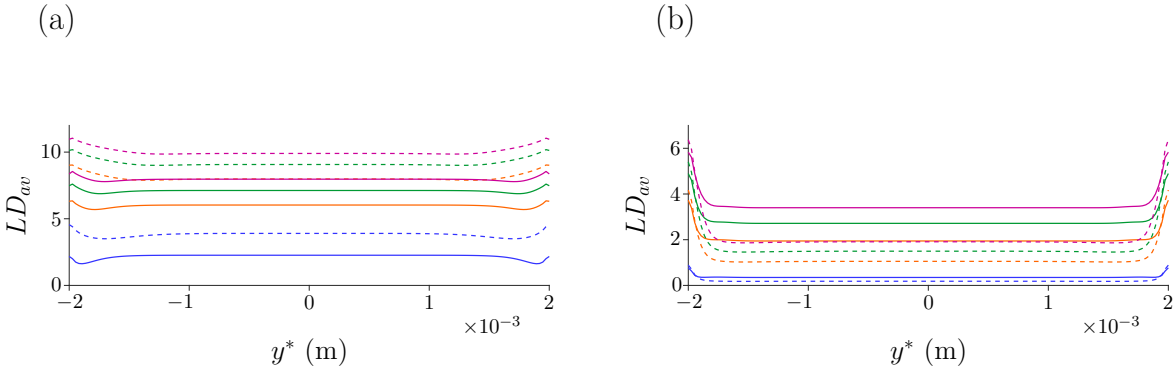

Figure 3.11: Linear dichroism signal for multiple pressure gradient and channel depth values, calculated for small and large oscillating frequencies. Here, $W^* = 2 \times 10^{-3}$ m and $n_d^* = 1 \times 10^{18}$ phage/m^3. The solid lines represent $h^* = 2 \times 10^{-4}$ m and the dashed lines represent $h^* = 4 \times 10^{-4}$ m. The values of G^* are: $G^* = 2 \times 10^3$ Pa/m (blue lines), $G^* = 6 \times 10^3$ Pa/m (orange lines), $G^* = 8 \times 10^3$ Pa/m (green lines) and $G^* = 1 \times 10^4$ Pa/m (pink lines). (a) $\omega^* = 10$ rad/s, (b) $\omega^* = 200$ rad/s.

Table 3.3: The orientation parameter, averaged over the depth and centre third of the channel, compared for both a time average ($\overline{S}_{av}$) and the peak value over a period ($\overline{S}_{peak}$) for the results displayed in figure 3.12. Throughout these results, $G^* = 8 \times 10^3$ Pa/m and $n_d^* = 1 \times 10^{17}$ phage/m^3.

ω^*	W^*	h^*	$\overline{S}_{av}$	$\overline{S}_{peak}$
10	0.5×10^{-3}	2×10^{-4}	0.279	0.360
		4×10^{-4}	0.363	0.454
	2×10^{-3}	2×10^{-4}	0.251	0.359
		4×10^{-4}	0.363	0.444
200	0.5×10^{-3}	2×10^{-4}	0.121	0.151
		4×10^{-4}	0.081	0.099
	2×10^{-3}	2×10^{-4}	0.111	0.139
		4×10^{-4}	0.057	0.074

a very limited effect on the depth-averaged orientation parameter; when the oscillations are slow we can see a slight decrease by increasing the number density, however this is not seen for larger oscillating frequencies. Figures 3.12a and b show $h^* = 2 \times 10^{-4}$ m and figures 3.12c and d show $h^* = 4 \times 10^{-4}$ m; for all other parameters, increasing the channel depth increases the depth-averaged orientation parameter, a characteristic mirrored in previous results of this section. The channel width increases the orientation parameter overall, by decreasing the space in which the alignment is at a minimum.

For the results in figure 3.12 the orientation parameter, averaged over the depth and centre third of the channel, is summarised in table 3.3; here the orientation parameter is only calculated for $n_d^* = 1 \times 10^{17}$ phage/m^3 since the number density has minimal impact on S. For both the average and peak orientation parameters, when ω^* is large, the orientation parameter decreases with increasing h^*. Further, increasing the channel width W^* decreases the orientation parameter due to the minimum occurring for a larger portion of the channel. Finally, we note again that the values of $\overline{S}_{av}$ are smaller than $\overline{S}_{peak}$.

3.5 Discussion

In this chapter we have modelled steady and oscillatory flows of suspensions of passive M13 bacteriophage in thin rectangular channels; the channel is assumed to be much longer than its depth and width, enabling a simplification via lubrication theory. The steady flow problem was solved by discretising the spatial variables using a finite difference approximation then expressing the resulting equations in sparse matrix form. The oscillating problem was solved in a similar manner using an ADI method to simplify time discretisation. The flow was iteratively coupled with the Fokker-Planck equation, where the orientation distribution is calculated at each point in the cross-sectional face of the channel using spherical harmonics. This method reduces the Fokker-Planck equation to a system of equations that were solved numerically either by setting up a matrix system or using an ODE solver.

The 3D oscillatory problem was computationally expensive and so a smaller range of parameter space was considered to highlight the key characteristics of the flow and orientation. The solution for each set of parameters was split across five cores and the walltime varied from 33 to 69 hours, depending on the number of iterations required. In future, to explore a larger parameter space we would need to utilise high performance computer clusters such as BlueBEAR or HPC Midlands+. Changes in channel width, depth, pressure gradient, particle number density and oscillating frequency have been plotted and compared for both cases and the simplified channel solution in chapter 2 was compared with current work.

In both steady and oscillatory flows, increasing the pressure gradient increases the shear rate and hence the degree of orientation in the system. The same can be said for increasing the channel depth, although there is an indication that for large oscillating frequencies this relationship is reversed. As shown in the simplified channel (chapter 2), for oscillating frequencies greater than $\omega^* \approx 30$ rad/s, the relationship between the orientation parameter and the channel depth reverses. This is an important factor when considering the use of oscillatory flow; the alignment may increase for larger oscillations

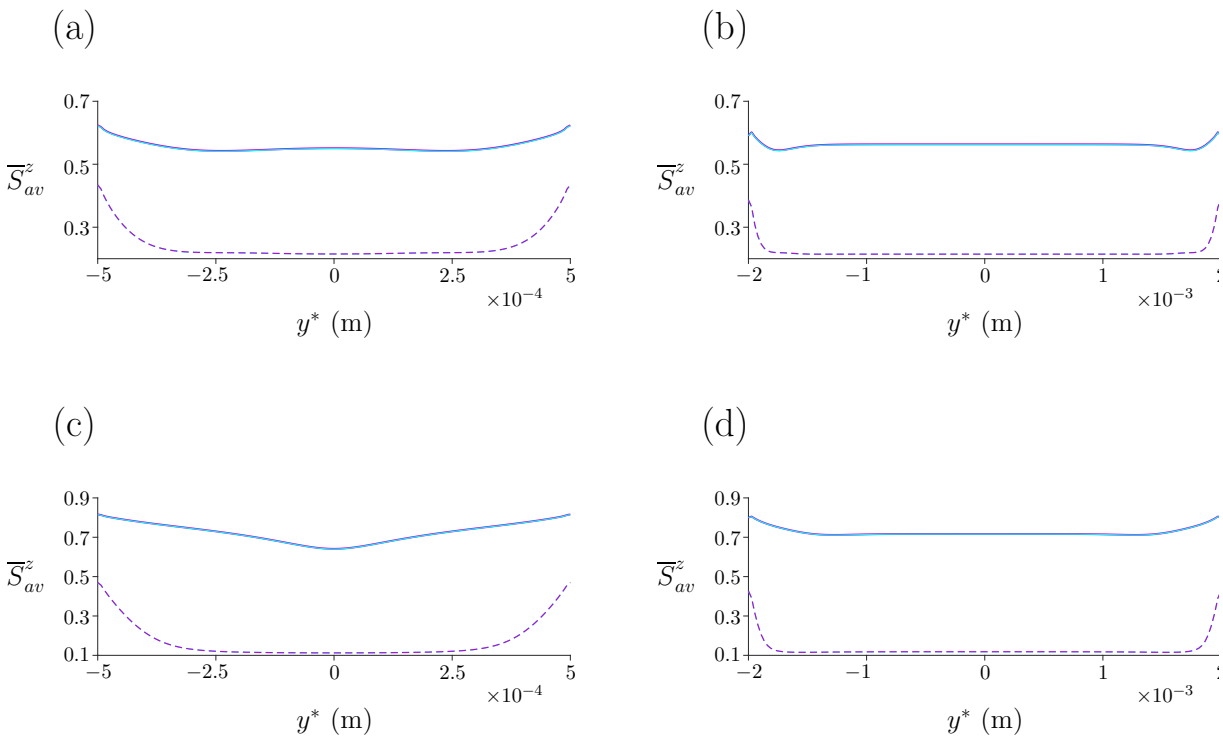

Figure 3.12: Depth-averaged orientation parameter $\overline{S}_z$ for a range of channel width, number density and oscillating frequency, where $G^* = 8 \times 10^3$ Pa/m. We plot two oscillating frequencies: $\omega^* = 10$ rad/s (solid line) and $\omega^* = 200$ rad/s (dashed line), and two different number densities: $n_d^* = 1 \times 10^{17}$ phage/m^3 (purple line) and $n_d^* = 1 \times 10^{18}$ phage/m^3 (blue line). The channel width and depth vary as follows: (a) $W^* = 0.5 \times 10^{-3}$ m and $h^* = 2 \times 10^{-4}$ m, (b) $W^* = 2 \times 10^{-3}$ m and $h^* = 2 \times 10^{-4}$ m (c) $W^* = 0.5 \times 10^{-3}$ m and $h^* = 4 \times 10^{-4}$ m and (d) $W^* = 2 \times 10^{-3}$ m and $h^* = 4 \times 10^{-4}$ m.

and a thinner channel, however it would be reduced in comparison with steady flow and slow oscillations.

Changing the width of the channel has only a small impact on the steady flow results; the key change is that near the walls the orientation parameter increases and so the spatial average will increase in general. The channel width predominantly impacts the orientation parameter when it is close in size to the channel depth, *i.e.* when the channel is close to square, and here it increases S in the same way as the depth. A larger orientation parameter is seen in the 3D model in comparison with the simplified case (section 2.4 of chapter 2); the walls increase the induced shear rate in the channel, which is key in aligning the bacteriophage. For oscillating flow we see a slight reduction in the peak orientation parameter due to averaging over the centre third of the channel.

The number density has a limited impact on the orientation parameter, and this effect is further reduced when the oscillating frequency is large. Increasing the number density of particles slightly decreases the degree of orientation, we postulate that this is due to the particles increasing the apparent viscosity of the fluid and reducing the shear rate. Since the particles are dilute in suspension, we do not expect interactions between particles that could impact the overall alignment. However, due to its linear relationship with the linear dichroism signal, the particle number density drastically increases the signal as it increases. Care needs to be taken with this prediction since an increase in the number of particles may result in more light diffraction and hence increased levels of noise in the resulting signal.

In general for oscillating flow, the average over half a time period is lower than the peak orientation parameter. The average takes into account a range of values and so we would expect it to be smaller. It would be recommended to have a sensor that rapidly measures absorbance to detect the maximum achieved signal rather than averaging over multiple time points.

We highlight a key difference between the 2D and 3D channel approximations in this chapter. The orientation at the centre of the channel was in good agreement with the

simplified model; moving away from the centre, the walls are increasing the shear rate and hence the alignment comparative to the work in chapter 2. In general, the characteristics deduced from the work in the current chapter compare well with those discussed in section 2.4 of chapter 2; that work, considering fluid in 3D bound by two walls, may not accurately predict the alignment in the channel. The 3D channel is a more computationally expensive problem, and so the simplified channel provides an effective prediction of the general behaviour of the orientation of bacteriophage and the key parameters which would optimise the signal to noise ratio. To accurately describe the flow profile and orientation distribution, the full channel should still be considered.

Continuing on from this study, it would be imperative to further explore parameter space, specifically for oscillating flow. The relationship between orientation and channel depth with large and small oscillating frequencies is of particular interest; understanding how, and at what value of ω^*, this relationship changes would be imperative in determining the feasibility of oscillating flow. We believe that the oscillations reduce the alignment in the system but may still produce useful alignment for slow oscillations. Further, it will be beneficial to test certain conclusions experimentally; understanding how the number density of particles affects the linear dichroism signal would aid in more accurate calculations. This work provides insight into flows of passive particle suspensions in thin rectangular channels; future work may include investigating how an active suspension behaves in this system, or alternatively how the flow of both passive and active suspensions would change due to peristaltic motion.

3.5.1 Summary

The key findings in chapter 3 are summarised here:

- The pressure gradient increases the shear rate and hence the orientation parameter in both steady and oscillatory flow.

- By increasing the depth of the channel, the alignment of the bacteriophage increases

for steady and slow oscillatory flows.

- There is an indication that the channel depth and orientation parameter have a non-monotonic relationship, dependent on the oscillating frequency. Further investigation, considering a larger parameter space, would be necessary to confirm this proposition.

- Varying the channel width has only a small impact on all results, predominantly seen when the channel is close to square.

- The general characteristics of the full 3D model are demonstrated well by the simplified channel model in section 2.4 of chapter 2.

- Higher degrees of orientation are calculated in the current work compared with chapter 2; this is due to the extra shear contribution from the walls, not accounted for in the previous model.

CHAPTER 4

VISCOUS PROPULSION IN ACTIVE TRANSVERSELY ISOTROPIC MEDIA

In this chapter, Taylor's swimming sheet model is adapted to account for an aligned fibrous fluid; a variation on the previous work but within the theme of fibrous fluids for biological and medical application. We use Ericksen's transversely-isotropic constitutive equations to adapt Taylor's swimming sheet model to account for an aligned fibrous structure.

4.1 Introduction

Large organisms propel themselves through a fluid by utilising the inertia of the surrounding fluid. For very small organisms and cells swimming at low Reynolds numbers, inertial propulsion is not possible [26, 54]; time-reversible kinematics result in no net displacement for the small body. G.I. Taylor's 'swimming sheet' is one of the classical models of zero-Reynolds-number swimming; time-reversal symmetry is broken by the wave direction.

These cells and organisms encounter many biological fluids with non-Newtonian properties; hence modelling swimming in such fluids is of interest. The present study is motivated by the fibrous nature of many biological media, for example the cervical mucus encountered by spermatozoa in many internally-fertilising species. Throughout the menstrual cycle, the rheology of cervical mucus changes due to hormonally-induced variations in hydration and associated changes in the glycofilament mucin structure. During ovula-

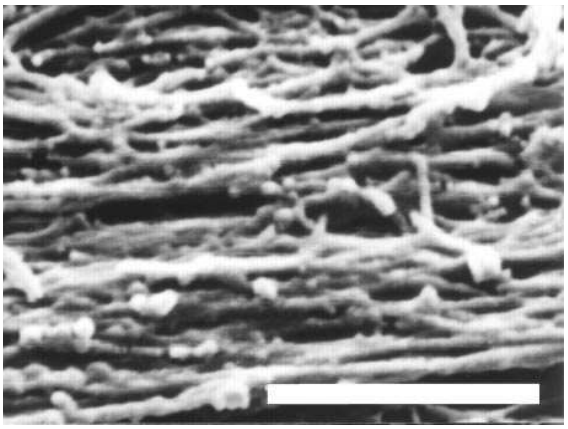

Figure 4.1: Parallel filament mesh in cervical mucus during the time of ovulation. Bar = 10 μm. Republished with permission of Oxford University Press, from 'Ultrastructure of the Human Periovulatory Cervical Mucus', F. Ceric et al, 54 (5), 2005; permission conveyed through Copyright Clearance Center, Inc.

tion these fibres form a parallel network (figure 4.1), and sperm migration occurs through this glycofilament structure [8, 14]. Whilst this work differs from chapters 2 and 3, it is of great interest to determine how Stokesian swimming is modified by the presence of an aligned fibrous network; understanding the propulsive efficiency of spermatozoa can aid with understanding infertility.

Taylor's pioneering study of Stokesian swimming consists of an infinite sheet undergoing waves of lateral displacement (figure 4.2). This model was formulated as the far-field Stokes flow produced by a swimming motion given by a small amplitude sinusoidal wave, and the associated mean rate of working was calculated as a measure of the energetic cost of swimming. Subsequent studies included a 3D model of a waving cylindrical tail [91], investigations into larger amplitude motion [20] and more recently the unsteady Stokes flow problem [73].

Generalising Taylor's model to non-Newtonian fluids has been an area of significant interest, for a detailed review see [54]. Chaudhury [9] initially extended the model to incorporate viscoelastic fluids; it was found that the properties of the fluid leads to an increased steady swimming velocity for lower Reynolds numbers. This problem was reconsidered more recently by Lauga [53], who deduced that the mean swimming velocity

in a nonlinear viscoelastic fluid is reduced relative to that in a Newtonian fluid, in certain cases the swimming direction is reversed [27], see also [28, 93]. Velez [94] found propulsion in shear-thinning fluids to be more efficient than in Newtonian or shear-thickening fluids. Riley [78] modelled active propulsion with fluid-structure interaction, and in a subsequent study deduced that for multiple travelling waves, the mean swimming velocity of the sheet is enhanced [79]. Further to this, the effect of liquid crystals on the swimming of micro-organisms was considered [49, 50, 51]. Steady state and start-up models for hexatic liquid crystals were considered along with a nematic steady state model.

The waving sheet model can be adapted for peristaltic pumping mechanisms, which have been studied in great detail. Peristaltic pumping has a wide range of applications, including the ureter, gastro-intestinal tract, small blood vessels [89], the movement of eggs in the fallopian tube and aiding the transport of spermatozoa though the cervical canal [32]. There is also an opportunity to utilise these pumping designs in the devices used by Linear Diagnostics Ltd; providing a method to recirculate a sample without it coming into contact with the pumping mechanism. These studies have comprised an infinite sheet with long wavelength sinusoidal waves propagating along it [85] with applications to the ureter [61]. For detailed review of initial works see [43]. Extensions to the solution method have encompassed finite difference approximations [89], boundary integral methods [77] and an asymptotic expansion for arbitrary wave shapes [64]. Peristaltic pumping of complex fluids has been a vast area of development; some examples are in viscoelastic fluids [6, 92] and micropolar fluids [32].

A transversely-isotropic fluid exhibits a (perhaps spatially and temporally varying) preferred direction, and has been used to model fibre-laden fluids. Previous applications include the mechanical behaviour of collagen gel, the growth of plant root cell walls, suspensions of biomolecules and a multiphase model of extracellular matrix [21, 22, 31, 40]. These models comprise a modified constitutive equation describing a viscous fluid with suspended aligned fibres and an expression for the evolution of fibre orientation. A transversely-isotropic fluid also provides a model of 'active' suspensions of elongated

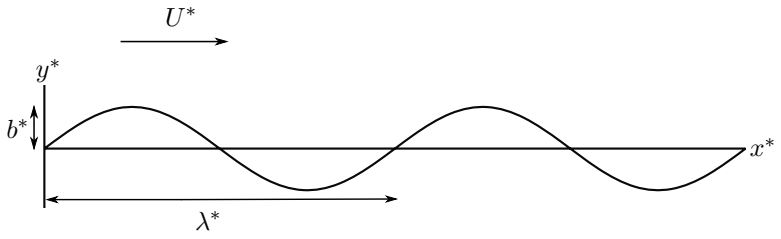

Figure 4.2: A schematic of Taylor's swimming sheet in a Newtonian fluid. Working in a frame of reference in which the sheet is stationary, b^* is the amplitude, $\lambda^* = 2\pi/k^*$ is the wavelength and k^* is the wavenumber. The flow at infinity in the x^*-direction is U^*. A travelling wave traverses the sheet with speed $c^* = \omega^*/k^*$ where ω^* is the angular velocity.

swimmers [39].

In this chapter we consider swimming in transversely-isotropic fluids via Ericksen's constitutive law [24], a specific case of the active fluid model introduced in chapter 1 where the particles are perfectly aligned. In section 4.2 we introduce the governing equations associated with transversely-isotropic fluids. The problem is solved in section 4.3, solving for the leading order velocity field, mean swimming velocity at next order and mean rate of working. The dependence of these quantities on the rheological parameters is explored in section 4.4, and discussed in section 4.5.

4.2 Governing equations for perfectly aligned fluids

The incompressibility and generalised Navier-Stokes equations are

$$\nabla^* \cdot \mathbf{u}^* = 0, \tag{4.1}$$

$$\rho^* \left(\frac{\partial \mathbf{u}^*}{\partial t^*} + (\mathbf{u}^* \cdot \nabla^*)\mathbf{u}^* \right) = \nabla^* \cdot \boldsymbol{\sigma}^*, \tag{4.2}$$

where $\boldsymbol{u}^* = (u^*, v^*)$ is velocity, ρ^* is density and $\boldsymbol{\sigma}^*$ is the stress tensor. We work in a 2D Cartesian coordinate system (x^*, y^*); asterisk notation represents dimensional variables. A constitutive law is also required for $\boldsymbol{\sigma}^*$, which we prescribe in the next section.

4.2.1 Transversely-isotropic stress tensor

Ericksen's model [24] consists of a stress tensor which is linear in strain rate, and depends on a unit vector $\boldsymbol{a}$ describing the fibre orientation; this model takes the simplest form that satisfies the required invariances,

$$\sigma^*_{ij} = -p^*\delta_{ij} + 2\mu^* e^*_{ij} + \mu^*_1 a_i a_j + \mu^*_2 a_i a_j a_k a_l e^*_{kl} + 2\mu^*_3 (a_l a_i e^*_{lj} + a_m a_j e^*_{im}). \tag{4.3}$$

We define p^* as the pressure, δ_{ij} as the Kronecker delta function and $e^*_{ij} = \frac{1}{2}\left(\frac{\partial u^*_i}{\partial x^*_j} + \frac{\partial u^*_j}{\partial x^*_i}\right)$ as the rate-of-strain tensor [24].

By considering a simple fluid with 2D deformations in the plane of fibres [22], we may interpret the rheological parameters as follows: by setting $\mu^*_1 = \mu^*_2 = \mu^*_3 = 0$, the stress tensor for an incompressible Newtonian fluid remains, with 'matrix viscosity' μ^* [40]. The term with μ^*_1 has no dependence on velocity, suggesting that μ^*_1 relates to a tension in the fibre direction [22]. This term can also be related to the stresslet-type active behaviour of fibres in a perfectly aligned active fluid [39]. We will therefore refer to this quantity as the *active parameter*. This term can be taken as a simple model for suspensions of self-propelling microscopic bodies such as bacteria or active gels of molecular motor proteins. The viscosity associated with extensional flow parallel to the fibre direction is $\mu^*_{||} = \mu^* + (\mu^*_2 + 4\mu^*_3)/2$, the viscosity associated with the flow orthogonal to the fibre direction is $\mu^*_\perp = \mu^*$ and the viscosity of shear flow in the fibre direction is $\mu^*_s = \mu^* + \mu^*_3$ [22]. Since μ^*_2 only has an impact on extensional viscosity parallel to the fibre direction, $\mu^*_{||}$, it is termed the *anisotropic extensional viscosity*. The parameter μ^*_3 distinguishes $\mu^*_\perp$ from μ^*_s and so is labelled the *anisotropic shear viscosity*; this parameter represents the difference between shear viscosities parallel and perpendicular to the fibre direction [22, 31, 40].

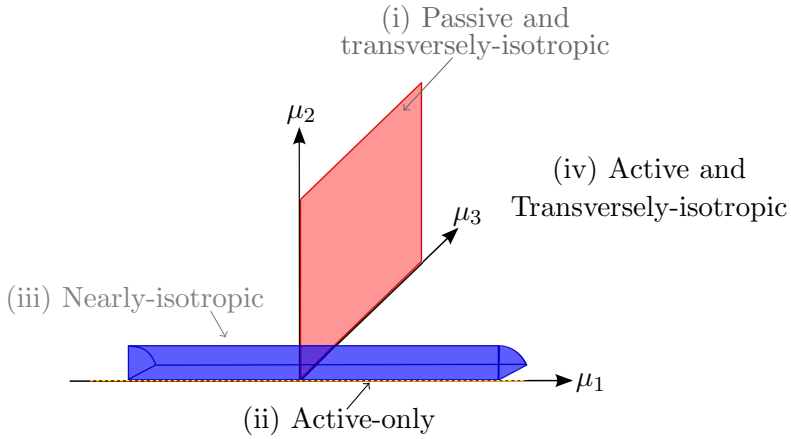

Figure 4.3: Regimes of interest in parameter space. (i) The plane $\mu_1 = 0$ is the passive transversely-isotropic regime, (ii) the dashed line represents the active-only regime where $\mu_2 = \mu_3 = 0$, (iii) the quarter cylinder is the nearly-isotropic regime where neither μ_2 nor μ_3 are large and (iv) the remaining region is the fully active and transversely-isotropic regime.

4.2.2 Fibre evolution equation

A fibre evolution equation describes the evolution of fibre orientation with time. We use the form given by [31],

$$\frac{\partial \boldsymbol{a}}{\partial t^*} + \boldsymbol{u}^* \cdot \nabla^* \boldsymbol{a} + [\boldsymbol{a} \cdot (\boldsymbol{a} \cdot \nabla^* \boldsymbol{u}^*)]\boldsymbol{a} = \boldsymbol{a} \cdot \nabla^* \boldsymbol{u}^*, \tag{4.4}$$

which corresponds to a specific case of Ericksen's [24] equation in the long-fibre limit. Note that $|\boldsymbol{a}| = 1$ and thus the model only considers local alignment of fibres and not their length. This gives a generalised form of Jeffery's treatment for long ellipsoidal particles aligning with flow [22, 44].

Since $\boldsymbol{a} \cdot \boldsymbol{a} = 1$, the component of equation (4.4) in the $\boldsymbol{a}$-direction is automatically satisfied. The orthogonal component of equation (4.4) is

$$\boldsymbol{a}^{\perp} \cdot \left[\frac{\partial \boldsymbol{a}}{\partial t^*} + \boldsymbol{u}^* \cdot \nabla^* \boldsymbol{a} + [\boldsymbol{a} \cdot (\boldsymbol{a} \cdot \nabla^* \boldsymbol{u}^*)]\boldsymbol{a} - \boldsymbol{a} \cdot \nabla^* \boldsymbol{u}^* \right] = 0, \tag{4.5}$$

where $\boldsymbol{a}^{\perp}$ is a unit vector perpendicular to $\boldsymbol{a}$.

4.2.3 Boundary conditions

We work in a frame of reference moving with the swimmer in the x^*-direction; the horizontal flow as $y^* \to \infty$ therefore gives the mean swimming velocity. No-slip conditions on the sheet, representing a travelling wave with speed $c^* = \omega^*/k^*$, are thus

$$u^* = 0, \quad v^* = -\omega^* b^* \cos(k^* x^* - \omega^* t^*), \quad \text{on } y^* = y_s^* = b^* \sin(k^* x^* - \omega^* t^*). \tag{4.6}$$

The parameter b^* is amplitude, k^* is wave number, y_s^* is the equation of the sheet surface and $\lambda^* = 2\pi/k^*$ is wavelength. The velocity must remain bounded as $y^* \to \infty$.

4.2.4 Non-dimensionalisation

The model is non-dimensionalised as follows:

$$\boldsymbol{u^*} = \frac{\omega^*}{k^*}\boldsymbol{u}, \quad \boldsymbol{x}^* = \frac{\boldsymbol{x}}{k^*}, \quad t^* = \frac{t}{\omega^*}, \quad p^* = \omega^*\mu^* p, \quad \boldsymbol{\sigma}^* = \omega^*\mu^*\boldsymbol{\sigma}. \tag{4.7}$$

The continuity and fibre evolution equations are unchanged. For microscopic swimmers, the Reynolds number, $Re = \rho^*\omega^*/k^{*2}\mu^*$, is much less than one so we neglect inertial terms. The resulting system of partial differential equations is therefore

$$\nabla \cdot \boldsymbol{u} = 0, \tag{4.8}$$

$$\nabla \cdot \boldsymbol{\sigma} = \boldsymbol{0}, \tag{4.9}$$

$$\boldsymbol{a}^\perp \cdot \left[\frac{\partial \boldsymbol{a}}{\partial t} + \boldsymbol{u}\cdot\nabla\boldsymbol{a} + [\boldsymbol{a}\cdot(\boldsymbol{a}\cdot\nabla\boldsymbol{u})]\boldsymbol{a} - \boldsymbol{a}\cdot\nabla\boldsymbol{u}\right] = 0, \tag{4.10}$$

where

$$\sigma_{ij} = -p\delta_{ij} + 2e_{ij} + \mu_1 a_i a_j + \mu_2 a_i a_j a_k a_l e_{kl} + 2\mu_3(a_l a_i e_{lj} + a_m a_j e_{im}), \tag{4.11}$$

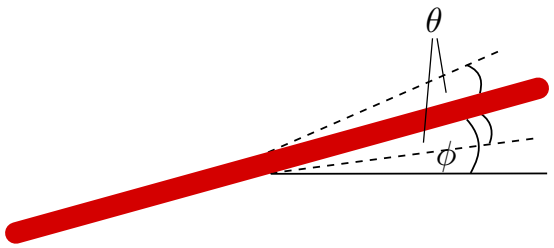

Figure 4.4: A schematic showing the initial uniform orientation angle ϕ and the small perturbation away from this angle, θ.

with dimensionless groups,

$$\mu_1 = \frac{\mu_1^*}{\mu^*\omega^*}, \qquad \mu_2 = \frac{\mu_2^*}{\mu^*}, \qquad \mu_3 = \frac{\mu_3^*}{\mu^*}. \tag{4.12}$$

The boundary conditions (4.6) become

$$u = 0, \quad v = -\varepsilon\cos(x-t), \quad \text{on } y = y_s = \varepsilon\sin(x-t), \tag{4.13}$$

where $\varepsilon = k^*b^* \ll 1$. Also u, v must remain bounded as $y \to \infty$.

Four regimes in parameter space, depicted in figure 4.3, will be considered in our results: (i) a passive transversely-isotropic fluid, occurring when $\mu_1 = 0$, (ii) an active fluid (μ_1 non-zero) with $\mu_2 = \mu_3 = 0$, (iii) a nearly-isotropic regime, where all parameters take values up to 5, and (iv) the regime where at least one of μ_1, μ_2 and μ_3 are much larger than one. Note that μ_1 may be positive or negative, representing active 'puller' or 'pusher' behaviour respectively [80].

4.3 Asymptotic solution

4.3.1 Stream function formulation

To determine the effect of fibres on the mean swimming velocity we consider an initially spatially-uniform fibre angle, ϕ, aligned such that $\boldsymbol{a}(x, y, 0) = (\cos\phi, \sin\phi)$. As the sheet

swims this alignment will evolve, initially as a small perturbation $\theta(x, y, t)$ such that

$$\begin{aligned} \boldsymbol{a} &= (\cos(\phi+\theta), \sin(\phi+\theta)) \\ &\approx (\cos\phi - \theta\sin\phi, \sin\phi + \theta\cos\phi), \end{aligned} \tag{4.14}$$

(see figure 4.4). The components of the stress tensor in terms of ϕ and θ are given in Appendix C.1. Taking the curl of equation (4.9) eliminates pressure, reducing (4.9) to a single equation. Since the flow is incompressible, we introduce a dimensionless stream function

$$u = \frac{\partial\psi}{\partial y}\,, \quad v = -\frac{\partial\psi}{\partial x}\,, \tag{4.15}$$

transforming equation (4.9) to

$$\begin{aligned} &(1+\frac{\mu_2}{4}\sin^2 2\phi+\mu_3)\nabla^4\psi - \mu_1\left[2\sin 2\phi\left(\theta\left(\frac{\partial^2\theta}{\partial y^2}-\frac{\partial^2\theta}{\partial x^2}\right)+\left(\frac{\partial\theta}{\partial y}\right)^2-\left(\frac{\partial\theta}{\partial x}\right)^2\right.\right. \\ &\qquad\left.\left.+\frac{\partial^2\theta}{\partial x\partial y}\right)+\cos 2\phi\left(\frac{\partial^2\theta}{\partial x^2}-\frac{\partial^2\theta}{\partial y^2}+4\left(\frac{\partial\theta}{\partial x}\frac{\partial\theta}{\partial y}+\theta\frac{\partial^2\theta}{\partial x\partial y}\right)\right)\right] \\ &-\mu_2\left[\sin 4\phi\left(-\frac{\theta}{2}\left(\frac{\partial^4\psi}{\partial x^4}-3\frac{\partial^4\psi}{\partial x^2\partial y^2}+\frac{\partial^4\psi}{\partial y^4}\right)-\frac{\partial\theta}{\partial y}\left(\frac{\partial^3\psi}{\partial y^3}-3\frac{\partial^3\psi}{\partial x^2\partial y}\right)\right.\right. \\ &\qquad+\frac{1}{2}\left(\frac{\partial^2\theta}{\partial x^2}-\frac{\partial^2\theta}{\partial y^2}\right)\left(\frac{\partial^2\psi}{\partial y^2}-\frac{\partial^2\psi}{\partial x^2}\right)+2\frac{\partial^2\theta}{\partial x\partial y}\frac{\partial^2\psi}{\partial x\partial y} \\ &\qquad+\frac{\partial\theta}{\partial x}\left(3\frac{\partial^3\psi}{\partial x\partial y^2}-\frac{\partial^3\psi}{\partial x^3}\right)+\theta\frac{\partial^4\psi}{\partial x^2\partial y^2}+\frac{1}{2}\left(\frac{\partial^4\psi}{\partial x^3\partial y}-\frac{\partial^4\psi}{\partial x\partial y^3}\right)\Bigg) \\ &\quad+\cos 4\phi\left(2\theta\left(\frac{\partial^4\psi}{\partial x^3\partial y}-\frac{\partial^4\psi}{\partial x\partial y^3}\right)+\left(\frac{\partial^2\theta}{\partial x^2}-\frac{\partial^2\theta}{\partial y^2}\right)\frac{\partial^2\psi}{\partial x\partial y}\right. \\ &\qquad-\frac{\partial\theta}{\partial x}\left(\frac{\partial^3\psi}{\partial y^3}-3\frac{\partial^3\psi}{\partial x^2\partial y}\right)-\frac{\partial\theta}{\partial y}\left(3\frac{\partial^3\psi}{\partial x\partial y^2}-\frac{\partial^3\psi}{\partial x^3}\right) \\ &\qquad\left.\left.-\frac{\partial^2\theta}{\partial x\partial y}\left(\frac{\partial^2\psi}{\partial y^2}-\frac{\partial^2\psi}{\partial x^2}\right)-\frac{\partial^4\psi}{\partial x^2\partial y^2}\right)\right] = 0. \end{aligned} \tag{4.16}$$

When $\mu_1 = \mu_2 = \mu_3 = 0$, equation (4.16) reduces to the familiar biharmonic equation of Newtonian Stokes flow. The evolution equation (4.10) becomes

$$\begin{aligned}\frac{\partial\theta}{\partial t} + \left[\frac{\partial\psi}{\partial y}\frac{\partial\theta}{\partial x} - \frac{\partial\psi}{\partial x}\frac{\partial\theta}{\partial y}\right] + (\sin^2\phi + \frac{\theta}{2}\sin 2\phi)\frac{\partial^2\psi}{\partial y^2} \\ + (\sin 2\phi + \theta\cos 2\phi)\frac{\partial^2\psi}{\partial x\partial y} + (\cos^2\phi - \frac{\theta}{2}\sin 2\phi)\frac{\partial^2\psi}{\partial x^2} \\ + \theta\Bigg(\left[(\cos\phi - \theta\sin\phi)^2 - (\sin\phi + \theta\cos\phi)^2\right]\frac{\partial^2\psi}{\partial x\partial y} \\ + (\cos\phi - \theta\sin\phi)(\sin\phi + \theta\cos\phi)\left(\frac{\partial^2\psi}{\partial y^2} - \frac{\partial^2\psi}{\partial x^2}\right)\Bigg) = 0.\end{aligned} \tag{4.17}$$

The boundary conditions (4.13) become

$$\frac{\partial\psi}{\partial y} = 0, \quad \frac{\partial\psi}{\partial x} = \varepsilon\cos(x-t) \quad \text{on } y = \varepsilon\sin(x-t), \tag{4.18}$$

with ψ having bounded first derivatives as $y \to \infty$.

4.3.2 Perturbation expansion

To apply the boundary conditions at $y = 0$ rather than on the sheet, we make the small amplitude expansion

$$\left.\frac{\partial\psi}{\partial y}\right|_{y=0} + \varepsilon\sin(x-t)\left.\frac{\partial^2\psi}{\partial y^2}\right|_{y=0} + \ldots = 0, \tag{4.19}$$

$$\left.\frac{\partial\psi}{\partial x}\right|_{y=0} + \varepsilon\sin(x-t)\left.\frac{\partial^2\psi}{\partial y\partial x}\right|_{y=0} + \ldots = \varepsilon\cos(x-t). \tag{4.20}$$

The velocity and fibre angle perturbations thus take the form

$$\psi(x,y,t;\varepsilon) = \varepsilon\psi_0(x,y,t) + \varepsilon^2\psi_1(x,y,t) + \ldots \tag{4.21}$$

$$\theta(x,y,t;\varepsilon) = \varepsilon\theta_0(x,y,t) + \varepsilon^2\theta_1(x,y,t) + \ldots \tag{4.22}$$

As in Taylor's analysis, the background flow (*i.e.* the sheet swimming velocity) will occur at order ε^2.

4.3.3 Leading-order solution

Substituting the expansions into the equations (4.16) and (4.17) and equating coefficients of powers of ε yields the leading order partial differential equation. At order ε, equation (4.16) yields

$$\begin{aligned}(1+\frac{\mu_2}{4}\sin^2 2\phi+\mu_3)\nabla^4\psi_0-\mu_1\left(2\sin 2\phi\,\frac{\partial^2\theta_0}{\partial x\partial y}+\cos 2\phi\left(\frac{\partial^2\theta_0}{\partial x^2}-\frac{\partial^2\theta_0}{\partial y^2}\right)\right)\\ +\mu_2\left(\cos 4\phi\,\frac{\partial^4\psi_0}{\partial x^2\partial y^2}+\frac{\sin 4\phi}{2}\left(\frac{\partial^4\psi_0}{\partial x\partial y^3}-\frac{\partial^4\psi_0}{\partial x^3\partial y}\right)\right)=0,\end{aligned} \tag{4.23}$$

and equation (4.17)

$$\frac{\partial\theta_0}{\partial t}+\sin 2\phi\,\frac{\partial^2\psi_0}{\partial x\partial y}+\cos^2\phi\,\frac{\partial^2\psi_0}{\partial x^2}+\sin^2\phi\,\frac{\partial^2\psi_0}{\partial y^2}=0. \tag{4.24}$$

The boundary conditions (4.19) and (4.20) become

$$\frac{\partial\psi_0}{\partial y}=0,\quad \frac{\partial\psi_0}{\partial x}=\cos(x-t),\quad \text{on } y=0, \tag{4.25}$$

combined with the requirement that the derivatives of ψ_0 are bounded as $y\to\infty$.

Equations (4.23) and (4.24) are solved with the ansatz,

$$\psi_0 = f_1(y)\cos(x-t)+f_2(y)\sin(x-t), \tag{4.26}$$

$$\theta_0 = g_1(y)\cos(x-t)+g_2(y)\sin(x-t), \tag{4.27}$$

for some functions f_1, f_2, g_1, g_2. Comparing coefficients of sine and cosine leads to a

system of four ordinary differential equations

$$(1+\frac{1}{4}\mu_2\sin^2 2\phi+\mu_3)(f_1''''-2f_1''+f_1)+\mu_1(\cos 2\phi\,(g_1+g_1'')-2\sin 2\phi\,g_2') \\ +\mu_2(\frac{1}{2}\sin 4\phi\,(f_2'''+f_2'')-\cos 4\phi\,f_1'')=0, \tag{4.28}$$

$$(1+\frac{1}{4}\mu_2\sin^2 2\phi+\mu_3)(f_2''''-2f_2''+f_2)+\mu_1(\cos 2\phi\,(g_2+g_2'')+2\sin 2\phi\,g_1') \\ -\mu_2(\frac{1}{2}\sin 4\phi\,(f_1'''+f_1'')+\cos 4\phi\,f_2'')=0, \tag{4.29}$$

$$g_1-\sin 2\phi\,f_1'+\sin^2\phi\,f_2''-\cos^2\phi\,f_2=0, \tag{4.30}$$

$$g_2-\sin 2\phi\,f_2'-\sin^2\phi\,f_1''+\cos^2\phi\,f_1=0, \tag{4.31}$$

where the prime notation denotes differentiation with respect to y.

Substituting equations (4.30) and (4.31) into (4.28) and (4.29), the system reduces to two ordinary differential equations for f_1 and f_2,

$$(1+\frac{1}{4}\mu_2\sin^2 2\phi+\mu_3)(f_1''''-2f_1''+f_1)+\mu_1\Big(\frac{1}{2}\sin 4\phi(f_1'''+f_1') \\ -2\sin\phi\left(\sin^2\phi f_1'''-\cos^2\phi f_1'\right)\Big)-\mu_2\cos 4\phi f_1'' \\ +\mu_1\Big(\cos 2\phi\left(\cos^2\phi(f_2''+f_2)-\sin^2\phi(f_2''''+f_2'')\right)-2\sin^2 2\phi f_2''\Big) \\ +\frac{\mu_2}{4}\sin 4\phi(f_2'''+f_2''), \tag{4.32}$$

$$(1+\frac{1}{4}\mu_2\sin^2 2\phi+\mu_3)(f_2''''-2f_2''+f_2)+\mu_1\Big(\frac{1}{2}\sin 4\phi(f_2'''+f_2') \\ -2\sin\phi\left(\sin^2\phi f_2'''-\cos^2\phi f_2'\right)\Big)-\mu_2\cos 4\phi f_2'' \\ -\mu_1\Big(\cos 2\phi\left(\cos^2\phi(f_1''+f_1)-\sin^2\phi(f_1''''+f_1'')\right)-2\sin^2 2\phi f_1''\Big) \\ -\frac{\mu_2}{4}\sin 4\phi(f_1'''+f_1''). \tag{4.33}$$

Assuming a basis of solutions of the form

$$\begin{pmatrix} f_1 \\ f_2 \end{pmatrix} = \begin{pmatrix} f_1^0 \\ f_2^0 \end{pmatrix} e^{\lambda y}, \tag{4.34}$$

reduces the problem to the linear system,

$$\boldsymbol{L} \begin{pmatrix} f_1^0 \\ f_2^0 \end{pmatrix} = \begin{pmatrix} 0 \\ 0 \end{pmatrix} \quad \text{where} \quad \boldsymbol{L} = \begin{pmatrix} L_{11} & L_{12} \\ L_{21} & L_{22} \end{pmatrix}, \tag{4.35}$$

where components of $\boldsymbol{L}$ are given in Appendix C.2. Note that $L_{11} = L_{22}$ and further that $L_{12} = -L_{21}$. For a non-trivial solution, the determinant of the matrix $\boldsymbol{L}$ must be zero, yielding the equation

$$L_{11}^2 + L_{12}^2 = 0, \tag{4.36}$$

hence

$$L_{11} = \pm i L_{12}, \tag{4.37}$$

and so

$$\begin{aligned} f_2^0 &= -\frac{L_{11}}{L_{12}} f_1^0, \\ &= \mp i f_1^0. \end{aligned} \tag{4.38}$$

Equation (4.36) has eight complex roots, λ_j, four with positive real part and four with negative real part. Since the velocity must remain bounded as $y \to \infty$, we disregard the positive roots. The other four form two complex conjugate pairs,

$$\lambda_1 = \alpha_1 + i\beta_1, \qquad \lambda_3 = \alpha_1 - i\beta_1, \tag{4.39}$$

$$\lambda_2 = \alpha_2 + i\beta_2, \qquad \lambda_4 = \alpha_2 - i\beta_2. \tag{4.40}$$

Note that λ_j are known analytically, however they are not given here due to space constraints.

The solution form for ψ_0 is thus

$$\psi_0 = \sum_{j=1}^{4} \hat{A}_j(\cos(x-t) + \xi_j \sin(x-t))e^{\lambda_j y}, \tag{4.41}$$

where $\xi_j = -i$ for $j = 1, 2$ and $\xi_j = i$ for $j = 3, 4$. Assuming that the constants take the general form $\hat{A}_j = A_j + iB_j$ for $j = 1,\ 2,\ 3,\ 4$, boundary conditions (4.25) give

$$\begin{aligned}
A_1 &= \frac{\alpha_1\beta_2 - \alpha_2\beta_1}{2((\alpha_1-\alpha_2)^2 + (\beta_1-\beta_2)^2)}, \quad A_2 = -A_1, \quad A_3 = A_1, \quad A_4 = -A_1, \\
B_1 &= \frac{\alpha_2(\alpha_2-\alpha_1) + \beta_2(\beta_2-\beta_1)}{2((\alpha_1-\alpha_2)^2 + (\beta_1-\beta_2)^2)}, \quad B_3 = -B_1, \\
B_2 &= \frac{\alpha_1(\alpha_1-\alpha_2) + \beta_1(\beta_1-\beta_2)}{2((\alpha_1-\alpha_2)^2 + (\beta_1-\beta_2)^2)}, \quad B_4 = -B_2.
\end{aligned}$$

The fibre angle perturbation is then of the form

$$\begin{aligned}
\theta_0 = \sum_{j=1}^{4} \hat{A}_j \Big[&(\lambda_j \sin 2\phi + \xi_j(-\lambda_j^2 \sin^2\phi + \cos^2\phi)) \cos(x-t) \\
&+ (\xi_j\lambda_j \sin 2\phi + \lambda_j^2 \sin^2\phi - \cos^2\phi) \sin(x-t) \Big] e^{\lambda_j y}.
\end{aligned} \tag{4.42}$$

The change in the small perturbation to the orientation, θ_0, is dependent on the initial orientation angle of the fibres along with their position.

4.3.4 Order ε^2 solution and mean swimming velocity

The mean swimming velocity is determined by the horizontal component of the flow as y tends to infinity. The leading-order stream function, (4.41), tends to zero and hence the non-zero mean swimming velocity is determined at order ε^2

$$U \sim \varepsilon^2 U_1 = \lim_{y\to\infty} \varepsilon^2 \frac{\partial \psi_1}{\partial y}. \tag{4.43}$$

We neglect the oscillatory terms to determine the leading-order term in the expansion of mean swimming velocity, which we denote as $\overline{U}_1$. The bar notation represents an average over one time period.

At order ε^2, the boundary conditions (4.19) and (4.20) become

$$\left.\frac{\partial \psi_1}{\partial y}\right|_{y=0} + \sin(x-t)\left.\frac{\partial^2 \psi_0}{\partial y^2}\right|_{y=0} = 0, \quad \left.\frac{\partial \psi_1}{\partial x}\right|_{y=0} + \sin(x-t)\left.\frac{\partial^2 \psi_0}{\partial y \partial x}\right|_{y=0} = 0, \tag{4.44}$$

and hence

$$\begin{aligned}\left.\frac{\partial \psi_1}{\partial y}\right|_{y=0} = \frac{1}{2}\big((\alpha_1\alpha_2 - \beta_1\beta_2)(1-\cos 2(x-t)) \\ -(\alpha_1\beta_2 - \alpha_2\beta_1)\sin 2(x-t)\big),\end{aligned} \tag{4.45}$$

$$\left.\frac{\partial \psi_1}{\partial x}\right|_{y=0} = 0. \tag{4.46}$$

Because of the form of the boundary conditions, the ansatz is

$$\psi_1 = \hat{f}_1(y) + \hat{f}_2(y)\cos 2(x-t) + \hat{f}_3(y)\sin 2(x-t), \tag{4.47}$$

for some functions $\hat{f}_1$, $\hat{f}_2$ and $\hat{f}_3$. Substituting the solution form (4.47) into the order ε^2 expansion of (4.16), shown in full in Appendix C.3, and equating coefficients of non-oscillating terms, we have

$$\hat{f}_1'''' = 0, \tag{4.48}$$

and hence

$$\hat{f}_1(y) = Ay^3 + By^2 + Cy + D. \tag{4.49}$$

To ensure the velocity remains bounded as $y \to \infty$, we set $A = B = 0$. From the boundary conditions (4.45) and (4.46) we find that $C = (\alpha_1\alpha_2 - \beta_1\beta_2)/2$ and $D = 0$, and hence

$$\hat{f}_1(y) = \frac{y}{2}(\alpha_1\alpha_2 - \beta_1\beta_2). \tag{4.50}$$

Differentiating $\hat{f}_1(y)$ with respect to y, the leading-order term in the expansion of mean swimming velocity is calculated as

$$\overline{U}_1 = \frac{1}{2}(\alpha_1\alpha_2 - \beta_1\beta_2). \tag{4.51}$$

4.3.5 Mean rate of working

To determine how Stokesian swimming is affected by transverse isotropy, the mean rate of working at order ε is investigated, *i.e.* the rate of working per unit area of the sheet against viscous stress, $\varepsilon^2\overline{W}$ [90]. The mean value of this quantity is given by

$$\varepsilon^2\overline{W} = -\overline{\frac{\partial y_s}{\partial t}\sigma_{22}|_{y=0}}, \tag{4.52}$$

where y_s is the equation of the sheet surface and $\sigma_{22}|_{y=0}$ is the normal stress evaluated on the sheet. The no-slip condition is $u = 0$ on the sheet and hence $\partial u/\partial x = 0$ and, via (4.8), $\partial v/\partial y = 0$. In terms of the stream function, σ_{22} is

$$\sigma_{22} = -p + \mu_1 \sin^2\phi + (\mu_2 \cos\phi \sin^3\phi + \mu_3 \sin 2\phi)\left(\frac{\partial^2\psi}{\partial y^2} - \frac{\partial^2\psi}{\partial x^2}\right). \tag{4.53}$$

Solving equation (4.9), using the leading-order expression for the stream function (4.41), determines pressure. Noting that $\overline{\cos^2(x-t)} = 1/2$, we obtain an expression for the leading order term in the expansion of mean rate of working,

$$\begin{aligned}\overline{W} = -\frac{1}{16}\Big[&\big(\alpha_1^2\alpha_2 - \alpha_2\beta_1(\beta_1 + 2\beta_2) \\ &+\alpha_1(\alpha_2^2 - \beta_2(2\beta_1 + \beta_2))\big)\left(8 + \mu_2(1 + \cos 4\phi) + 8\mu_3\right) \\ &+ 4(\alpha_2\beta_1 + \alpha_1\beta_2)\mu_2 \sin 4\phi\Big].\end{aligned} \tag{4.54}$$

4.4 Results

The leading-order terms in the expansions of mean swimming velocity (4.51), mean rate of working (4.54), fibre perturbation (4.42), velocities $u_0 = \partial\psi_0/\partial y$, $v_0 = -\partial\psi_0/\partial x$ and stream function (4.41), have been found analytically in terms of lengthy expressions for α_j, β_j. The analytical results for the mean rate of working have been recreated numerically using finite differences and integration by the midpoint method. Each separate component has been verified along with the full solution. The solutions agreed to within a small degree of numerical error. For brevity we will refer to the time averages of the leading order terms in the expressions for swimming velocity and rate of working as the *mean swimming velocity* and *mean rate of working* respectively, and we will plot terms without the leading ε^2 factors as defined by $\overline{U}_1$, $\overline{W}$ in equations (4.43) and (4.52).

We now discuss the results in more detail. Four different flow regimes are considered (figure 4.3): (i) a passive transversely-isotropic fluid, occurring when $\mu_1 = 0$, (ii) an active fluid where $\mu_2 = \mu_3 = 0$ and μ_1 is non-zero, (iii) a nearly isotropic regime, where all parameters take values up to 5 and (iv) the regime where at least one of μ_1, μ_2 and μ_3 are much larger than one. A range of initial orientation angle ϕ, between 0 and 2π are considered for all regimes and the active parameter, μ_1, is allowed to take both positive and negative values to account for 'puller' and 'pusher' active behaviour respectively. Note that since the fibres have no directionality, the regime $\phi = 0$ to π is identical to $\phi = \pi$ to 2π.

4.4.1 Regime (i): Effect of passive fibres on mean swimming velocity and rate of working

Passive fibres exert no shear-independent force and have no self-propulsive properties, hence the active parameter μ_1 is set to zero. In this regime the mean swimming velocity takes on the Newtonian value, $\overline{U}_1 = 1/2$, and the mean rate of working is independent of the initial orientation angle ϕ. In figure 4.5 (a), the mean rate of working is always greater

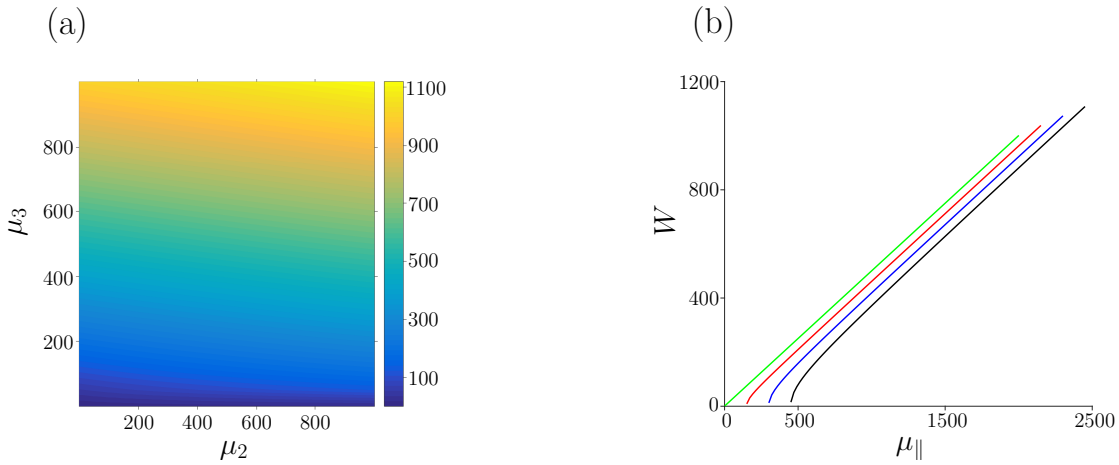

Figure 4.5: Mean rate of working by the swimmer in a transversely-isotropic fluid where $\mu_1 = 0$. (a) Depicts mean rate of working for varying μ_2 and μ_3. This result is identical for all initial angles ϕ. (b) Depicts how mean rate of working changes for increasing $\mu_\parallel$ for a range of μ_3 and set μ_2 values; $\mu_2 = 0$ (green line), $\mu_2 = 300$ (red line), $\mu_2 = 600$ (blue line) and $\mu_2 = 900$ (black line).

than or equal to the Newtonian case, $\overline{W} = 1$; the Newtonian solution is independent of viscosity and so the matrix viscosity μ is not varied throughout. The increase in mean rate of working is linear throughout, with μ_3 having a bigger impact than μ_2. Figure 4.5 (b) depicts the relationship between the mean rate of working and the parallel viscosity $\mu_\parallel = 1 + (\mu_2 + 4\mu_3)/2$, where each line represents a different μ_2. The increase in mean rate of working with $\mu_\parallel$ is linear, apart from the case where μ_3 is small and μ_2 is large, with a large mean rate of working as μ_2 increases.

4.4.2 Regime (ii): Active-only effects on mean swimming velocity and rate of working

The active-only regime considers $\mu_2 = \mu_3 = 0$ with μ_1 non-zero. The mean swimming velocity is considered in figure 4.6 and the mean rate of working in figure 4.7. For $\mu_1 = 0$ we regain the Newtonian result and hence both mean swimming velocity and mean rate of working are independent of fibre angle. For non-zero active parameter μ_1, the mean swimming velocity and mean rate of working vary considerably with fibre angle. In particular negative mean swimming velocity – *i.e.* reversal of swimming direction – and

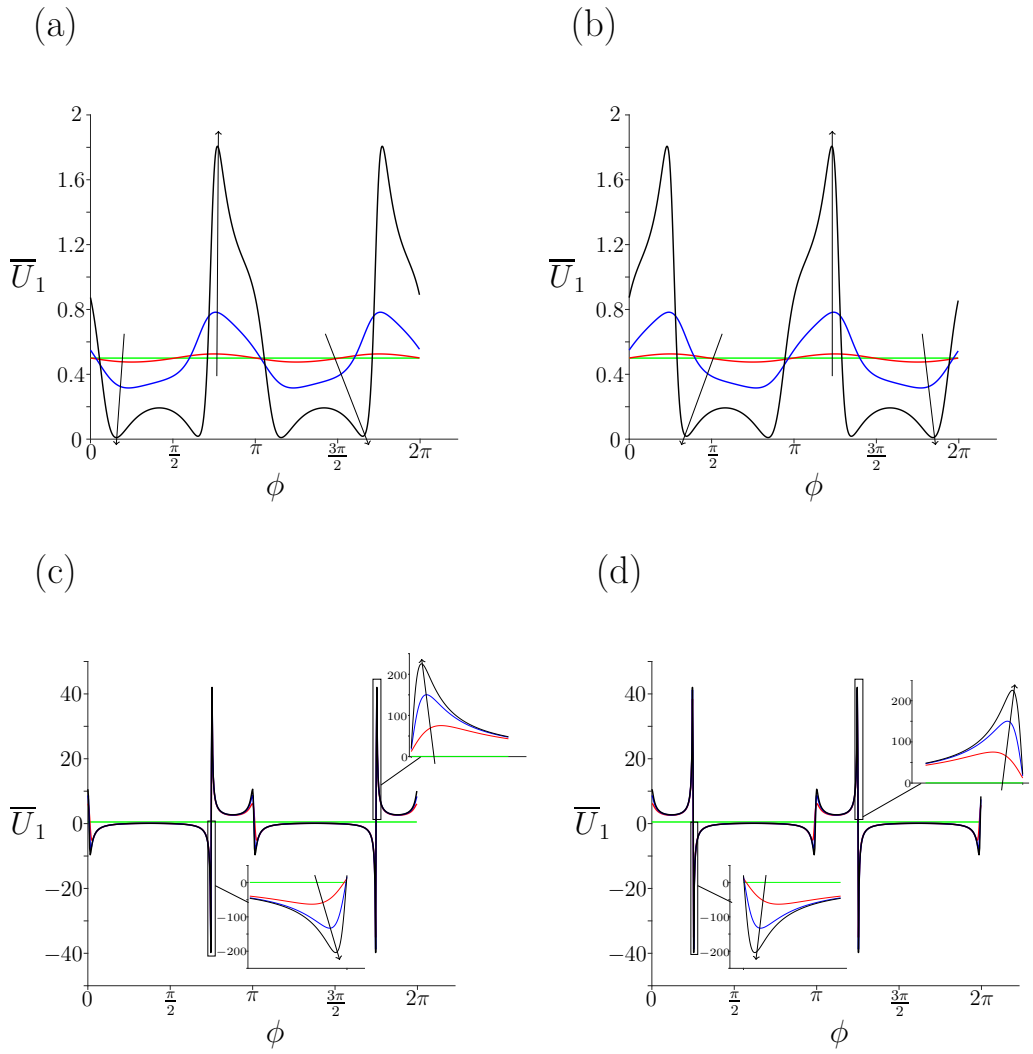

Figure 4.6: Mean swimming velocity versus the initial orientation ϕ, where $\mu_2 = \mu_3 = 0$. (a) and (b) depict small positive and negative μ_1 values: 0 (green line), ± 0.1 (red line), ± 1 (blue line) and ± 5 (black line). (c) and (d) depict larger μ_1 values; 0 (green line), ± 300 (red line), ± 600 (blue line), ± 900 (black line), where the arrows denote increasing μ_1.

negative mean rate of working are observed in certain regimes for large μ_1, with a sudden and dramatic switch in sign close to $\phi = 3\pi/4$ (figures 4.6 (c), (d) and 4.7 (c), (d)). Note that this can be resolved through refinement of the plotting grid and is not a discontinuity. A change from 'pusher' to 'puller' type active behaviour (equivalent to a change in sign of μ_1) is equivalent to a reflection in the line $\phi = \pi/2$ $(3\pi/2)$.

4.4.3 Regime (iii): Nearly-isotropic behaviour in leading order mean swimming velocity and rate of working

A small perturbation away from the isotropic case is considered here; μ_1, μ_2 and μ_3 take values up to 5. When μ_1 is much smaller than one and positive (figures 4.8 (a) and (b)) a small perturbation away from the Newtonian case is observed. As μ_1 continues to increase, angular dependence becomes more prevalent. For the mean swimming velocity, μ_2 has minimal impact, while μ_3 reduces the range of values the background flow can take. For the mean rate of working (figure 4.9), μ_2 again has little impact on the results and the effect of increasing μ_3 is to increase the cost of swimming. When $\mu_1 = \pm 5$ (figures 4.9 (e) and (f)), the mean rate of working may become negative and the effect of increasing μ_3 is to reduce the range of values the mean rate of working will take.

4.4.4 Regime (iv): The effect of large rheological parameters on leading order mean swimming velocity and rate of working

The final regime is where at least one of μ_1, μ_2 and μ_3 are much larger than one. Figures 4.10 and 4.11 depict how the mean swimming velocity and mean rate of working change with initial orientation angle, ϕ. When either μ_2 or μ_3 are non-zero, the steep peaks which occurred at $\phi = 3\pi/4\,(7\pi/4)$ (figure 4.6 (c)) and at $\phi = \pi/4\,(5\pi/4)$ (figure 4.6 (d)) within regime (ii) no longer appear. Further, when μ_2 is non-zero and $\mu_3 = 0$, the mean swimming velocity becomes negative for certain initial orientation angles, *i.e.* the swimming direction is reversed. When μ_3 becomes non-zero, the results collapse down towards the Newtonian case, altered predominantly by the active parameter, μ_1. Similar

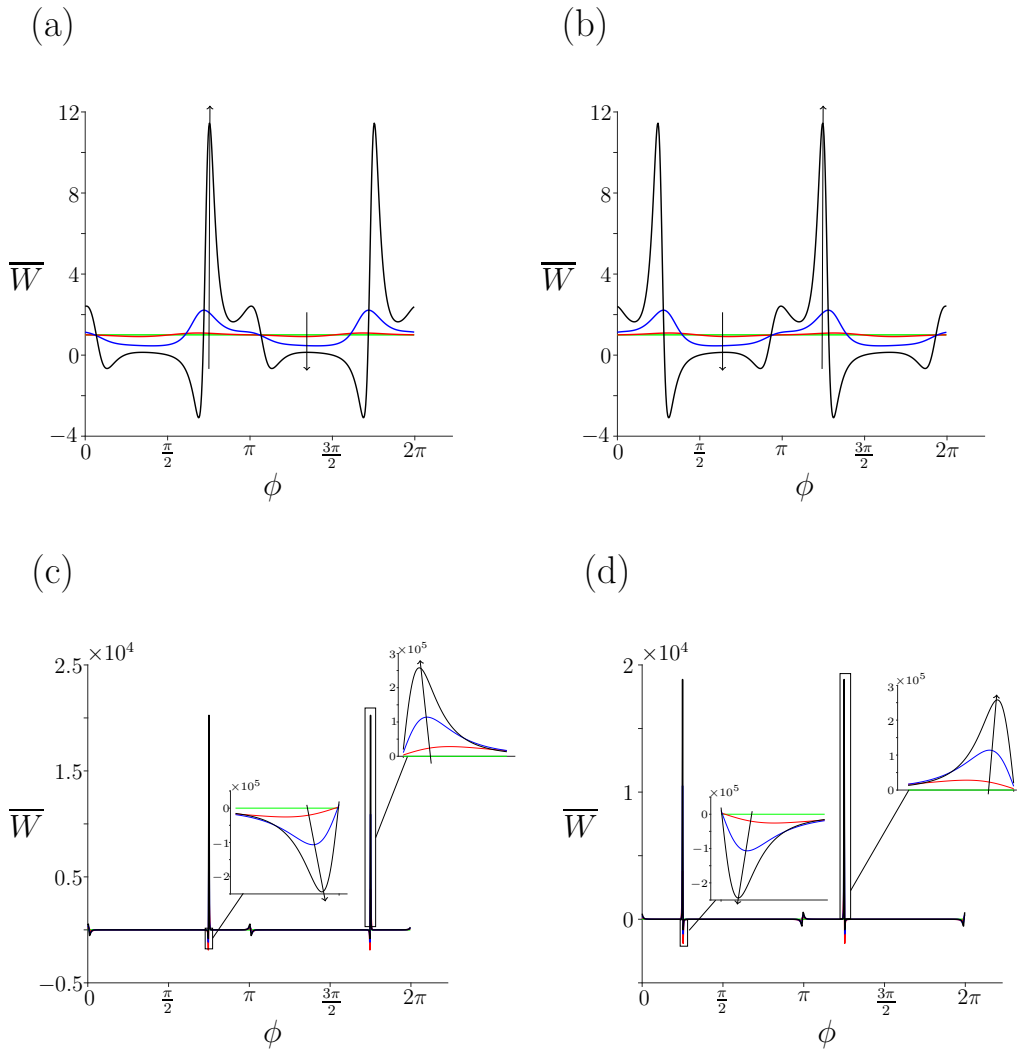

Figure 4.7: Mean rate of working versus the initial orientation ϕ, where $\mu_2 = \mu_3 = 0$. (a) and (b) depict small positive and negative μ_1 values: 0 (green line), ± 0.1 (red line), ± 1 (blue line) and ± 5 (black line). (c) and (d) depict larger μ_1 values; 0 (green line), ± 300 (red line), ± 600 (blue line), ± 900 (black line), where the arrows denote increasing μ_1.

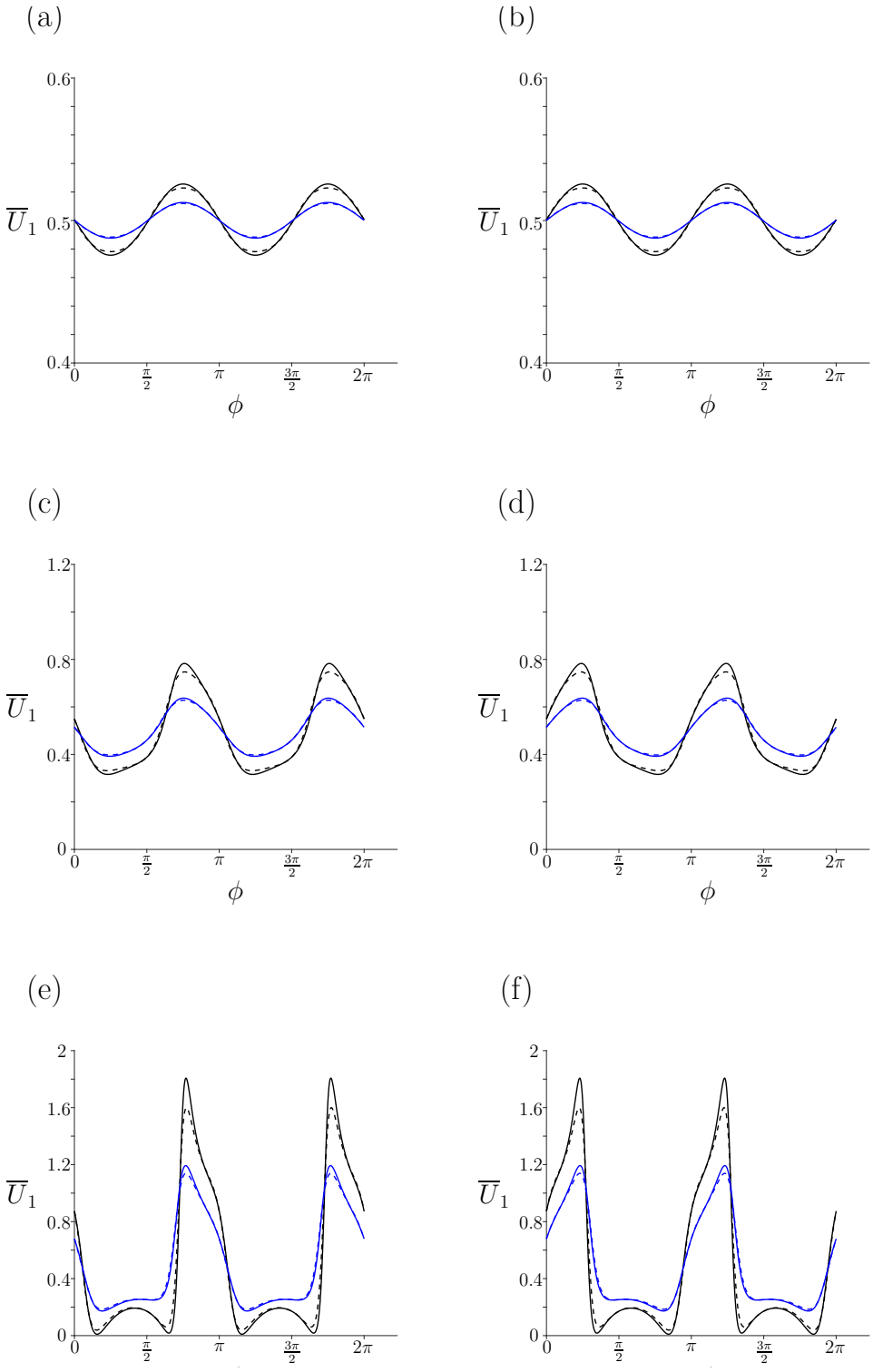

Figure 4.8: Mean swimming velocity versus ϕ where parameters μ_1, μ_2 and μ_3 take values up to 5. (a) and (b) show $\mu_1 = \pm 0.1$, (c) and (d) show $\mu_1 = \pm 1$ and (e) and (f) show $\mu_1 = \pm 5$. Two choices are taken for μ_3: $\mu_3 = 0$ (blue line) and $\mu_3 = 1$ (black line). For each of these, two different μ_2 values are taken: $\mu_2 = 0$ (solid line) and $\mu_2 = 1$ (dashed line).

results are seen for the mean rate of working, however for non-zero μ_3 (figure 4.11 (c) and (d)) the reference value about which variations occur is significantly increased.

4.4.5 Orientation, velocity and stream function

Finally, to understand how fibre orientation and velocity are impacted by the anisotropic fluid properties, the orientation angle ($\phi + \theta$) and velocity are considered in an active and passive regime, and the stream function is considered in all four regimes of interest (figures 4.12, 4.13 and 4.14 respectively). Each variable is plotted for one wavelength of the sheet, $x = 0$ to 2π. We focus on the case where the fibres are aligned with the sheet, *i.e.* $\phi = 0$ and plot results at time $t = 0$ (*i.e.* the start of one oscillation period). Supplementary movies can be found alongside the online publication of this work [16].

Considering first the fibre orientation, in all cases perturbations to the initial orientation angle are greater in the vicinity of the sheet and are displaced with the movement of the sheet (figure 4.12). For passive rheology, the fibre reorientation is dampened very quickly moving away from the sheet (figure 4.12 (a)). Once μ_1 is non-zero, fibre displacement appears further away from the sheet (figures 4.12 (b)) and movements propagate to the right.

Figure 4.13 shows the velocity components in x and y. The leading-order velocity decays quickly moving away from the sheet, evident in figure 4.13 (a); in the active-only regime (figure 4.13 (b)) the flow decays more slowly. The velocity field shows a similar rightward propagation to fibre angle in the active fluid case (figures 4.12 (b) and 4.13 (b)). These results are mirrored in figure 4.14, where the streamlines of the resulting flow are displayed. In the passive regime (i), the streamlines are symmetric about $x = \pi$ with anticlockwise flow between $x = 0$ and π and clockwise flow for $x = \pi$ to 2π. Introducing μ_1 distorts the streamlines and, when $\mu_2 = \mu_3 = 0$, the streamlines are deflected to the right (figure 4.14(b)); introducing the other two parameters dampens this deflection (figures 4.14 (c) and (d)).

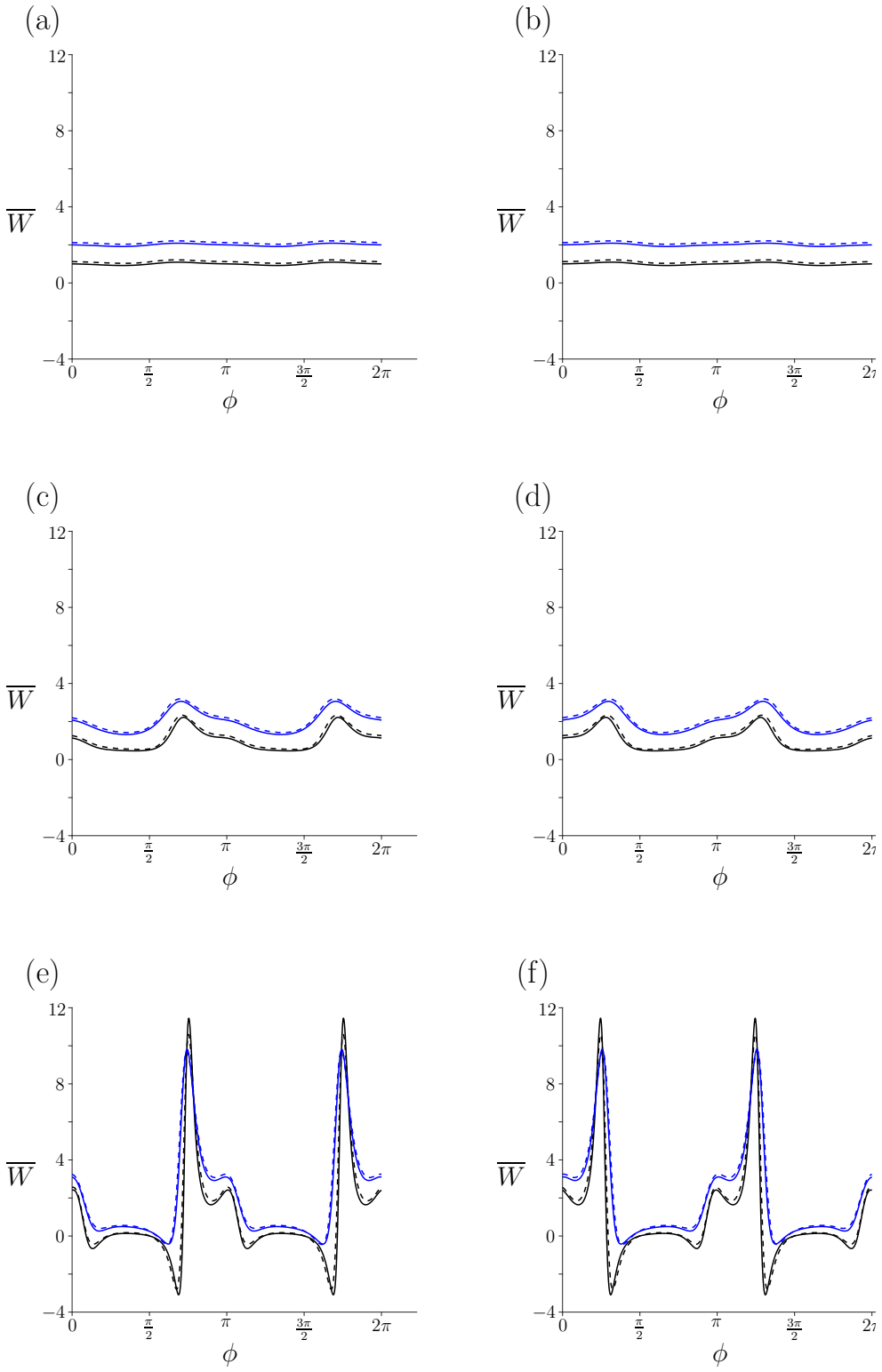

Figure 4.9: Mean rate of working versus ϕ where parameters μ_1, μ_2 and μ_3 take values up to 5. (a) and (b) show $\mu_1 = \pm 0.1$, (c) and (d) show $\mu_1 = \pm 1$ and (e) and (f) show $\mu_1 = \pm 5$. Two choices are taken for μ_3: $\mu_3 = 0$ (blue line) and $\mu_3 = 1$ (black line). For each of these, two different μ_2 values are taken: $\mu_2 = 0$ (solid line) and $\mu_2 = 1$ (dashed line).

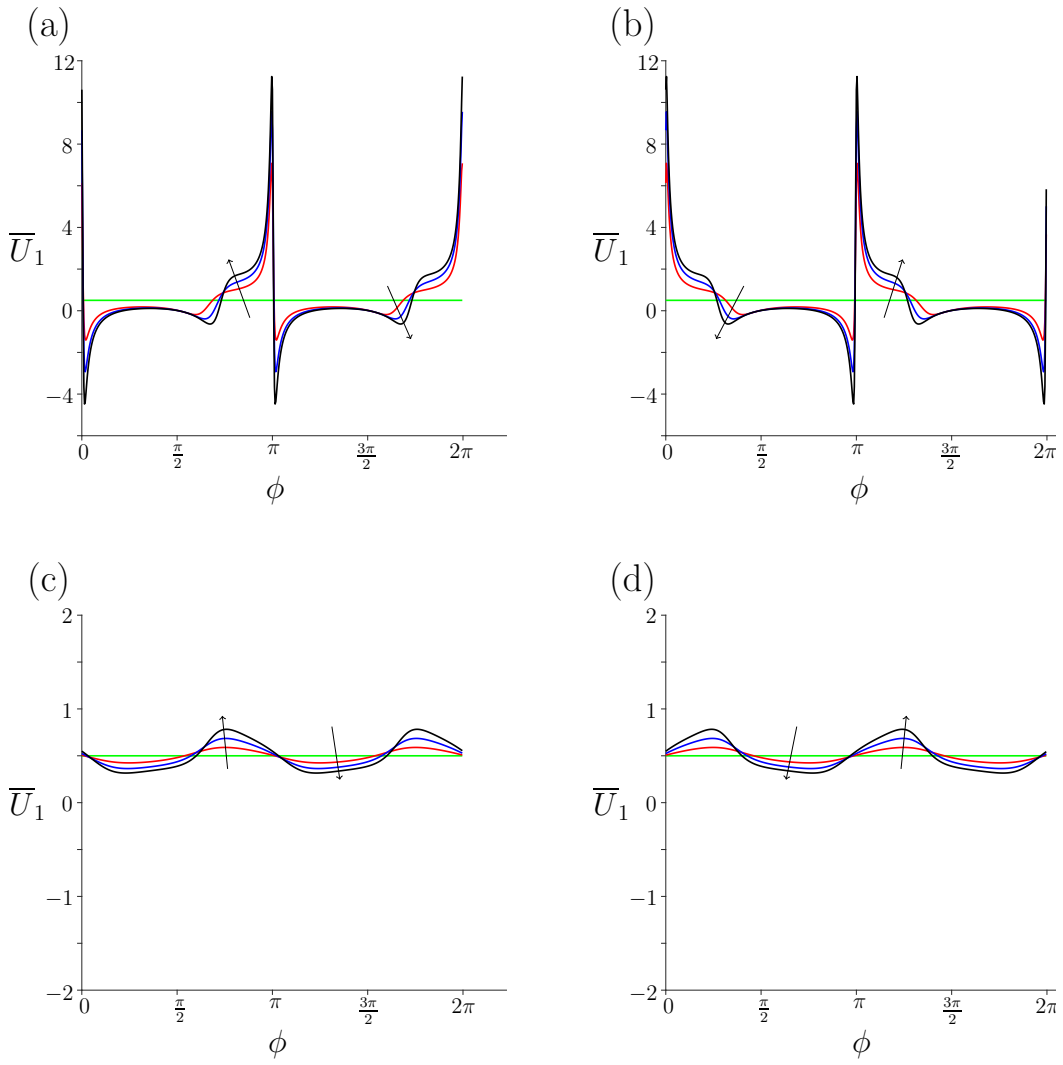

Figure 4.10: Mean swimming velocity versus ϕ where at least one of μ_1, μ_2 and μ_3 are much larger than one. (a) and (c) depict positive μ_1 values and (b) and (d) depict negative μ_1 values. The values μ_1 takes are 0 (green line), ± 300 (red line), ± 600 (blue line) and ± 900 (black line). In (a) and (b), $\mu_2 = 900$, $\mu_3 = 0$ and in (c) and (d), $\mu_2 = 0$, $\mu_3 = 900$, where the arrows denote increasing μ_1.

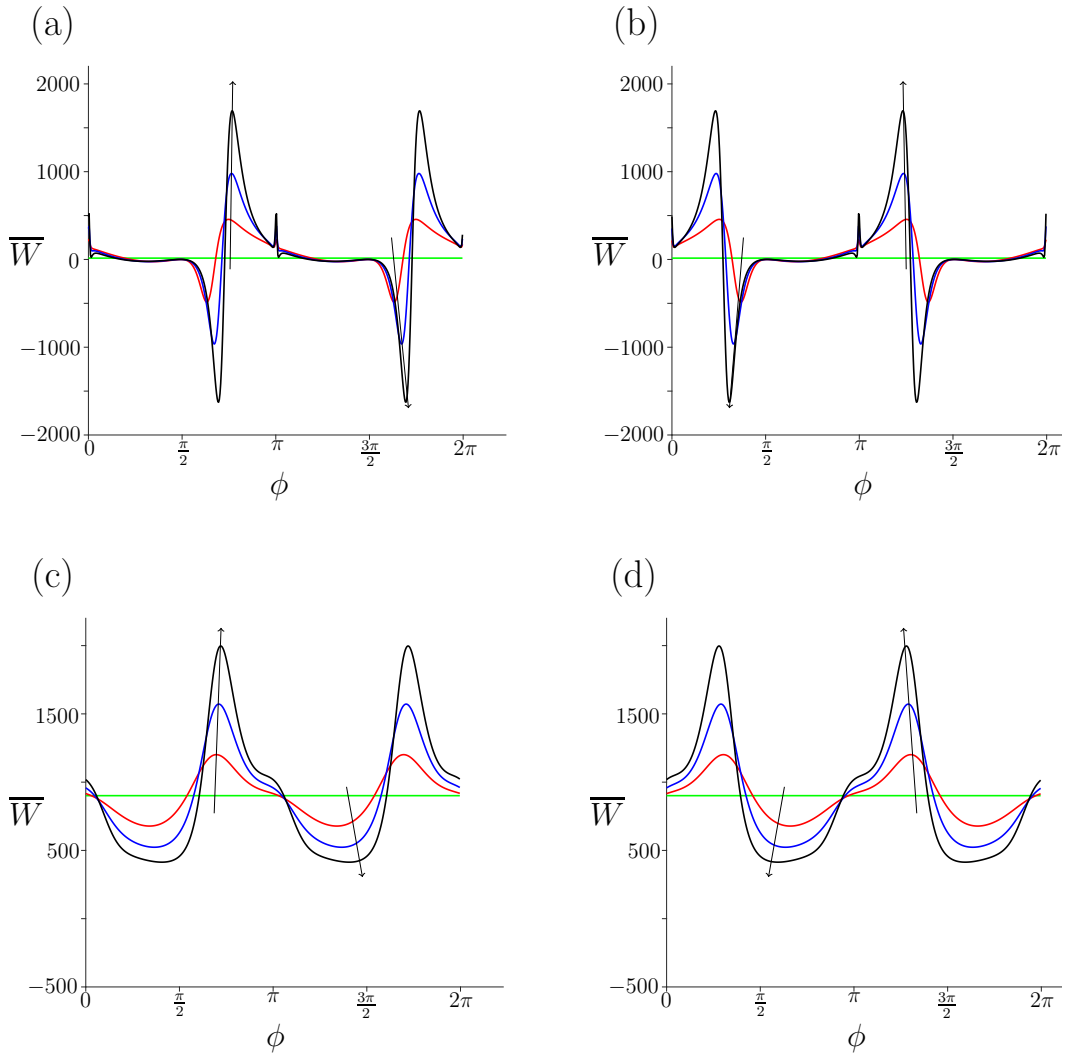

Figure 4.11: Mean rate of working versus ϕ where at least one of μ_1, μ_2 and μ_3 are much larger than one. (a) and (c) depict positive μ_1 values and (b) and (d) depict negative μ_1 values. The values μ_1 takes are 0 green line), ± 300 (red line), ± 600 (blue line) and ± 900 (black line). In (a) and (b), $\mu_2 = 900$, $\mu_3 = 0$ and in (c) and (d), $\mu_2 = 0$, $\mu_3 = 900$, where the arrows denote increasing μ_1.

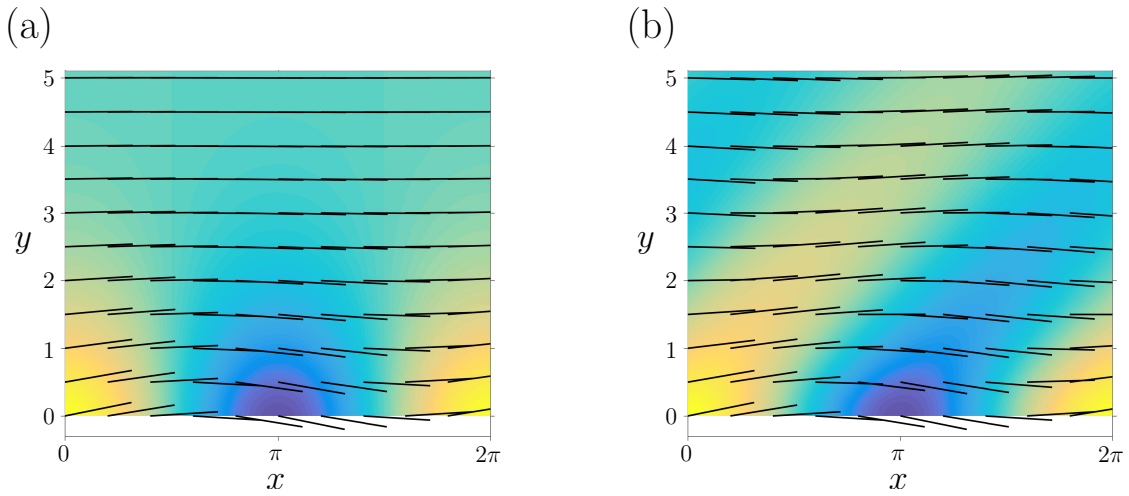

Figure 4.12: Fibre angle, $\phi + \varepsilon\theta_0$, in passive and active regimes: (a) the passive regime ($\mu_1 = 0$, $\mu_2 = \mu_3 = 5$) and (b) the active-only regime ($\mu_1 = 5$, $\mu_2 = \mu_3 = 0$). In each graph $t = 0$, $\varepsilon = 0.2$ and the initial orientation angle is $\phi = 0$.

4.5 Discussion

The classical Taylor's swimming sheet problem was modified to account for transverse isotropy, modelling swimming in fibre-laden fluids or active media. Quantities of interest were the steady background flow, which corresponds to the mean swimming velocity, and mean rate of working. The results presented were non-dimensional; the dimensional velocity scales with the wave speed, and the rate of working scales with the square of the frequency, the viscosity and the wavenumber. The ratio of the mean swimming speed to the wave speed is proportional to $1/\varepsilon^2$. When $\overline{U}_1$ takes the maximum value found here, such that $\overline{U}_1 \approx 40$, this corresponds to swimming faster than the wave speed when $\varepsilon > 1/\sqrt{\overline{U}_1} \approx 0.16$. Note that swimming with a prescribed beat amplitude and frequency, regardless of the rheology of the fluid, will not in general be achievable in a real biological system.

When μ_1 is zero, no dependence on initial orientation angle is observed and the mean swimming velocity takes on the Newtonian value, regardless of the size of the other parameters. For non-zero μ_1 certain initial orientation angles enable less energetically costly but slower swimming, with lower mean rates of working and swimming velocities. The initial angle maximising the mean swimming velocity and the mean rate of working are

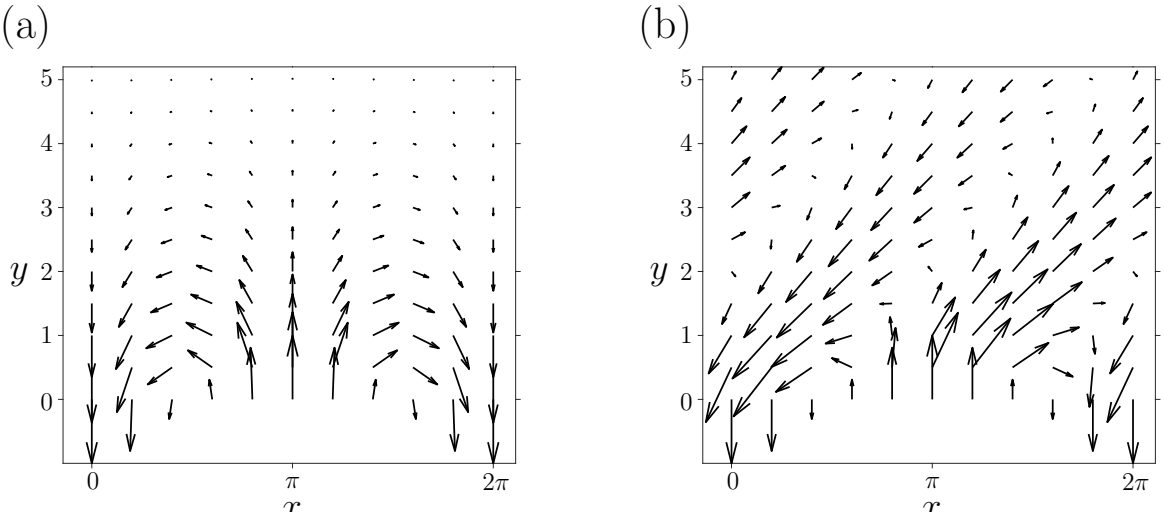

Figure 4.13: Velocity field in passive and active regimes: (a) passive regime ($\mu_1 = 0$, $\mu_2 = \mu_3 = 5$) (b) active-only regime ($\mu_1 = 5$, $\mu_2 = \mu_3 = 0$). In each graph $t = 0$ and the initial orientation angle is $\phi = 0$.

not in general the same. When active fibres are parallel to the swimming direction, swimming is both faster and more energetically costly compared to active fibres perpendicular to the swimming direction. The sheet utilises the surrounding environment to boost its velocity, a result seen in [57], for point-like obstacles, and for swimming in viscoelastic fluids near walls [15]. However, we also predict an increased swimming efficiency, a result not seen here.

A change from 'pusher' to 'puller' behaviour (equivalent to a change in sign of μ_1) equates to a reflection of the initial fibre angle in the y-axis. The activity parameter μ_1 allows the mean rate of working to take on negative values, suggesting that the tension/stresslet exerted by the fibres on the sheet may at times overcome the work the sheet does on the fluid to move. For some values of μ_1 the mean swimming velocity may be negative, indicating a reversal of swimming direction; this change is dependent on the uniform orientation angle ϕ, a result also observed for rotated viscoelastic networks [96]. The inclusion of active behaviour dramatically changes the streamlines and flow field.

For a passive transversely-isotropic fluid, *i.e.* $\mu_1 = 0$, increasing the magnitude of the viscosity-like parameters increases the work the sheet must do on the fluid to swim; the fluid becomes more difficult to move through. The mean rate of working was found

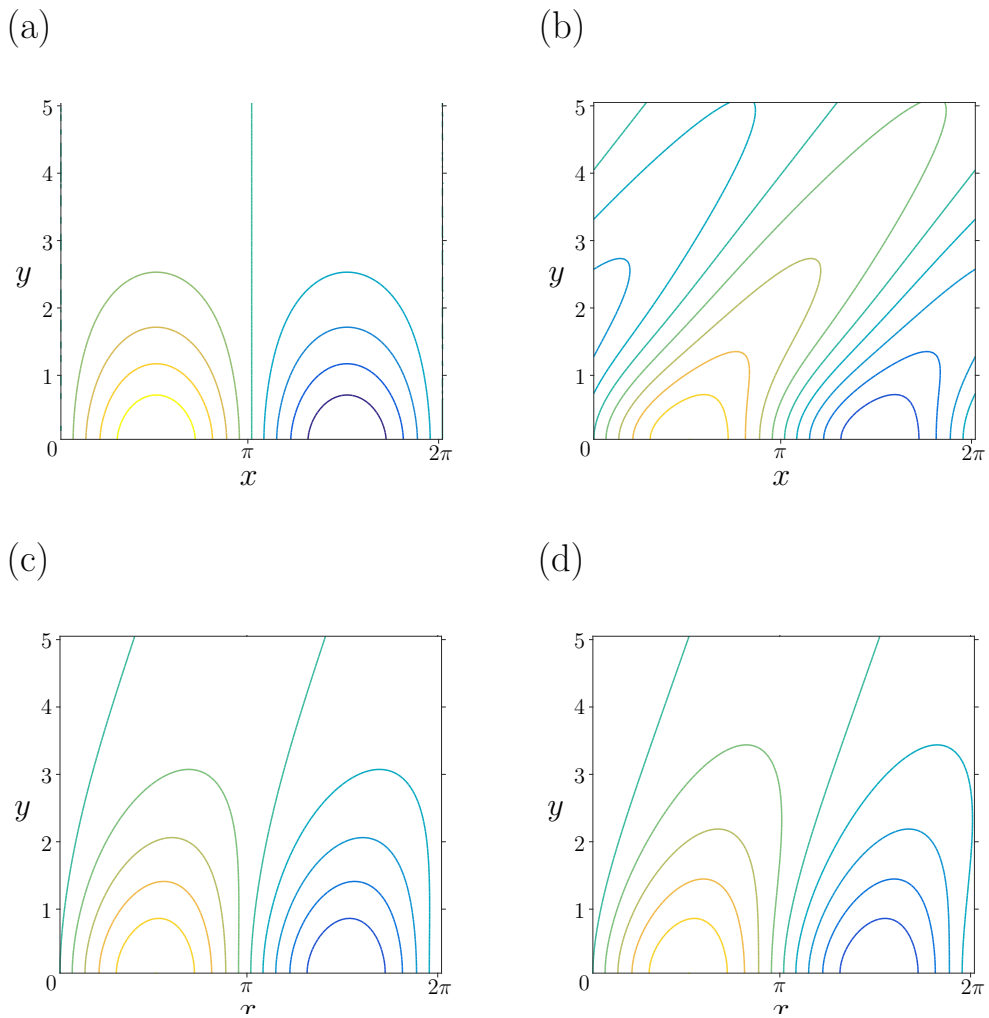

Figure 4.14: Instantaneous streamlines in the four regimes considered: (a) passive regime ($\mu_1 = 0$, $\mu_2 = \mu_3 = 5$), (b) active-only regime ($\mu_1 = 5$, $\mu_2 = \mu_3 = 0$), (c) nearly-isotropic regime ($\mu_1 = \mu_3 = 1$, $\mu_2 = 0$) and (d) regime where at least one of the parameters is much larger than one ($\mu_1 = \mu_2 = \mu_3 = 900$). In each graph $t = 0$ and the initial orientation angle is $\phi = 0$.

to be approximately linear in the parallel viscosity $\mu_{\parallel} = 1 + (\mu_2 + 4\mu_3)/2$, with a small additional dependence on μ_3. For an active isotropic fluid (μ_1 is non-zero and $\mu_2 = \mu_3 = 0$) we observe potentially unphysical behaviour when μ_1 is increased sufficiently, with rapid large variations with respect to ϕ in both mean swimming velocity and rate of working. Note however that a large value of μ_1 with $\mu_2 = \mu_3 = 0$ may not represent a physically realistic fluid. These unphysical effects are reduced by the inclusion of μ_3 in particular, and to a lesser extent μ_2, damping these large variations.

When the rheological parameters are all non-zero, increasing the anisotropic shear viscosity causes the mean swimming velocity to collapse down towards the Newtonian result, altered slightly by the active properties of the fluid. However the mean rate of working is increased in general. The anisotropic extensional viscosity has a similar but much smaller effect.

This study demonstrates that locomotion in active fluids is dramatically different from locomotion in passive fluids. Our finding of zero, and indeed negative rate of working for some angular configurations and sufficiently large values of the active parameter μ_1 is a consequence of the energy input to the system by active stress. This phenomenon may be related to superfluid behaviour recently observed in bacteria suspensions [59]. Further, these results are suggestive that active stresses in the bulk may enhance the motion of individual swimmers. It has long been known that some flagellated swimmers may propel more rapidly in polymeric than Newtonian fluids [84]. An increase in the anisotropy of the slender body drag coefficients has been proposed as one underlying mechanism [4, 62]; recently Martinez [67] demonstrated that viscosity reduction associated with high speed flagellar rotation provides an alternative explanation. The present model does not support a change to mean swimming speed purely through fluid anisotropy; because we analysed only 2D propulsion with constant viscosity-like parameters we are unable to comment on the effect of shear-thinning on rotation.

The passive region of parameter space with $\mu_1 = 0$ represents the anisotropic characteristics of the aligned passive microstructure of cervical mucus. Key aspects which

may be explored in future work include shear-dependent viscosity and dispersion of fibre alignment. The active regime $\mu_1 \neq 0$ may be considered as a model of motility through an active aligned medium, which may capture some of the essential physics of sperm migration through ciliated epithelium in the female reproductive tract. Our predictions could be tested experimentally by constructing an actuated membrane and studying the dynamics of an overlying suspension of swimming bacteria or microrods.

This study has opened up a number of exciting future research directions. These include (but are not limited to) investigating the effects of viscoelasticity [52], fibre dispersion [95] or the presence of walls [46]. Similarly, coupling the flagellar elastic behaviour to the viscous fluid mechanics to determine the effect on the beat pattern [78], or a full 3D computational treatment of the problem would be of interest since tumbling and rotating of the bacteriophage does not happen in only one plane. The model may also be developed to apply to peristaltic pumping by taking into account cylindrical tube geometry. Peristaltic pumping is a mechanism for inducing flow in channels, which is a method proposed to recirculate a sample in the device designed by Linear Dichroism Ltd. Taylor's swimming sheet has inspired decades of research into biological propulsion; the study presented here shows that Taylor's model continues to enable insight into novel areas of active fluid mechanics.

4.5.1 Summary

A summary of the findings in the current chapter are given here:

- For a passive suspension ($\mu_1 = 0$), no change in the mean swimming velocity was observed; the mean rate of working increased with both μ_2 and μ_3.

- For an active suspension, certain initial orientation angles proved more efficient for propulsion, however the sheet was seen to have a lower mean swimming velocity for these orientation angles.

- When the active parameter μ_1 is large and the other two parameters are small, potentially non-physical behaviour was observed; this was dampened by the inclusion of μ_2 and μ_3.

- Throughout all results, the anisotropic shear viscosity had a larger impact than the anisotropic extensional viscosity.

CHAPTER 5

CONCLUSION

This thesis has comprised two physical examples of fibre-laden fluids, the first being a flow device aimed at detecting pathogens in biological fluids. Bacteriophage, suspended in a fluid sample, are recirculated in a thin rectangular channel using a pumping device; the alignment induced from this flow leads to a specific linear dichroism signal. To efficiently detect pathogens the signal to noise ratio needs to be optimised, this can be done by increasing the alignment in the channel. The second is an investigation into microscopic propulsion in aligned fibrous media, biologically relevant to spermatozoa swimming through fibrous cervical mucus. Taylor's classical swimming sheet model is adapted to include an aligned fibrous fluid, similar to the alignment of glycofilaments in cervical mucus at certain stages in the menstrual cycle.

For chapters 2 and 3, models describing suspensions of fibres with a dispersion of orientation were used. This model, originally proposed by Batchelor [2, 3] and discussed by Hinch & Leal [35], comprised a contribution to the bulk stresses in a fluid due to suspended particles. Following Pedley & Kessler [76], the flow dynamics were coupled to the distribution of particle orientation, described by probability density function $\psi(\boldsymbol{p}, \boldsymbol{x}^*, t^*)$, via a Fokker-Planck equation; the moments of ψ were used to calculate the extra stress terms. Previous work has consisted of prescribing a flow, typically simple shear [55, 80] or parabolic Poiseuille flow [25], and calculating the distribution of orientation; here we have extended upon these works by iteratively coupling the flow and distribution equations

for more complex 3D channels and incorporated all bulk stresses associated with particle suspensions.

By considering uniform alignment and an average particle direction $\boldsymbol{a} = \langle \boldsymbol{p} \rangle$, the work by Pedley & Kessler was linked with Ericksen's transversely-isotropic fluid [24]; these equations are a limit of Pedley & Kessler's model for perfectly aligned media. This model was used in chapter 4, where we investigated propulsion through aligned cervical mucus. A transversely-isotropic fluid has a preferred direction; the properties of the fluid are identical normal to this preferred direction. Ericksen's model consists of extra stress terms, similar to those in Pedley & Kessler's model, but instead uses an equation for the evolution of the preferred direction. To examine propulsion through aligned media, Taylor's swimming sheet model was adapted to account for the extra stresses produced from an alignment of particles. Applying Taylor's model to non-Newtonian fluids is of significant interest; this work provides insight into microscopic propulsion in a different type of complex fluid, one displaying alignment and active properties. We summarise the work undertaken in this thesis here and outline possibilities for future work.

5.1 Summary of results

5.1.1 Flow-induced alignment in thin rectangular channels

Chapters 2 and 3 sought to calculate the degree of orientation, and hence the linear dichroism signal, of a bacteriophage suspension aligned due to the shear induced by flow in thin rectangular channels; the length of the channel is much longer than its width and depth. Passive M13 bacteriophage were suspended in a Newtonian fluid and so there was no active contribution to the flow. We began with a simple approximation in chapter 2, and improved on this to calculate and compare solutions to more accurate flow set-ups. To calculate the degree of orientation in the system, we defined an orientation parameter S related to the difference in alignment parallel and perpendicular to the flow direction. This

orientation parameter, suitable for biaxial samples, differed from that used by McLachlan et al. [68]; their definition, assuming a uniaxial sample, is not applicable to the biaxial orientation of particles in flow channels. Throughout both chapters, the velocity, degree of orientation and linear dichroism signal were compared for a range of parameter values

In chapter 2, we initially consider a 2D rectangular channel; the resulting flow problem, including the extra stress terms from [76], was coupled with the 2D Fokker-Planck equation. Steady flow, forced by a constant pressure gradient, and an oscillatory problem were considered. The steady flow equations were solved semi-analytically and coupled iteratively, initially taking a Newtonian flow profile. For oscillatory flow, a perturbation expansion in the volume fraction of particles reduced the flow problem to the Newtonian case, and hence de-coupled the equations; the Fokker-Planck equation was then solved using a Fourier transform and ODE solvers.

The results obtained using parameter values supplied by Linear Diagnostics Ltd indicated that the elongated particles prefer to align in the flow direction, as expected, and their alignment increases with increasing pressure gradient and channel depth for steady and slow oscillations. For larger oscillations, we found that inertial effects dominate the flow; the degree of orientation drastically reduces and the relationship with the channel width reverses so that increasing the channel width decreases the orientation. It was determined that this reversal occurs for oscillating frequencies larger than approximately $\omega^* = 30$ rad/s, beyond this inertial effects dominate the flow.

Linear dichroism signal is calculated by integrating the orientation over the depth of the channel; it is defined as the difference in absorption of light polarised parallel and perpendicular to the flow direction. We approximate the signal by calculating and comparing the degree of orientation in these directions; however, this needs to be in the plane in which the light source is pointing. Hence, to predict the linear dichroism signal, we considered a 3D system where a fibre-laden fluid is bound between two walls, with the light passing through the walls to obtain a signal. With this change we then coupled the flow problem, similar in nature to the 2D case previously discussed, with the 3D

Fokker-Planck equation, and dealt with steady and oscillatory problems. Steady flow is again solved semi-analytically, however the solution to the Fokker-Planck equation now follows McLachlan et al. [68] (and originally Strand, Kim & Karrila [87]); the distribution function was discretised spatially via spherical harmonics, which are the solution to the angular part of Laplace's equation. This discretisation lead to a system of equations that were written in matrix form and solved numerically. For oscillating flow, rather than expanding in terms of the volume fraction, the full problem was solved numerically via an implicit finite difference scheme. Using spherical harmonics, the Fokker-Planck equation reduces to a system of ordinary differential equations which are solved using inbuilt numerical solvers in Matlab. The degree of orientation was lower in comparison to the 2D approximation in the same chapter, due to the particles rotating out of the plane. Although the values of the variables of interest change, the general characteristics and key parameters that would affect the signal to noise ratio are similar.

In both cases, the orientation parameter used in [68] (equation (1.21)) was compared to the one defined in this work for steady flow. The degree of orientation predicted from the uniaxial equation for S was lower than that predicted by equation (1.20); in the 2D solution, the orientation parameter defined by McLachlan [68] also did not predict zero alignment at the centre of the channel as expected. We have shown that equation (1.21) is not an accurate prediction of the orientation in channel flow. We also found, for steady flow, that the orientation parameter appears to have an upper limit of $S \approx 0.74$ when increasing the channel depth and pressure gradient. This suggests there is a maximum possible alignment that can be achieved in the channel.

Expanding on this work, chapter 3 considers a full 3D channel, closely aligned with the industrial problem of a thin rectangular channel containing a fibre-laden fluid. Here, the width of the channel is now comparable to its height, while the length scale is still much larger. For both steady and oscillatory problems the flow was treated numerically; a finite difference discretisation was used to solve the flow problem, with an ADI method employed to deal with time derivatives in oscillating flow. As before, the Fokker-Planck

equation was solved by discretising spatially in the basis of spherical harmonics then solved at each point in the flow where the shear rate a particle experiences is assumed approximately constant. The work in this chapter proved to be far more computationally expensive and complex and so a smaller range of parameter space was taken, specifically for oscillating flow.

The trend of the results generally agreed with the work in chapter 2: increasing the pressure gradient increases the orientation, increasing the channel width for steady and small oscillations has the same effect; for large oscillations the channel depth has an inverse relationship with the orientation and signal. In general, oscillating flow produced a lower degree of alignment overall. Comparisons were made between the orientation parameter calculated in the 3D channel and the channel bound by two walls. At the centre of the channel the two are equivalent, however closer to the walls the orientation changes, since the shear rate in the channel is increased by including the channel width. By averaging over the width we deduced that the orientation produced by the 3D channel was higher than the simplified version. In general, to highlight the key parameters that influence changes in the orientation and signal in the system, the simplified channel model is acceptable; however, to accurately predict the degree of alignment in the channel, the 3D model discussed in chapter 3 would need to be considered.

Recommendations for Linear Diagnostics Ltd

Based on the work in chapters 2 and 3, we make the following recommendations for Linear Diagnostics Ltd to improve the signal to noise ratio in their handheld devices:

- Increasing the inlet pressure gradient and channel depth will lead to larger shear-induced alignment and hence a stronger signal in the steady flow case.
- Increasing the pressure gradient and channel depth beyond $G^* = 5 \times 10^4$ Pa/m and $h^* = 3 \times 10^{-3}$ m will no longer improve the alignment in the system.
- Tentatively we suggest increasing the volume fraction of bacteriophage in the sample

to increase the number of aligned particles passing under the light source. However, care must be taken here as more particles could lead to a higher degree of light scattering which increases the signal noise.

- The theoretical oscillatory case may be feasible if the fluid is oscillated slowly (*i.e.* $\omega^* \leq 30$ rad/s), the signal is reduced from the steady case but may still produce useful alignment.

5.1.2 Microscopic propulsion in transversely-isotropic media

The final part of this project focussed on a different problem, inspired by reproductive biology, and made use of the transversely-isotropic fluid model of Ericksen [24]. Spermatozoa must penetrate fibrous cervical mucus in many internally fertilising species; this glycofilament-mucin structure forms parallel networks due to hormonally induced changes in the hydration of the mucus at various stages in the menstrual cycle. The swimming of microscopic organisms like spermatozoa cannot occur through these fluids via inertial propulsion; a travelling wave traverses the tail of certain cells to aid propulsion. The classical Taylor's swimming sheet model, consisting of an infinite waving sheet in a Newtonian fluid at zero-Reynolds number, was adapted to account for aligned fibrous networks. Alongside the fluid problem, the evolution of fibre orientation due to the waving motion of the tail is calculated. To do this we use Ericksen's equations for a transversely isotropic fluid [24], which encapsulate a suspension of fibres with a preferred direction instead of a dispersion of orientation. This model was linked to the suspension model of Pedley & Kessler in chapter 1 and in recent work by Holloway et al. [39].

Following the outline of Taylor's established method, we expressed the velocity in terms of a stream function which satisfied the incompressibility condition. Inertial terms are neglected, due to zero Reynolds number swimming associated with microorganism propulsion, and a perturbation expansion about a small parameter ε is taken, equivalent to the wavenumber multiplied by the amplitude of the sheet. We arrive at a set of partial

differential equations accounting for the extra stress terms associated with the fibres, which agree with those derived by Taylor when the extra viscosity parameters are set to zero. These equations, describing the fluid velocity and fibre evolution, are solved at leading order to deduce the mean rate of working of the sheet, and at next order, by considering terms independent of time, to calculate the mean swimming velocity. We considered four regions of parameter space for the dimensionless active parameter (μ_1), anisotropic extensional viscosity (μ_2) and the anisotropic shear viscosity (μ_3): an active only region ($\mu_2 = \mu_3 = 0$), a passive region ($\mu_1 = 0$), a nearly isotropic region (μ_1, μ_2 and μ_3 are small) and a region where the parameters are greater than order one.

We found that the behaviour of a swimming sheet in a transversely-isotropic fluid was drastically different to Newtonian fluids. For a passive transversely-isotropic fluid, there was no change to the mean swimming velocity and the mean rate of working was found to increase with both the anisotropic extensional and shear viscosities; we believe this is due to an enhancement in the apparent viscosity of the fluid increasing the difficulty of swimming. For active fibres, *i.e.* those that self-propel, certain initial particle orientations prove more beneficial for swimming than others; the mean rate of working decreases for angles such as $\phi = 0$, though this also corresponds to a decrease in the mean swimming velocity.

For certain orientation angles and when μ_1 is sufficiently large, we found a reversal in the swimming direction and occasionally a negative mean rate of working, this may be due to the stresses produced by the fibre motility overcoming the work the sheet does on the fluid. This change in swimming direction has also been noted in rotated viscoelastic networks [96]. Throughout all results, the anisotropic shear viscosity had a far greater impact than the anisotropic extensional viscosity, notable when the active parameter μ_1 was large; here we see sharp positive and negative peaks in the mean swimming velocity and mean rate of working, which may represent unphysical behaviour, reduced more convincingly by μ_3 than μ_2. We believe that the extra stresses due to the glycofilaments may be acting as a selection process to choose the strongest swimming spermatozoa.

5.2 Future work

This thesis provides many interesting options for further investigation. For fibre alignment in 3D thin channel flow, the assumption of uniform distribution could be reassessed; if particles accumulate in certain areas of the channel it could alter the signal, and so a spatially dependent fibre concentration would be useful to visualise this. It is possible that the fibres interact and may become entangled which would actively reduce the alignment and linear dichroism signal; this could be accounted for by incorporating models of entanglement discussed in [56]. Another aspect that could be considered is investigating steady and oscillatory flows of an active suspension of particles, akin to modelling cells such as spermatozoa or *E. coli*.

Experimental validation of the predictions made in chapters 2 and 3 would be integral to improving our understanding of fibre-laden fluids in thin channels. Some experimental work has already been undertaken to qualitatively determine the change in signal when pathogens are added to a suspension of M13 bacteriophage. The bacteriophage were conjugated with Anti-Salmonella IgG antibody and AlexaFluor Dye 555 molecules then suspended in a 50mM potassium phosphate buffer. To test a fluid sample, the bacteriophage suspension is diluted in the fluid sample to a concentration around 0.02 g/l.

The diluted sample was tested in the AKTA pure chromatography system, a column chromatography system which separates different compounds in a sample depending on their structural characteristics. The column is filled with a solid or stationary phase where different compounds have varying binding affinities with this absorbent surface, depending on their polarity and structural characteristics. The solution to be tested is inserted into the top of the column and the components of the sample that are more attracted to the stationary phase will remain in the column for a longer period. At each stage, the sample leaving the column is processed using UV light to determine the amount of each component in the sample. The aim is to detect any unbound dye or antibody molecules that have not been removed from the system as they could disrupt the signal and give false positive results. The conjugation method appears to be effective, with the majority

(a) (b)

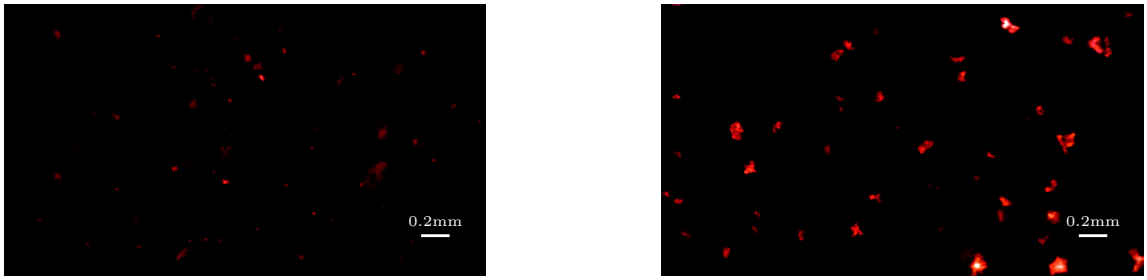

Figure 5.1: Fluorescence image of flow channel under 10× magnification. The bacteriophage in solution have dye molecules and salmonella specific antibodies attached to their surface. (a) A sample of bacteriophage, (b) a sample containing salmonella.

of the components being M13 bacteriophage. We then subject a further diluted sample (around one in one hundred of the 0.02 g/l solution) to fluorescence imaging to visualise the alignment of the bacteriophage and to understand how it changes when the anticipated pathogen is present. Thus far we have examined the fluid on both a microscope slide, in an attempt to image the bacteriophage, and in the flow channel itself.

When the flow channel contains a sample free from pathogens, the channel is mainly dark (figure 5.1a), a small number of light sources can be seen from the bacteriophage in the sample. When a concentration of salmonella is added to the fluid, the antibodies on the surface of the bacteriophage attach to a specific pathogen and so the bacteriophage in the sample congregate around the salmonella (figure 5.1b). It can clearly be seen that the system is working effectively since at first the bacteriophage do not appear to bundle together, then when salmonella are present the bacteriophage collect at the pathogen and the resulting bundles can be seen more clearly. These bundles are not elongated molecules that will align properly in flow and so will result in a drop in signal, which has been detected on the prototype handheld reader. We seek to track the orientation and any collective behaviour of bacteriophage in channel flow; to obtain a detailed image, a camera of higher resolution is necessary. There are various other predictions that would be beneficial to verify experimentally, including determining if the maximum degree of alignment can be achieved and if this matches our prediction. Further, the impact of

particle number density on the signal and noise, due to light diffraction, could be tested experimentally; increasing the number of particles should increase the signal however the effect on the light diffraction must be determined.

For the adaptation of Taylor's swimming sheet, there are a number of possible research opportunities; considering a numerical simulation of 3D geometries is one interesting option. We could also examine motility in a suspension of active or passive particles by coupling Taylor's model with a Fokker-Planck equation; this would also require numerical solution. An investigation into the effects of non-Newtonian fluids such as viscoelastic fluids or fluids with shear dependent viscosities would aid in modelling a range of biological fluids. Finally, the model could be extended to describe peristaltic pumping by considering circular geometry.

Suspensions of particles in biological media occur in a variety of situations; models of these suspensions can be used as a method to predict pathogen detection or to describe microscopic propulsion in fibrous biological media. It is important to understand how the flow of these suspensions varies from Newtonian fluids in order to accurately predict how the particles impact their environment. We believe this work provides an insight into the flow-induced alignment of particles, and how the alignment of a fluid can impact the swimming of microorganisms.

APPENDIX A

THE DISCRETE FOURIER TRANSFORM METHOD FOR SOLVING PARTIAL DIFFERENTIAL EQUATIONS

To demonstrate the use of fast Fourier transforms to solve ordinary differential equations, consider the advection-diffusion equation with constant coefficients,

$$y_t + uy_x = y_{xx}, \tag{A.1}$$

subject to periodic boundary conditions. To solve this, take the Fourier transform of y,

$$y(x,t) = \sum_{k=-L}^{L} Y_k(t) e^{ikx}, \tag{A.2}$$

$$Y_k(t) = \frac{1}{2\pi} \int_0^{2\pi} y(x,t) e^{-ikx} \, \mathrm{d}x, \tag{A.3}$$

for integer L and where, (A.2) is the Fourier transform and (A.3) is its inverse. Substituting (A.2) into (A.1) we obtain an ordinary differential equation

$$\frac{\mathrm{d}Y_k}{\mathrm{d}t} + ikuY_k = -k^2 Y_k, \tag{A.4}$$

this is solved using an integrating factor to give

$$Y_k(t) = Y_k(0) \exp(-k(iu + k)t), \tag{A.5}$$

where $Y_k(0)$ is the transformed initial condition; this initial condition is expressed by writing the integral of the inverse Fourier transform using the left hand rule,

$$\begin{aligned} Y_k(0) &= \frac{1}{2\pi}\int_0^{2\pi} y(x,0)e^{-ikx}\,\mathrm{d}x \\ &\approx \frac{1}{2\pi}\sum_{j=1}^{M} y\left(\frac{2\pi(j-1)}{M},0\right)e^{-ik\left(\frac{2\pi(j-1)}{M}\right)}\frac{2\pi}{M} \\ &\approx \frac{1}{M}\sum_{j=1}^{M} y\left(\frac{2\pi(j-1)}{M},0\right)e^{-ik\left(\frac{2\pi(j-1)}{M}\right)}, \end{aligned} \tag{A.6}$$

where $M = 2L+1$. Let $\omega_M = \exp(\frac{-2\pi i}{M})$, then

$$Y_k(0) \approx \frac{1}{M}\sum_{j=1}^{M} y\left(\frac{2\pi(j-1)}{M},0\right)\omega_M^{k(j-1)}. \tag{A.7}$$

Currently, the Fourier transform contains a sum from $k=-L$ to L, however to numerically solve the problem in Matlab, the negative values (the first M entries) must be shifted along to $L+1,\ldots 2L$.

For $-L \le k \le -1$,

$$\begin{aligned} \omega_M^{(j-1)(k-M)} &= \omega_M^{(j-1)k}\omega_M^{-(j-1)M} \\ &= \omega_M^{(j-1)k}e^{\frac{2\pi i}{M}(j-1)M} \\ &= \omega_M^{(j-1)k}e^{2\pi i(j-1)} \\ &= \omega_M^{(j-1)k}, \end{aligned} \tag{A.8}$$

Since j is an integer, $e^{2\pi i(j-1)} = 1$ for all j; we can add or subtract multiples of M without altering the solution. Hence, for $L+1 \le k \le 2L$, we rewrite (A.7) as

$$Y_k(0) = \frac{1}{M}\sum_{j=1}^{M} y\left(\frac{2\pi(j-1)}{M},0\right)\omega_M^{(j-1)(k-M)}. \tag{A.9}$$

In Matlab, the notation used is

$$v0(j) = y\left(\frac{2\pi(j-1)}{M}, 0\right), \quad j = 1, 2, \ldots L \tag{A.10}$$

$$V0(k+1) = \begin{cases} \frac{1}{M}\sum_{j=1}^{M} v0(y)\omega_M^{(j-1)k} & 0 \le k \le M \\ \\ \frac{1}{M}\sum_{j=1}^{M} v0(y)\omega_M^{(j-1)(k-M)} & L+1 \le k \le 2L, \end{cases} \tag{A.11}$$

which can be computed numerically using the fast Fourier transform function

$$V0 = \frac{1}{M}\text{fft}(v0). \tag{A.12}$$

The solution is then given as

$$V(k+1) = \begin{cases} Y_k(t) & 0 \le k \le L \\ \\ Y_{k-M}(t) & L+1 \le k \le 2L, \end{cases} \tag{A.13}$$

where Y_k are given by (A.5). The initial conditions are

$$\begin{aligned} Y_k(0) &= V0(k+1), \quad k = 0, 1, \ldots L, \\ Y_{k-M}(0) &= V0(k+1), \quad k = L+1, L+2, \ldots 2L+1. \end{aligned} \tag{A.14}$$

Let $l = k - M$, then

$$\begin{aligned} k+1 &= l + M + 1 \\ &= l + 2L + 2, \end{aligned}$$

then the initial condition can be written as

$$\begin{aligned} Y_l(0) = V0(l+2L+2), \qquad & l = L+1-M, \ldots, 2L-M \\ & = L+1-2L-1, \ldots, 2L-2L-1 \\ & = -L, \ldots, -1 \end{aligned} \tag{A.15}$$

The solution steps are taken in the following order:

$$V0 \xrightarrow[(A.14)]{} Y_k(0) \xrightarrow[(A.5)]{} Y_k(t) \xrightarrow[(A.13)]{} V. \tag{A.16}$$

Once the solution has been calculated, the inverse transform is taken to convert back to the solution for (A.1). This is done as follows,

$$y\left(\frac{2\pi(j-1)}{M}, t\right) = \sum_{k=-L}^{L} Y_k(t) e^{ik\frac{2\pi(j-1)}{M}} = \sum_{k=-L}^{L} Y_k(t)\omega_M^{-(j-1)k}. \tag{A.17}$$

To numerically evaluate (A.17), we again change the summation limits to $k = 1, \ldots M+1$ by splitting the limit of integration,

$$\begin{aligned} y\left(\frac{2\pi(j-1)}{M}, t\right) &= \sum_{k=0}^{L} Y_k(t)\omega_M^{-(j-1)k} + \sum_{k=-L}^{-1} Y_k(t)\omega_M^{-(j-1)k} \\ &= \sum_{k=1}^{L+1} Y_k(t)\omega_M^{-(j-1)(k-1)} + \sum_{k=-L}^{-1} Y_k(t)\omega_M^{-(j-1)k}. \end{aligned} \tag{A.18}$$

Consider the second sum, the limits must be $k = L+1$ to $2L+1$. Let $l = k+2L+2 = k+M+1$, then $l = L+2, \ldots 2L+1$.

$$\begin{aligned} y\left(\frac{2\pi(j-1)}{M}, t\right) &= \sum_{k=1}^{L+1} Y_{k-1}(t)\omega_M^{-(j-1)(k-1)} + \sum_{l=L+2}^{2L+1} Y_{l-M-1}(t)\omega_M^{-(j-1)(l-M-1)} \\ &= \underbrace{\sum_{k=1}^{L+1} V(k,:)\omega_M^{-(j-1)(k-1)} + \sum_{l=L+2}^{2L+1} V(l,:)\omega_M^{-(j-1)(l-1)}}_{\text{can be combined}} \end{aligned} \tag{A.19}$$

using (A.13) to write the solution in terms of V. Combining the two sums and using the inverse fast Fourier transform, as each time step, the solution to the original problem is

$$y\left(\frac{2\pi(j-1)}{M}, t\right) = \sum_{k=1}^{2L+1} V(k,:)\omega_M^{-(j-1)(k-1)} = M\,\text{ifft}(V). \tag{A.20}$$

This method can be applied to the more complex Fokker-Planck equation, following the same steps and incorporating non-constant coefficients.

A.1 Peak orientation parameter and linear dichroism signal over one time period in oscillating flow

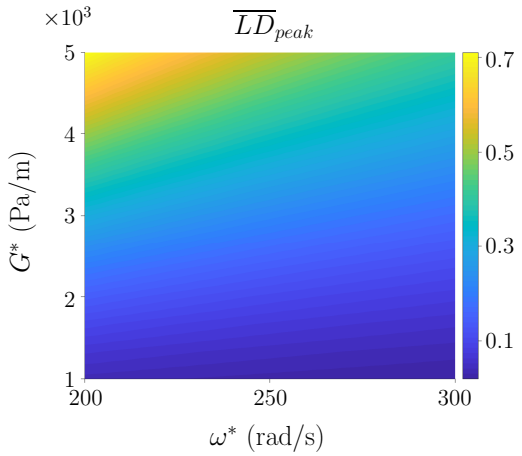

Figure A.1: Peak Linear dichroism signal, over one time period, for a range of inlet pressure gradient and oscillating frequency. The channel depth and number density remain the same, $h^* = 3 \times 10^{-4}$ m and $n_d^* = 7.33 \times 10^{17}$ phage/m^3 respectively.

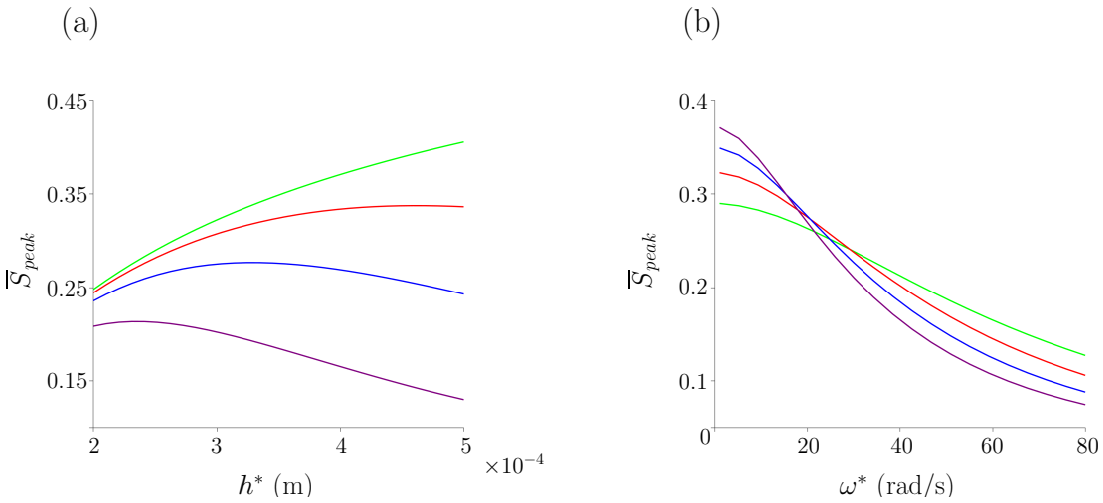

Figure A.2: Peak orientation parameter, over one time period, changing with channel depth and oscillating frequency. (a) $\overline{S}_{peak}$ changing with channel width for multiple oscillating frequencies: $\omega^* = 1$ rad/s (green line), $\omega^* = 10$ rad/s (red line), $\omega^* = 20$ rad/s (blue line) and $\omega^* = 40$ rad/s (purple line). (b) $\overline{S}_{av}$ changing with oscillating frequency for multiple h^* values: $h^* = 2.5 \times 10^{-4}$ m (green line), $h^* = 3 \times 10^{-4}$ m (red line), $h^* = 3.5 \times 10^{-4}$ m (blue line), $h^* = 4 \times 10^{-4}$ m (purple line). The pressure gradient is $G^* = 4.4 \times 10^3$ Pa/m and the number density is $n_d^* = 7.33 \times 10^{17}$ phage/m^3 throughout.

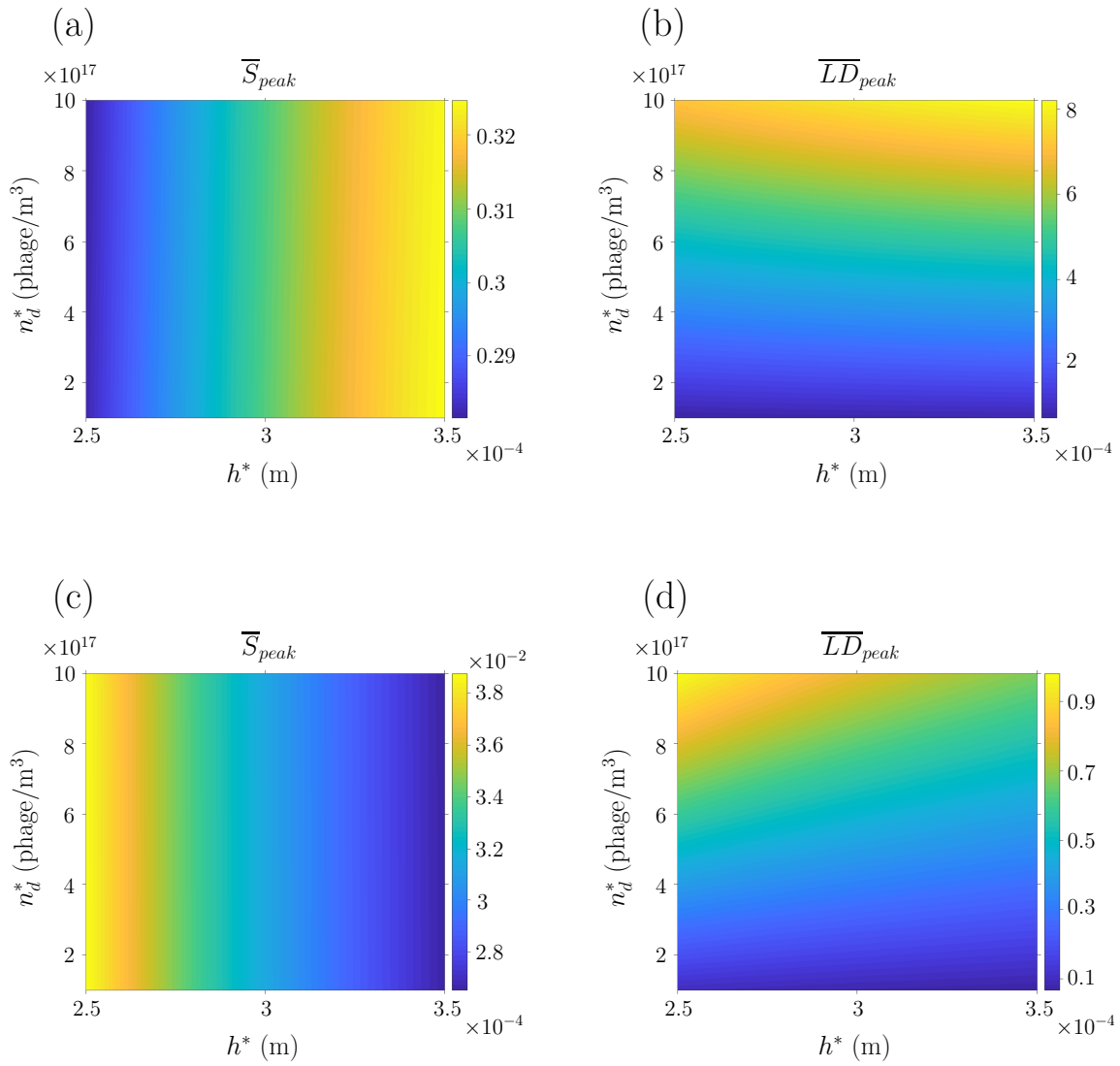

Figure A.3: Peak orientation parameter and linear dichroism signal, over one time period, for a range of particle number density and channel depth. (a) and (c) $\overline{S}_{peak}$ and (b) and (d) $\overline{LD}_{peak}$. The pressure gradient is $G^* = 4.4 \times 10^3$ Pa/m and the oscillating frequency is $\omega^* = 10$ rad/s for (a) and (b) and $\omega^* = 200$ rad/s for (c) and (d).

APPENDIX B

MATRIX ENTRIES FOR THE FINITE DIFFERENCE DISCRETISATION OF THE FIBRE-LADEN FLOW PROBLEM

B.1 Finite difference matrix entries for steady flow of a suspension

The matrices (3.41)-(3.43) have entries in terms of (3.34)-(3.39) and are dependent on the sign of $\boldsymbol{G}$ (equation (3.35)) and $\boldsymbol{H}$ (equation (3.36)). The coefficient for the mixed derivatives does not change and is given by $E_{i,j} = L_{i,j}/4\Delta y\Delta z$. The other coefficients can be summarised for each case as follows:

For $G_{i,j}$, $H_{i,j} \geq 0$,

$$\begin{aligned} C_{i,j}^{(0,0)} =& -2\left(\frac{J_{i,j}}{\Delta y^2}+\frac{K_{i,j}}{\Delta z^2}\right)+\frac{G_{i,j}}{\Delta y}+\frac{H_{i,j}}{\Delta z}, \qquad C_{i,j}^{(e,0)} = \frac{J_{i,j}}{\Delta y^2}, \\ C_{i,j}^{(w,0)} =& \frac{J_{i,j}}{\Delta y^2}-\frac{G_{i,j}}{\Delta y}, \qquad C_{i,j}^{(0,e)} = \frac{K_{i,j}}{\Delta z^2}, \qquad C_{i,j}^{(0,w)} = \frac{K_{i,j}}{\Delta z^2}-\frac{H_{i,j}}{\Delta z}. \end{aligned} \tag{B.1}$$

For $G_{i,j} \geq 0$ and $H_{i,j} < 0$,

$$\begin{aligned} C_{i,j}^{(0,0)} =& -2\left(\frac{J_{i,j}}{\Delta y^2}+\frac{K_{i,j}}{\Delta z^2}\right)+\frac{G_{i,j}}{\Delta y}-\frac{H_{i,j}}{\Delta z}, \qquad C_{i,j}^{(e,0)} = \frac{J_{i,j}}{\Delta y^2}, \\ C_{i,j}^{(w,0)} =& \frac{J_{i,j}}{\Delta y^2}-\frac{G_{i,j}}{\Delta y}, \qquad C_{i,j}^{(0,e)} = \frac{K_{i,j}}{\Delta z^2}+\frac{H_{i,j}}{\Delta z}, \qquad C_{i,j}^{(0,w)} = \frac{K_{i,j}}{\Delta z^2}. \end{aligned} \tag{B.2}$$

For $G_{i,j} < 0$ and $H_{i,j} \geq 0$,

$$C_{i,j}^{(0,0)} = -2\left(\frac{J_{i,j}}{\Delta y^2} + \frac{K_{i,j}}{\Delta z^2}\right) - \frac{G_{i,j}}{\Delta y} + \frac{H_{i,j}}{\Delta z}, \qquad C_{i,j}^{(e,0)} = \frac{J_{i,j}}{\Delta y^2} + \frac{G_{i,j}}{\Delta y},$$
$$C_{i,j}^{(w,0)} = \frac{J_{i,j}}{\Delta y^2}, \qquad C_{i,j}^{(0,e)} = \frac{K_{i,j}}{\Delta z^2}, \qquad C_{i,j}^{(0,w)} = \frac{K_{i,j}}{\Delta z^2} - \frac{H_{i,j}}{\Delta z}. \tag{B.3}$$

For $G_{i,j}$, $H_{i,j} < 0$,

$$C_{i,j}^{(0,0)} = -2\left(\frac{J_{i,j}}{\Delta y^2} + \frac{K_{i,j}}{\Delta z^2}\right) - \frac{G_{i,j}}{\Delta y} - \frac{H_{i,j}}{\Delta z}, \qquad C_{i,j}^{(e,0)} = \frac{J_{i,j}}{\Delta y^2} + \frac{G_{i,j}}{\Delta y},$$
$$C_{i,j}^{(w,0)} = \frac{J_{i,j}}{\Delta y^2}, \qquad C_{i,j}^{(0,e)} = \frac{K_{i,j}}{\Delta z^2} + \frac{H_{i,j}}{\Delta z}, \qquad C_{i,j}^{(0,w)} = \frac{K_{i,j}}{\Delta z^2}. \tag{B.4}$$

B.2 Matrix entries for oscillating flow of suspensions

To calculate the velocity of pressure-driven flow of a suspension of elongated bacteriophage, we utilise an ADI method, discretising using finite differences and splitting the time step in half. In the first half-time step, the problem is solved implicitly in y and explicitly in z and mixed derivatives. In the second half time step, the problem is solved implicitly in z, where the explicit terms are the solution to the first equation at the intermediate time step. The matrix entries and right hand side vector depend upon the sign of the coefficients of the single derivatives and are summarised here.

For the first time step, the coefficients of each term in equation (3.59) are given by (3.34)-(3.39). The operator matrix is given by (3.58) and the terms are dependent on the sign of $\boldsymbol{G}$ as follows:

For $G_{i,j}^{n+1/2} \geq 0$,

$$C_0 = 1 + \frac{\Delta t}{\alpha^2 \Delta y}\left(\frac{J_{i,j}^{n+1/2}}{\Delta y} - \frac{G_{i,j}^{n+1/2}}{2}\right), \quad C_e = -\frac{\Delta t J_{i,j}^{n+1/2}}{\alpha^2 \Delta y^2},$$
$$C_w = -\frac{\Delta t}{\alpha^2 \Delta y^2}\left(\frac{J_{i,j}^{n+1/2}}{\Delta y} - G_{i,j}^{n+1/2}\right). \tag{B.5}$$

For $G_{i,j}^{n+1/2} < 0$,

$$C_0 = 1 + \frac{\Delta t}{\alpha^2 \Delta y}\left(\frac{J_{i,j}^{n+1/2}}{\Delta y} + \frac{G_{i,j}^{n+1/2}}{2}\right), \quad C_e = -\frac{\Delta t}{\alpha^2 \Delta y^2}\left(\frac{J_{i,j}^{n+1/2}}{\Delta y} + G_{i,j}^{n+1/2}\right), \\ C_w = -\frac{\Delta t J_{i,j}^{n+1/2}}{\alpha^2 \Delta y^2}. \tag{B.6}$$

The right hand side vector is given by

$$b_i = b_0^n u_{i,j}^n + b_e^n u_{i,j+1}^n + b_w^n u_{i,j-1}^n + \frac{\Delta t}{2\alpha^2}\left(F_{i,j}^{n+1/2} - \exp(i(t^{n+1/2} + \pi/2))\right) \\ + \frac{\Delta t L_{i,j}^n}{8\alpha^2 \Delta y \Delta z}(u_{i+1,j+1}^n - u_{i-1,j+1}^n - u_{i+1,j-1}^n + u_{i-1,j-1}^n), \tag{B.7}$$

where for $H_{i,j}^n \geq 0$,

$$b_0 = 1 - \frac{\Delta t}{\alpha^2 \Delta z}\left(\frac{K_{i,j}^n}{\Delta z} - \frac{H_{i,j}^n}{2}\right), \quad b_e = \frac{\Delta t K_{i,j}^n}{2\alpha^2 \Delta z^2}, \quad b_w = \frac{\Delta t}{2\alpha^2 \Delta z}\left(\frac{K_{i,j}^n}{\Delta z} - H_{i,j}^n\right), \tag{B.8}$$

and for $H_{i,j}^n < 0$,

$$b_0 = 1 - \frac{\Delta t}{\alpha^2 \Delta z}\left(\frac{K_{i,j}^n}{\Delta z} + \frac{H_{i,j}^n}{2}\right), \quad b_e = \frac{\Delta t}{2\alpha^2 \Delta z^2}\left(\frac{K_{i,j}^n}{\Delta z} + H_{i,j}^n\right), \quad b_w = \frac{\Delta t K_{i,j}^n}{2\alpha^2 \Delta z}. \tag{B.9}$$

The second time step is constructed similarly; the coefficients of the operator matrix can be defined as follows: For $H_{i,j}^{n+1} \geq 0$,

$$C_0 = 1 + \frac{\Delta t}{\alpha^2 \Delta z}\left(\frac{K_{i,j}^{n+1}}{\Delta z} - \frac{H_{i,j}^{n+1}}{2}\right), \quad C_e = -\frac{\Delta t K_{i,j}^{n+1}}{\alpha^2 \Delta z^2}, \\ C_w = -\frac{\Delta t}{\alpha^2 \Delta z^2}\left(\frac{K_{i,j}^{n+1}}{\Delta z} - H_{i,j}^{n+1}\right). \tag{B.10}$$

For $H_{i,j}^{n+1} < 0$,

$$C_0 = 1 + \frac{\Delta t}{\alpha^2 \Delta z}\left(\frac{K_{i,j}^{n+1}}{\Delta y} + \frac{H_{i,j}^{n+1}}{2}\right), \quad C_e = -\frac{\Delta t}{\alpha^2 \Delta z^2}\left(\frac{K_{i,j}^{n+1}}{\Delta z} + H_{i,j}^{n+1}\right), \\ C_w = -\frac{\Delta t K_{i,j}^{n+1}}{\alpha^2 \Delta z^2}. \tag{B.11}$$

The right hand side vector is given by

$$\begin{aligned} b_j =& b_0^{n+1/2} u_{i,j}^{n+1/2} + b_e^{n+1/2} u_{i,j+1}^{n+1/2} + b_w^{n+1/2} u_{i,j-1}^{n+1/2} \\ &+ \frac{\Delta t}{2\alpha^2}\left(F_{i,j}^{n+1} - \exp(i(t^{n+1} + \pi/2))\right) \\ &+ \frac{\Delta t L_{i,j}^{n+1/2}}{8\alpha^2 \Delta y \Delta z}(u_{i+1,j+1}^{n+1/2} - u_{i-1,j+1}^{n+1/2} - u_{i+1,j-1}^{n+1/2} + u_{i-1,j-1}^{n+1/2}), \end{aligned} \tag{B.12}$$

where for $G_{i,j} \geq 0$,

$$b_0 = 1 - \frac{\Delta t}{\alpha^2 \Delta y}\left(\frac{J_{i,j}^{n+1/2}}{\Delta y} - \frac{G_{i,j}^{n+1/2}}{2}\right), \quad b_e = \frac{\Delta t J_{i,j}^{n+1/2}}{2\alpha^2 \Delta y^2}, \\ b_w = \frac{\Delta t}{2\alpha^2 \Delta y}\left(\frac{J_{i,j}^{n+1/2}}{\Delta y} - G_{i,j}^{n+1/2}\right), \tag{B.13}$$

and for $G_{i,j} < 0$,

$$b_0 = 1 - \frac{\Delta t}{\alpha^2 \Delta y}\left(\frac{J_{i,j}^{n+1/2}}{\Delta y} + \frac{G_{i,j}^{n+1/2}}{2}\right), \quad b_e = \frac{\Delta t}{2\alpha^2 \Delta y^2}\left(\frac{J_{i,j}^{n+1/2}}{\Delta y} + G_{i,j}^{n+1/2}\right), \\ b_w = \frac{\Delta t J_{i,j}^{n+1/2}}{2\alpha^2 \Delta y}. \tag{B.14}$$

APPENDIX C

COMPONENTS OF THE ERICKSEN STRESS TENSOR FOR SMALL AMPLITUDE PROPULSION

C.1 Components of the stress tensor

Assuming that the velocity takes the form $\boldsymbol{u} = (u(x, y, t), v(x, y, t))$, the components of the stress tensor are calculated as,

$$\begin{aligned}\sigma_{11} = &-p + \mu_1(\cos\phi - \theta\sin\phi)^2 + \big(2 + \mu_2(\cos\phi - \theta\sin\phi)^4 \\ &+4\mu_3(\cos\phi - \theta\sin\phi)^2\big)\frac{\partial u}{\partial x} + \Big(\mu_2(\cos\phi - \theta\sin\phi)^3(\sin\phi + \theta\cos\phi) \\ &+ 2\mu_3(\cos\phi - \theta\sin\phi)(\sin\phi + \theta\cos\phi)\Big)\left(\frac{\partial u}{\partial y} + \frac{\partial v}{\partial y}\right) \\ &+ \mu_2(\cos\phi - \theta\sin\phi)^2(\sin\phi + \theta\cos\phi)^2\frac{\partial v}{\partial y}\,,\end{aligned} \tag{C.1}$$

$$
\begin{aligned}
\sigma_{12} &= \sigma_{21} \\
&= \mu_1(\cos\phi - \theta\sin\phi)(\sin\phi + \theta\cos\phi) \\
&+ \left(1 + \mu_2(\cos\phi - \theta\sin\phi)^2(\sin\phi + \theta\cos\phi)^2 + \mu_3(1-\theta^2)\right)\left(\frac{\partial u}{\partial y} + \frac{\partial v}{\partial x}\right) \\
&+ \mu_2(\cos\phi - \theta\sin\phi)^3(\sin\phi + \theta\cos\phi)\,\frac{\partial u}{\partial x} \\
&+ \mu_2(\cos\phi - \theta\sin\phi)(\sin\phi + \theta\cos\phi)^3\,\frac{\partial v}{\partial y}\,,
\end{aligned}
\tag{C.2}
$$

$$
\begin{aligned}
\sigma_{22} = &-p + \mu_1(\sin\phi + \theta\cos\phi)^2 + \big(2 + \mu_2(\sin\phi + \theta\cos\phi)^4 \\
&+4\mu_3(\sin\phi + \theta\cos\phi)^2\big)\,\frac{\partial v}{\partial y} + \Big(\mu_2(\cos\phi - \theta\sin\phi)(\sin\phi + \theta\cos\phi)^3 \\
&2\mu_3(\cos\phi - \theta\sin\phi)(\sin\phi + \theta\cos\phi)\Big)\left(\frac{\partial u}{\partial y} + \frac{\partial v}{\partial x}\right) \\
&+ \mu_2(\cos\phi - \theta\sin\phi)^2(\sin\phi + \theta\cos\phi)^2\,\frac{\partial u}{\partial x}\,.
\end{aligned}
\tag{C.3}
$$

C.2 Eigenvalue matrix entries for $\mathcal{O}(\varepsilon)$ swimming

The components of the matrix $\boldsymbol{L}$ in equation (4.35) are calculated as

$$
\begin{aligned}
L_{11} =&(1 + \frac{\mu_2}{4}\sin^2 2\phi + \mu_3)(\lambda^4 - 2\lambda^2 + 1) - \mu_2\lambda^2\cos 4\phi \\
&+ \mu_1\left[2\sin 2\phi(\lambda\cos^2\phi - \lambda^3\sin^2\phi) + (\lambda + \lambda^3)\cos 2\phi\sin 2\phi\right],
\end{aligned}
\tag{C.4}
$$

$$
\begin{aligned}
L_{12} = &-\mu_1\left[2\lambda^2\sin^2 2\phi + \cos 2\phi((\lambda^2 + \lambda^4)\sin^2\phi - (1 + \lambda^2)\cos^2\phi)\right] \\
&+ \frac{\mu_2}{2}(\lambda^3 + \lambda)\sin 4\phi,
\end{aligned}
\tag{C.5}
$$

where $L_{22} = L_{11}$ and $L_{21} = -L_{12}$.

C.3 Governing equation for $\mathcal{O}(\varepsilon^2)$ swimming

The balance of (4.16) at order ε^2 is given by

$$
\begin{aligned}
&(1+\frac{\mu_2}{4}\sin^2 2\phi+\mu_3)\nabla^4\psi_1-\mu_1\left(2\sin 2\phi\,\frac{\partial^2\theta_1}{\partial x\partial y}+\cos 2\phi\left(\frac{\partial^2\theta_1}{\partial x^2}-\frac{\partial^2\theta_1}{\partial y^2}\right)\right)\\
&+\mu_2\left(\cos 4\phi\,\frac{\partial^4\psi_1}{\partial x^2\partial y^2}+\frac{\sin 4\phi}{2}\left(\frac{\partial^4\psi_1}{\partial x\partial y^3}-\frac{\partial^4\psi_1}{\partial x^3\partial y}\right)\right)\\
&-\mu_1\left[2\sin 2\phi\left(\theta_0\left(\frac{\partial^2\theta_0}{\partial y^2}-\frac{\partial^2\theta_0}{\partial x^2}\right)+\left(\frac{\partial\theta_0}{\partial y}\right)^2-\left(\frac{\partial\theta_0}{\partial x}\right)^2\right)\right.\\
&\qquad\left.+4\cos 2\phi\left(\frac{\partial\theta_0}{\partial x}\,\frac{\partial\theta_0}{\partial y}+\theta_0\,\frac{\partial^2\theta_0}{\partial x\partial y}\right)\right]-\mu_2\left[\sin 4\phi\left(2\,\frac{\partial^2\theta_0}{\partial x\partial y}\,\frac{\partial^2\psi_0}{\partial x\partial y}\right.\right.\\
&\quad-\frac{\theta_0}{2}\left(\frac{\partial^4\psi_0}{\partial x^4}-6\,\frac{\partial^4\psi_0}{\partial x^2\partial y^2}+\frac{\partial^4\psi_0}{\partial y^4}\right)+\frac{1}{2}\left(\frac{\partial^2\theta_0}{\partial x^2}-\frac{\partial^2\theta_0}{\partial y^2}\right)\left(\frac{\partial^2\psi_0}{\partial y^2}-\frac{\partial^2\psi_0}{\partial x^2}\right)\\
&\qquad-\frac{\partial\theta_0}{\partial y}\left(\frac{\partial^3\psi_0}{\partial y^3}-3\,\frac{\partial^3\psi_0}{\partial x^2\partial y}\right)+\frac{\partial\theta_0}{\partial x}\left(3\,\frac{\partial^3\psi_0}{\partial x\partial y^2}-\frac{\partial^3\psi_0}{\partial x^3}\right)\Big)\\
&\qquad+\cos 4\phi\left(2\theta_0\left(\frac{\partial^4\psi_0}{\partial x^3\partial y}-\frac{\partial^4\psi_0}{\partial x\partial y^3}\right)+\left(\frac{\partial^2\theta_0}{\partial x^2}-\frac{\partial^2\theta_0}{\partial y^2}\right)\frac{\partial^2\psi_0}{\partial x\partial y}\right.\\
&\qquad-\frac{\partial\theta_0}{\partial x}\left(\frac{\partial^3\psi_0}{\partial y^3}-3\,\frac{\partial^3\psi_0}{\partial x^2\partial y}\right)-\frac{\partial\theta_0}{\partial y}\left(3\,\frac{\partial^3\psi_0}{\partial x\partial y^2}-\frac{\partial^3\psi_0}{\partial x^3}\right)\\
&\qquad\left.\left.\left.-\frac{\partial^2\theta_0}{\partial x\partial y}\left(\frac{\partial^2\psi_0}{\partial y^2}-\frac{\partial^2\psi_0}{\partial x^2}\right)\right)\right]=0.
\end{aligned}
\tag{C.6}
$$

LIST OF REFERENCES

[1] KL Aubrey and GJ Thomas Jr. Raman spectroscopy of filamentous bacteriophage Ff (fd, m13, f1) incorporating specifically-deuterated alanine and tryptophan side chains. Assignments and structural interpretation. *Biophys J*, 60(6):1337–1349, 1991.

[2] GK Batchelor. The stress system in a suspension of force-free particles. *J Fluid Mech*, 41(3):545–570, 1970.

[3] GK Batchelor. The stress generated in a non-dilute suspension of elongated particles by pure straining motion. *J Fluid Mech*, 46(4):813–829, 1971.

[4] HC Berg and L Turner. Movement of microorganisms in viscous environments. *Nature*, 278:349–351, 1979.

[5] RB Bird, RC Armstrong, O Hassager, and CF Curtiss. *Dynamics of polymeric liquids*, volume 1. Wiley New York, 1977.

[6] G Böhme and R Friedrich. Peristaltic flow of viscoelastic liquids. *J Fluid Mech*, 128:109–122, 1983.

[7] BM Bulheller, A Rodger, and JD Hirst. Circular and linear dichroism of proteins. *Phys Chem Chem Phys*, 9(17):2020–2035, 2007.

[8] F Ceric, D Silva, and P Vigil. Ultrastructure of the human periovulatory cervical mucus. *J Electron Microsc*, 54(5):479–484, 2005.

[9] TK Chaudhury. On swimming in a visco–elastic liquid. *J Fluid Mech*, 95(01):189–197, 1979.

[10] C Chauviere and A Lozinski. Simulation of complex viscoelastic flows using the Fokker–Planck equation: 3D FENE model. *J Non-Newton Fluid*, 122(1):201–214, 2004.

[11] SB Chen and DL Koch. Rheology of dilute suspensions of charged fibers. *Phys Fluids*, 8(11):2792–2807, 1996.

[12] K Chiba, K Yasuda, and K Nakamura. Numerical solution of fiber suspension flow through a parallel plate channel by coupling flow field with fiber orientation distribution. *J Non-Newton Fluid*, 99(2):145–157, 2001.

[13] F Chinesta, G Chaidron, and A Poitou. On the solution of Fokker–Planck equations in steady recirculating flows involving short fiber suspensions. *J Non-Newton Fluid*, 113(2):97–125, 2003.

[14] FC Chrétien. Sperm cell–cervical mucus interaction. In ESE Hafez and P Kenemans, editors, *Atlas of Human Reproduction*, pages 219–222. Springer, 1982.

[15] JC Chrispell, LJ Fauci, and M Shelley. An actuated elastic sheet interacting with passive and active structures in a viscoelastic fluid. *Phys Fluids*, 25(1):013103, 2013.

[16] G Cupples, RJ Dyson, and DJ Smith. Viscous propulsion in active transversely isotropic media. *J Fluid Mech*, 812:501–524, 2017.

[17] S Dong, X Feng, M Salcudean, and I Gartshore. Concentration of pulp fibers in 3D turbulent channel flow. *Int J Multiph Flow*, 29(1):1–21, 2003.

[18] J Douglas and Donald W Peaceman. Numerical solution of two-dimensional heat-flow problems. *AIChE J*, 1(4):505–512, 1955.

[19] R Dreyfus, J Baudry, ML Roper, M Fermigier, HA Stone, and J Bibette. Microscopic artificial swimmers. *Nature*, 437(7060):862–865, 2005.

[20] JE Drummond. Propulsion by oscillating sheets and tubes in a viscous fluid. *J Fluid Mech*, 25(04):787–793, 1966.

[21] RJ Dyson, JEF Green, JP Whiteley, and HM Byrne. An investigation of the influence of extracellular matrix anisotropy and cell–matrix interactions on tissue architecture. *J Math Biol*, pages 1–35, 2015.

[22] RJ Dyson and OE Jensen. A fibre-reinforced fluid model of anisotropic plant cell growth. *J Fluid Mech*, 655:472–503, 2010.

[23] WA Eaton and J Hofrichter. Polarized absorption and linear dichroism spectroscopy of hemoglobin. *Method Enzymol*, 76:175–261, 1981.

[24] JL Ericksen. Transversely isotropic fluids. *Colloid Polym Sci*, 173(2):117–122, 1960.

[25] B Ezhilan and D Saintillan. Transport of a dilute active suspension in pressure–driven channel flow. *J Fluid Mech*, 777:482–522, 2015.

[26] LJ Fauci and R Dillon. Biofluidmechanics of reproduction. *Annu Rev Fluid Mech*, 38:371–394, 2006.

[27] HC Fu, TR Powers, and CW Wolgemuth. Theory of swimming filaments in viscoelastic media. *Phys Rev Lett*, 99(25):258101, 2007.

[28] HC Fu, CW Wolgemuth, and TR Powers. Swimming speeds of filaments in nonlinearly viscoelastic fluids. *Phys Fluids*, 21(3):033102, 2009.

[29] Győző Garab and Herbert van Amerongen. Linear dichroism and circular dichroism in photosynthesis research. *Photosyn Res*, 101(2-3):135–146, 2009.

[30] MJ Glucksman, S Bhattacharjee, and L Makowski. Three-dimensional structure of a cloning vector: X-ray diffraction studies of filamentous bacteriophage M13 at 7 å resolution. *J Mol Biol*, 226(2):455–470, 1992.

[31] JEF Green and A Friedman. The extensional flow of a thin sheet of incompressible, transversely isotropic fluid. *Eur J Appl Math*, 19(03):225–257, 2008.

[32] T Hayat, N Ali, and Z Abbas. Peristaltic flow of a micropolar fluid in a channel with different wave forms. *Phys Lett A*, 370(3):331–344, 2007.

[33] NA Hill and MA Bees. Taylor dispersion of gyrotactic swimming micro-organisms in a linear flow. *Phys Fluids*, 14(8):2598–2605, 2002.

[34] NA Hill and TJ Pedley. Bioconvection. *Fluid Dyn Res*, 37(1):1–20, 2005.

[35] EJ Hinch and LG Leal. The effect of Brownian motion on the rheological properties of a suspension of non-spherical particles. *J Fluid Mech*, 52(4):683–712, 1972.

[36] EJ Hinch and LG Leal. Time–dependent shear flows of a suspension of particles with weak Brownian rotations. *J Fluid Mech*, 57(4):753–767, 1973.

[37] EJ Hinch and LG Leal. Constitutive equations in suspension mechanics. Part 1. General formulation. *J Fluid Mech*, 71(03):481–495, 1975.

[38] EJ Hinch and LG Leal. Constitutive equations in suspension mechanics. Part 2. Approximate forms for a suspension of rigid particles affected by Brownian rotations. *J Fluid Mech*, 76(01):187–208, 1976.

[39] CR Holloway, G Cupples, DJ Smith, JEF Green, RJ Clarke, and RJ Dyson. Influences of transversely–isotropic rheology and translational diffusion on the stability of active suspension. *Under review with Eur Phys J E*, 2018.

[40] CR Holloway, RJ Dyson, and DJ Smith. Linear Taylor–Couette stability of a transversely isotropic fluid. *P Roy Soc Lond A Mat*, 471(2178), 2015.

[41] Y Hwang and TJ Pedley. Bioconvection under uniform shear: linear stability analysis. *J Fluid Mech*, 738:522–562, 2014.

[42] T Ishikawa and TJ Pedley. The rheology of a semi–dilute suspension of swimming model micro-organisms. *J Fluid Mech*, 588:399–435, 2007.

[43] MY Jaffrin and AH Shapiro. Peristaltic pumping. *Ann Rev Fluid Mech*, 3(1):13–37, 1971.

[44] GB Jeffery. The motion of ellipsoidal particles immersed in a viscous fluid. *Proc R Soc Lond A*, 102(715):161–179, 1922.

[45] MR Kamal and AT Mutel. The prediction of flow and orientation behavior of short fiber reinforced melts in simple flow systems. *Polym Composite*, 10(5):337–343, 1989.

[46] DF Katz. On the propulsion of micro–organisms near solid boundaries. *J Fluid Mech*, 64(01):33–49, 1974.

[47] J Kim, S Michelin, M Hilbers, L Martinelli, E Chaudan, G Amselem, E Fradet, J Boilot, AM Brouwer, CN Baroud, et al. Monitoring the orientation of rare–earth–doped nanorods for flow shear tomography. *Nat Nanotechnol*, 2017.

[48] DL Koch and G Subramanian. Collective hydrodynamics of swimming microorganisms: Living fluids. *Annu Rev Fluid Mech*, 43:637–659, 2011.

[49] MS Krieger, MA Dias, and TR Powers. Minimal model for transient swimming in a liquid crystal. *Eur Phys J E*, 38(8):1–9, 2015.

[50] MS Krieger, SE Spagnolie, and T Powers. Microscale locomotion in a nematic liquid crystal. *Soft Matt*, 11(47):9115–9125, 2015.

[51] MS Krieger, SE Spagnolie, and TR Powers. Locomotion and transport in a hexatic liquid crystal. *Phys Rev E*, 90(5):052503, 2014.

[52] K Kruse, J-F Joanny, F Jülicher, J Prost, and K Sekimoto. Generic theory of active polar gels: a paradigm for cytoskeletal dynamics. *Eur Phys J E*, 16(1):5–16, 2005.

[53] E Lauga. Propulsion in a viscoelastic fluid. *Phys Fluids*, 19(8):083104, 2007.

[54] E Lauga and TR Powers. The hydrodynamics of swimming microorganisms. *Rep Prog Phys*, 72(9):096601, 2009.

[55] LG Leal and EJ Hinch. The rheology of a suspension of nearly spherical particles subject to Brownian rotations. *J Fluid Mech*, 55(04):745–765, 1972.

[56] MEM Lee and H Ockendon. A continuum model for entangled fibres. *Eur J Appl Math*, 16(02):145–160, 2005.

[57] AM Leshansky. Enhanced low–Reynolds-number propulsion in heterogeneous viscous environments. *Phys Rev E*, 80(5):051911, 2009.

[58] FM Leslie. Some constitutive equations for liquid crystals. *Arc Rational Mech Anal*, 28(4):265–283, 1968.

[59] HM López, J Gachelin, C Douarche, H Auradou, and E Clément. Turning bacteria suspensions into superfluids. *Phys Rev Lett*, 115(2):028301, 2015.

[60] A Lozinski, RG Owens, and J Fang. A Fokker–Planck-based numerical method for modelling non-homogeneous flows of dilute polymeric solutions. *J Non-Newton Fluid*, 122(1):273–286, 2004.

[61] PS Lykoudis and R Roos. The fluid mechanics of the ureter from a lubrication theory point of view. *J Fluid Mech*, 43(4):661–674, 1970.

[62] Y Magariyama and S Kudo. A mathematical explanation of an increase in bacterial swimming speed with viscosity in linear–polymer solutions. *Biophys J*, 83(2):733–739, 2002.

[63] M Manhart. Rheology of suspensions of rigid–rod like particles in turbulent channel flow. *J Non-Newton Fluid*, 112(2):269–293, 2003.

[64] MJ Manton. Long-wavelength peristaltic pumping at low Reynolds number. *J Fluid Mech*, 68(3):467–476, 1975.

[65] JM Marchal and MJ Crochet. A new mixed finite element for calculating viscoelastic flow. *J Non-Newton Fluid*, 26(1):77–114, 1987.

[66] C Marchioli, M Fantoni, and A Soldati. Orientation, distribution, and deposition of elongated, inertial fibers in turbulent channel flow. *Phys Fluids*, 22(3):033301, 2010.

[67] VA Martinez, J Schwarz-Linek, M Reufer, LG Wilson, AN Morozov, and WCK Poon. Flagellated bacterial motility in polymer solutions. *P Natl Acad Sci*, 111(50):17771–17776, 2014.

[68] JRA McLachlan, DJ Smith, NP Chmel, and A Rodger. Calculations of flow-induced orientation distributions for analysis of linear dichroism spectroscopy. *Soft Matter*, 9(20):4977–4984, 2013.

[69] PH Mortensen, HI Andersson, JJJ Gillissen, and BJ Boersma. Dynamics of prolate ellipsoidal particles in a turbulent channel flow. *Phys Fluids*, 20(9):093302, 2008.

[70] Z Niu, MA Bruckman, B Harp, CM Mello, and Q Wang. Bacteriophage m13 as a scaffold for preparing conductive polymeric composite fibers. *Nano Res*, 1(3):235–241, 2008.

[71] B Nordén. *Circular dichroism and linear dichroism*, volume 1. Oxford University Press, USA, 1997.

[72] B Norden, M Kubista, and T Kurucsev. Linear dichroism spectroscopy of nucleic acids. *Q Rev Biophys*, 25(1):51–170, 1992.

[73] OS Pak and E Lauga. The transient swimming of a waving sheet. *Proc R Soc Lond A*, 466(2113):107–126, 2010.

[74] RL Panton. *Incompressible flow*. New Jersey: John Wiley & Sons Inc, 2004.

[75] AE Patteson, A Gopinath, and PE Arratia. Active colloids in complex fluids. *Curr Opin Colloid In*, 21:86–96, 2016.

[76] TJ Pedley and JO Kessler. A new continuum model for suspensions of gyrotactic micro-organisms. *J Fluid Mech*, 212:155–182, 1990.

[77] C Pozrikidis. A study of peristaltic flow. *J Fluid Mech*, 180:515–527, 1987.

[78] EE Riley and E Lauga. Enhanced active swimming in viscoelastic fluids. *Europhys Lett*, 108(3):34003, 2014.

[79] EE Riley and E Lauga. Small–amplitude swimmers can self-propel faster in viscoelastic fluids. *J Theor Biol*, 382:345–355, 2015.

[80] D Saintillan. The dilute rheology of swimming suspensions: A simple kinetic model. *Exp Mech*, 50(9):1275–1281, 2010.

[81] D Saintillan. Extensional rheology of active suspensions. *Phys Rev E*, 81(5):056307, 2010.

[82] D Saintillan and MJ Shelley. Instabilities, pattern formation, and mixing in active suspensions. *Phys Fluids*, 20(12):123304, 2008.

[83] D Saintillan and MJ Shelley. Active suspensions and their nonlinear models. *C R Phys*, 14(6):497–517, 2013.

[84] WR Schneider and RN Doetsch. Effect of viscosity on bacterial motility. *J Bacteriol*, 117(2):696–701, 1974.

[85] AH Shapiro, MY Jaffrin, and SL Weinberg. Peristaltic pumping with long wavelengths at low Reynolds number. *J Fluid Mech*, 37(4):799–825, 1969.

[86] CA Stover, DL Koch, and C Cohen. Observations of fibre orientation in simple shear flow of semi-dilute suspensions. *J Fluid Mech*, 238:277–296, 1992.

[87] SR Strand, S Kim, and SJ Karrila. Computation of rheological properties of suspensions of rigid rods: stress growth after inception of steady shear flow. *J Non-Newton Fluid*, 24(3):311–329, 1987.

[88] G Subramanian, DL Koch, and SR Fitzgibbon. The stability of a homogeneous suspension of chemotactic bacteria. *Phys Fluids*, 23(4):041901, 2011.

[89] S Takabatake and K Ayukawa. Numerical study of two-dimensional peristaltic flows. *J Fluid Mech*, 122:439–465, 1982.

[90] GI Taylor. Analysis of the swimming of microscopic organisms. *Proc R Soc Lond A*, 209(1099):447–461, 1951.

[91] GI Taylor. The action of waving cylindrical tails in propelling microscopic organisms. *Proc R Soc Lond A*, 211(1105):225–239, 1952.

[92] J Teran, L Fauci, and M Shelley. Peristaltic pumping and irreversibility of a Stokesian viscoelastic fluid. *Phys Fluids*, 20(7):073101, 2008.

[93] J Teran, L Fauci, and M Shelley. Viscoelastic fluid response can increase the speed and efficiency of a free swimmer. *Phys Rev Lett*, 104(3):038101, 2010.

[94] JR Vélez-Cordero and E Lauga. Waving transport and propulsion in a generalized Newtonian fluid. *J Non-Newton Fluid*, 199:37–50, 2013.

[95] FG Woodhouse and RE Goldstein. Spontaneous circulation of confined active suspensions. *Phys Rev Lett*, 109(16):168105, 2012.

[96] JK Wróbel, S Lynch, A Barrett, L Fauci, and R Cortez. Enhanced flagellar swimming through a compliant viscoelastic network in Stokes flow. *J Fluid Mech*, 792:775–797, 2016.

[97] F Zhao and BGM Van Wachem. Direct numerical simulation of ellipsoidal particles in turbulent channel flow. *Acta Mech*, 224(10):2331–2358, 2013.